HEAT TRANSPORT EXPERIMENTS ON THE HSX STELLARATOR

by

Gavin McCabe Weir

A dissertation submitted in partial fulfillment of

the requirements for the degree of

Doctor of Philosophy

(Electrical Engineering)

at the

University of Wisconsin–Madison

2014

Date of final oral examination: 12/4/2014

The dissertation is approved by the following members of the Final Oral Committee:
David T. Anderson, Professor, Electrical Engineering
William N. Hitchon, Professor, Electrical Engineering
Chris C. Hegna, Professor, Engineering Physics
Paul W. Terry, Professor, Physics
Konstantin M. Likin, Senior Scientist, Electrical Engineering

ABSTRACT

It has been observed in tokamaks that temperature profiles are resilient to changes in heating, and that this effect has not been observed in conventional stellarators. Electron temperature profile resiliency is attributed to anomalous transport driven by turbulent micro-instabilities, and the resulting stiffness in the electron heat flux is measured using a combination of steady-state and perturbative experiments. In this work, stiffness measurements are presented in the quasihelically symmetric configuration of the Helically Symmetric eXperiment (HSX), in which the neoclassical transport is comparable to a tokamak and turbulent transport dominates throughout the plasma. A second gyrotron and transmission line have been installed and tested to facilitate modulated heating experiments on HSX, and a multi-pass absorption model accurately predicts the total absorption and spatial extent of the electron cyclotron resonance heating during a modulation experiment. The electron cyclotron emission measured by an absolutely calibrated 16-channel radiometer is used to measure the local electron temperature and its response to the modulated heating. The amplitude and phase of the heat wave through the foot of the steep electron temperature gradient region of the plasma, $0.2 \leq r/a \leq 0.4$, are used to determine a transient electron thermal diffusivity that is close to the steady-state diffusivity. The low stiffness in this region agrees with the scaling of the steady-state electron heat flux with temperature gradient. The results from these experiments are compared to gyrokinetic calculations using the GENE code with two kinetic species. Linear calculations demonstrate that the Trapped Electron Mode (TEM) is the dominant long-wavelength microturbulence instability across most of the plasma, and the TEM is primarily driven by the density gradient. The measured heat flux is comparable to the saturated heat flux driven by the TEM in non-linear calculations.

ACKNOWLEDGMENTS

Thank you to my parents, Michael and Lois, for their support, encouragement, and very effective (if slightly strange) motivation, as well as my sisters, Michaela and Larina, for their enduring friendship. Thank you to my Uncle Paul whose editing help (including early morning phone calls), ensured that I put pen to paper.

Thank you to the students and staff of the HSX stellarator for their friendship, support and participation over the course of this research. I'd specifically like to thank Dr. Konstantin Likin, who was extensively involved in all aspects of this research, and Benjamin Faber, who performed the gyrokinetic simulations used in this work.

...

Skol, Vikings

DISCARD THIS PAGE

TABLE OF CONTENTS

Page

Appendix

Page

DISCARD THIS PAGE

LIST OF TABLES

DISCARD THIS PAGE

LIST OF FIGURES

Appendix
Figure Page

Appendix
Figure Page

Appendix
Figure Page

Chapter 1

Introduction and Motivation

Tokamaks and stellarators each have qualities that are desirable for fusion reactors. Tokamaks have good single-particle confinement, as well as simple coils, and have been built extensively at low-aspect ratio, whereas stellarators are intrinsically steady-state devices that have no need for a driven current. A stellarator reactor will have low-recirculated power because no power will be required to drive a toroidal current, and a stellarator reactor will not have the disruptions that are caused by current driven instabilities in tokamaks. Quasi-symmetric devices possess a direction of symmetry in their magnetic field strength, and quasi-symmetry combines the benefits of the conventional stellarator with good single-particle confinement at low collisionality.

The Helically Symmetric eXperiment (HSX) is the worlds first and only operational quasi-symmetric stellarator. Quasi-symmetry is predicted to reduce the neoclassical transport of conventional stellarators at low-collisionality where direct loss orbits lead to unacceptable losses for a magnetic confinement fusion reactor [1]. HSX is designed to produce a Quasi-Helically Symmetric (QHS) configuration [2], and transport in the QHS configuration has been shown to be reduced in comparison with a conventional stellarator [3]. Consequently, anomalous transport is dominant in the QHS configuration of HSX [4].

It has been observed in tokamaks that temperature profiles are resilient to changes in heating, and this phenomenon is attributed to anomalous transport driven by turbulent micro-instabilities. Profile resiliency, or stiffness in the electron heat flux, has not been observed in conventional stellarators. Perturbative heat transport experiments can be used to measure the local variation of the heat flux as a function of temperature gradient, whereas steady-state heat transport experiments are used to measure the total heat flux. Together, perturbative and steady-state heat transport experiments can be used to measure the stiffness in the electron heat flux, and to investigate the role of turbulent microinstabilities in heat transport. The heat transport driven by drift wave turbulence such as the Electron Temperature Gradient (ETG) mode and the Trapped Electron Mode (TEM) are candidates to explain the experimental heat transport in HSX [5] [6], and the physics goal of this work is to measure the stiffness in the electron heat flux in the QHS configuration of HSX, and compare these results to linear and non-linear gyrokinetic simulations.

A heating source that is capable of modulated electron heating, and an electron temperature diagnostic with sufficient resolution are necessary to perform heat pulse propagation experiments. The absolutely calibrated electron cyclotron emission diagnostic is used to measure the electron temperature and its response to modulation heating, and the analysis of the diagnostic is described in Chapter 3. The installation and testing of a second transmission line for electron cyclotron resonance heating is described in Chapter 4. The power launched from the second antenna is modulated during heat pulse propagation experiments on HSX and measurements and modeling of the absorbed power profile are also presented in Chapter 4. Results from modulated heating experiments in HSX are presented, along with the experimental and analytical techniques used in their analysis, in Chapter 5. These results are compared to linear and non-linear simulations of the TEM and ETG mode in

Chapter 6. The results from this dissertation are summarized in Section 7.1, and additional work beyond that reported in this dissertation is proposed in Section 7.2.

The importance of electron heat transport in fusion plasma is discussed in Section 1.1, and electron heat transport in magnetically confined devices is described in Section 1.2. The HSX stellarator is described in Section 1.3, and this section includes a brief introduction to quasi-helical symmetry, as well as previous electron heat transport experiments and modeling on HSX. The differences between steady state and perturbative experiments are discussed in Section 1.4, and this section includes a selected review of perturbative heat transport experiments and stiffness measurements in stellarators and tokamaks.

1.1 The Importance of Electron Heat Transport in Fusion Plasma

Heat and particle losses from magnetically confined plasmas are commonly characterized as classical, neoclassical or anomalous transport. Classical transport is the diffusive transport caused by collisions in homogeneous fields, and neoclassical transport is the additional transport caused by magnetic field inhomogeneity in toroidal devices. Any remaining experimental transport is considered anomalous. The sourcing of fuel and the removal of impurities in a fusion reactor depends on particle transport, while the size of the reactor is primarily driven by thermal transport [7], making accurate predictions of the heat transport necessary for fusion experiments. Electron heat transport is particularly important because the alpha-particles generated in fusion experiments, such as the Deuterium-Tritium fusion reaction, damp their energy primarily onto the bulk electron population. The electrons must then be confined in the reactor long enough to thermalize with the ions, drive additional fusion reactions, and achieve a burning plasma in which the reactions are self-sustaining.

Anomalous transport typically dominates the electron channel for heat and is thought to be turbulent and driven by plasma microinstabilities. Microinstabilities contribute to

the inverse cascade of energy from small-scale fluctuations to large-scale turbulent eddies, which serve to increase the level of particle and thermal loss observed in experiments. This transport of heat and particles is one of the greatest hurdles to the implementation of magnetically confined fusion as an energy source. Understanding and controlling the anomalous transport driven by micro-instabilities would contribute significantly to the development of an economical fusion reactor.

1.2 Thermal Transport

The evolution of particle densities, n_s, and pressures, p_s, for a particle species, s, in a plasma may be expressed in conservative form as

$$\frac{\partial n_s}{\partial t} + \vec{\nabla} \cdot \vec{\Gamma}_s = \sum S, \tag{1.1}$$

$$\frac{3}{2}\frac{\partial p_s}{\partial t} + \vec{\nabla} \cdot \vec{q}_s = \sum Q, \tag{1.2}$$

where $\vec{\Gamma}_s$, $\vec{q}_s$ represent the particle and heat flux respectively, and the right is a sum over sources and sinks of particles (S) and heat (Q). Thermodynamic forces drive these fluxes and currents through interactions with the plasma, which in general can be represented as a matrix of transport coefficients,

$$-\begin{pmatrix} \vec{\Gamma} \\ \vec{q_e}/n_e \\ \vec{q_i}/n_i \\ \vec{j}_\parallel \end{pmatrix} = \begin{pmatrix} D & L_{1,2} & L_{1,3} & W \\ L_{2,1} & \chi_e & L_{2,3} & L_{2,4} \\ L_{3,1} & L_{3,2} & \chi_i & L_{3,4} \\ B & L_{4,2} & L_{4,3} & \sigma \end{pmatrix} \begin{pmatrix} \nabla n \\ \nabla T_e \\ \nabla T_i \\ E_\parallel \end{pmatrix}. \tag{1.3}$$

Here $\vec{\Gamma}, \vec{q_e}$, and $\vec{q_i}$ represent the cross-field particle and heat fluxes, while $\vec{j}_\parallel$ and $\vec{E}_\parallel$ represent the current and electric field parallel to the magnetic field. The gradients are taken perpendicular to the flux surfaces [7]. Experimental estimates of transport coefficients are commonly derived from steady-state measurements in which the transport matrix is

assumed to be diagonal. These effective diffusion coefficients contain all the parametric dependencies of the transport matrix. Perturbative transport experiments allow greater access to off-diagonal terms that contribute to "convective" transport than steady-state transport experiments alone, and are discussed in the context of power-balance thermal analysis versus heat pulse propagation analysis in Section 1.4.

The transport coefficients of Equation 1.3 include contributions from classical, neoclassical, and anomalous transport. The study of anomalous electron heat transport requires accurate calculation of the classical and neoclassical contributions to the total transport, so that the anomalous heat transport may be determined.

1.2.1 Neoclassical Transport

The strong inverse temperature dependence of classical transport causes the lowest collisionality regime to be the most relevant to fusion reactors. In an inhomogeneous magnetic field, a particle's energy may be written using its velocity parallel to a field line and the magnetic moment, $\mu = \frac{mv_\perp^2}{2B}$ (which remains constant to maintain the magnetic flux through the Larmor orbit in analogy with a current loop) as $E = \frac{1}{2}m_s v_\parallel^2 + \mu B$.

Due to the conservation of energy and the conservation of the magnetic moment, a particle that moves into a region of increasing magnetic flux density, B, will speed up in the direction perpendicular to the magnetic field line, $v_\perp$, and slow down in the direction parallel to the magnetic field line, $v_\parallel$. If the increase in magnetic field strength is great enough, the particle will reflect as its parallel velocity passes through zero and changes sign. In this way, inhomogeneous magnetic fields cause particles to mirror between regions of varying magnetic field densities when their velocities parallel to the field are insufficient to pass through regions of increasing magnetic field strength. At low collisionality, these trapped particles have their orbits altered by the varying magnetic field and undergo banana orbits which are named for

their characteristic shape. The step length in a random walk is the banana width, which is larger than the gyroradius in toroidal geometry [8] [9].

In the low-collisionality regime, or Long Mean Free Path (LMFP) regime, diffusion in a conventional stellarator and a tokamak scale differently. Tokamaks have axisymmetric magnetic fields; consequently, particles undergoing banana orbits have no net drift radially unless they undergo a collision. Neoclassical particle diffusion monotonically decreases with decreasing collision frequency. Conventional stellarators do not generally possess a direction of symmetry in their magnetic field strength, and particles drift radially outward while undergoing banana orbits due to the asymmetry in the turning points.

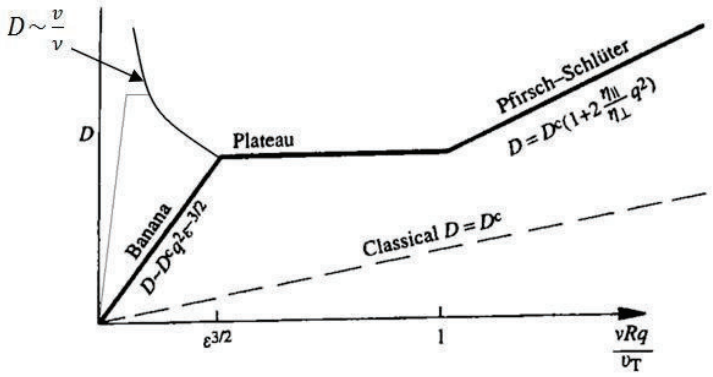

Figure 1.1: Neoclassical diffusion coefficient scaling vs normalized collision frequency, $\frac{\nu_e}{\nu_{tr}} = \frac{\nu Rq}{v_t}$. Adapted from [9] to include $1/\nu$ stellarator scaling at low collisionality.

This neoclassical transport increases as collisionality decreases, resulting in $1/\nu$ neoclassical transport in the LMFP regime for stellarators, which is illustrated in Figure 1.1. In this regime, diffusion increases strongly with increasing temperature, $D_{\perp,1/\nu} \propto B^{-2}T^{7/2}$, making classical stellarators an unappealing fusion reactor concept. Non-ambipolar transport, meaning that the loss of electrons and ions is not necessarily equal [10], leads to a radial electric field that acts to suppress the $1/\nu$ neoclassical transport in stellarators [11] [12] [13]. This effect is illustrated in Figure 1.2. Turbulence, fast ion orbit loss, highly localized ECRH, and

asymmetry in the magnetic field strength can drive transport that is not intrinsically ambipolar, and radial electric fields arises as ambipolar transport develops in the steady-state [14].

Neglecting contributions from impurities, the neoclassical particle flux, Γ_s^{nc}, and heat flux, Q_s^{nc}, are

$$\frac{\Gamma_s^{nc}}{n_s} = -\left[D_{11}^s\left(\frac{n_s'}{n_s} - \frac{q_s E_r}{T_s}\right) + D_{12}^s\frac{T_s'}{T_s}\right], \tag{1.4}$$

$$\frac{Q_s^{nc}}{n_s T_s} = -\left[D_{21}^s\left(\frac{n_s'}{n_s} - \frac{q_s E_r}{T_s}\right) + D_{22}^s\frac{T_s'}{T_s}\right]. \tag{1.5}$$

Here E_r is the radial electric field. The neoclassical transport coefficients, D_{11}, D_{12}, D_{21} and D_{22}, are calculated for use on HSX from the mono-energetic transport coefficients from the Drift Kinetic Equation Solver (DKES) [15]. The neoclassical diffusion coefficients result from energy convolution of the mono-energetic coefficients over a Maxwellian distribution function [11].

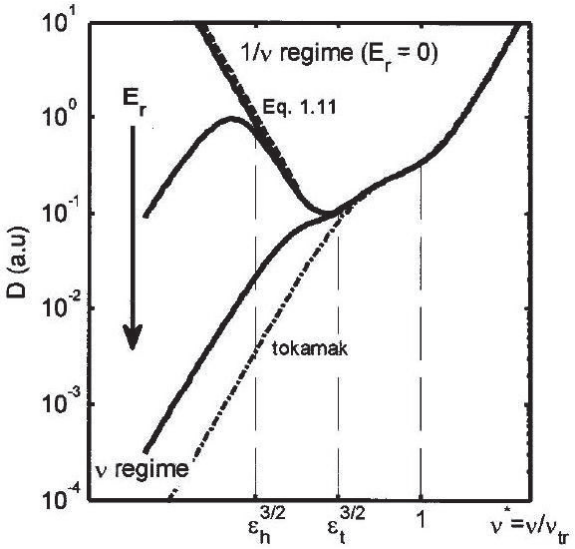

Figure 1.2: Neoclassical transport coefficient, D_{11}, as a function of radial electric field in the HSX stellarator. Reproduced from [13].

Neoclassical particle transport, or the radial electron flux driven by ECRH [16] [17], can result in a large positive radial electric field in stellarators [12]. The ambipolarity requirement leads to an Equation for the radial electric field that has an odd number of roots through solution of $\Sigma_s q_s \Gamma_s = 0$. When the electron flux dominates the ambipolarity condition, a large positive radial electric field develops that is referred to as the electron-root solution. When the ion flux dominates, a small, sometimes negative radial electric field develops that is referred to as the ion-root solution. A third unstable root generally exists in which a small perturbation generates a current that pushes the electric field to either ion or electron root. The transition between a region dominated by the ion-root radial electric field and a region dominated by the electron-root radial electric field can result in radial electric field shear that can drive ExB flow shear. This flow shear has been shown to suppress anomalous transport by decreasing the radial correlation length of turbulence [18] [19] [20], in some cases eliminating it entirely [18] [21].

An electron Internal Transport Barrier (eITB) is characterized by a discontinuity in the electron temperature gradient and peaked electron temperature profiles. Core electron root confinement has been invoked to explain eITBs in the CHS [22], TJ-II [23], LHD [24], and W7-AS [25] stellarators [26] as well as in HSX [4]. ITB's strongly modify the propagation of heat pulses during perturbative heat transport experiments, and this effect is discussed in Section 1.4.1.

1.2.2 Anomalous Transport

In tokamaks and stellarators, the cross-field ion and electron thermal diffusion, the cross-field particle diffusion, and the impurity diffusion are not described only by neoclassical processes [27] [14]. The radial electric field, E_r, plays an important role in determining the neoclassical transport in stellarators, making the determination of the anomalous transport

difficult when measurements of the radial electric field are unavailable. The convective transport caused by the off-diagonal elements of the transport matrix contribute to effective diffusion coefficients [14] and make steady-state analysis of heat transport in stellarator configurations insufficient. Pairing steady-state transport experiments with perturbative transport experiments of particles and heat provides the necessary information to effectively determine the transport coefficients in Equation 1.3 using methods referenced in Section 5.3 and described in Appendix B.

Gradients act as thermodynamic forces in plasma that drive plasma modes and lead to charge separation. When the particle motion is unimpeded, charges move to cancel the resulting potential. In electrostatic drift-wave turbulence, this motion is impeded, and fluctuating electric-fields arise that cause cross-field transport through the resulting ExB drift. When collisions are frequent enough to cause significant resistance to parallel motion, the dissipative drift instability develops; whereas in lower collisionality plasma, inverse Landau damping leads to the universal, or collisionless, drift wave instability. In the LMFP regime, trapped electrons can lead to the Trapped Electron Mode (TEM) instability [8].

Three drift wave type modes that are believed to be important for fusion experiments are the TEM, the Electron Temperature Gradient (ETG) mode, and the Ion Temperature Gradient (ITG) mode. TEMs arise when magnetic field gradients leads to a magnetic drift of the banana-centers for trapped electrons whose precession resonates with the wave [8]. The diamagnetic drift of the ions driven by ion temperature gradients leads to ITG modes when the parallel motion of adiabatic electrons is impeded. ETG modes are analogous to ITG modes with the roles of the ions and electrons exchanged.

Drift wave driven anomalous transport is characterized by critical gradients. Below the critical gradient the drift wave is stable, while above the critical gradient the growth rate is non-zero and the drift wave is unstable. Above these critical gradients thermal transport

is observed to increase from some (not necessarily neoclassical) background level to a large anomalous level. The theoretical critical gradient for this transition is different for ETG modes, ITG modes and TEMs [28], which allows experimental study of drift wave turbulence through heat pulse propagation experiments [29].

1.3 Thermal Transport in the HSX stellarator

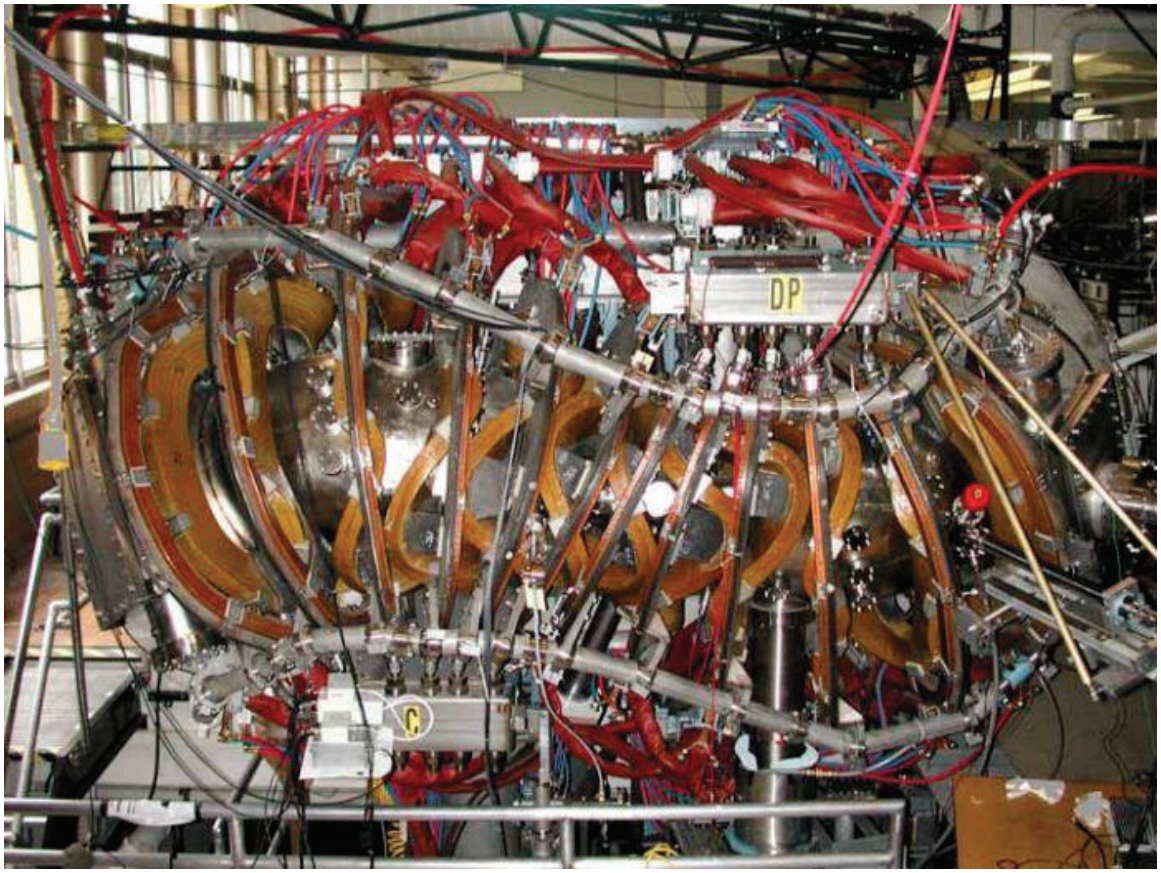

Figure 1.3: The HSX stellarator at the University of Wisconsin-Madison has 48 modular coils that are used to generate an approximately Quasi-Helical Symmetric magnetic field.

HSX is a four field period quasi-symmetric stellarator with 48 non-planar modular coils [30] [2] that are used to make the magnetic field that approximates quasi-helical symmetry. The machine has an average major radius of 1.20 m, average plasma minor radius of 0.12

m, and plasma volume of 0.44 m^3, with 48 additional planar auxiliary coils that may be energized independently for configuration flexibility as shown in Figure 1.3. The plasma is heated to a core temperature up to 2.5 keV by the ordinary wave at the fundamental harmonic of the electron gyrofrequency during 1T operation, where the electron density is limited to 1.0×10^{19} m^{-3}. The extraordinary wave at the second harmonic of the electron gyrofrequency is used during 0.5T operation where the electron density is limited to 0.5×10^{19} m^{-3}. The plasma duration is 50 ms with a maximum heating power of 100 kW.

The plasma is primarily diagnosed by a 10 spatial channel Thomson scattering system that yields electron temperature and density profiles using two lasers. The Charge eXchange Recombination Spectroscopy diagnostic indicates impurity ion temperatures of 20-70 eV [31]. The temporal evolution of the line-average density is determined by a 9-channel microwave interferometer, and the temporal evolution of the electron temperature is determined through analysis of a 16 spectral-channel ECE system. The primary diagnostic and heating systems are laid out in Figure 1.4.

The first ECRH antenna is located in boxport C, and the second ECRH antenna shares boxport B with the CHERS diagnostic neutral beam and poloidal collection optics. The interferometer is located in boxport A, and the ECE and Thomson scattering diagnostics share boxport D. The internal diamagnetic loops are located between field periods B and C.

1.3.1 Optimization for Neoclassical Transport

Neoclassical transport in conventional stellarators increases in the low collisionality regime, making them an unattractive fusion reactor concept. The radial drift of trapped electrons that results in the $1/\nu$ regime can be minimized through stellarator optimization [32]. One method of stellarator optimization is to restore symmetry in the magnetic field

Figure 1.4: HSX diagnostic and system layout.

strength to the magnetic configuration. HSX approximates Quasi-Helical Symmetry (QHS) by maintaining a helical direction of nearly constant magnetic field strength. The magnetic field strength is most easily represented by a cosine series in Boozer coordinates where the toroidal, ζ, and poloidal, θ, angles are related by the rotational transform, $\theta = \iota\zeta$,

$$B = B_o(1 + \sum_{m,n} \varepsilon_{n,m} \cos(n - \iota m)\zeta). \tag{1.6}$$

In a perfectly axisymmetric device, the only variation in the magnetic field strength is due to toroidicity, and the $\varepsilon_{0,1} = -\varepsilon_t \approx r/R_o$ term adequately describes the magnetic field spectrum. An example of the magnetic field strength in this configuration is plotted in Figure 1.5 versus Boozer angles with a magnetic field line of rotational transform equal to 1.05 overlaid, which is representative of HSX. The magnetic field strength along the field line as a function of toroidal angle, ϕ, is also shown in Figure 1.5.

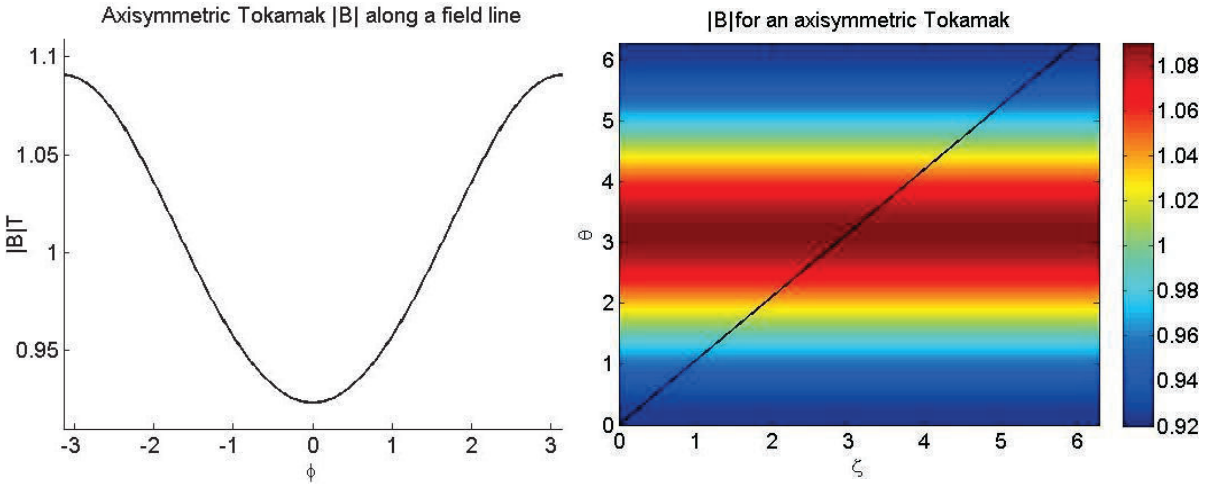

Figure 1.5: Magnetic field strength along a field line versus toroidal angle (left), and magnetic field strength as a function of Boozer poloidal and toroidal angles (right) in an axisymmetric tokamak.

Similarly, a QHS device can be represented by a single term in the helical direction. The $\varepsilon_{4,1}$ term dominates the QHS configuration of HSX with symmetry-breaking terms that are less than 1%. The toroidal curvature term due to toroidicity is 0.0023 in QHS, which is equivalent to a tokamak of aspect ratio over 400. The magnetic field spectrum of the QHS configuration is plotted in Figure 1.6.

$$\begin{aligned} B &= B_o(1-\varepsilon_t\cos(\iota\zeta)) && \text{Ideal tokamak field} \\ B &= B_o(1-\varepsilon_h\cos(n-\iota m)\zeta) && \text{Ideal quasi-helical field (general } n,m) \\ \iota_{eff} &= |n-\iota m|(n=4,m=1,\iota\approx 1)\approx 3 && \text{Effective } \iota \text{ of HSX} \end{aligned} \tag{1.7}$$

The magnetic field strength at $r/a = 0.6$ in the QHS configuration is plotted versus Boozer angles in Figure 1.7, along with a magnetic field line on the same surface. The field line samples three peaks and troughs in the magnetic field strength during one toroidal transit of HSX. The magnetic field strength along the field line is also shown in Figure 1.7,

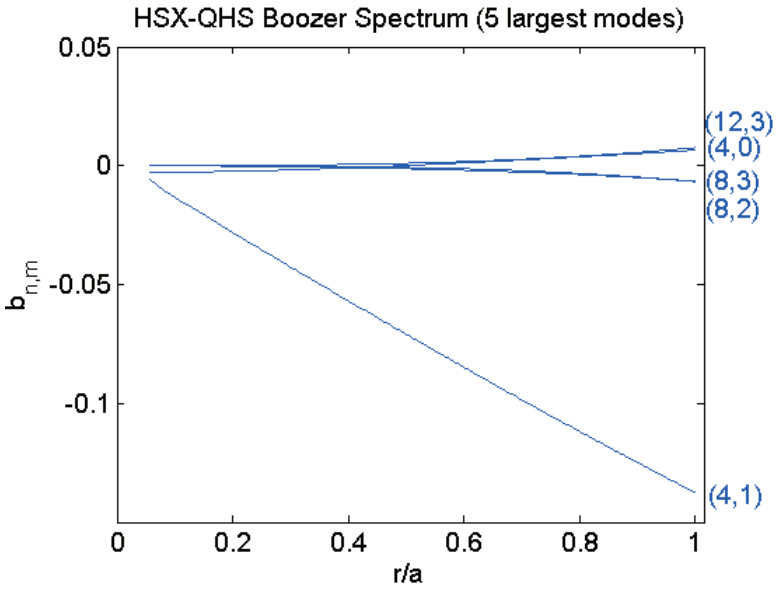

Figure 1.6: Mode amplitude of the magnetic spectrum as a function of normalized minor radius for HSX in the QHS configuration. The helical mode, $\varepsilon_{4,1}$ dominates the spectrum.

which is presented in contrast to the same field line in an equivalent tokamak in Figure 1.5. Although the physical transform of HSX is approximately 1, the effective transform of HSX

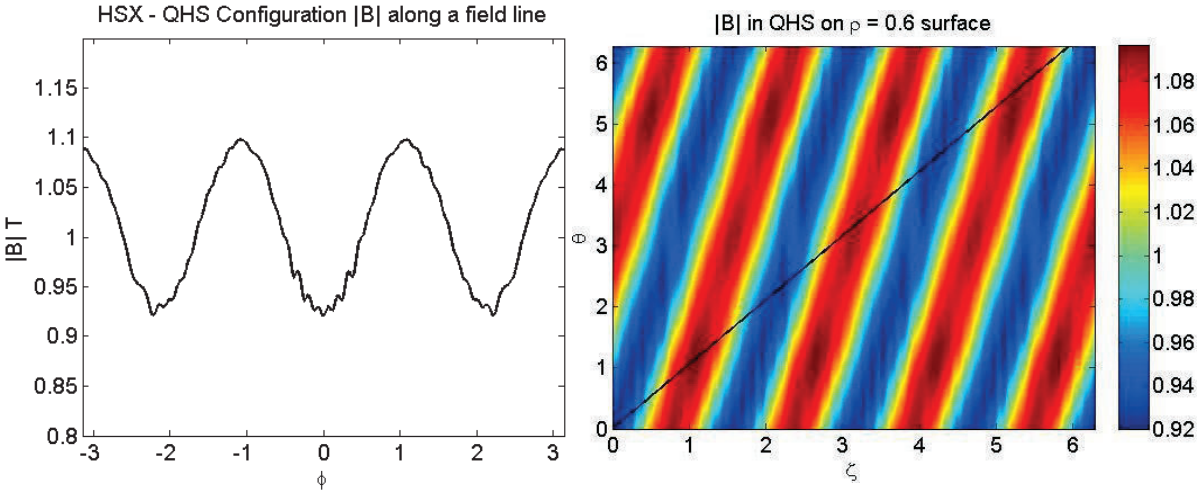

Figure 1.7: Magnetic field strength along a field line versus toroidal angle (left), and magnetic field strength as a function of Boozer poloidal and toroidal angles (right) in the QHS configuration.

is approximately 3, as is shown in Equation 1.7 and illustrated in Figure 1.7. This results in smaller drifts off flux-surfaces and lower neoclassical transport.

Forty eight planar coils are used to add symmetry-breaking terms to the magnetic configuration in HSX. This configuration flexibility allows the quasi-helical symmetry of HSX to be intentionally degraded by adding terms to the magnetic field spectrum shown in Figure 1.6. The Flip-14 Mirror configuration, referred to as Mirror in this work, is produced by energizing the planar coils with a variable fraction of the total magnet current and reversing the current through two of the coils in each half field-period to produce a magnetic mirror. This adds the $\varepsilon_{4,0}$ and $\varepsilon_{8,0}$ spectral components to the QHS field spectrum producing the magnetic spectrum shown in Figure 1.8 (in this case with 10% of the main current flowing through the planar coils). This configuration is used to compare the plasma confinement in QHS to that of a conventional stellarator experiment.

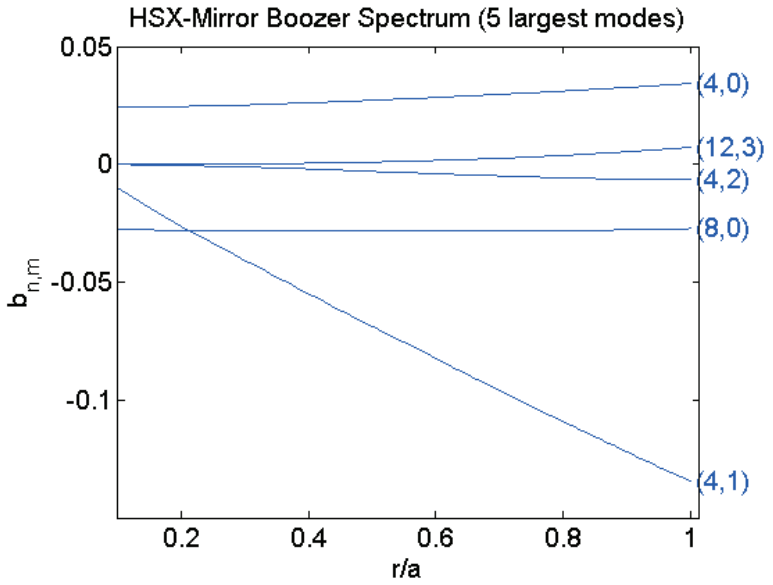

Figure 1.8: Mode amplitude of the magnetic spectrum as a function of normalized minor radius for HSX in the 10% Mirror configuration.

The magnetic field strength at $r/a = 0.6$ in the Mirror configuration is shown in Figure 1.9 with a field line from the same surface overlaid. The magnetic field strength along this field line is also shown versus toroidal angle.

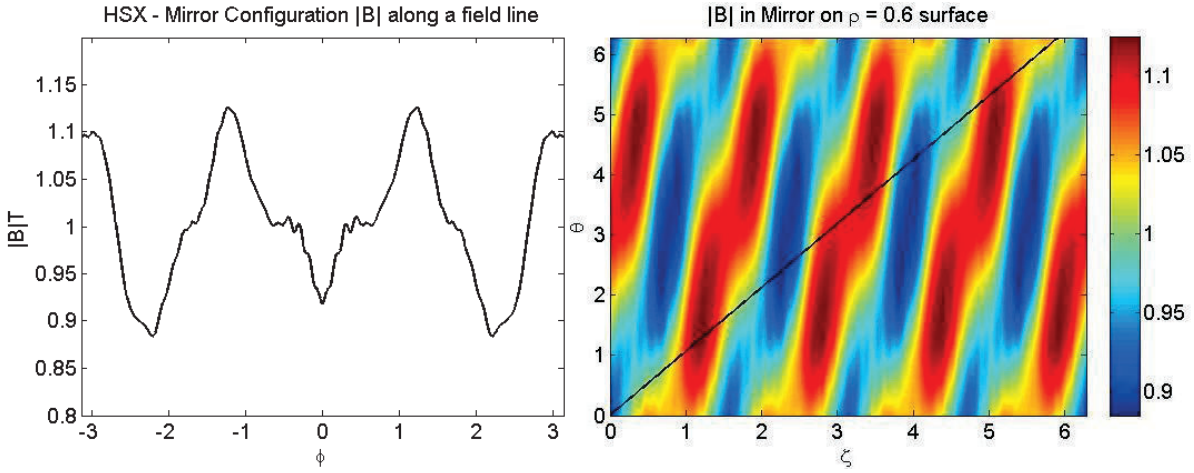

Figure 1.9: Magnetic field strength along a field line versus toroidal angle (left), and magnetic field strength as a function of Boozer poloidal and toroidal angles (right) in the QHS configuration.

The intentionally degraded symmetry in the Mirror configuration leads to increased thermal transport which is easily observed by comparing the electron temperature profiles in QHS and Mirror with the same heating power. For the same launched ECRH power, the electron temperature in QHS is significantly higher than that in Mirror. Figure 1.10 compares Thomson scattering measurements of the electron temperature and density for 100 kW of launched power in the QHS and Mirror configurations during 1T operation (at left). The central electron temperature reaches 1800 eV in the QHS configuration and 1200 eV in the Mirror configuration. The difference is due to increased thermal transport in the Mirror configuration [3].

Figure 1.10 also shows the electron temperature and density from an experiment in which the heating power in the QHS configuration was varied until the electron temperature profile

matched that of the Mirror configuration with 100 kW of launched power (at right). The QHS configuration required 50 kW of launched power, half of that required for the Mirror configuration, to match the electron temperature profiles.

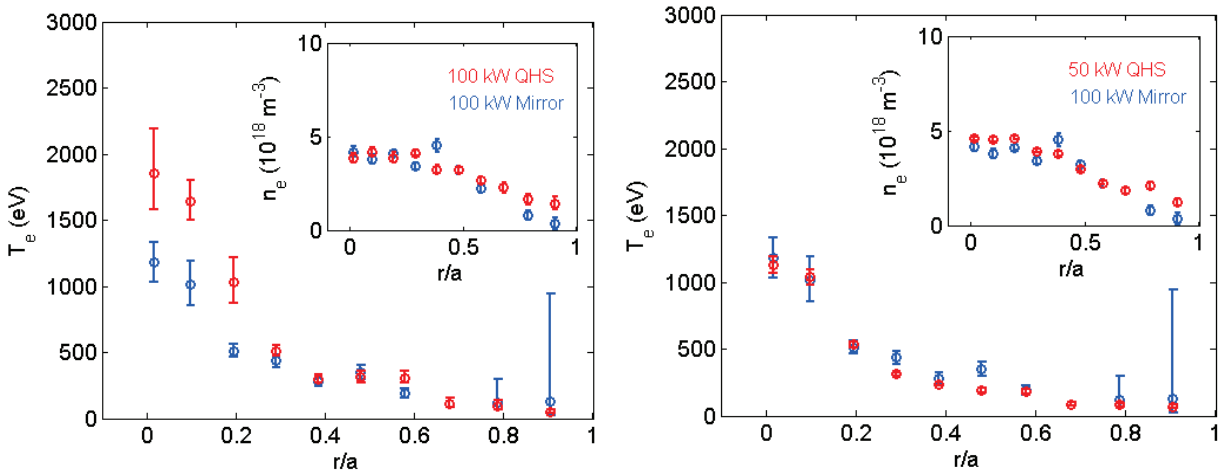

Figure 1.10: Electron temperature and plasma density profiles during 1T operation in the QHS and Mirror configurations at two heating powers with matched density profiles. Matched ECRH power (left) and matched electron temperature profiles (right).

1.3.2 Previous Electron Thermal Transport Experiments

During 0.5T operation at similar heating powers, the temperature profile of QHS is substantially higher than that of Mirror, and the plasma density profile is hollow in Mirror, which is driven by an outward neoclassical convective particle flux referred to as the thermo-diffusive flux. Comparisons between QHS and Mirror transport in [3] are made by varying the heating power until the temperature profiles match as closely as possible in the same manner as the experiment shown in Figure 1.10.

Figure 1.11 illustrates the neoclassical and experimental thermal diffusivities for each configuration during 0.5T operation. Power-balance analysis, discussed in Section 5.2, using

the diffusive assumption for electron heat transport, $q_e = -n_e \chi_e \nabla T_e$, yields thermal diffusivities that are dominated by anomalous transport outside of $r/a = 0.4$ in both configurations. For $0.2 < r/a < 0.4$, the experimental thermal transport in QHS, $\chi_e \approx 2$ m^2/s, is reduced in comparison to the Mirror configuration, $\chi_e \approx 4$ m^2/s, commensurate with the decrease in the calculated neoclassical transport, $\Delta\chi_e^{neo} \approx 2.5$ m^2/s [3].

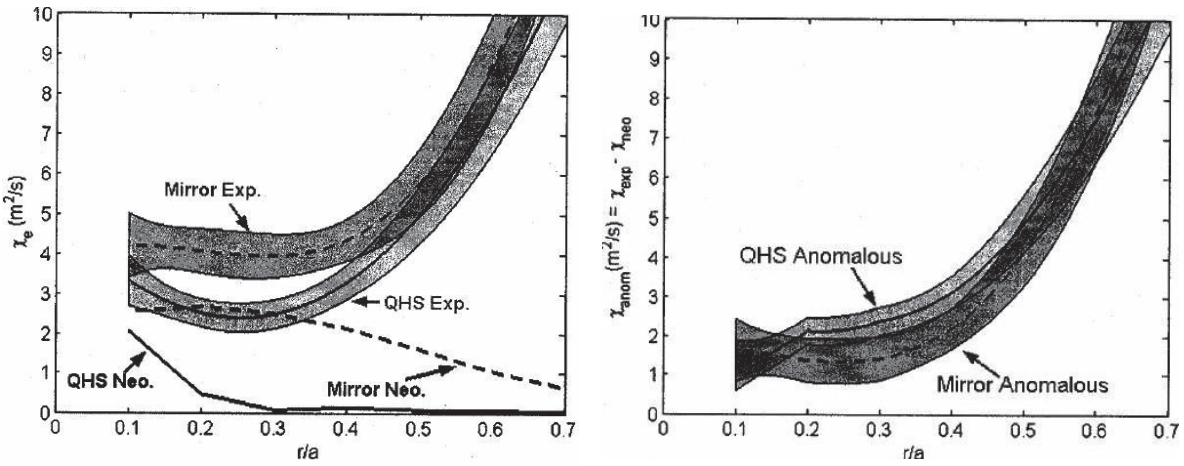

Figure 1.11: Neoclassical and power balance electron thermal diffusivity in the QHS and Mirror configurations during 0.5T operation (left), and the corresponding anomalous thermal diffusivity, $\chi_e^{anom} = \chi_e^{exp} - \chi_e^{neo}$ (right). Reproduced from [3].

Figure 1.12 illustrates the neoclassical and experimental thermal diffusivities for the QHS and Mirror configurations. The decrease in experimental transport while operating at 1T on-axis magnetic field strength is of the same order as the decrease during 0.5T operation. Peaked electron temperatures are observed during 1T operation. Figure 1.12 shows the estimated anomalous transport for Mirror and QHS at 1T. Both figures show the neoclassical calculation for the electron- and ion-root plasma. Large radial electric field shear resulting from the transition between the ion-root and the electron-root may be responsible for the

decrease in thermal transport at 1T [13]. This may be due to a decrease in anomalous transport driven by TEM turbulence [5].

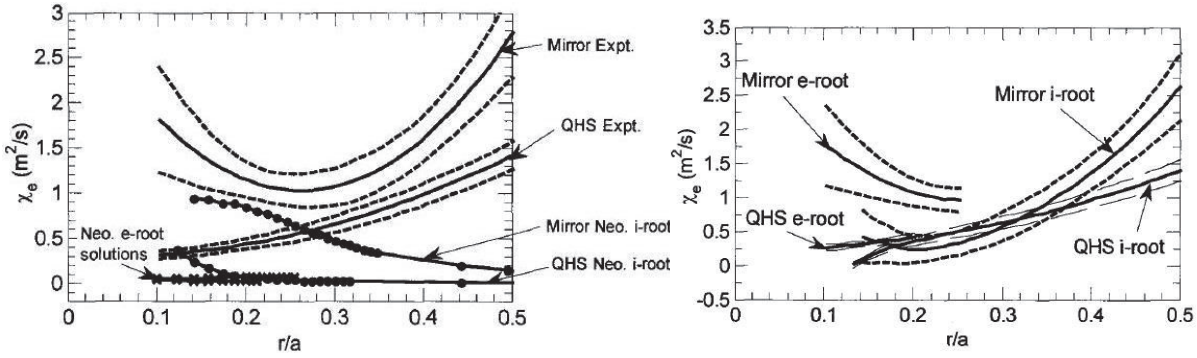

Figure 1.12: Neoclassical and power balance electron thermal diffusivities in the QHS and Mirror configurations during 1T operation (left), and the corresponding anomalous thermal diffusivity for electron-root and ion-root neoclassical calculations (right). Reproduced from [13].

1.3.3 Predictions for Drift Wave Driven Anomalous Transport

The 3D gyrokinetic code GS2 was used to calculate the linear growth rate of the TEM on HSX in reference [33]. The TEM linear growth rates in the QHS and Mirror configuration are shown at three effective radii (the $r/a = 0.24, 0.51$ and 0.86 surfaces) versus normalized electron temperature gradient, $a \ln \nabla T = a/L_T$, and normalized density gradient, $a \ln \nabla n = a/L_n$, in Figure 1.13. The electron-to-ion temperature ratio, electron and ion collisionality, and normalized wave number were fixed to $T_e/T_i = 2$, $\nu_e = \nu_i = 0$, and $k_\theta \rho_s = 0.8$ for the calculations in Figure 1.13.

Experimentally, the normalized plasma density gradient is nearly zero near the axis and between 2 and 5 near the edge. The normalized electron temperature gradient varies between 1 and 4 across the majority of the minor radius, but can exceed 5 near $r/a = 0.2$ with peaked

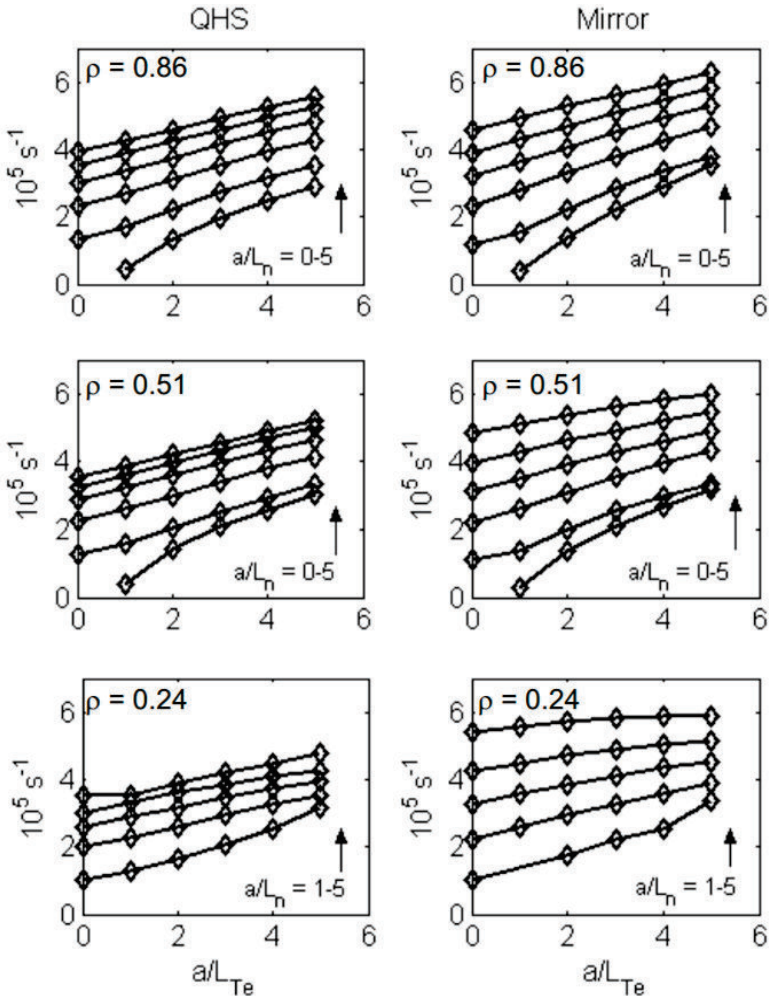

Figure 1.13: TEM linear growth rates at three surfaces in the QHS and Mirror configuration versus normalized temperature and density gradient from the GS2 code. Reproduced from [33].

electron temperature profiles in HSX. Figure 1.13 indicates that the TEM linear growth rate is non-zero for experimental conditions in both the QHS and Mirror configurations of HSX.

Magnetic curvature is unfavorable for drift wave stability when the curvature is in the same direction as the gradient in the field strength, and the TEM has been shown to be highly localized to the boxports in HSX where the curvature is unfavorable [6] [5]. The strong localization was used in reference [5] to justify using local values from the boxports

in an axisymmetric fluid code to model the anomalous transport on HSX. The axisymmetric Weiland model for quasilinear transport [34] [35], with some HSX-specific corrections discussed below, was used to calculate linear growth rates for TEM turbulence in the QHS configuration of HSX in [5]. These calculations were benchmarked for the QHS configuration against linear 3D gyrokinetic calculations from the GS2 code.

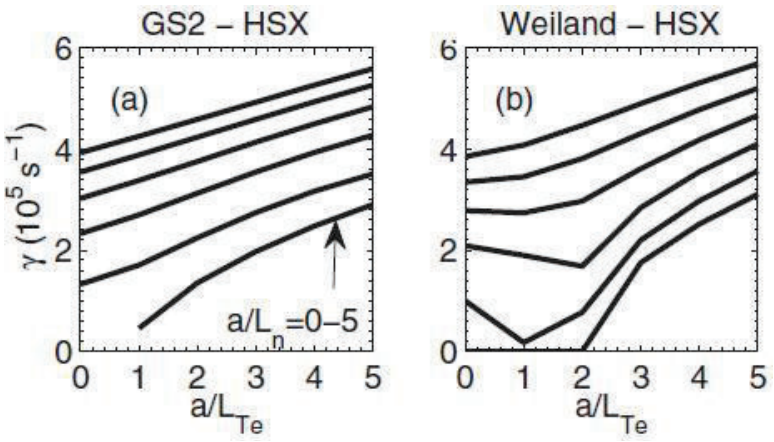

Figure 1.14: TEM linear growth rate at the ρ =0.86 surface vs normalized temperature and density gradient from the GS2 code and the Weiland model. Reproduced from [5].

Figure 1.14 shows the calculated linear growth rates for TEM turbulence from GS2 (left) and the axisymmetric Weiland model (right) versus normalized temperature gradient at the $\rho = 0.86$ surface of HSX. The Weiland model was within 30% of the GS2 calculations for experimentally relevant electron temperature and density gradients in HSX when the tokamak curvature and magnetic field scale length, $\kappa_N = \frac{\nabla B}{B} = \frac{1}{R}$, and the tokamak connection length, qR, were replaced by effective values for HSX. The average normal curvature, κ_N, in the magnetic field of HSX is increased by the high effective transform of HSX so that $\omega_B \propto \frac{\nabla B}{B} = \kappa_N \approx 3/R$. The effective connection length, qR, is decreased due to the periodicity in the HSX magnetic field, $q_{eff}R = R/\iota_{eff} \approx R/3$, which acts to decrease the effective collisionality of HSX.

The increased curvature and decreased collisionality act to drive the TEM more unstable in the QHS configuration than they would be in the equivalent tokamak. The dispersion relation of the ITG and TEM decouples when $R/L_n < 2$ [36] and the critical electron temperature gradient for TEM turbulence in the axisymmetric Weiland model is analytic and written in Table 1.1 in terms of the trapped particle fraction, $f_t = \sqrt{\epsilon}$, the temperature scale length, R/L_{T_e}, and the density scale length, R/L_n.

ETG-driven turbulence is comprised of electron gyroradius scale fluctuations, $k_\theta \rho_s >> 1$, while ITG- and TEM-driven turbulence are characterized by ion gyroradius scale fluctuations, $k_\theta \rho_s \leq 1$. The dimensionless wave-number, $k_\theta \rho_s$, is the product of the poloidal wave number of the unstable mode, k_θ, and the ion acoustic gyroradius (the sound speed divided by the ion cyclotron frequency), $\rho_s = c_s/\omega_c = \sqrt{m_i T_e}/(eB)$. TEMs are stabilized by increasing collisionality due to detrapping, and the critical gradient is dependent on normalized temperature, R/L_{T_e}, and density gradient, R/L_n, rotational transform, ι, and magnetic shear, $\hat{s} = \frac{r}{q}\frac{dq}{dr}$ [37].

ITG turbulence is independent of collisionality, and has a critical gradient in the ratio of the temperature and density length scales, $\eta_i = \frac{L_{n_i}}{L_{T_i}}$ [38]. ETG is isomorphic to ITG turbulence, but non-linear simulations predict that ETG develops radially elongated streamers that allow non-local radial electron heat transport to occur [29]. The critical gradients for an axisymmetric tokamak are summarized in Table 1.1. The ITG mode is linearly stable in HSX, because of the small ion-to-electron temperature ratio, $T_i/T_e \approx 1/10$, and weak ion temperature gradient, $a/L_{T_i} \leq 1$. The TEM is linearly unstable in HSX for the accessible plasma parameters [5] [39] [40] [6].

The ETG and TEM linear critical electron temperature gradients from Table 1.1 are applied for HSX parameters by replacing $\sqrt{\epsilon}$ with the fraction of helically trapped particles, which is approximated as $f_t = \sqrt{\epsilon}$, where $\epsilon \approx b_{4,1}$ is the helical component of the HSX

Table 1.1: Critical gradients for the onset of ITG, ETG [38], and (Weiland model) TEM [36] [41] [42] turbulence in a tokamak. The TEM critical gradient from a fit to linear gyrokinetic calculations at ASDEX Upgrade [43] is included as well.

Mode	Critical Gradient: R/L_T, Note: $\eta_i = L_{n_i}/L_{T_i}$
ITG	$\eta_{i,c} = \left(1 + \frac{T_i}{T_e}\right)\left(1.1 + 1.4\hat{s} + 1.91\frac{\hat{s}}{q}\right)$
ETG	$\left(\frac{R}{L_{T_e}}\right)_c = \max\left[\left(1 + \frac{Z_{eff}T_e}{T_i}\right)\left(1.33 + 1.91\frac{\hat{s}}{q}\right), \left(0.8\frac{R}{L_n}\right)\right]$
TEM	$\left(\frac{R}{L_{T_e}}\right)_c = \frac{0.357\sqrt{\epsilon}+0.271}{\sqrt{\epsilon}}\left[4.90 - 1.31\frac{R}{L_n} + 2.68\hat{s} + \ln\left(1 + 20\nu_{eff}\right)\right]$
TEM	$\left(\frac{R}{L_{T_e}}\right)_c = \frac{20(1-f_t)}{9f_t} + \frac{2}{3}\frac{R}{L_n} + 0.5\frac{f_t}{1-f_t}\left(1 - 0.5\frac{R}{L_n}\right)^2$

magnetic field spectrum discussed in Section 1.3.1, and assuming $Z_{eff} \approx 1$ throughout the plasma volume. The effective collisionality in Table 1.1 is the collisionality of trapped electrons normalized by the bounce frequency of the trapped electron population, $\nu_{eff} = \frac{\nu_e/\epsilon}{\omega_B}$, where the trapped electron bounce frequency is $\omega_B = \sqrt{\epsilon}\frac{v_{th,e}}{qR}$.

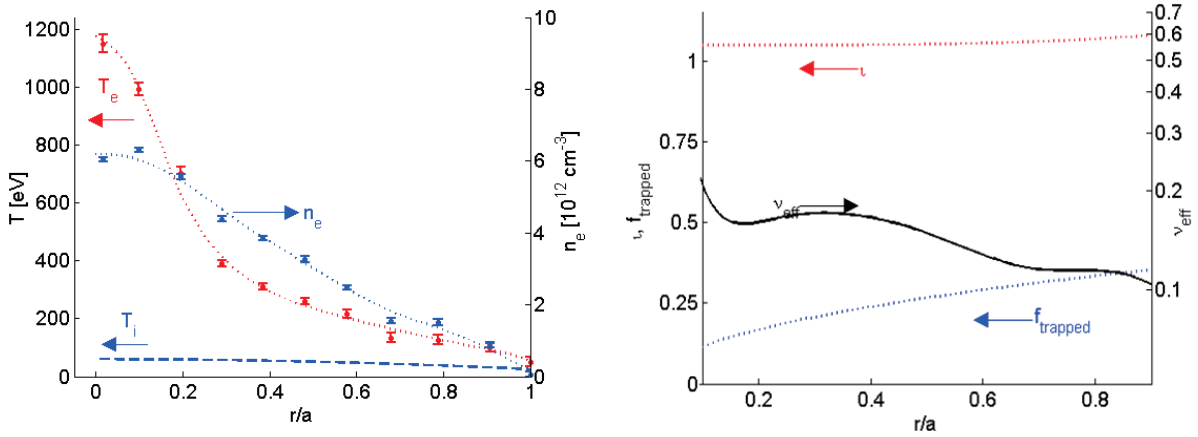

Figure 1.15: Fits for the electron and ion temperature, as well as plasma density, with Thomson scattering measurements (left). The inverse safety factor ($\frac{1}{q} = \frac{\iota}{2\pi}$) and trapped particle fraction in QHS, as well as the effective collisionality (right).

Thomson scattering measurements of the electron temperature and plasma density during an ECRH modulation experiment, as well as the fits that result from the power balance analysis, are shown at left in Figure 1.15. Ion temperature measurements were unavailable during this experiment, but an estimate of the ion temperature from similar experiments measured using the CHarge Echange Recombination Spectroscopy (CHERS) diagnostic is also shown at left in Figure 1.15. The rotational transform, or inverse safety factor, the trapped particle fraction in QHS, and the effective collisionality during an ECRH modulation experiment are shown at right in Figure 1.15. There is no source of ion heating on HSX, and the low plasma denstiy and high electron temperature of HSX causes thermal equilibration to occur on a long time-scale compared to the plasma duration; consequently, the ion temperature and its scale length remain small during experiments on HSX.

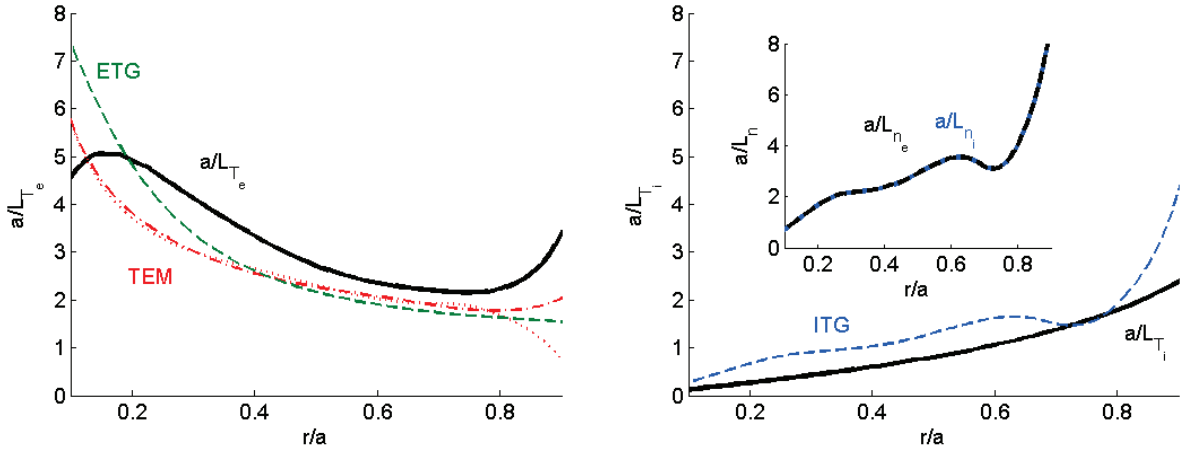

Figure 1.16: The linear critical gradient of the TEM, ETG and ITG modes for experimental parameters are compared to a/L_{Te} (left) and a/L_{Ti} (right). The plasma density gradient scale length is inset at right.

The linear critical gradients for experimental temperature and plasma density profiles measured during an ECRH modulation experiment are shown in Figure 1.16. The electron

and ion temperature gradient scale length, a/L_{T_e} and a/L_{T_i}, are compared to the linear critical temperature gradients from Table 1.1 in Figure 1.16. The plasma density gradient scale length is included for completeness in Figure 1.16. The experimental temperature gradient scale length is above the linear threshold for ETG and TEM turbulence across most of the HSX minor radius and below the linear threshold for $r/a < 0.2$. This is consistent with the linear gyrokinetic calculations presented in Figure 1.14 which show that there is finite growth rate for the TEM on all three magnetic surfaces. The ITG mode is stable across the minor radius for experimental parameters, $\eta_i < \eta_{i,crit}$.

The plasma density gradient scale length is greater than 2 across most of the plasma minor radius, and the TEM and ITG mode are coupled. Gyrokinetic calculations are necessary to study microinstabilities in HSX, and linear and non-linear gyrokinetic calculations with two kinetic species are presented in Chapter 6. Additionally, the quasi-linear and non-linear heat flux is compared to experimental measurements in Chapter 6.

1.4 Power Balance Analysis versus Incremental Heat Transport Measurements

In steady state power balance analysis, the electron thermal diffusivity is determined by balancing the total heat flux through a magnetic surface against the local temperature gradient. This procedure yields an effective transport coefficient that includes all of the off-diagonal components of the transport matrix. Perturbative heat transport experiments are used to measure the temperature gradient dependence of the transport and yield an incremental diffusivity,

$$\chi^{eff} = -\frac{q}{n\nabla T} \qquad \chi^{inc} = -\frac{\partial q/n}{\partial(\nabla T)} = \chi + \frac{\partial \chi}{\partial \nabla T}\nabla T. \tag{1.8}$$

The convective and diffusive contributions to the heat flux may be separated by comparing the results of the steady state analysis with an incremental analysis of the heat pulse diffusivity [44].

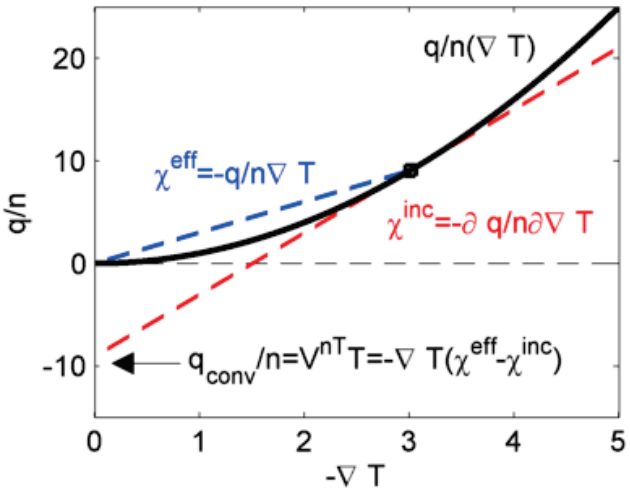

Figure 1.17: The incremental, χ^{inc}, and effective, χ^{eff}, diffusivities measure different aspects of the relationship between the heat flux (q) and temperature gradient (∇T).

The effective power balance diffusivity is the slope between the origin and the experimental operating point on the heat flux-temperature gradient diagram illustrated in Figure 1.17, and the incremental diffusivity is the local slope of the heat flux versus temperature gradient at the operating point. The convective heat flux is the intercept that results from extrapolating the local slope back to $\nabla T = 0$. The total heat flux is $q = -n\chi\nabla T + q_{conv}$. The convective heat flux in terms of the incremental and effective diffusivities is

$$q_{conv} = -n\nabla T\left(\chi^{eff} - \chi^{inc}\right). \tag{1.9}$$

The diffusive heat flux carries all of the terms from the transport matrix that are proportional to the temperature gradient, while the convective heat flux contains any term that is not proportional to the temperature gradient, including the convective heat flux carried with the particle flux, $(5/2)\Gamma T$ [45].

In perturbative electron heat transport experiments the incremental diffusivity is often referred to as the heat pulse electron thermal diffusivity. Local measurements of the heat pulse thermal diffusivity, χ_e^{HP}, are sensitive to changes in the gradient of the heat flux, and perturbative heat transport experiments are conducted to find critical gradient thresholds and bifurcations in the heat flux. Figure 1.18 illustrates three scenarios in which the heat flux is a non-linear function of the temperature gradient, and the steady-state and perturbative measurement of the electron thermal diffusivity yield different results: a smoothly varying heat flux with temperature gradient, $\chi_e^{HP} > \chi_e^{PB}$ and $\chi_e^{HP} < \chi_e^{PB}$; and a critical gradient threshold in the heat flux, $\chi_e^{HP} > \chi_e^{PB}$.

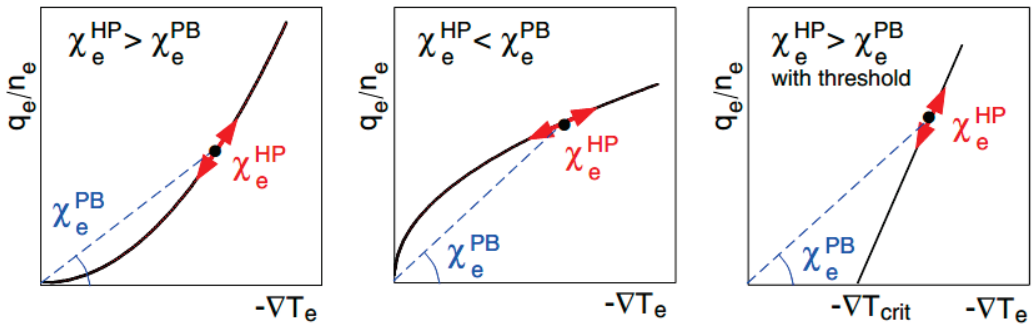

Figure 1.18: Heat flux vs temperature gradient showing difference between χ_e^{PB} and χ_e^{HP} in three scenarios: a smoothly varying heat flux with $\chi_e^{HP} > \chi_e^{PB}$ or $\chi_e^{HP} < \chi_e^{PB}$ and a critical gradient. Reproduced from [46].

The second scenario, $\chi_e^{HP} < \chi_e^{PB}$, is indicative of electron heat transport that is a weak function of the electron temperature gradient or is not driven by the electron temperature gradient. The third scenario, $\chi_e^{HP} > \chi_e^{PB}$ with a threshold beneath which $\chi_e^{HP} \approx \chi_e^{PB}$, is characteristic of drift-wave driven anomalous transport and has been observed in the ASDEX Upgrade (AUG) [47] and DIII-D [48] tokamaks. All three scenarios are shown in Figure 1.19, which are reproduced from [47], and discussed in Section 1.4.1.

1.4.1 Stiffness in the Electron Heat Flux

Many tokamak experiments have observed electron temperature profiles that are resilient to changes in heating power [49], where large changes in the heat flux are necessary to change the local profile gradient [48]. This phenomena is referred to as profile resiliency, or stiffness in the electron heat flux, and is closely linked to critical gradients. For a diffusive heat flux, this phenomenon is quantified by the logarithmic gradient of the heat flux versus logarithmic temperature gradient,

$$S = \frac{\nabla T_e}{q_e}\frac{\partial q_e}{\partial \nabla T_e} = \frac{\partial \ln q_e}{\partial \ln \nabla T_e} = \frac{\chi_e^{HP}}{\chi_e^{PB}}. \tag{1.10}$$

A detailed study of electron temperature profile resiliency on the AUG tokamak experiment showed that the electron heat flux was a strong function of the normalized electron temperature gradient above a critical electron temperature gradient [47]. Figure 1.19 shows the heat flux and TEM linear growth rate plotted as a function of normalized electron temperature gradient scale length, $R/L_{T_e} = R \ln \nabla T_e$, in the AUG tokamak. The heat flux, which was controlled by varying the ECRH input power and heating location, increases quickly with temperature gradient above a critical electron temperature gradient where the TEM becomes unstable.

Figure 1.19 shows a decrease in stiffness in the electron heat flux as collisionality increases in the AUG tokamak. Gyrokinetic modeling indicated that the decrease in stiffness was due to transition from an electron heat flux driven by the TEM, which is sensitive to the electron temperature gradient and is stabilized by increasing collisionality, to an electron heat flux driven by the ITG mode, which is not sensitive to the electron temperature gradient or collisionality [47].

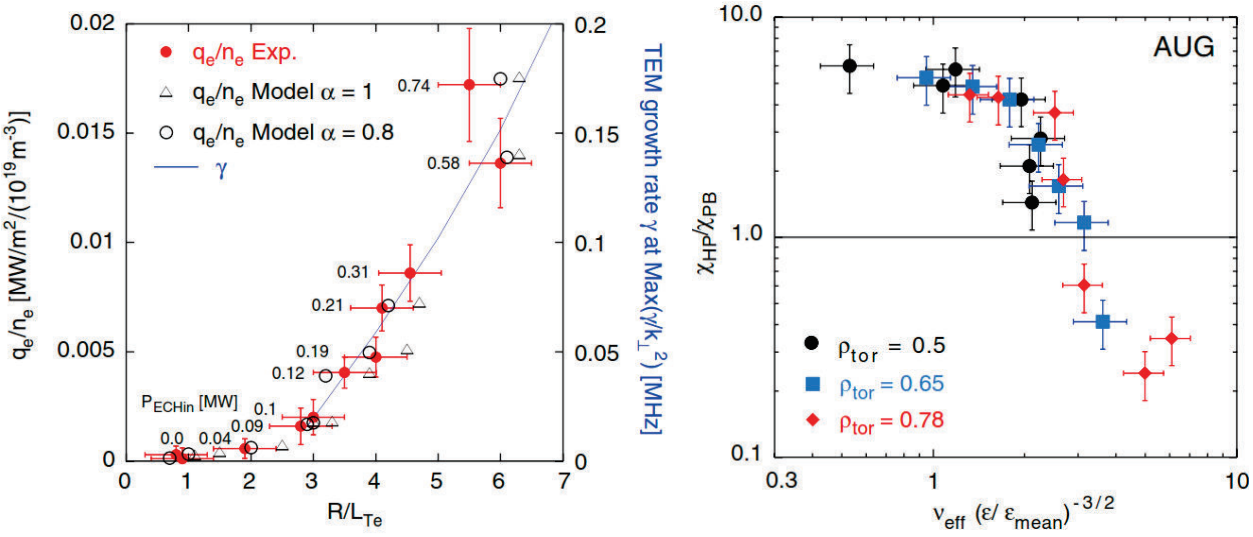

Figure 1.19: Heat flux and TEM linear growth rate vs normalized electron temperature gradient on the AUG tokamak (left). The electron stiffness decreases through the transition from TEM to ITG driven turbulence (right). Reproduced from [47].

A generalized critical gradient model, Equation 1.11, was developed for AUG ECRH heated plasmas based on linear GS2 calculations and on the empirical existence of the threshold in normalized temperature gradient [29],

$$\chi_e = \chi_s q^{3/2} \frac{T_e}{eB}\frac{\rho_s}{R}[\frac{R}{L_{T_e}} - \frac{R}{L_{T_{e,crit}}}]^{\alpha} H(\frac{R}{L_{T_e}} - \frac{R}{L_{T_{e,crit}}}) + \chi_0 \frac{T_e}{eB}\frac{\rho_s}{R}. \tag{1.11}$$

The model includes the local gyro-Bohm magnetic field and temperature scaling, $\frac{T_e}{eB}\frac{\rho_s}{R}$, and enforces the empirically-observed dependence on plasma current in tokamaks, $q^{3/2}$. χ_s is an alternative quantification of stiffness in the electron heat flux and is sometimes referred to as the "intrinsic" stiffness.

Commonly α is taken as equal to unity in the empirical model [47] (although the Weiland critical gradient model mentioned in Section 1.2.2 calls for α =0.5 [36].) The empirical model is applied by fitting χ_s, χ_0, and $R/L_{T_{e,crit}}$ to experimental data derived from scanning the

electron heat flux and normalized gradient, R/L_{T_e}. Figure 1.19 also shows results from the empirical model of Equation 1.11 for $\alpha = 0.8$ and $\alpha = 1$. The critical gradient in the electron heat flux is different for TEM and ETG mode driven turbulence, and the "apparent" critical gradient can be determined far above the threshold, $\chi_e^{HP} > 2\chi_e^{PB}$, by interpolation between the incremental and power balance thermal diffusivity [43],

$$\left(\frac{R}{L_{Te}}\right)_{crit} = \left(\frac{R}{L_{Te}}\right) \frac{\chi_e^{HP} - \chi_e^{PB}}{\chi_e^{HP}}. \tag{1.12}$$

With concurrent power modulation, both power balance and heat pulse propagation analysis can be used to provide information about the heat flux and may be used to determine χ_e^{PB}, χ_e^{HP}, and $R/L_{T_{e,crit}}$. The critical gradient model has been applied successfully in conjunction with transient experiments on several machines, including the AUG, TCV, JET, FTU, Tore Supra and DIII-D tokamaks, as well as the W7-AS stellarator [47], and is a useful model for empirical studies of turbulence.

1.4.2 A Review of Perturbative Heat Transport Experiments in Toroidal Devices

Table 1.2: The ratio of electron heat diffusivity χ_e^{HP} as measured by ECRH modulation (mECH) or by sawtooth (STH) propagation to χ_e^{PB}, as deduced from standard power balance analysis for various experiments up to 1993. Adapted from [44].

Experiment	χ_e^{HP}/χ_e^{PB}	Mode	Reference
ASDEX	3	STH	Giannone et al 1990
DIII-D	≈ 1	mECH	Lopes Cardozo et al 1992b
DITE	≈ 1	mECH	Hugill et all 1988
FTU	$1.5 - 2.2$	STH	Alladio et al 1992b
ISX-B	≈ 1	STH	Bell et al 1984
JET	2.5	STH	Tubbing et al 1987
JT-60U	$2 - 4$	STH	de Haas et al 1992
RTP	$2 - 4$	STH	Lopes Cardozo et al 1992a
RTP	$2 - 4$	mECH	Lopes Cardozo et al 1992a
TEXT	2.25	STH	Brower et al 1990
TEXTOR	> 4	STH	Kramer-Flecken, ([44])
TFTR	$1 - 10$	STH	Fredrickson et al 1986
TORE SUPRA	$2.5 - 3.5$	STH	Lopes Cardozo et al 1992b
T10	≈ 1	STH	Sillen et al 1986
W7-AS	$1 - 1.5$	mECH	Giannone et al 1991

Before 1993, very few perturbative heat transport experiments were performed in stellarators, and electron heat transport was inferred to be diffusive, based on the agreement between χ_e^{HP} and χ_e^{PB} in magnitude and scaling with plasma parameters in the W7-AS

stellarator [44]. The ratio of the incremental to power balance value was generally observed to be positive and greater than unity in tokamaks, and a short comparison of results from different tokamaks is shown in Table 1.2 that is reproduced from [44].

The analysis of temperature perturbations from sawteeth [50] and modulated ECRH [51] yields similar results in RTP and other tokamaks [52], and χ_e^{HP} was observed to be independent of plasma current, ohmic power, and line-average density in the JET tokamak in both L- and H-mode plasma [52]. The conclusion that the incremental thermal diffusivity is independent of plasma current in JET is in conflict with the $q^{3/2}$ dependence of Equation 1.11.

Table 1.3 is a brief comparison of perturbative and steady-state heat transport experiments since 1993 (including the results from the ORMAK tokamak which were excluded from Table 1.2). Perturbative heat transport experiments have been used to measure critical electron temperature gradients in the DIII-D [48], TCV, and AUG [47]. Tokamak experiments and show that the perturbative and steady-state measurements agree (disagree) in regions or regimes below (above) the critical electron temperature gradient. No critical electron temperature gradient has been directly observed on a stellarator experiment, although evidence for a critical electron temperature gradient near that predicted for ETG driven transport on the W7-AS stellarator at moderate heating powers has been reported recently [47].

Table 1.3: The ratio of electron heat diffusivity χ_e^{HP} as measured by ECRH modulation (mECH), cold pulse (COLD) or by sawtooth (STH) propagation and χ_e^{PB}, as deduced from standard power balance analysis for various experiments and analysis locations ρ.

Experiment	χ_e^{HP}/χ_e^{PB}	Analysis Location	Mode	Reference
TFTR	≈ 2	$\rho < 1.5\rho_{mix}$	STH	Fredrickson et al, 2000 [53]
DIII-D	≈ 1	$\rho < 1.5\rho_{mix}$	STH	Fredrickson et al, 2000 [53]
AUG	≈ 1	$\rho < 0.4$	mECH	Ryter et al, 2003 [54]
RTP	≈ 1	$\rho < 0.3$	mECH	Gorini et al, 1993 [55]
RTP	$2-4$	$\rho > 1.5\rho_{mix}$	mECH/STH	Mantica et al,1996 [56]
JET	$2-4$	$\rho > 1.5\rho_{mix}$	STH	Fredrickson et al, 2000 [53]
TFTR	≈ 5	$\rho > 1.5\rho_{mix}$	STH	Fredrickson et al, 2000 [53]
DIII-D	≈ 10	$\rho > 1.5\rho_{mix}$	STH	Fredrickson et al, 2000 [53]
ORMAK	$2.5-15$	$\rho > 1.5\rho_{mix}$	STH	Callen and Jahns, 1977 [50]
AUG	$\gg 1$	$\rho > 0.4$	mECH	Ryter et al, 2003 [54]
DIII-D	$2-5$	$\rho = 0.45$	mECH	Gentle et al, 2006 [57]
JT-60U	≈ 1	ITB present	mECH/COLD	Inagaki et al, 2006 [58]
JT-60U	$1-3$	No ITB	mECH/COLD	Inagaki et al, 2006 [58]
WVII-A	$\approx 1-3$		mECH	Hartfuss et al, 1986 [59]
W7-AS	≈ 1		mECH	Gasparino et al, 1998 [60]
WEGA	≈ 1		mECH	Zhang et al, 2012 [61]
L-2M	$\gg 1$		mECH	Akulina et al, 2001 [62]
CHS	$0.2-0.5$		STH	Takagi et al, 2003 [63]
TJ-II	≈ 1		mECH	Eguilior et al, 2003 [64]
LHD	0.3	$\rho < \rho_{ITB}$	COLD	Ida et al, 2004,2009 [65][66]
LHD	≈ 1		mECH/COLD	Inagaki et al, 2006 [58]

The electron heat flux, normalized by the gyro-Bohm electron temperature dependence of W7-AS at the plasma mid-radius, is reproduced from [47] in Figure 1.20. The empirical model, Equation 1.11, predicts a stiffness of approximately 3 for this data. The thermal diffusivity and temperature profiles from two experiments are shown at right in Figure 1.20. The heating power was varied between a source located on-axis and a source located off-axis with 0.8 MW launched on-axis in the first experiment and the total power reduced to 0.1 MW on-axis and 0.4 MW launched off-axis in the second experiment. Modulated ECH experiments on W7-AS at higher heating powers (0.6 MW on- and 0.6 MW off-axis) yielded incremental thermal diffusivities that were similar to the power balance values [67]. This suggests that there is a decrease in stiffness with additional heating power in W7-AS [47].

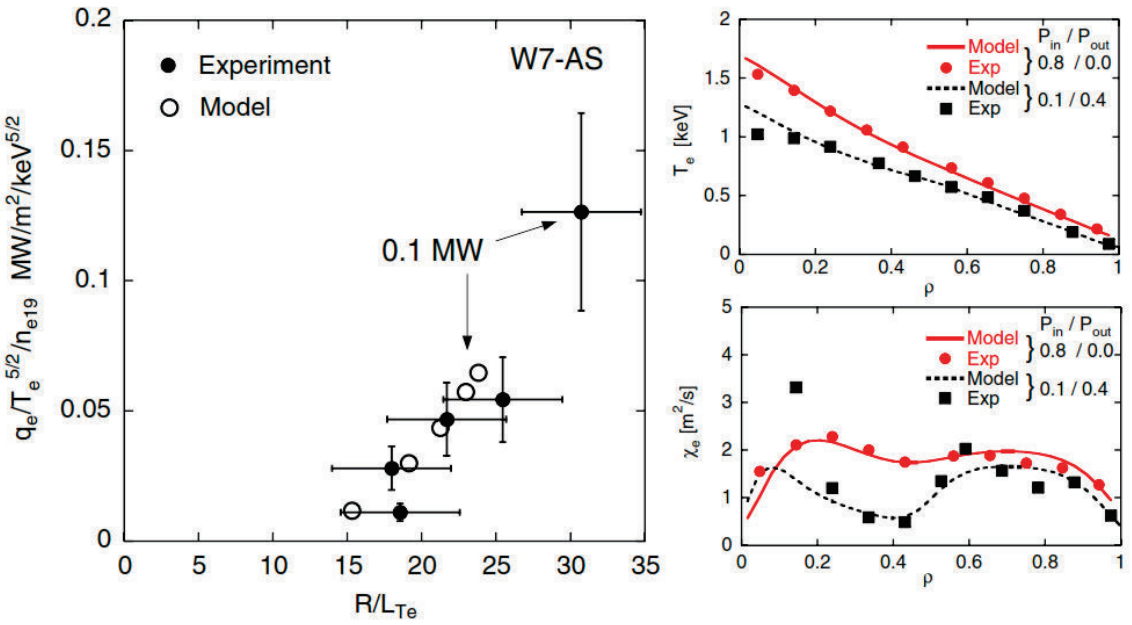

Figure 1.20: Normalized electron heat flux vs temperature gradient in W7-AS from steady-state experiments and the empirical model at the mid-radius (left). The heat flux and temperature profiles from two experiments (right). Reproduced from [47].

The transition behavior of an eITB was investigated in the JET tokamak using a combination of heat pulse propagation and cold pulse propagation experiments in [68]. Reference [68] showed evidence that the eITB in JET was a narrow region of improved confinement, in which the critical gradient in the electron heat flux increased above the experimental gradient in that region, resulting in a complete loss of stiffness in the electron heat flux ($\chi_e^{HP} \approx \chi_e^{PB}$ within the eITB layer and $\chi_e^{HP} > \chi_e^{PB}$ outside of the eITB layer). The eITB observed in LHD covers the inner third of the minor radius and the thermal diffusivity is reduced within the eITB; but results were not so clear on the JT-60U tokamak where the thermal diffusivity was reduced across the minor radius when an transport barrier was present in the plasma [58]. Modeling of cold pulse propagation experiments on JET showed that the eITB was fragile near the eITB foot and could be removed during cold pulse propagation from outside of the eITB layer [68]. This result may affect the results from the JT-60U tokamak and LHD stellarator where cold pulses were used in the perturbative heat transport analysis of plasma with eITBs.

Modulated ECH and cold pulse propagation were used to study electron heat transport, with and without an eITB [69], for a variety of heating powers and plasma densities [65] on LHD. The steady-state and incremental thermal diffusivities were reduced by a factor of 5 within the eITB. Before the transition to an eITB, the stiffness was measured to be comparable to, or larger than, unity; however, after the transition into an eITB, the stiffness was reduced to approximately 1/3 [65].

Figure 1.18 shows that when $\chi_e^{HP} < \chi_e^{PB}$, a small increase in heat flux can lead to a large increase in electron temperature gradient. This was interpreted as evidence of an eITB on LHD when accompanied by a large increase in core electron temperature [70], but not as evidence of an eITB on the CHS stellarator, where $\chi_e^{HP} < \chi_e^{PB}$ occurred without the commensurate increase in electron temperature [63]. Additionally, the thermal diffusivity in

LHD was shown to be independent of the temperature gradient, but to have a gyro-Bohm temperature dependence, $T_e^{1.5}$, in plasmas without an eITB, and a strong inverse temperature dependence in plasma with an eITB. This was in contrast to results at JT-60U, where there was little temperature dependence but a strong temperature gradient dependence in plasmas without an eITB [58].

Since 1993 there have been several perturbative heat transport experiments in stellarators, but only results on the L-2M stellarator have shown the strong temperature gradient dependence of tokamak experiments. It is unclear whether the results from the L-2M stellarator are significant, because further experiments have not been published, there was no test for temperature dependence of the thermal diffusivity. Additionally, the W7-AS, CHS, TJ-II, and LHD stellarators have been shown to have eITBs. This complicates the comparison between stellarators (where stiffness in the electron heat flux is not observed) and tokamaks (where stiffness in the electron heat flux is observed) because JET and JT-60U showed that there was no stiffness in the electron heat flux within eITBs. All of these results encourage perturbative heat transport experiments on a device that has been optimized for neoclassical transport and is dominated by anomalous heat transport across the minor radius. An eITB has been predicted to exist in the core of HSX, and experimental measurements of the electron heat flux are available in the region where the eITB is predicted to exist.

Bibliography

1. Boozer, A. H. *Phys. Fluids* **26,** 496 (1983).
2. Almagri, A. F., Anderson, D. T., Anderson, F. S. B., *et al. IEEE. Trans. Plasma. Sci.* **27,** 114–115 (1999).
3. Canik, J. M., Anderson, D. T., Anderson, F. S. B., *et al. Phys. Rev. Lett.* **98,** 085002 (2007).
4. Lore, J., Guttenfelder, W., Briesemeister, A., *et al. Phys. Plasmas* **17,** 056101 (2010).
5. Guttenfelder, W., Lore, J., Anderson, D. T., *et al. Phys. Rev. Lett.* **101,** 215002 (2008).
6. Rafiq, T. & Hegna, C. C. *Phys. Plasmas* **13,** 62501–1 (2006).
7. Cardozo, N. J. L., de Haas, J. C. M., Hogeweij, G. M. D., *et al. Plasma Phys. Control. Fusion* **32,** 983 (1990).
8. Kadomtsev, B. B. & Pogutse, O. P. *Nucl. Fusion* **11,** 67–92 (1971).
9. Wesson, J. & Connor, J. W. (*Tokamaks*, Clarendon Press, Oxford; New York, 1987).
10. Chen, F. 2nd Ed., *Introduction to plasma physics and controlled fusion* (Springer, 1984).
11. Maassberg, H., Beidler, C. D., Gasparino, U., *et al. Phys. Plasmas* **7,** 295–311 (2000).
12. Mynick, H. E. & Hitchon, W. N. G. *Nucl. Fusion* **23,** 1053–1059 (1983).
13. Lore, J. PhD thesis (The University of Wisconsin - Madison, United States, 2010).
14. Maassberg, H., Brakel, R., Burhenn, R., *et al. Plasma Phys. Control. Fusion* **35,** B319 (1993).
15. Hirshman, S. P., Shaing, K. C., Rij, W. I. v., *et al. Phys. Fluids (1958-1988)* **29,** 2951–2959 (1986).
16. Murakami, S., Gasparino, U., Idei, H., *et al. Nucl. Fusion* **40,** 693–700 (2000).
17. Shimozuma, T., Kubo, S., Idei, H., *et al. Plasma Phys. Control. Fusion* **45,** 1183–1192 (2003).
18. Terry, P. W. *Reviews of Modern Physics* **72,** 109 (2000).

19. Horton, W. *Reviews of Modern Physics* **71,** 735 (1999).

20. Garbet, X. *Comptes Rendus Physique* **7,** 573–583.

21. Terry, P. W., Newman, D. D. & Ware, A. S. *Phys. Rev. Lett.* **87,** 185001 (2001).

22. Fujisawa, A., Iguchi, H., Sanuki, H., *et al. Plasma Phys. Control. Fusion* **40,** 627 (1998).

23. Castejon, F., Tribaldos, V., Garcia-Cortes, I., *et al. Nucl. Fusion* **42,** 271–280 (2002).

24. Takeiri, Y., Shimozuma, T., Kubo, S., *et al. Phys. Plasmas* **10,** 1788–1795 (2003).

25. Baldzuhn, J., Kick, M., Maassberg, H., *et al. Plasma Phys. Control. Fusion* **40,** 967 (1998).

26. Yokoyama, M., Maassberg, H., Beidler, C. D., *et al. Nucl. Fusion* **47,** 1213–1219 (2007).

27. Stroth, U. *Plasma Phys. Control. Fusion* **40** (1998).

28. Jacchia, A., DeLuca, F., Ryter, F., *et al. Nucl. Fusion* **45,** 40–47 (2005).

29. Mantica, P. & Ryter, F. *Comptes Rendus Physique* **7,** 634–649.

30. Anderson, F. S. B., Almagri, A. F., Anderson, D. T., *et al. Fusion Technol.* **27,** 273–277 (1995).

31. Briesemeister, A., Zhai, K., Anderson, D. T., *et al. Contrib. Plasm. Phys.* **50,** 741–744 (2010).

32. Grieger, G., Lotz, W., Merkel, P., *et al. Phys. Fuids B.* **4,** 2081 (1992).

33. Guttenfelder, W. PhD thesis (University of Wisconsin, Madison, 2008).

34. Nordman, H., Weiland, J. & Jarmen, A. *Nucl. Fusion* **30,** 983–996 (1990).

35. Bateman, G., Kritz, A. H., Kinsey, J. E., *et al. Phys. Plasmas* **5,** 1793 (1998).

36. Asp, E., Weiland, J., Garbet, X., *et al. Plasma Phys. Control. Fusion* **49,** 1221–1243 (2007).

37. Ryter, F., Angioni, C., Peeters, A. G., *et al. Phys. Rev. Lett.* **95,** 085001 (2005).

38. Horton, W., Hoang, G. T., Bourdelle, C., *et al. Phys. Plasmas* **11,** 2600–2606 (2004).

39. Guttenfelder, W., Anderson, D. T., Anderson, F. S. B., *et al. Phys. Plasmas* **16,** 082508 (2009).

40. Rafiq, T. & Hegna, C. C. *Phys. Plasmas* **12,** 112505 (2005).

41. Kirov, K. K., Andreev, V. F., Leuterer, F., *et al. Plasma Phys. Control. Fusion* **48,** 245–262 (2006).

42. Weiland, J., Jarmen, A. & Nordman, H. *Nucl. Fusion* **29,** 1810–1814 (1989).

43. Peeters, A. G., Angioni, C., Apostoliceanu, M., *et al. Phys. Plasmas* **12,** 022505 (2005).

44. Wagner, F. & Stroth, U. *Plasma Phys. Control. Fusion* **35,** 1321–1371 (1993).

45. Callen, J. D., Christiansen, J. P., Cordey, J. G., *et al. Nucl. Fusion* **27,** 1857 (1987).

46. Ryter, F., Dux, R., Mantica, P., *et al. Plasma Phys. Control. Fusion* **52,** 124043 (2010).

47. Ryter, F., Camenen, Y., DeBoo, J. C., *et al. Plasma Phys. Control. Fusion* **48,** B453–B463 (2006).

48. DeBoo, J. C., Petty, C. C., White, A. E., *et al. Phys. Plasmas* **19,** 082518–082518–8 (2012).

49. Garbet, X., Mantica, P., Ryter, F., *et al. Plasma Phys. Control. Fusion* **46,** 1351–1373 (2004).

50. Callen, J. D. & Jahns, G. L. *Phys. Rev. Lett.* **38,** 491–494 (1977).

51. Giannone, L., Erckmann, V., Gasparino, U., *et al. Nucl. Fusion* **32,** 1985–2000 (1992).

52. Cardozo, N. J. L. *Plasma Phys. Control. Fusion* **37,** 799–852 (1995).

53. Fredrickson, E. D., Austin, M. E., Groebner, R., *et al. Phys. Plasmas (1994-present)* **7,** 5051–5063 (2000).

54. Ryter, F., Tardini, G., Luca, F. D., *et al. Nucl. Fusion* **43,** 1396–1404 (2003).

55. Gorini, G., Mantica, P., Hogeweij, G. M. D., *et al. Phys. Rev. Lett.* **71,** 2038–2041 (1993).

56. Mantica, P., Peters, M., Luca, F. D., *et al. Nucl. Fusion* **36,** 1317 (1996).

57. Gentle, K. W., Austin, M. E., DeBoo, J. C., *et al. Phys. Plasmas* **13,** 012311 (2006).

58. Inagaki, S., Takenaga, H., Ida, K., *et al. Nucl. Fusion* **46,** 133–141 (2006).

59. Hartfuss, H. J., Maassberg, H., Tutter, M., *et al. Nucl. Fusion* **26,** 678 (1986).

60. Gasparino, U., Erckmann, V., Hartfuss, H. J., *et al. Plasma Phys. Control. Fusion* **40,** 233–244 (1998).

61. Zhang, D., Glaubitz, M., Laqua, H. P., *et al. Nucl. Fusion* **52,** 043002 (2012).

62. Akulina, D., Batanov, G., Berezhetskii, M., *et al. Fusion Eng. and Des.* **53,** 321–328 (2001).

63. Takagi, S. in. **27A.** (ECA., *30th EPS Confereence on Contr. Fusion and Plasma Phys.* St. Petersburg, Russia, 2003), 3.26.

64. Eguilior, S., Castejon, F., De la Luna, E., *et al. Plasma Phys. Control. Fusion* **45,** 105–120 (2003).

65. Ida, K., Inagaki, S., Shimozuma, T., *et al. Phys. Plasmas* **11,** 2551 (2004).

66. Ida, K., Sakamoto, Y., Inagaki, S., *et al. Nucl. Fusion* **49,** 015005 (2009).

67. Wagner, F., Baumel, S., Baldzuhn, J., *et al. Phys. Plasmas* **12,** 072509–072509–22 (2005).

68. Mantica, P., Van Eester, D., Garbet, X., *et al. Phys. Rev. Lett.* **96,** 095002 (2006).

69. Inagaki, S., Ida, K., Tamura, N., *et al. Plasma Phys. Control. Fusion* **46,** A71 (2004).

70. Ida, K., Shimozuma, T., Funaba, H., *et al. Phys. Rev. Lett.* **91,** 085003 (2003).

Chapter 2

Electron Cyclotron Waves: the Kitchen Physics

Heat pulse propagation experiments require a source capable of modulating its output power, and a time-resolved electron temperature diagnostic with high spatial resolution. Electron Cyclotron Resonance Heating (ECRH) is used as the source for heat pulse propagation experiments on HSX, and the Electron Cyclotron Emission (ECE) diagnostic is used to measure the electron temperature and its response to modulated heating. This chapter provides the theoretical background in electron cyclotron wave propagation, emission, and absorption that is used in the analysis of the ECE diagnostic in Chapter 3, and the ECRH system in Chapter 4.

Electron cyclotron waves are absorbed and emit radiation at harmonics of the cyclotron frequency. Blackbody radiation represents an upper limit to the amount of radiation that a physical object may emit, and in most cases the ECE radiation from a dense, hot plasma. Planck's law describes the spectral radiation intensity, I_ω (the radiative power per unit area per unit solid angle per unit cyclic frequency), from a body with a stationary temperature, T. In the microwave band, where $\hbar\omega \ll \kappa T$, Planck's law reduces to the Rayleigh-Jeans approximation, $I_{bb,\omega} \approx \frac{\omega^2 \kappa T}{4\pi^2 c^2}$. The spectral intensity of a blackbody is directly proportional to its temperature, and electron cyclotron emission is used as a temperature diagnostic in modern fusion devices.

At very high plasma temperatures, strong wave absorption occurs across a large volume of the plasma, and re-absorption of the ECE power can occur before the radiation reaches the antenna. Conversely at low plasma density or temperature, the absorption is weak and the ECE power may undergo many wall reflections without being re-absorbed. In the limit of weak wave absorption, modeling is necessary to determine the electron temperature from the electron cyclotron emission from a plasma.

The accessibility of electron cyclotron waves to the plasma is briefly introduced in Section 2.1, and the Doppler and relativistic mechanisms of spectral line broadening are introduced in Section 2.2. The theory of linear absorption and emission of cyclotron waves from a weakly relativistic plasma is introduced in Section 2.3.

Kinetic theory is necessary to model non-thermal plasma, and the regime that nonthermal plasma is generated in HSX is described in Section 2.4. The radiation transport of cyclotron emission is introduced in Section 2.5, and the effect of multi-pass emission and wave damping is discussed in Section 2.6. A summary of the important concepts from this Chapter is included in Section 2.7.

2.1 Electron Cyclotron Wave Propagation and Accessibility

The basics of electron cyclotron wave propagation and accessiblity are governed by the linearized dispersion relation for cold plasma waves [71], $\vec{n}\times\vec{n}\times\vec{E}+\varepsilon\cdot\vec{E}=0$, where $\vec{n}=\frac{c\vec{k}}{\omega}$ is the wave index of refraction, and the cold plasma dielectric tensor is

$$\frac{\varepsilon}{\varepsilon_o}=1-\Sigma_s\begin{pmatrix}\frac{\omega_{p,s}^2}{\omega^2-\Omega_{c,s}^2} & \frac{\omega_{p,s}^2}{i\omega^2}\frac{\omega\Omega_{c,s}}{\omega^2-\Omega_{c,s}^2} & 0\\ \frac{\omega_{p,s}^2}{i\omega^2}\frac{\omega\Omega_{c,s}}{\omega^2-\Omega_{c,s}^2} & \frac{\omega_{p,s}^2}{\omega^2-\Omega_{c,s}^2} & 0\\ 0 & 0 & \frac{\omega_{p,s}^2}{\omega^2}\end{pmatrix}. \tag{2.1}$$

Here n_s is the plasma density for species s, $\omega_{p,s}=\frac{n_s q_s^2}{\varepsilon_o m_s}$ is the plasma frequency, and $\vec{\Omega}_{c,s}=\frac{q_s\vec{B}}{m_s}$ is the algebraic cyclotron frequency. The first two coordinates are perpendicular to the

direction of the magnetic field, and the third coordinate is aligned along the magnetic field direction.

For parallel wave propagation, $\vec{n} \parallel \vec{B}$, the transverse ($E_1$,$E_2$,0) and the longitudinal (0,0,E_3) waves decouple, and the transverse right-hand and left-hand circularly polarized waves and the longitudinal electrostatic plasma wave may propagate. The right-hand circularly polarized wave resonates with the Larmor motion of the electrons, where the wave frequency equals the electron cyclotron frequency, $\omega = \Omega_{c,e}$. Similarly, the left-hand circularly polarized wave resonates with Larmor motion of the ions, where the wave frequency equals the ion cyclotron frequency, $\omega = \Omega_{c,i}$.

Waves propagating oblique to the background magnetic field are elliptically polarized. In this case, the electric vectors of the ordinary and the extraordinary wave rotate in opposite directions as they propagate. For perpendicular wave propagation, $\vec{n} \perp \vec{B}$, the ordinary wave is linearly polarized, with its electric field parallel to the background magnetic field, and it cannot propagate below the plasma frequency. The electric field of the extraordinary wave is perpendicular to the background magnetic field, and it has two cut-off densities. The cut-offs of the extraordinary wave are $\omega_{\pm} = \frac{1}{2}\left(\sqrt{\Omega_{c,e}^2 + 4\omega_{p,e}^2} \pm |\Omega_{c,e}|\right)$. The extraordinary wave also has two hybrid-resonances that occur where the wave interacts with both the ions and electrons at either the upper-hybrid frequency, $\omega_{UH} = \sqrt{\omega_{p,e}^2 + \Omega_{c,e}^2}$, or the lower-hybrid frequency, $\omega_{LH} \approx \sqrt{\Omega_{c,e}\Omega_{c,i}}$.

The extraordinary wave at the fundamental cylotron frequency is prevented from accessing the cyclotron resonance by the evanescent region between the low-density cut-off and the upper-hybrid resonance during 1T machine operation. The extraordinary wave cut-off, upper-hybrid and resonance layers are illustrated in the boxport of HSX in Figure 2.1. The extraordinary wave at the fundamental cyclotron frequency must be launched from the high magnetic field side of the machine, for its resonance to be accessible to the wave. Higher

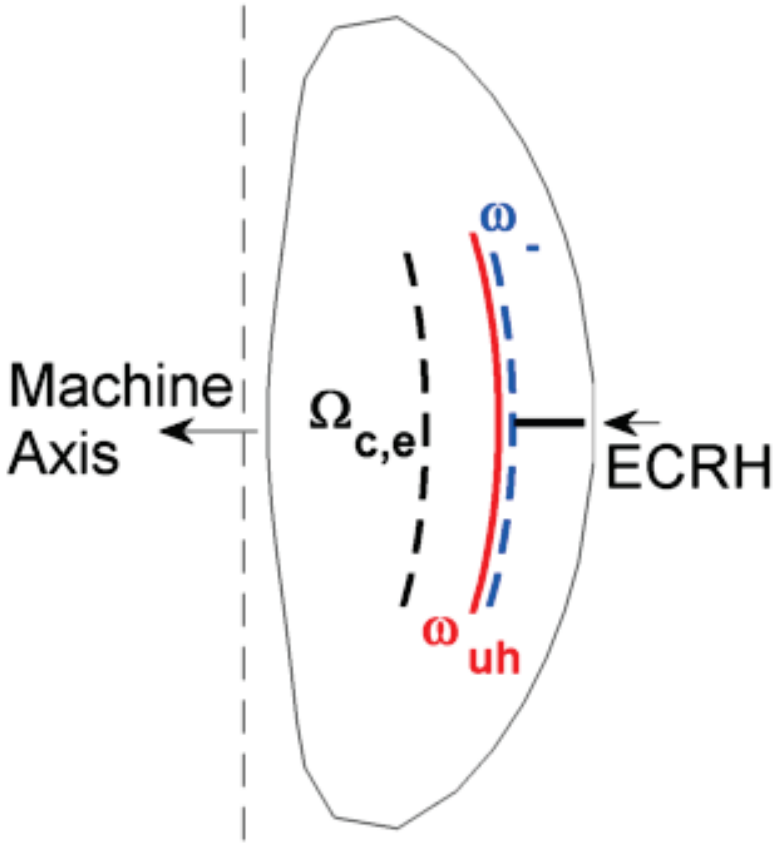

Figure 2.1: Extraordinary wave cut-off (ω_{-}), upper-hybrid (ω_{uh}), and electron cyclotron resonance ($\Omega_{c,e}$) layers in the HSX boxport.

harmonics of the extraordinary wave retain access to the resonance regardless of the magnetic field gradient as long as the frequency remains above the cut-off frequency. Similarly, the ordinary wave has access to the cyclotron resonance from any launching position, as long as the wave frequency remains above the plasma frequency.

The plasma wave resonances and cut-offs intercepted by the 28 GHz ECRH beam along the mid-plane of the boxport of HSX are shown in Figure 2.2 for a 1T on-axis magnetic field. The ordinary wave is used for plasma start-up and heating during 1T machine operation.

Both of the ECRH antennas on HSX are located on the outboard-side of the device. During 0.5T machine operation, the extraordinary wave at the 2nd harmonic of the cyclotron frequency is used for plasma start-up and heating.

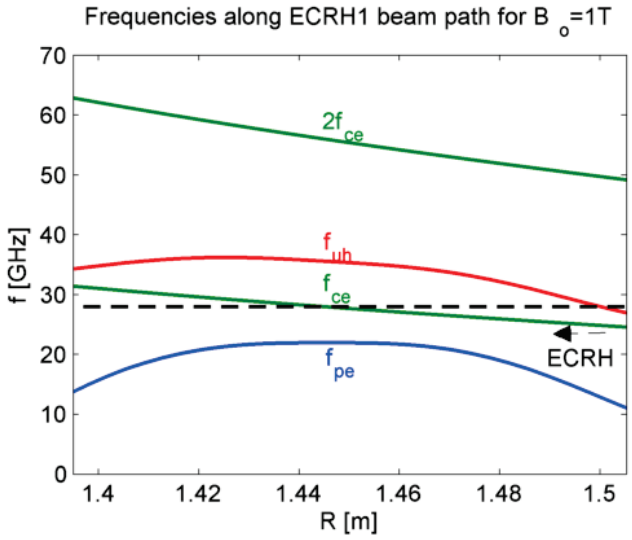

Figure 2.2: The fundamental and 2nd harmonic of the electron cyclotron frequency, f_{ce}, the plasma frequency, f_{pe}, and the upper-hybrid frequency, f_{uh}, are shown along the mid-plane of the HSX boxport during 1T machine operation. The 28 GHz ECRH frequency used for ECRH is shown as a black dashed line.

The ECE diagnostic observes the 2nd harmonic of the electron cyclotron frequency, and this frequency is also shown in Figure 2.2. The ECE antenna couples to the wave emitted from the plasma that has its wave electric field perpendicular to the background magnetic field, which corresponds to the extraordinary wave. The fundamental electron cyclotron resonance is above the plasma frequency cut-off, and it is below the upper-hybrid frequency during 1T machine-operation.

2.2 Spectral Broadening of Electron Cyclotron Emission

The cyclotron resonance for harmonic, m is

$$\omega_m = m\Omega_{c,e} + k_{\|} v_{\|}, \tag{2.2}$$

In the limit of $k_{\|} = 0$ (perpendicular observation), the relativistic effect on the electron mass leads to a shift in the cyclotron frequency. In the opposite limit of high $k_{\|}$ (oblique observation), the relativistic effect can be small compared to the Doppler shift due to high parallel electron velocity. In addition to shifting the electron cyclotron frequency, finite electron temperature causes both relativistic and finite temperature broadening of the absorption and emission. Figure 2.3 illustrates the temperature broadening mechanism of changing the ECE spectral shape. With the observation angle set at 45°, the spectral shape of the ECE is broadened by increasing the electron temperature from 3 keV to 10 keV.

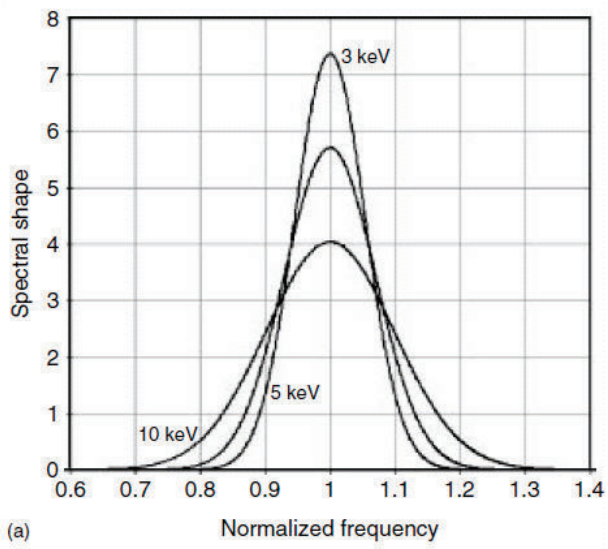

Figure 2.3: Broadening of the ECE spectral shape is illustrated as the temperature is increased from 3 keV to 5 keV to 10 keV under a fixed observation angle of 45°. Reproduced from [72].

The relativistic shift and finite temperature broadening of the ECE spectrum is demonstrated in Figure 2.4. The spectral shape of the ECE is shifted to lower frequencies and broadened as the electron temperature is increased from 3 keV to 5 keV to 10 keV.

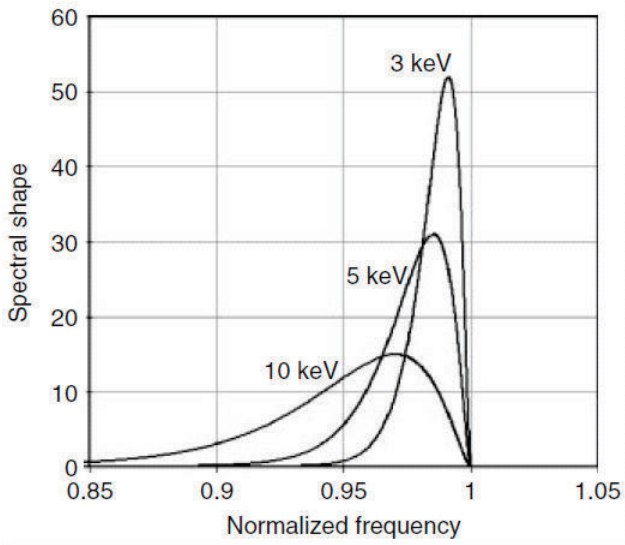

Figure 2.4: The spectral shape of the ECE is downshifted and broadened by increasing temperature from 3 keV to 5 keV to 10 keV under perpendicular observation. Reproduced from [72].

2.3 Linear Theory: Absorption and Emission

As the plasma density increases, the re-absorption of the radiation by the plasma becomes important and must be included to calculate the total emission. When the plasma density and temperature are insufficient for the plasma to be considered a perfect absorber, the re-absorption and emission along the line of sight of a diagnostic is described by the radiation transport equation [73],

$$n_r^2 \frac{d}{ds}\left(\frac{I_\omega}{n_r^2}\right) = j_\omega - \alpha_\omega I_\omega, \tag{2.3}$$

where j_ω and α_ω are the plasma emissivity and absorption along ray-trajectories with ray-refractive indice n_r that originate at the observation point [73]. Electron cyclotron absorption

and emission are complementary processes, and the damping of a wave carrying heating power, P, along a ray trajectory is $\frac{dP}{ds} = \alpha_\omega P$ in the geometric optics approximation.

The elements of the cold plasma dielectric tensor used in the introduction of wave propagation and accessibility in Section 2.1 are insufficient for modeling the absorption of cyclotron waves. Absorption requires an imaginary component to the dielectric tensor, and the anti-Hermitian portion of the cold plasma dielectric tensor is identically zero.

The collisionless absorption of electromagnetic waves through weak wave damping can be used to calculate the absorption coefficient in a hot, dense plasma, $\alpha \equiv 2\Im[\vec{k}] \cdot \vec{s}$, by using the Poynting theorem to determine the spatial damping rate along the direction of the energy flux, $\vec{s} = \frac{\vec{S}(\vec{k},\omega)}{|\vec{S}(\vec{k},\omega)|}$. The emission can be determined in a similar way, and the absorption coefficent and the emission coefficient are

$$\alpha(\omega) = \frac{\omega}{4\pi} \frac{\vec{E^*} \cdot \bar{\epsilon}_a \cdot \vec{E}}{|\vec{S}(\vec{k},\omega)|}, \tag{2.4}$$

$$j(\omega) = \pi n_r^2 \left(\frac{\omega}{c}\right)^2 \frac{\vec{E^*} \cdot \bar{G} \cdot \vec{E}}{|\vec{S}(\vec{k},\omega)|}. \tag{2.5}$$

Here $\bar{\epsilon}_a = \frac{1}{2}[\bar{\epsilon} + \bar{\epsilon}^\dagger]$ is the anti-Hermitian part of the dielectric tensor ($\bar{\epsilon}$), and $\dagger$ indicates the conjugate transpose (Hermitian conjugate). $\vec{E}$ is the Fourier transformed wave-electric field, and $\bar{G}$ is the micro-correlation tensor [71]. The wave absorption and emission depends sensitively on the wave polarization, but the absorption also depends on the anti-Hermitian portion of the dielectric tensor.

In the weakly-relativistic limit, the anti-Hermitian part of the dielectric tensor is

$$\bar{\epsilon}_a = -\pi \frac{\omega_p^2}{\omega^2} \sum_{m=-\infty}^{+\infty} \int d^3p \frac{1}{\gamma} \left[\frac{m\Omega_{ce}}{\omega} \frac{\partial f}{\partial p_\perp} + n_\parallel \frac{p_\perp}{m_e c} \frac{\partial f}{\partial p_\parallel} \right] \bar{S}^{(m)} \delta \left(\gamma - \frac{k_\parallel v_\parallel}{\omega} - \frac{m\Omega_{ce}}{\omega} \right), \tag{2.6}$$

and the micro-correlation tensor, $\bar{G}$, is

$$\bar{G} = -\frac{\pi}{(2\pi)^5} \frac{1}{m_e} \frac{\omega_p^2}{\omega^2} \sum_{m=-\infty}^{+\infty} \int d^3p \frac{p_\perp f}{\gamma} \bar{S}^{(m)} \delta \left(\gamma - \frac{k_\parallel v_\parallel}{\omega} - \frac{m\Omega_{ce}}{\omega} \right), \tag{2.7}$$

where

$$\bar{S}^{(m)} = \begin{pmatrix} p_\perp \left(\frac{mJ_m}{b}\right)^2 & -ip_\perp \frac{mJ_m J'_m}{b} & p_\parallel \frac{mJ_m^2}{b} \\ ip_\perp \frac{mJ_m J'_m}{b} & p_\perp \left(J'_m\right)^2 & ip_\parallel J_m J'_m \\ p_\parallel \frac{mJ_m^2}{b} & -ip_\parallel J_m J'_m & \frac{p_\parallel^2}{p_\perp} J_m^2 \end{pmatrix}.$$

$J_m(b)$ is the Bessel function of the first kind, and its argument is the ratio of the electron Larmor radius to perpendicular wavelength, $b = \left|\frac{k_\perp p_\perp}{m_e \Omega_{c,e}}\right|$, J'_m is its derivative, $n_\parallel$ is the parallel refractive index, and γ is the Lorentzian factor. The emissivity depends on the electron distribution function, $f(p_\parallel, p_\perp)$, where $p_\parallel$ and $p_\perp$ are the parallel momentum and the perpendicular momentum respectively, and the absorption depends on the derivative of the electron distribution function in momentum space [74].

2.4 Consequences of Nonthermal Electrons in HSX

When the absorbed power density is high enough, $p_{abs}/n_e T_e \nu_e \ll 1$ where ν_e is the collision frequency of the resonant electrons, collisional relaxation is insufficient to thermalize the electrons, and the deviation from a Maxwellian distribution function can be large [75].

The ECE radiation temperature from an experiment with low power density, where the plasma may be considered Maxwellian, and high power density, where the effect of nonthermal electrons modifies the measurement, are shown in Figure 2.5. In the low-ECRH power density case of Figure 2.5a, 44 kW of launched power is used to support a plasma of line-average density 4.3×10^{12}cm^{-3}, and the ECE radiation temperature at the edge, half-radius, and core of the plasma are thermal. In the high power density case of Figure 2.5b, 96 kW of launched power is used to support a plasma of line-average density 2.0×10^{12}cm^{-3}, and the ECE radiation temperature at the half-radius and core of the plasma have bursty behavior with a duration less than 0.1 ms.

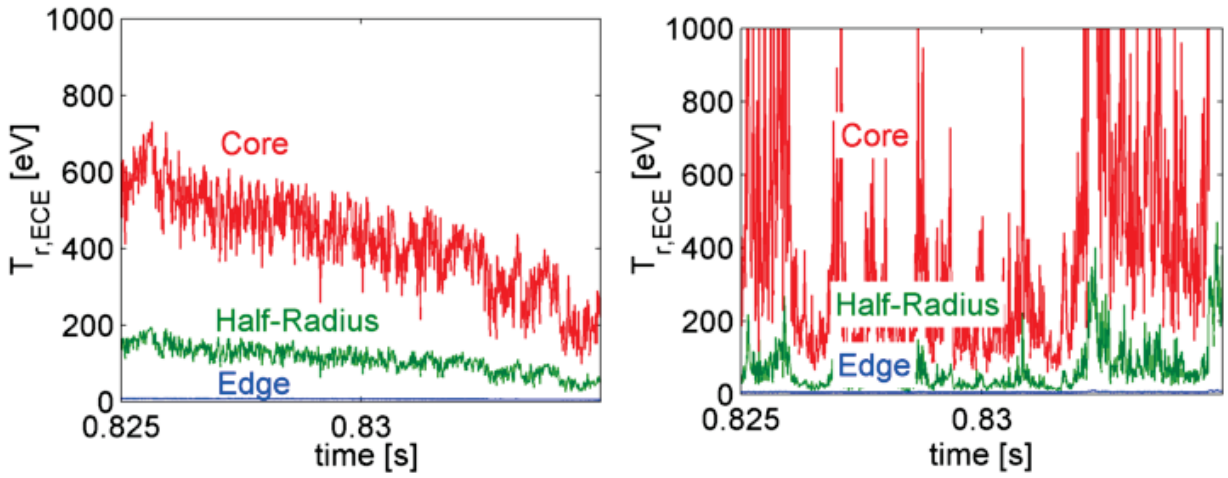

(a) Low P/n: 44 kW, 4.3×10^{12}cm^{-3} (b) High P/n: 96 kW, 2×10^{12}cm^{-3}

Figure 2.5: Edge (blue), half-radius (green), and core (red) ECE radiation temperature for two ECRH power densities. Bursty behavior is measured at high power density.

Similar behavior was observed in the W7-AS experiment with high ECRH power densities. In W7-AS, the bursty phenomena were attributed to local degradation of the power absorption due to flattening of the distribution function, and the flattening of the distribution function was followed by increased absorption by collisionless ripple trapped electrons that were resonant at high energies [76]. Investigation of the bursty behavior on HSX through kinetic modeling is suggested as future work in Chapter 7.

The ECE signal after ECRH turn-off is also modified by high-energy, collisionless electrons in HSX. The decay of the ECE signal after ECRH turn-off is shown for a channel near the HSX half-radius in Figure 2.6, for the two ECRH power densities of Figure 2.5. In the low-ECRH power density case, the ECE signal decays to zero quickly after ECRH turn-off. In the high power density case, the ECE signal decays with two time-scales: a fast decay-time that is associated with thermal electrons, and a slow decay-time that is associated with non-thermal electrons. The non-thermal electrons have high residency time in HSX because of good fast particle confinement at a low-collisionality.

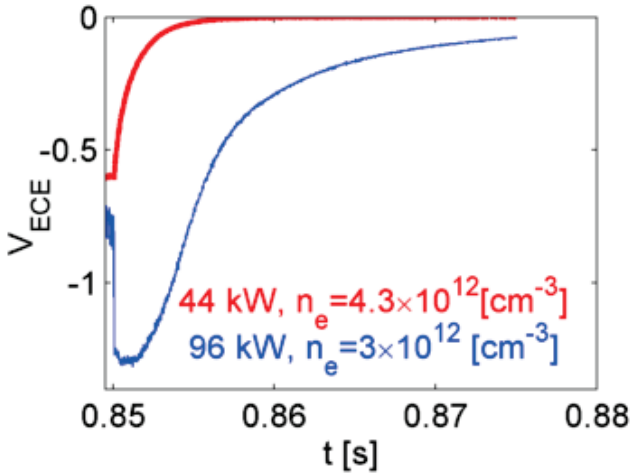

Figure 2.6: ECE signal near the HSX half-radius after ECRH turn-off for two power densities. At low power density (red), the signal decays quickly. At high power density (blue), there are two time-scales associated with the decay.

The analysis of the ECE and ECRH on HSX is limited to regimes where the plasma is Maxwellian. The total plasma stored energy, W_E^{diam} measured by a diamagnetic loop, includes the energy in the thermal and nonthermal populations of the plasma. This quantity is compared to the kinetic stored energy (the energy in the thermal electron population) inferred from Thomson scattering measurements to limit the experimental regimes explored in this work. The kinetic stored energy is approximated by the thermal energy of the ions and electrons, $W_E^{kin} = W_{E,e} + W_{E,i}$. An example of the diamagnetic stored energy measurement of a plasma supported by 85 kW of launched ECRH power at a line-average plasma density of $4{\times}10^{12}$cm^{-3} is shown in Figure 2.7.

The diamagnetic stored energy does not measurably change for line-average plasma densities between $2{\times}10^{12}$ cm^{-3} and $4.3{\times}10^{12}$ cm^{-3}; however, the kinetic stored energy does vary over this density range, and the change is attributed to a change in the energy carried by nonthermal electrons (the comparison is shown in Figure 2.10). The Thomson scattering diagnostic of HSX samples the thermal part of the electron distribution function. The thermal

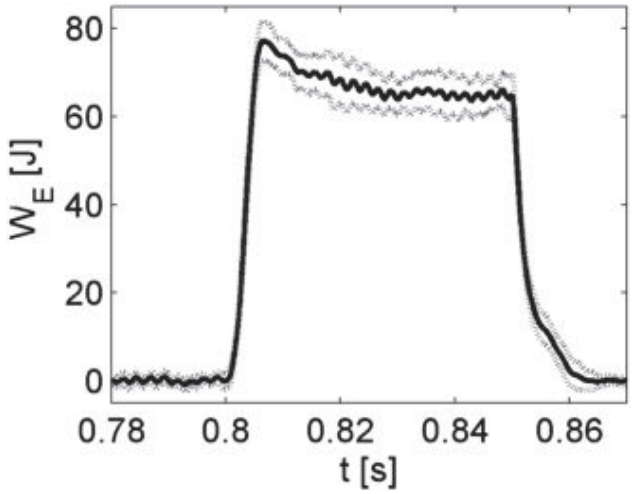

Figure 2.7: Diamagnetic stored energy measured by a flux loop versus time (solid line) with experimental uncertainty (dashed lines) at a plasma line-average density of 4×10^{12}cm^{-3}.

electron energy is obtained by integrating over the plasma density and electron temperature measured by Thomson scattering, $W_{E,e} = \int n_e T_e dV$ where V is the plasma volume.

The uncertainty in the kinetic stored energy is dominated by the systematic uncertainty in the fit to the electron temperature and plasma density profiles, and a Monte-Carlo approach is used to include this uncertainty by fitting four functions to the profiles: a piecewise linear fit, a stiff-spline fit, and a 5^{th} and 6^{th} order polynomial fit. The experimental uncertainties are also included by varying the fitted electron temperature and plasma density within their uncertainties. Twenty-five test profiles are used per fitting function. An example electron temperature and plasma density profile measured through Thomson scattering in a plasma supported by 85 kW of launched power at a line-average plasma density of 4×10^{12}cm^{-3} is shown in Figure 2.8 along with the fits used during integration.

The ion portion of the kinetic energy is estimated from previous impurity ion measurements using Charge Exchange Recombination Spectroscopy (CHERS). There are no impurity ion temperature measurements in these experiments, because the HSX CHERS system requires a significant fraction of carbon in the plasma; however, previous measurements have

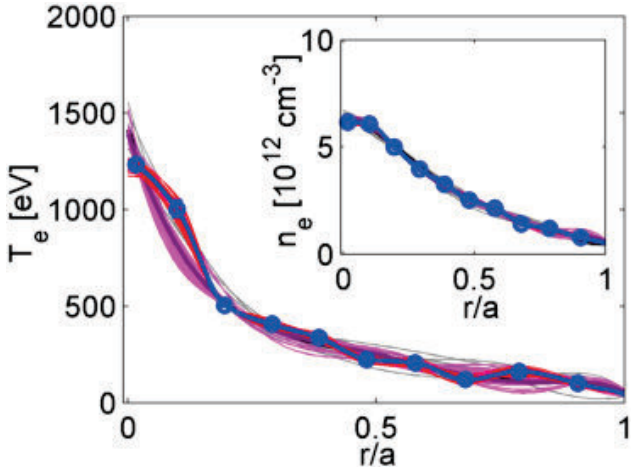

Figure 2.8: Four electron temperature and plasma density fiting functions, each with 25 fits that result from varying the measured temperature and density within their experimental uncertainties, are used to determine the electron thermal energy.

shown that the impurity ion temperature did not change significantly over a large parameter regime in HSX when carbon was present [77] [78]. The proton and impurity energy equilibration time is much faster than the ion confinement time, and the impurity temperature is assumed to be approximately equal to the proton temperature [77]. Additionally, the ion plasma density is assumed to be equal to the electron plasma density, $n_i \approx n_e$ (through quasi-neutrality with the effective charge of the thermal plasma ions equal to unity, $Z_{eff} \approx 1$). The kinetic energy carried by the ions is the integral of these profiles, $W_{E,i} = \int n_i T_i dV$. Figure 2.9 shows the impurity carbon (C^{+6}) ion temperature measured through CHERS in a plasma with significant carbon fraction. There is no measurable change in the ion temperature as the line-average density was changed from 3×10^{12}cm^{-3} to 4×10^{12}cm^{-3}.

The plasma stored energy from the diamagnetic loop is compared to the kinetic stored energy over a range of line-average densities measured using the central chord of the HSX interferometer in Figure 2.10. The launched power was held at 85 kW during this experiment. There is a discrepancy between the total plasma stored energy and the kinetic stored energy

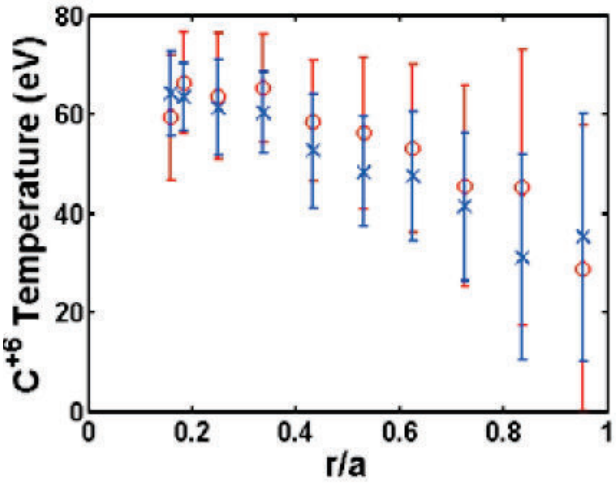

Figure 2.9: Impurity carbon (C^{+6}) ion temperature measured through CHERS at line-average plasma density of 3×10^{12}cm^{-3} (red circles) and 4×10^{12}cm^{-3} (blue crosses). Reproduced from [77].

at low-plasma density, and this discrepancy decreases with increasing line-average density. The two measurements converge near line-average plasma density of 3.5×10^{12}cm^{-3}. The change in kinetic stored energy is primarily attributed to increased electron thermal energy in the plasma, and a decrease in the portion of energy carried by nonthermal electrons.

As the launched ECRH power decreases, the threshold for assuming the plasma is thermal also decreases. The analyses of the ECE in Chapter 3 and of the ECRH in Chapter 4 are limited to experimental regimes above line-average plasma density of 3.5×10^{12}cm^{-3}, where the distribution function is expected to be Maxwellian. The heat transport experiments introduced in Chapter 5 and compared to gyrokinetic calculations in Chapter 6 are also in this density regime.

2.5 Radiation Transport

Following [73], a radiation temperature can be defined in analogy with Kirchoff's law in terms of a source function, $S_\omega = \frac{1}{n_r^2}\frac{j_\omega}{\alpha_\omega} = \frac{\omega^2}{8\pi^3c^2}\kappa T_{r,\omega}$, such that for a Maxwellian distribution

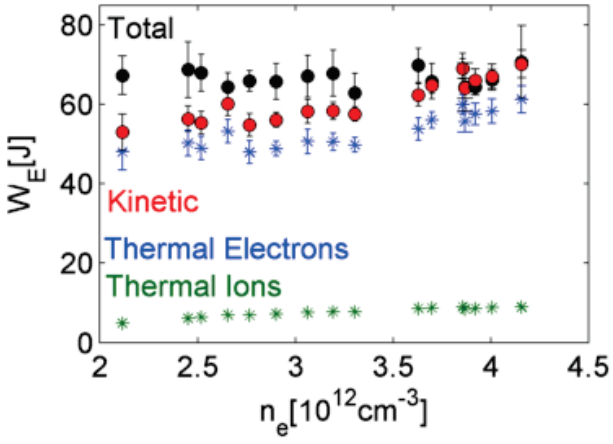

Figure 2.10: The total stored energy measurement (W_E^{diam}, black circles), electron stored energy measurement ($W_{E,e}$, blue asterisks), an estimate of the energy carried by the ions ($W_{E,i}$, green asterisks), and the kinetic stored energy ($W_E^{kin} = W_{E,e} + W_{E,i}$, red circles).

function the source reduces to the vacuum blackbody intensity, $I_{\omega,bb}$. The equation of radiation transfer along the ray direction, $\vec{s}$, in terms of the radiant intensity, I_ω and the source function, is

$$\frac{d}{ds}\left(\frac{I_\omega}{n_r^2}\right) = \frac{I_\omega}{n_r^2} - S_\omega. \tag{2.8}$$

The solution to Equation 2.8, including a radiation of intensity $I_{o,\omega}$ incident on the opposite side of the plasma from the observation point and located outside of the plasma, is

$$I_{r,\omega} = I_{o,\omega}e^{-\tau} + \int_0^s S_\omega(s)e^{-\tau'}ds, \tag{2.9}$$

where $\tau = \int \alpha ds$ is the integrated absorption from the back of the slab to the detector along the ray, and τ is an optical depth. The first term of Equation 2.9 represents damping of incident radiation as it passes through the resonant region, and the second term is a combination of emission, S_ω, and re-absorption, $e^{-\tau}$, within the plasma. The spectral radiant intensity $I_{r,\omega}$ that reaches the detector is the sum of the damped incident radiation and the remaining generated radiation along the ray.

The fundamental electron cyclotron resonance, neglecting the Doppler effect, is $\omega_{c,e} = \frac{e|B|}{m_e}\sqrt{1-\frac{T_e}{m_e c^2}}$, where $|B|$ is the magnetic field strength and m_e is the rest mass of the electron in this case. Finite electron temperature causes electrons to emit radiation at lower frequencies than the cold plasma resonance. The absorption coefficient (a), plasma optical depth (b), normalized emissivity (c), and integrated emissivity (d) along the view of the ECE antenna are shown in Figure 2.11 for the extraordinary wave at 56 GHz. Two central electron temperatures are shown in Figure 2.11 along with the cold plasma resonance of the wave at a central plasma density of 6×10^{12}cm^{-3} and an on-axis magnetic field of 1T.

The emissivity in Figure 2.11c is determined through Kirchoff's law by $j_\omega(s) = I_\omega(s)\alpha_\omega(s)e^{-\tau(s)}$ [74] [79]. The emissivity of Figure 2.11c is broadened and the spatial resolution is decreased by hot electrons, but the re-absorption stays low for the experimentally relevant density profile used in the calculation (this is evident from the integrated emissivity in Figure 2.11d). The natural line width is the width of the emitting layer from which 90% of the radiation escapes without re-absorption [79], and it is found by integrating the emissivity.

The measured radiation temperature in the absence of background radiation is $T_{r,\omega} = T_e(1-e^{-\tau})$. For an optically thick plasma, where $\tau \gg 1$, the radiant intensity perpendicular to the magnetic field can be considered blackbody. The measured radiation temperature in this case is the local electron temperature, $T_{r,\omega} = T_e$. In practice, the emission is considered blackbody when $\tau > 2$, and the natural line width of the ECE, Δd, can be defined as the point at which $\tau = \int_{\text{antenna}}^{\Delta d} \alpha ds = 2$ [80].

For an optically thin (semi-transparent or gray) plasma, where $\tau \ll 1$, the radiation temperature is proportional to the optical thickness of the plasma, $T_{r,\omega} \propto \tau T_e$. For the extraordinary wave at the 2$^{\text{nd}}$ harmonic of the cyclotron frequency, the optical depth is

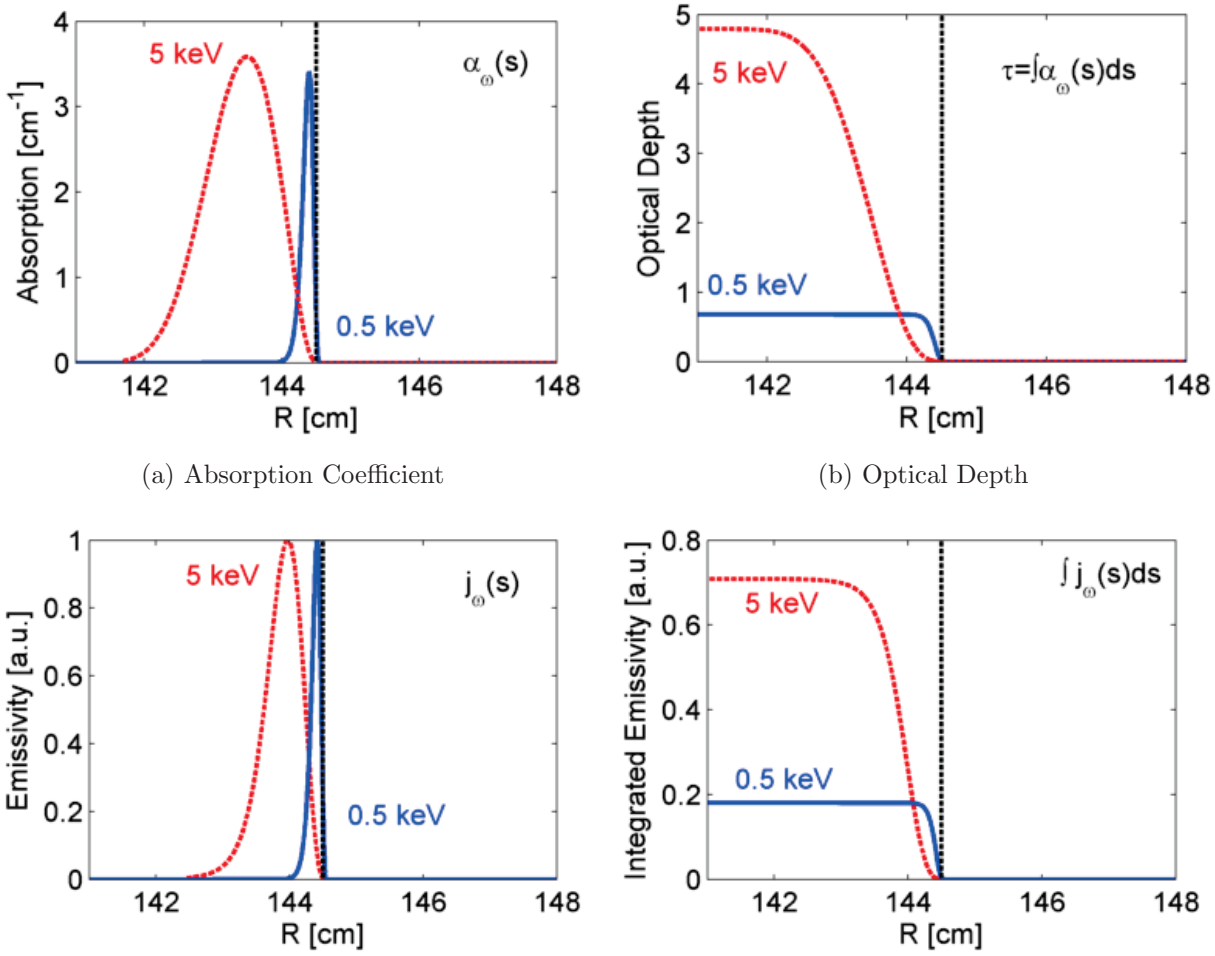

(a) Absorption Coefficient

(b) Optical Depth

(c) Emissivity (normalized)

(d) Integrated Emissivity

Figure 2.11: (a) Absorption, (b) optical depth, (c) normalized emissivity, and (d) integrated emissivity at central electron temperatures of 0.5 (blue line) and 5 keV (red line) are shown along the ECE viewing axis for the extraordinary wave at 56 GHz. The cold plasma resonance is also shown (black line).

proportional to the local temperature and plasma density, and the resulting plasma emission is linear in the electron density and quadratic in the electron temperature, $T_{r,\omega} \propto n_e T_e^2$.

Based upon the slab model for single-pass absorption, the percent of relative systematic error in interpreting the ECE radiation temperature as an electron temperature is 5% for

an optical depth of 3, but grows to 37% for an optical depth of 1. The first-pass optical depth of the plasma to the extraordinary wave at the 2nd harmonic of the electron cyclotron frequency is less than 3 across the minor radius of HSX, and the plasma is optically gray to the ECE diagnostic according to the single-pass model.

Similarly, the absorption efficiency of ECRH may also be related to the optical depth of the plasma to the incident radiation, $\eta = P_{abs}/P_0 = 1-e^{-\tau}$. The ECRH absorption efficiency after the first-pass through the plasma is 95% for an optical depth of 3, but decreases to below 30% for an optical depth lower than 0.35. The first-pass optical depth of the plasma to the ordinary wave at the fundamental resonance is less than 0.5, and there is low-first pass absorption during 1T machine operation in HSX according to the single-pass model.

2.6 Finite Reflectivity: Multi-pass Emission and Wave Damping

In low-optical depth plasma, electron cyclotron radiation undergoes multiple reflections from the vacuum vessel wall, and traverses the plasma many times before reaching the ECE diagnostic. With each pass through the plasma the intensity of emission is reinforced raising the effective optical depth of the plasma. This leads to spatial averaging across the ECE resonance, as regions that are not directly viewable by the ECE diagnostic are sampled through multi-pass absorption and emission. In the limit of infinite reflections between parallel planes, the collected radiation can be written as an infinite series

$$I_{r,\omega} = I_{bb}(1 - e^{-\tau}) \sum_{n=0}^{\infty} \rho^n e^{-n\tau} = I_{bb} \frac{1 - e^{-\tau}}{1 - \rho e^{-\tau}}, \tag{2.10}$$

where ρ represents the reflectivity of the planes. Equation 2.10 is the solution to the radiation transport equation in a slab, where the incident radiant intensity of Equation 2.9 has been replaced by an isotropic background intensity, $I_{o,\omega}$ (which includes contributions from

polarizations and harmonics other than the target mode and polarization) [81],

$$I_\omega(R,z,\theta,\phi) = I_{bb,\omega}[1-e^{-\tau}] + I_{o,\omega}e^{-\tau}. \tag{2.11}$$

Equations 2.10 and 2.11 are equivalent when the isotropic emission incident on the back of the slab is $I_{o,\omega} = I_{bb,\omega}\rho\frac{1-e^{-\tau}}{1-\rho e^{-\tau}}$, which explicitly includes the final reflection.

There are four limits of Equation 2.10. In the zero-reflectivity limit, $\rho = 0$, the single-pass absorption model is recovered and $T_{r,\omega} = T_e(1-e^{-\tau})$. In the total reflection limit, $\rho = 1$, the plasma behaves as a blackbody, $T_{r,\omega} = T_e$, and the radiation temperature is the average electron temperature over the resonance $T_{r,\omega} = T_e(R,z)$.

In the optically thick limit with finite reflections, where $\tau \gg 1$, Equation 2.10 reduces to $T_{r,\omega} \approx T_e$, and the plasma may be considered a blackbody. In the optically gray or thin limit with finite reflections, the emission is reinforced by taking multiple passes through the resonance, and Equation 2.10 describes the radiation transport with an effective optical depth greater than the optical depth from a single-pass through the plasma.

The systematic error in interpreting the average radiation temperature, $T_{r,e}$, as the average electron temperature, T_e, is plotted as a function of reflectivity and optical depth in Figure 2.12. The systematic error is unacceptably high for reflectivities less than 0.9, and the finite optical depth and reflectivity correction must be included for reflectivities less than 0.9 when determining the average electron temperature from ECE.

The reflectivity of the stainless steel vacuum vessel of HSX at 56 GHz is nearly unity (0.998); however, the reflectivity used in Equation 2.10 is an effective reflectivity that includes beam truncation losses and specular reflection [81]. The effective reflectivity of HSX is inferred to be greater than 0.9 (and approximately equal to unity) across the majority of the HSX minor radius by comparing the absolutely calibrated ECE radiation temperature with Thomson scattering measurements in Section 3.6.

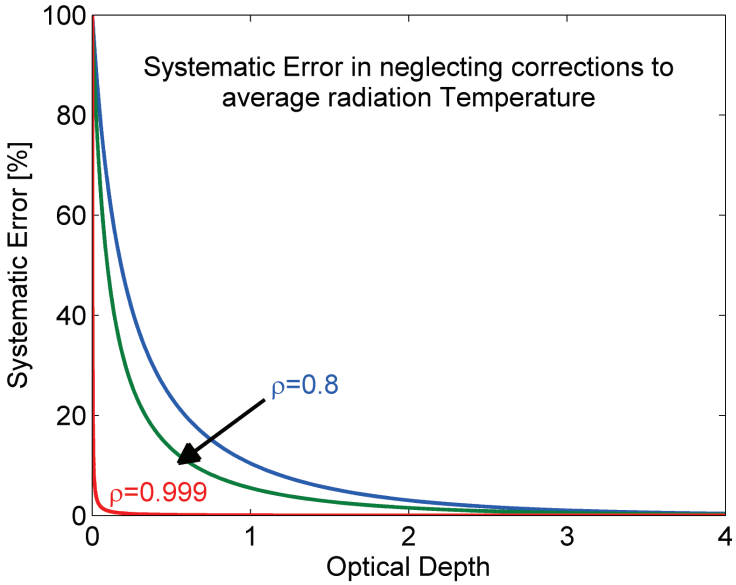

Figure 2.12: Systematic error in interpreting the average radiation temperature, $T_{r,e}$, as the average electron temperature, T_e, as a function of optical depth and reflectivity.

Similarly, previous measurements of the absorption of ECRH in HSX during 0.5T machine operation [82] indicate that the effective reflectivity of the first ECRH antenna is 0.9, and this value is consistent with absorption measurements during 1T machine operation, and modeling of the multi-pass wave damping in Section 4.2.2.

2.7 Summary of the Kitchen Physics

The electron cyclotron emission from a plasma is used as a spatially localized and time-resolved electron temperature diagnostic in magnetically confined fusion experiments; however modeling is necessary to determine the electron temperature in HSX. For the perpendicular view of the ECE diagnostic from the low field side of the device, there is a relativistic frequency shift due to the change in electron mass with energy, and the emission originates from the high field side of the cold plasma resonance. Fast electrons are efficient emitters and absorbers of cyclotron radiation, and nonthermal electrons can significantly alter the

electron cyclotron emission and absorption. A model for emission including multiple reflections from the vessel wall is necessary in plasma with low first pass optical depth, and wall reflections increase the optical depth of the plasma.

Electron cyclotron emission and absorption are complementary processes, and the challenges in modeling the electron cyclotron emission are shared in modeling the electron cyclotron absorption in a magnetically confined plasma. Electron cyclotron resonance heating is an efficient method of increasing the electron temperature of a plasma, but it can result in large deviations from a Maxwellian distribution function in low-collisionality plasma at high powers. Wave absorption is sensitive to the slope of the distribution function, and bursty phenomena are observed in the electron cyclotron emission at high power densities in HSX. The analysis of the ECE in Chapter 3, and the ECRH in Chapter 4, as well as the heat transport experiments in Chapter 5 and Chapter 6, are limited to line-average plasma densities above $3.5\times10^{12}\text{cm}^{-3}$. This is the operational regime with a negligible non-thermal electron population, and where the HSX plasma is assumed to be Maxwellian.

Bibliography

71. Stix, T. H. (*Waves in Plasmas*, Springer, 1992).

72. Hartfuss, H. J. & Geist, T. (*Fusion Plasma Diagnostics with mm-Waves*, John Wiley & Sons, 2013).

73. Bekefi, G. (Wiley, *Radiation Processes in Plasmas*, New York, 1966).

74. Bornatici, M., Cano, R., De Barbieri, O., *et al. Nucl. Fusion* **23,** 1153–1257 (1983).

75. Erckmann, V. & Gasparino, U. *Plasma Phys. Control. Fusion* **36,** 1869–1962 (1994).

76. Rome, M. *Plasma Phys. Control. Fusion* **39,** 117–158 (1997).

77. Briesemeister, A., Zhai, K., Anderson, D. T., *et al. Plasma Phys. Control. Fusion* **55,** 014002 (2013).

78. Briesemeister, A. PhD thesis (The University of Wisconsin - Madison, 2013).

79. Hartfuss, H. J., Geist, T. & Hirsch, M. *Plasma Phys. Control. Fusion* **39,** 1693–1769 (1997).

80. Watts, C., Hartfuss, H. J. & Hase, M. *Rev. Sci. Instrum.* **75,** 3177–3184 (2004).

81. Clark, W. H. M. *Plasma Physics* **25,** 1501–1529 (1983).

82. Likin, K. M., Talmadge, J. N., Almagri, A. F., *et al. AIP. Conference Proceedings* **694,** 331–334 (2003).

Chapter 3

ECE Diagnostic and Analysis

The emission of the extraordinary wave at the 2nd harmonic of the electron cyclotron frequency is used to diagnose the electron temperature on HSX using an absolutely calibrated, 16 channel heterodyne radiometer. The radiation temperature is in good agreement with the electron temperature measured through Thomson scattering, and it is significantly larger than that predicted by a model with an optical depth from the single pass absorption. The antenna pattern of the ECE diagnostic and the plasma parameters have a significant impact on the measured radiation temperature, and modeling of the emission sampled by the diagnostic is necessary to determine the radiation temperature. An iterative procedure is used to self-consistently determine the electron temperature from the measured radiation spectrum. Relativistically down-shifted emission causes asymmetry in the ECE intensity across the magnetic-axis at high ECRH power density in HSX; however, the channels on the high field side of the magnetic axis remain thermal. The spatial and temporal resolution of the ECE radiometer have been increased for use in heat pulse propagation experiments, and to ensure that emission is thermal the ECE channels on the high-field side of the magnetic-axis are used in the analysis of heat pulse propagation experiments on HSX.

The 16-channel ECE radiometer is described in Section 3.1, and the absolute calibration of the diagnostic is discussed in Section 3.2. The optical depth of the plasma is analytically modeled using a 1D analysis along the diagnostic view, as well as a 2D analysis in the

helical cut of the boxport, and these results are compared to a 3D model from ray tracing in Section 3.3. The absorption modeling is followed by an overview of changes made to the diagnostic to increase the spatial and temporal resolution of the radiometer in Section 3.4. The absolutely calibrated radiation temperature is compared to an analytic model of the first-pass emission in Section 3.5, and an iterative procedure for self-consistently determining the electron temperature from the measured radiation spectrum is presented in Section 3.6.

3.1 The ECE Radiometer

The HSX electron cyclotron emission diagnostic is a 16-channel heterodyne radiometer that measures the power radiated at the 2^{nd} harmonic of the electron cyclotron frequency in the extraordinary wave. The "front-end" of the ECE diagnostic converts microwave power within the HSX vacuum vessel to electrical power at the heterodyne receiver. The "front-end" consists of the ECE antenna, waveguide line, and microwave mixing element. The "back-end" is the heterodyne reciever of the ECE diagnostic where the signal from the "front-end" is divided, amplified, filtered and detected. The diagnostic layout of the ECE system is shown in a block diagram in Figure 3.1.

Outside of the plasma, the perpendicularly propagating extraordinary wave couples to a Transverse Electromagnetic (TEM) wave in vacuum that is linearly polarized with its wave electric field perpendicular to the background magnetic field [72]. An ellipsoidal mirror re-directs the wave to a pyramidal horn antenna that couples its power into a rectangular microwave waveguide. Two views of the ECE antenna within the HSX vacuum vessel are shown in Figure 3.2.

Figure 3.2a shows the view from behind the antenna, in which the back of the vacuum vessel wall in boxport D is visible. The ellipsoidal mirror of the antenna has three

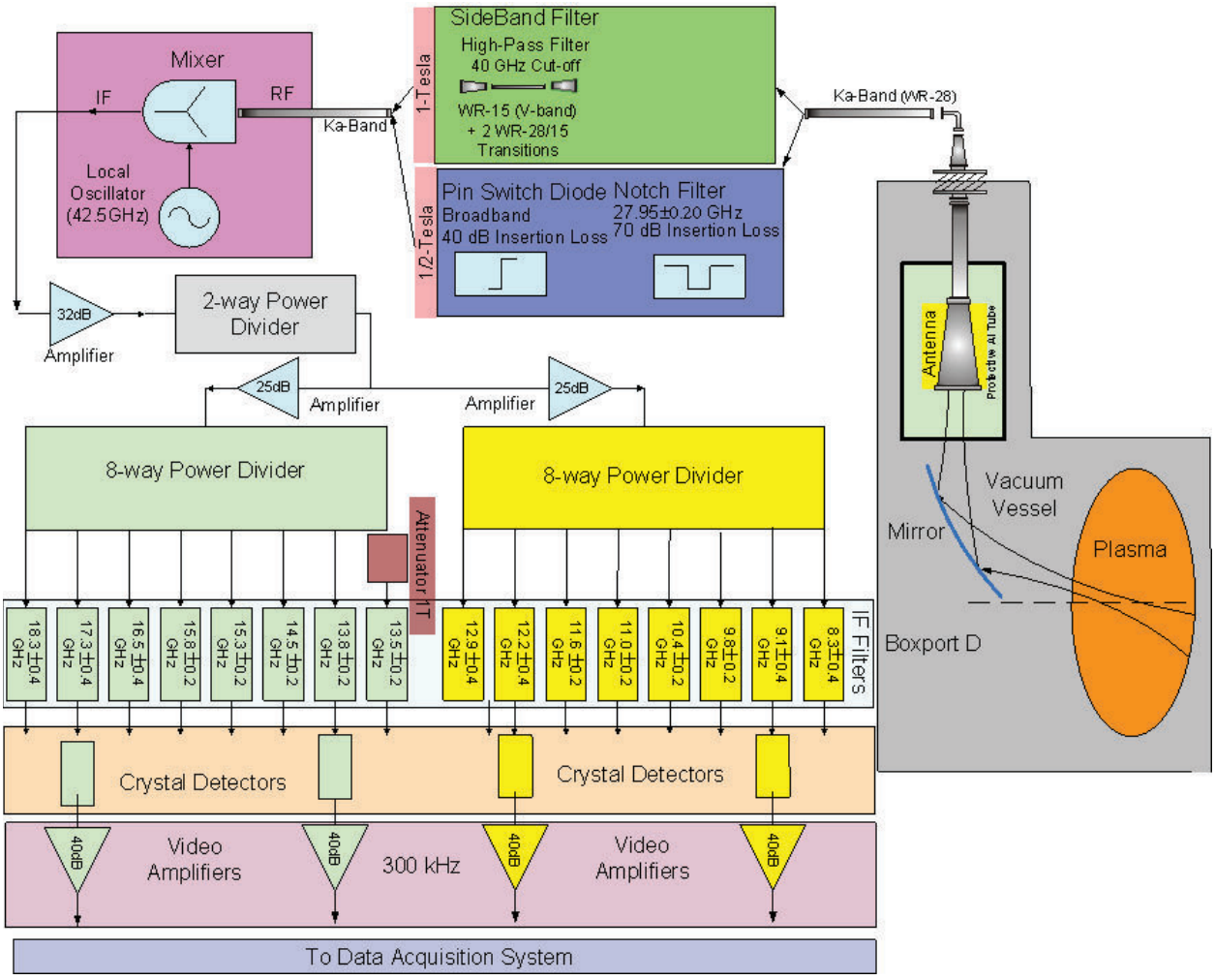

Figure 3.1: ECE diagnostic block diagram in the standard configuration. The diagnostic "front-end" is comprised of the ECE antenna, waveguide line, and mixing element. The diagnostic "back-end" is everything between the mixer and the data acquisition system.

hemisphereical detents that were machined into the back of its surface to facilitate antenna alignment with a Coordinate Measuring Machine (CMM).

Figure 3.2b is a view of the aperture of the pyramidal horn. The front of the ellipsoidal mirror is also visible in Figure 3.2b. The pyramidal horn is held in a protective tube, and it is aligned with the mirror by four set screws. The ECE antenna pattern is modeled

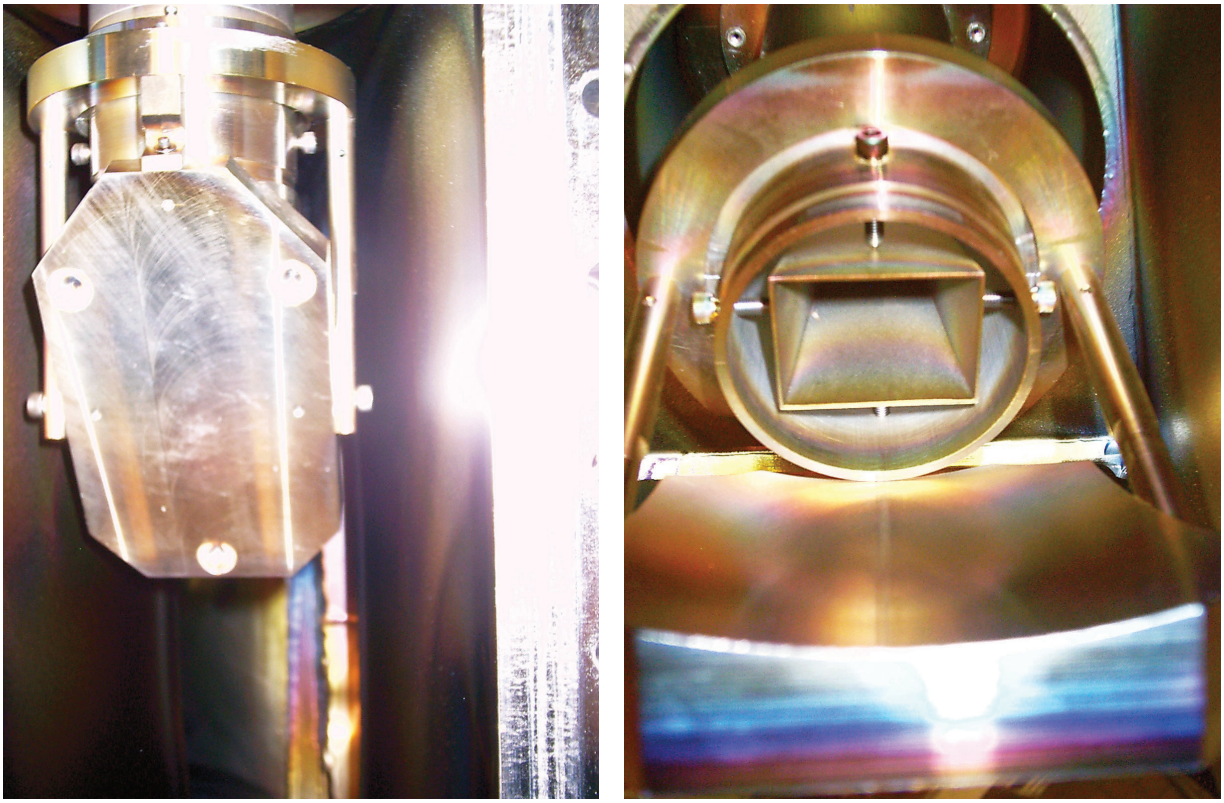

(a) ECE antenna from behind

(b) Ellipsoidal mirror and pyramidal horn

Figure 3.2: Two views of the ECE antenna within the HSX vacuum vessel: (a) the view into the vessel from the behind the antenna, and (b) the ellipsoidal focusing mirror and pyramidal horn that form the antenna.

as a Gaussian beam with its beam-waist in the plasma. Gaussian beams and the specific parameters used to model the antenna are described in Appendix C using methods presented in Reference [83] and Reference [84]. The antenna pattern has a significant impact on the radiation temperature measurement in the core of HSX ($r/a < 0.2$), and the effect of the antenna pattern on the measurement is discussed in Section 3.5. The solid angle of the of the plasma subtended by the antenna is discussed in detail in Section 3.2.2.

The first element of the heterodyne receiver is the mixing element. The mixing element is a square-law diode that shifts the input radiofrequency (RF) signal down to an intermediate

frequency (IF) signal using a 42.5 GHz local oscillator (LO). The output power is at the beat frequency of the RF and LO, $f_{IF} = |f_{RF} \pm k f_{LO}|$ $(k = 1, 2, ...)$. The power in the IF frequency of the heterodyne signal is a combination of the power from the LO and the power incident on the diode. The radiometer is tuned to the lower band during 0.5T machine operation, and to the upper band during 1T machine operation.

The ECE radiometer on HSX is a single-sideband receiver. The microwave signal that would contribute to the lower band is removed by a high-pass waveguide filter. The waveguide filter also protects the mixing element by attenuating unabsorbed ECRH power at 28 GHz. The high-pass filter is implemented using a WR-15 (V-band) waveguide, which has a 40 GHz cut-off frequency, and two waveguide transitions.

After the mixing element, the IF signal is amplified by 32 dB before being split into Low-Field Side (LFS) and High-Field Side (HFS) ECE channels by a 2-way power divider. Following an additional 25 dB amplification each side is split once again by an 8-way power divider to yield 16 channels. The power in the IF signal that is split between each channel is passed through a band-pass filter, before it is rectified and amplified by a crystal detector and a video-amplifier.

The radial resolution of each ECE channel is set by the IF bandwidth, B_{IF}, and the spectral broadening through $\frac{B_{IF}}{f_{RF}} = \frac{\Delta\Omega_{c,e}}{\Omega_{c,e}}$ [79] [80]. The power gathered by a single mode antenna is proportional to the IF bandwidth, as discussed in Section 3.2, and the signal level increases with plasma temperature and IF bandwidth, $P = k B_{IF} T_e$ (k is Boltzmann's constant). The minimum level of thermal noise that a radiometer can measure with a signal-to-noise level of 1 is [85]

$$\frac{\delta T_r}{T_r} = \sqrt{\frac{2B_v}{B_{IF}}}, \tag{3.1}$$

where B_v is the video bandwidth of the ECE radiometer [79]. For HSX, $B_v = 300$ kHz and the smallest fluctuation that each ECE channel can detect is on the order of 3-5%.

The diagnostic configuration shown in the block diagram in Figure 3.1 has channels with center frequencies spanning from 50.8 to 60.8 GHz. The HFS channels have center frequencies between 13.5 and 18.3 GHz, and the LFS channels have center frequencies between 8.3 and 12.9 GHz. An inline 3 dB attenuator is used to decrease the signal on the 13.5 GHz channel, which gathers emission at 56 GHz (twice the gyrotron frequency used for ECRH). The video amplifiers have a bandwidth of 300 kHz. The DC offset from the RF signal and LO are rejected by a DC block in the heterodyne receiver.

3.2 Absolute Calibration

The ECE signals for a representative thermal plasma are shown in Figure 3.3. The output voltages range between 20 mV from an edge channel to 4 V from a core channel, and these signals correspond to temperatures between 100 and 1200 eV. An absolute calibration is used to determine the sensitivity of each channel of the radiometer in terms of the power input to the ECE diagnostic "front-end" and the voltage output from the ECE radiometer "back-end."

During absolute calibration, the overall system gain is determined for each ECE channel by measuring the response to a noise source of known power at the input to the ECE diagnostic. The calibration performed on HSX does not include the ECE antenna because the antenna is within the HSX vacuum vessel, but the wave pattern of the antenna is modeled in the data analysis.

3.2.1 Measuring the Gain of the Radiometer

The Y-factor method [85] is used to calibrate the ECE radiometer on HSX. A noise-source that connects directly to the waveguide is used as the calibration load, and the source is attached as close to the vacuum barrier window as possible.

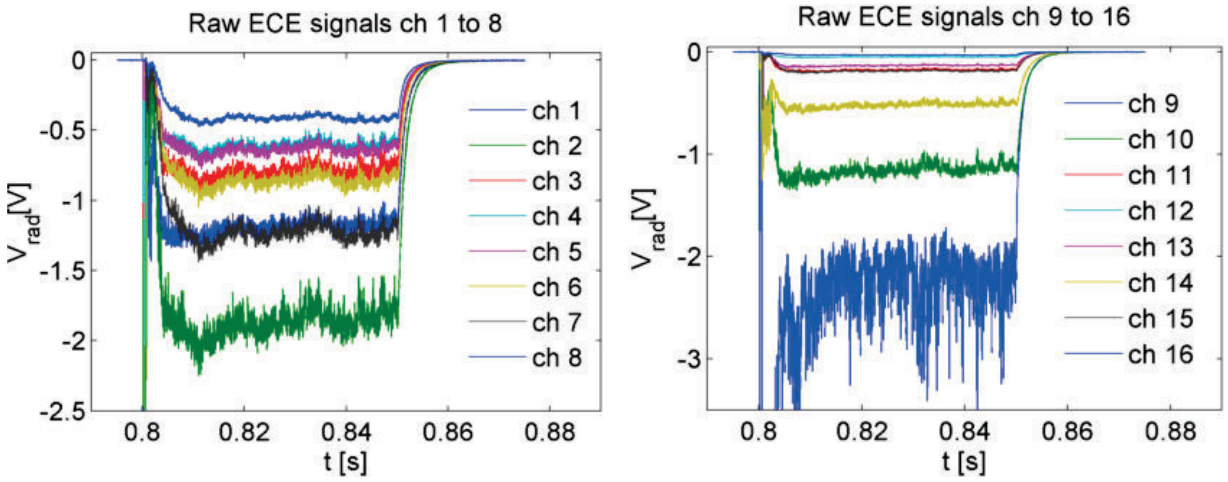

(a) Low-Field Side ECE

(b) High-Field Side ECE

Figure 3.3: Raw voltages from the LFS (a) and HFS (b) ECE channels for a representative thermal plasma.

The noise source is driven by a 28 VDC power supply that is full depth square wave modulated, and an analog lock-in amplifier is used to phase-lock average the signal. The gain of the radiometer is the difference in signal during the on- and off-phase, $\frac{\Delta T}{\Delta V}$.

The noise source generates white noise between 50 and 75 GHz that is amplified by more than 15 dB over the ambient temperature of the source with a variation of $\pm$ 2 dB over the frequency range of application. The amplification factor is referred to as the Excess Noise Ratio (ENR), and the equivalent temperature of the calibration load during the on-phase is $T_h = (290K)10^{ENR/10} + 290K$. During the off-phase, the radiometer measures signal generated at the ambient temperature, $T_c = 290K = 0.025eV$, and during the on-phase the radiometer measures amplified signal that is equivalent to $T_h = 950K = 0.82eV$.

Figure 3.2.1 shows the response of an ECE channel to the square wave modulated noise source. The signal from the 28 VDC driver is also shown in Figure 3.2.1. The DC signal measured by the oscilloscope is due to thermal (Johnson-Nyquist) noise [85]. The thermal noise

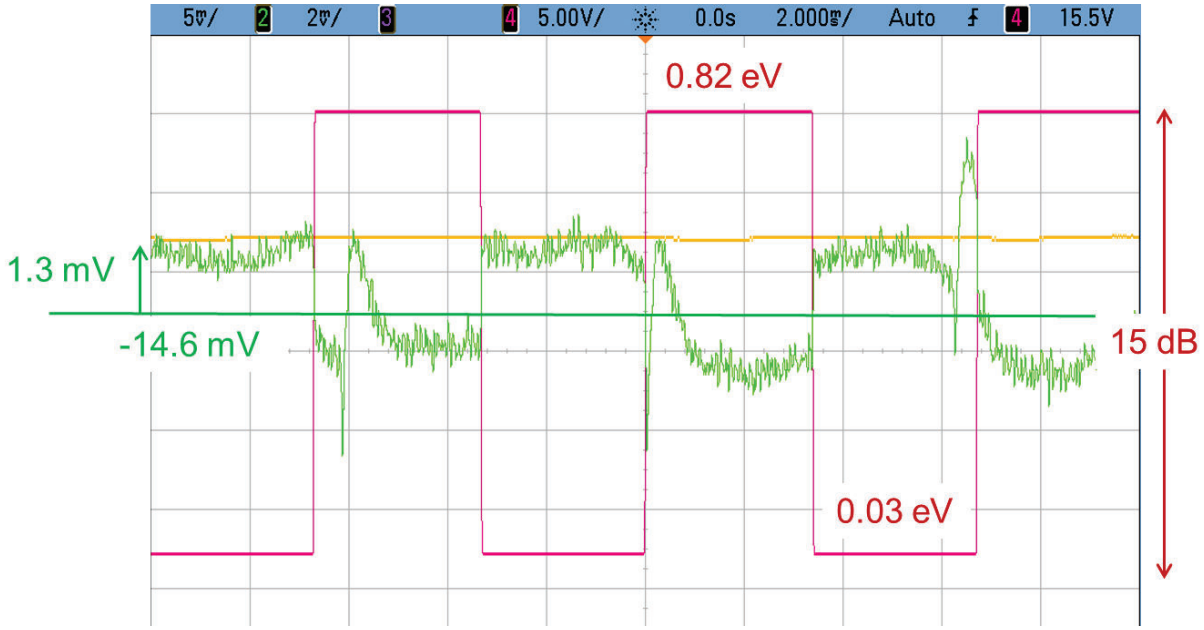

Figure 3.4: Response of an ECE channel (green) to the modulated noise source, and 28V noise source driver signal (purple).

power includes the noise from the Device Under Test (DUT: the waveguide and heterodyne radiometer), as well as the components used during calibration (the lock-in amplifier, noise source, and the oscilloscope itself). To measure the noise temperature of the DUT alone, T_N (the temperature of a resistor necessary to generate the same thermal noise), the noise temperature of the calibration components must be measured with the radiometer removed from the circuit, and this is not possible with the equipment used here. The noise temperature measured during the absolute calibration is negligible in comparison to the radiation temperature measured during the experiment, and it is not included in the analysis of the ECE in HSX.

During calibration, the gain is determined from the change in noise power, P over the change in radiometer output voltage V_{rad}, and is normalized by the IF bandwidth of each channel, $B = \delta\omega/2\pi$ to be put in terms of noise temperatures. The noise power during

the on-phase is $P_h = GV_h = kBT_h + kBT_N$, and the noise power during the off-phase is $P_c = GV_c = kBT_c + kBT_N$, where k is Boltzmann's constant. The power gain of the radiometer is

$$G = \frac{dP}{dV} = \frac{kBT_h - kBT_c}{V_h - V_c}. \tag{3.2}$$

The sensitivity in Table 3.2.1 is related to the power gain in Equation 3.2 by $S = B/G$, where the sensitivity is in mV/eV. The LFS channels have sensitivities between 2.3 and 4.1 mV/eV, while the HFS channels have lower sensitivities. The sensitivity and integrating time-constant of the lock-in amplifier (amplifier gain and integration time) can not be held constant during calibration because of the large difference in sensitivity between ECE channels. Channels with lower sensitivity require larger amplifier gain, and a longer integration time is necessary to maintain the stability of the output signal. A diagnostic upgrade to a 24 channel radiometer is suggested as future work, and the sensitivity of the radiometer can be balanced during that upgrade to improve the accuracy of the absolute calibration.

Table 3.1: The ENR of the noise source interpolated to the RF center frequency of each ECE channel, and the sensitivity measured during absolute calibration of the radiometer.

	ENR	S [mV/eV]		ENR	S [mV/eV]
Ch 1	16.7	2.8	Ch 9	17.3	0.9
Ch 2	16.9	2.3	Ch 10	17.1	3.7
Ch 3	17.2	4.1	Ch 11	16.7	0.7
Ch 4	17.5	2.3	Ch 12	17.4	0.2
Ch 5	17.5	2.4	Ch 13	17.6	0.6
Ch 6	17.4	2.7	Ch 14	17.5	1.3
Ch 7	17.4	3.8	Ch 15	17.4	2.1
Ch 8	17.3	3.4	Ch 16	17.9	0.8

3.2.2 Modeling the Gain of the Antenna

For a calibration of the complete system, the antenna wave pattern and the losses between the antenna and the noise source must be included. The power passing collected by the antenna, and can be cast as an antenna temperature [79] [85]. The antenna temperature, T_A, is the radiation temperature averaged over the antenna pattern (in terms of the aperture efficiency or effective aperture of the antenna, $A_e(\theta, \phi)$),

$$T_A = \frac{1}{\lambda^2} \int_{4\pi} A_e(\theta, \phi,) T_r(\theta, \phi) d\Omega. \tag{3.3}$$

For an isotropic source that completely fills the antenna, the antenna temperature reduces to the radiation temperature. This assumption is not satisfied in the core of HSX ($r/a < 0.2$), and modeling is necessary to correctly determine the radiation temperature from the ECE diagnostic in this region. The necessary correction to the effective aperture antenna temperature, and the resulting radiation temperature, are discussed in Section 3.5. The power carried in the IF signal of each channel is derived in Appendix D and is related to the measured radiation temperature through the antenna temperature, $T_A \approx \frac{1}{\lambda^2} A_e \Omega T_r$, as

$$kBT_r = \frac{2\pi\lambda^2}{\Omega A_e} \left(GV_{rad} + kBT_N \right) \approx \frac{2\pi\lambda^2}{\Omega A_e} GV_{rad}. \tag{3.4}$$

The power gain, G, is known from Section 3.2.1. The horn antenna aperture efficiency, $A_e = \eta A_{horn}$, where A_{horn} is the aperture area of the pyramidal horn, and $\eta \approx 0.49$ for the optimal horn antenna [86]. There is a significant change in aperture efficiency due to incomplete illumination of the antenna that is discussed in Section 3.5 and used in the analysis of the ECE diagnostic in Section 3.6. The solid angle of the plasma subtended by the ECE antenna is limited by the aperture area of the horn. The solid angle is

$$\Omega = \frac{A_{horn}}{\left(\Delta z_m + d_{res} \right)^2}, \tag{3.5}$$

where $\Delta z_m = 7.5$ cm is the distance between the aperture of the horn and the center of the ellipsoidal mirror, and d_{res} is the linear distance between the center of the ellipsoidal mirror and the location of the electron cyclotron resonance. The two distances necessary to calculate the solid angle of the ECE antenna are shown schematically in the block diagram of the absolute calibration in Figure 3.2.2.

The area of the horn aperture, and the distance from the horn aperture to the center of the ellipsoidal mirror are constant. The distance from the mirror to the resonance layer changes as the electron cyclotron resonance moves through the plasma. The calibration factors measured in Section 3.2.1 and shown in Table 3.2.1 relate the antenna temperature to the signal measured by the radiometer. Equation 3.4 relates the radiation temperature of the plasma to the antenna temperature. Together, they yield the absolutely calibrated radiation temperature.

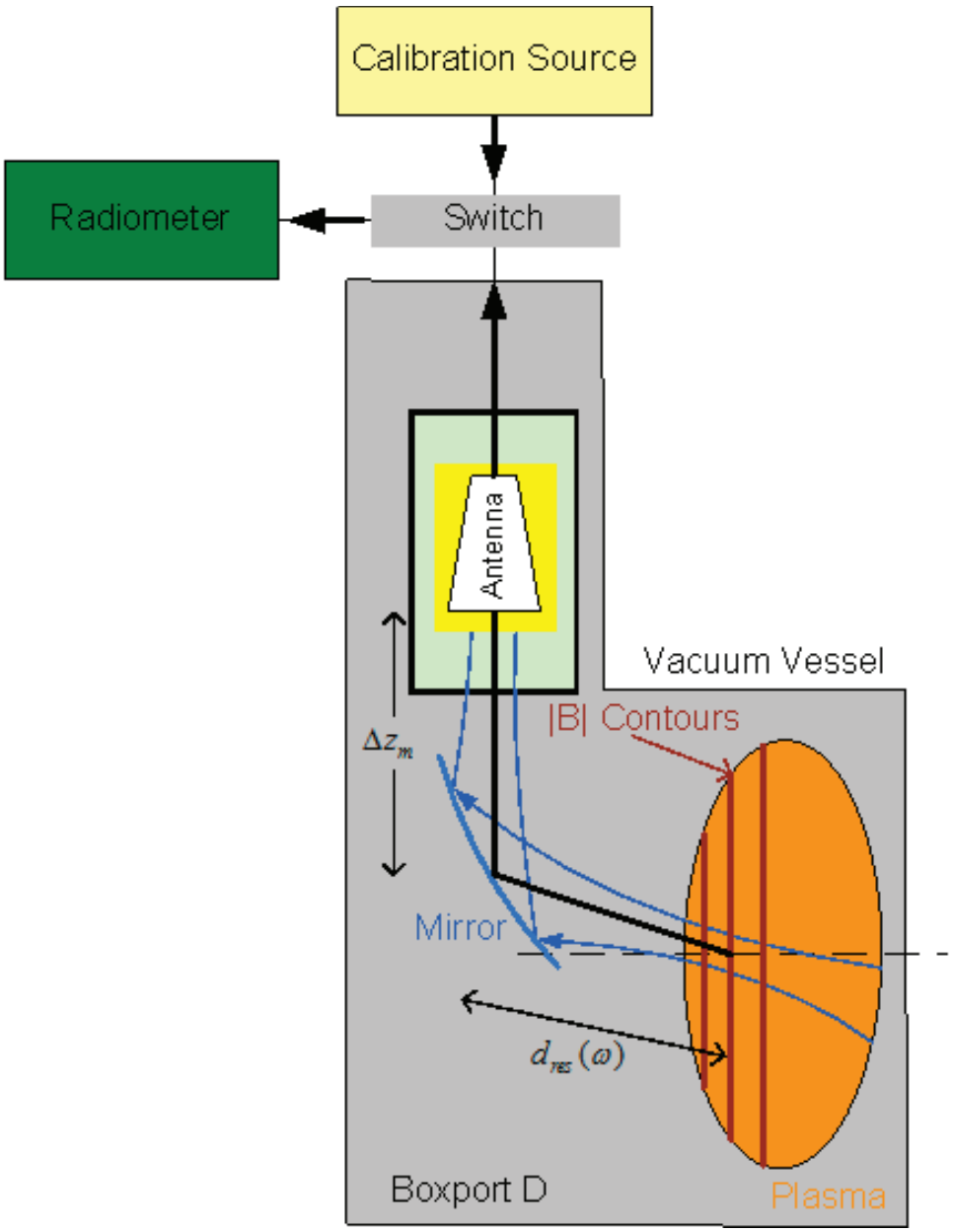

Figure 3.5: The block diagram of the absolute calibration and the quantities used to calculate the solid angle of the ECE antenna.

3.3 Absorption Calculations

The emission frequency of radiation corresponds to a specific plasma location through knowledge of the magnetic field strength in HSX and the resonance condition for the 2^{nd} harmonic of the electron gyrofrequency. The resonance location for each channel is calculated by propagating a qausi-optical beam from the horn to the mirror and through the plasma, and then calculating its intersection with the resonant vacuum field of HSX. This cold-plasma resonance has finite breadth due to the bandwidth of each ECE channel. The warm-plasma resonance including the bandwidth of each channel, the power-density distribution of the wave beam, and the finite absorption of each ECE channel is shown in Figure 3.6.

The resonance condition for each electron is dependent upon the the velocity of that electron due to the relativistic effect on the mass [87]. This mass dependence broadens the frequency band, and consequently the spatial range, in which electrons emit power. When a population of suprathermal electrons is present in the plasma, they emit at frequencies to lower than the cold plasma resonance [74].

The optical depth is the integrated absorption across the resonance, and it is calculated along the beam axis, $\tau = \int \alpha ds$, for each channel using the formula for the absorption of the extraordinary wave at the 2^{nd} harmonic of the cyclotron frequency under perpendicular observation (formula (28) from reference [88]).

Figure 3.7 shows the absorption shapes that are calculated along the beam propagation direction and the corresponding optical depth for each ECE channel. The spatial resonance position of each ECE channel for this calculation is determined by using an absorption weighted average of the position, and the effective radius and plasma optical depth are shown versus resonance frequency in Figure 3.8.

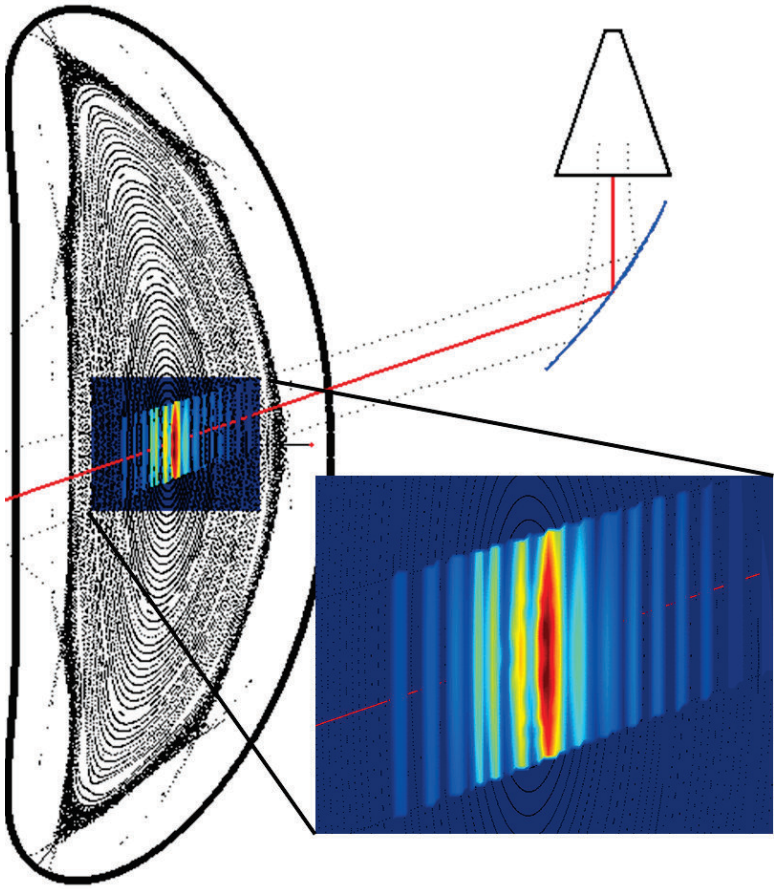

Figure 3.6: Warm-plasma resonance for each ECE channel in the boxport of HSX (horizontal is the major radial direction).

The absorption is also calculated across the resonance including the width of the ECE beam in the boxport. The optical depth determined from the 2D absorption is given by $\tau_\omega = \frac{1}{\delta Z}\int\int 2\alpha_\omega dRdZ$, where δZ is the beam-width at the resonance location. The integration is over the absorption region for each ECE channel, but the integral is truncated by the width of the ECE beam.

Quasi-optical beams carry 90% of their power within the beam waist, w_z, and the peak in the ECE beam intensity occurs along the beam-axis with a magnitude twice the total beam power divided by the area of the beam at the waist, $I(0,z) = \frac{2P_o}{\pi w_z^2}$ [83]. Consequently,

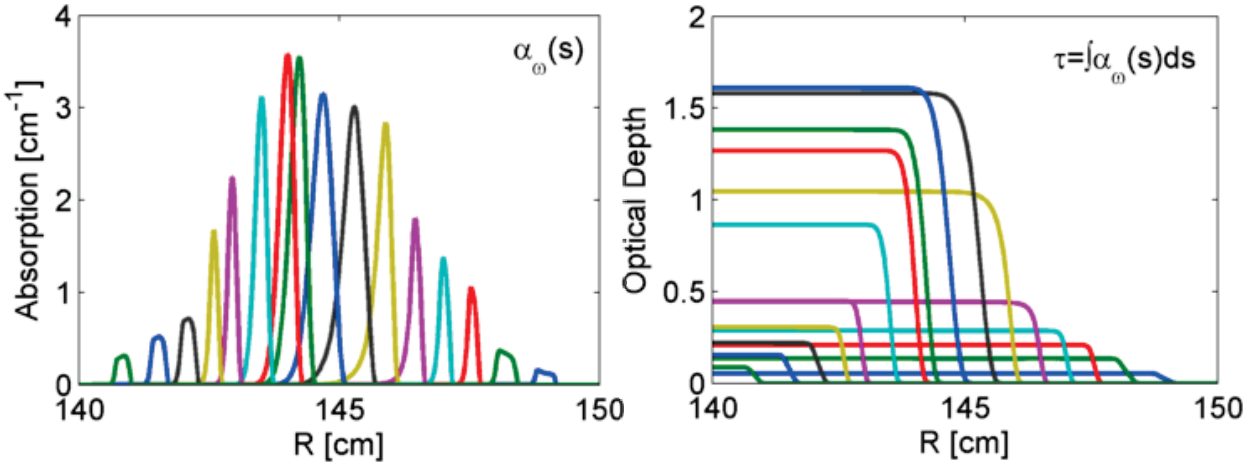

Figure 3.7: ECE absorption shapes (left) and optical depth (right) calculated for the standard ECE configuration using parameters from a modulation experiment with 85 kW of total launched power along the beam propagation direction.

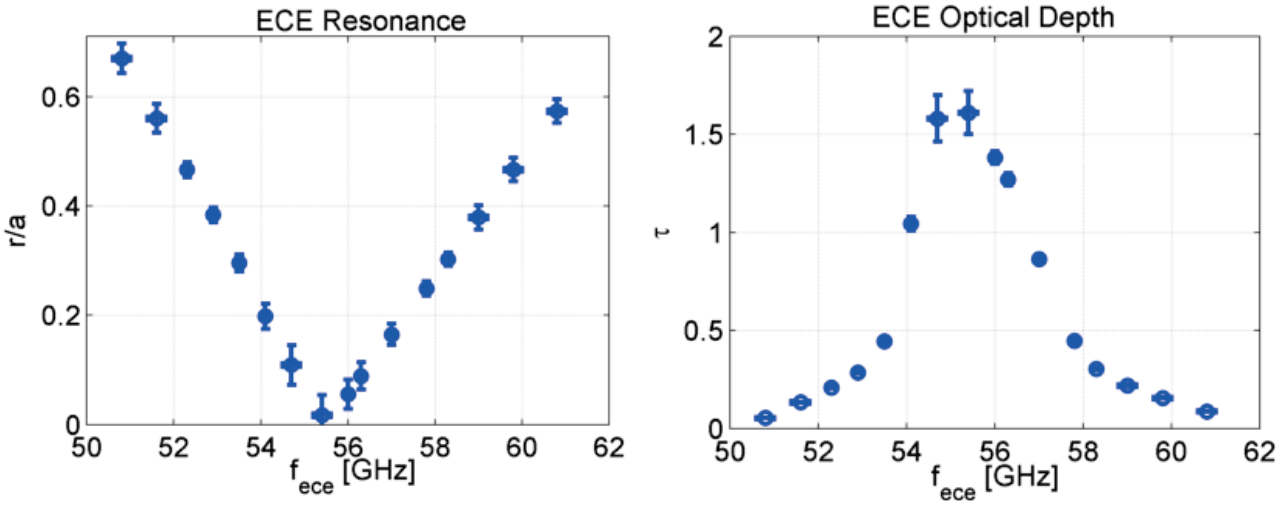

Figure 3.8: ECE resonance positions (left) and optical depth (right) calculated for the standard ECE configuration using parameters from a modulation experiment with 85 kW of total launched power along the ECE beam.

the 2D absorption calculation encapsulates 90% of the power of the ECE beam, and the 1D absorption calculation captures the peak intensity along the beam axis [83].

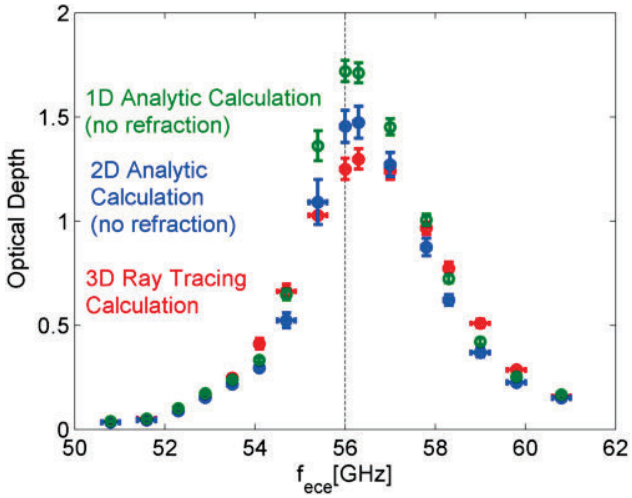

Figure 3.9: Optical depth from the 1D and 2D analytic calculations, and optical depth from 3D ray tracing, which includes refraction, in the real geometry of HSX.

The optical depth from the 1D absorption calculation along the ECE beam-axis, and the 2D absorption calculation in the boxport of HSX are shown in Figure 3.9. The optical depth calculated in the full 3D magnetic geometry of HSX using the ray tracing code TRAVIS, which includes refraction and is described in Section 4.2.1, is also shown in Figure 3.9. The maximum core density of HSX during 1T operation is approximately 35% of the cut-off density for the extraordinary wave at the 2nd harmonic electron cyclotron frequency, which is 2×10^{19} m^{-3}, and although it is included in the 3D calculation, refraction does not have a significant effect on the ECE wave propagation.

The 1D calculation over-estimates the optical depth in the core of the plasma, where the ECE beam-waist is greater than the dimension of the sampled flux-surfaces. All of the absorption occurs along the beam-axis in the 1D calculation, while the absorption from each flux-surface within the sampling volume is weighted by the power density of the quasi-optical beam in the 2D calculation.

Despite the power density weighting, the 2D analytic calculation over-estimates the solid angle of the plasma subtended by the ECE antenna, and this contributes to the over-estimate in the absorption in the core. The Gaussian beam-width of the ECE antenna at the resonance is sufficient in regions of the plasma where the resonance is larger than the beam width; however, in the core the plasma sampling volume is smaller than the ECE beam width. This significantly impacts the radiation temperature measured by the diagnostic within the core ($r/a < 0.2$), and an iterative procedure is necessary to calculated the ECE electron temperature in this region. The iterative calculation is discussed in Section 3.5.

3.4 The Increased Resolution Configuration

The heat pulse propagation experiments presented in Chapter 5 and Chapter 6 require an electron temperature diagnostic with high spatial and temporal resolution. High temporal and spatial resolution is also necessary for the absorption measurements presented in Chapter 4. For this reason, the resolution of the ECE diagnostic has been increased by re-arranging the "back-end" of the ECE radiometer to achieve maximum spatial resolution of the plasma core for 1T on-axis magnetic field strength. This was achieved at the expense of the edge resolution of the diagnostic, and for a 1T on-axis magnetic field, all 16 of the ECE channels are resonant within $r/a < 0.5$. The digitizers used to record the signal output by the radiometer have also been changed over the course of this work to take full advantage of the high temporal resolution offered by the 300 kHz bandwidth of the video amplifiers.

The intermediate frequency and bandwidth of each ECE channel in the standard and increased resolution configurations is shown in Table 3.2. In addition to shifting the ECE channels to gather emission from electrons resonating in the plasma core, the IF bandwidth of nearly all of the IF filters was reduced to 200 MHz.

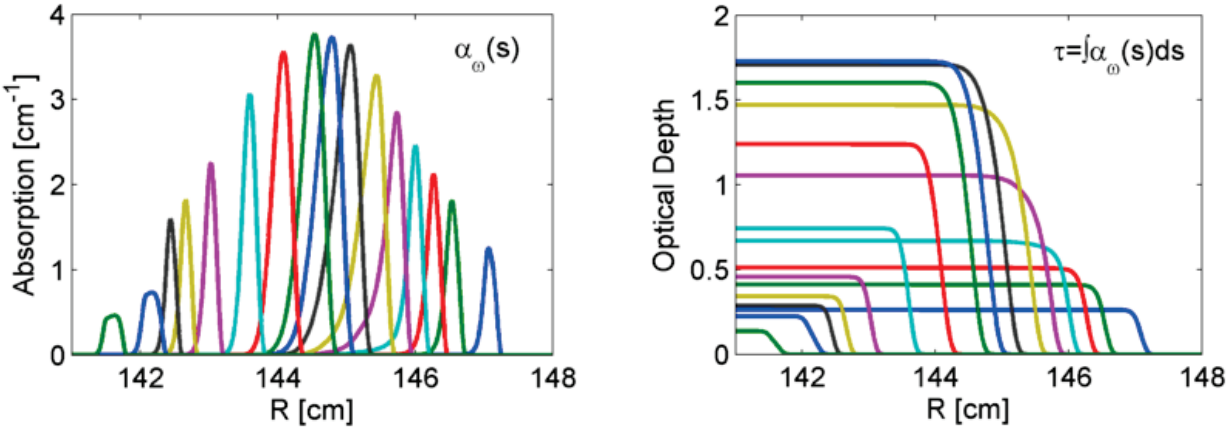

Figure 3.10: ECE Absorption shapes (left) and optical depth (right) calculated for the increased core resolution ECE configuration using parameters from a modulation experiment with 85 kW of total launched power.

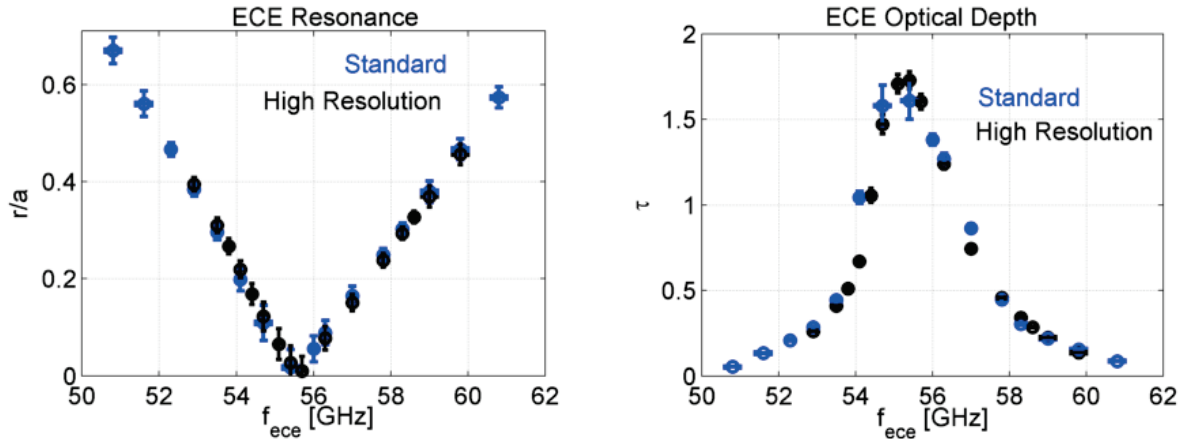

Figure 3.11: ECE resonance positions (left) and optical depth (right) calculated for ECE configurations using parameters from two matched ECRH modulation experiments with 85 kW of total launched power.

Figure 3.10 shows the absorption shapes and optical depth along the ECE beam-axis for an ECRH modulation experiment with 85 kW of launched power that was matched to the experiment used to produce 3.7. Figure 3.10 shows the effective radial locations and optical depth for both ECE configurations from the two experiments.

Table 3.2: The standard and increased resolution configurations of the ECE diagnostic.

	Standard Configuration			Increased Resolution Configuration		
	f_{RF} [GHz]	IF [GHz]	B [GHz]	f_{RF} [GHz]	IF [GHz]	B [GHz]
1	50.8	8.3	0.4	52.9	10.4	0.2
2	51.6	9.1	0.4	53.5	11	0.2
3	52.1	9.6	0.2	53.8	11.3	0.2
4	52.9	10.4	0.2	54.1	11.6	0.2
5	53.5	11	0.2	54.4	11.9	0.2
6	54.1	11.6	0.2	54.7	12.2	0.2
7	54.7	12.2	0.4	55.1	12.6	0.2
8	55.4	12.9	0.4	55.4	12.9	0.2
9	56	13.5	0.2	55.7	13.2	0.2
10	56.3	13.8	0.2	56.3	13.8	0.2
11	57	14.5	0.2	57	14.5	0.2
12	57.8	15.3	0.2	57.8	15.3	0.2
13	58.3	15.8	0.2	58.3	15.8	0.2
14	59	16.5	0.4	58.6	16.1	0.2
15	59.8	17.3	0.4	59	16.5	0.4
16	60.8	18.3	0.4	59.8	17.3	0.4

3.5 The Absolutely Calibrated Radiation Temperature

The absolutely calibrated ECE radiation spectrum is shown in Figure 3.12a, and the radiation temperature is shown versus plasma effective radius in Figure 3.12b, for a plasma supported by 66 kW of launched power. The radiation spectrum is symmetric with respect to the magnetic axis of the plasma at low ECRH power density.

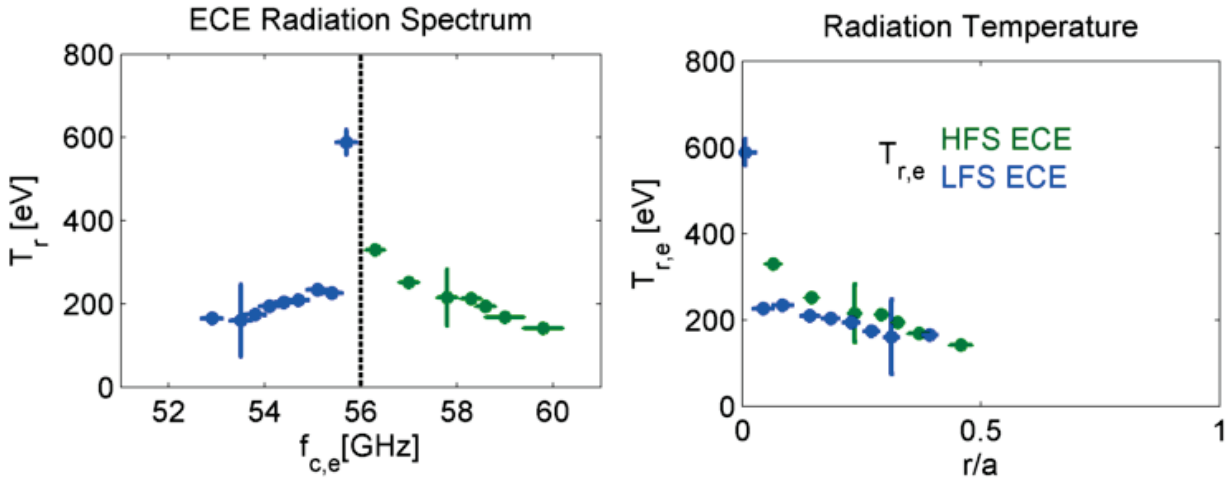

(a) Absolutely Calibrated ECE Spectrum

(b) Radiation Temperature: $P_0 = 66$ kW

Figure 3.12: Absolutely calibrated ECE spectrum (a) and the radiation temperature versus effective radius (b) for an ECRH modulation experiment with 66 kW of launched power.

The essential features of Figure 3.12b are reproduced at higher launched powers in Figure 3.13. The ECE radiation temperature is symmetric for $r/a > 0.2$; however, there is a shortfall for $r/a < 0.2$. As the launched ECRH power increases in HSX, the LFS channels gather relativistically down-shifted emission, and the spectrum becomes asymmetric. Figure 3.13a and Figure 3.13b show the radiation temperature versus plasma effective radius for ECRH modulation experiments with 78 kW and 85 kW of launched power respectively. The LFS

channels flatten with increasing ECRH power density, and the LFS channels are not representative of the electron temperature in HSX at high ECRH power density. Consequently, they are not used in the analysis of perturbative heat transport experiments in this work.

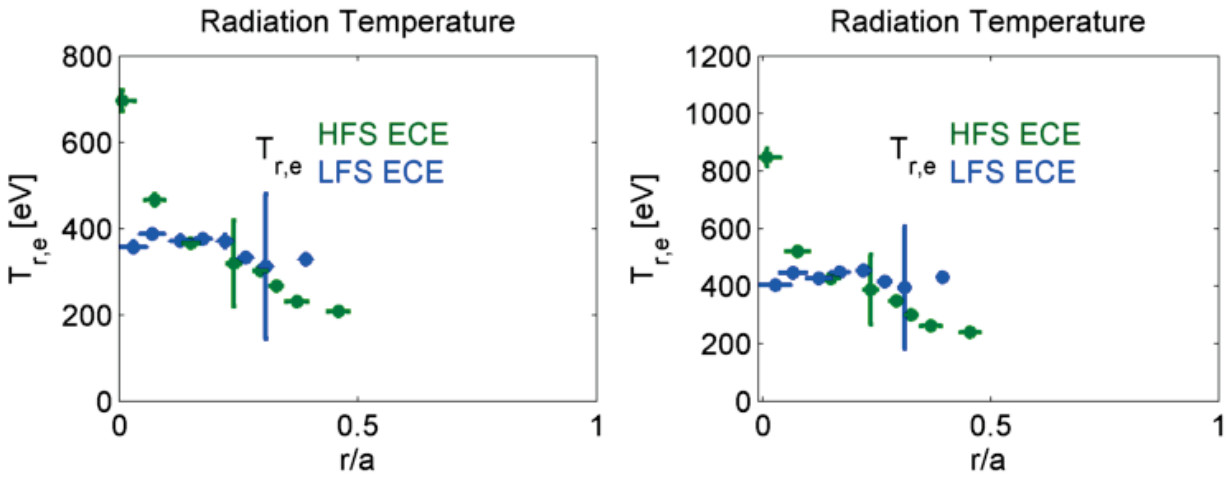

(a) Radiation Temperature: $P_0 = 78$ kW

(b) Radiation Temperature: $P_0 = 85$ kW

Figure 3.13: Radiation temperature versus effective radius for 78 kW (a) and 85 kW (b) of launched power.

The first-pass emission can be determined analytically in a slab from the emissivity [79], and a synthetic radiation temperature in terms of the absorption is $T_{r,\omega} = \int T_e(s)\alpha(s)e^{-\tau(s)}ds$. The synthetic radiation temperature is compared to the absolutely calibrated ECE spectrum from the HFS channels for each of the three launched powers in Figure 3.14. The electron temperature measured through Thomson scattering is also shown for each case.

The effective radius of each channel in Figure 3.12b, Figure 3.13, and Figure 3.14c use the 1D asorption model to calculate the plasma effective radius. The location and width of the emission of each channel changes with plasma parameters and main magnetic field, but the position calculated using either the 1D or the 2D absorption model are nearly identical. The full-width at half-max of the absorption calculated from the 1D model is on the order of

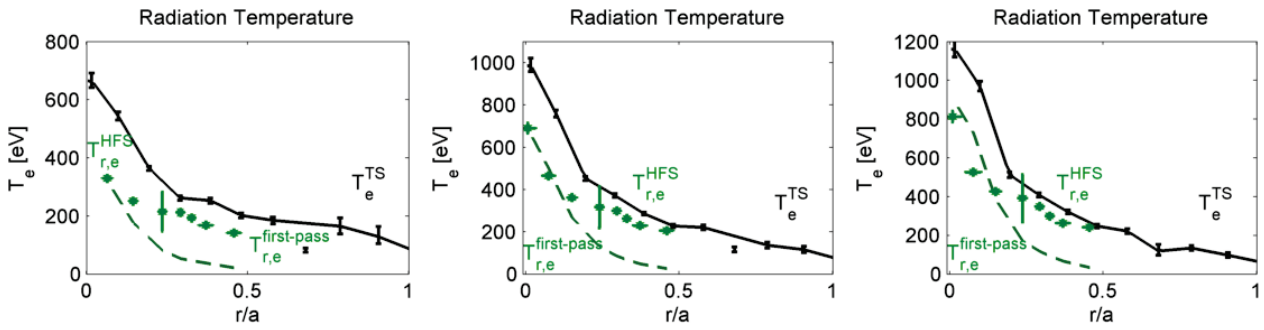

(a) $P_0 = 66$ kW (b) $P_0 = 78$ kW (c) $P_0 = 85$ kW

Figure 3.14: Absolutely calibrated ECE spectrum from the HFS channels is compared to the synthetic first-pass radiation temperature and the electron temperature measured through Thomson scattering at three launched powers: (a) 66 kW, (b) 78 kW, and (c) 85 kW.

2-5% of the minor radius, while the full-width at half-max calculated by the 2D absorption code on the order of 5% of the minor radius.

The absolutely calibrated radiation temperature is significantly larger than that calculated by the single-pass model outside of $r/a > 0.2$ indicating high optical depth due to multi-pass emission; however, there is a shortfall in the core (within $r/a < 0.2$), where the measured radiation temperature is small, and the measurement even appears to erroneously match the first-pass emission model. A reflectivity of approximately 0.9 is necessary to match Thomson scattering measurements of the blackbody electron temperature for $r/a > 0.2$, but a reflectivity of 0 (corresponding to the first-pass model) reproduces the core electron temperature (within $r/a < 0.2$). The wall reflectivity used in the multi-pass emission model does not change significantly at microwave frequencies and is expected to be constant for all of the channels (the reflectivity of the stainless steel vacuum vessel of HSX at 56 GHz is $\rho \approx 0.998$). Additionally, the shortfall decreases with increasing electron temperature. The results of Figure 3.14 imply a spatially varying reflectivity that is electron temperature dependent, which is unphysical.

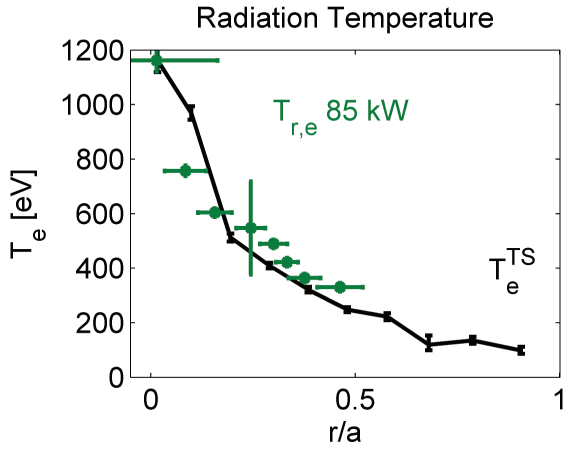

Figure 3.15: ECE radiation temperature versus effective radius using effective radii and effective aperture of the antenna calculated from the 2D absorption code.

In Section 3.2.2, the ECE antenna was assumed to be completely illuminated by the source and this was used to derive the antenna temperature in terms of the ECE radiation temperature, solid angle subtended by the antenna, and the effective aperture of the antenna. The absorption shapes from the 2D calculation do not extend across the beam width of the antenna (w_z), and the core channels do not fully illuminate the antenna. The effective aperture in Equation 3.4 is too large, and it is corrected by using the full-width at half-max of the absorption, w_{FWHM}, in the vertical direction of the boxport to write,

$$A_e = \eta A_{horn} \frac{w_{FWHM}}{w_z}. \tag{3.6}$$

Equation 3.6 may be implemented by calculating the absorption using the Thomson scattering electron temperature, or it may be implemented by iteratively calculating the absorption using the procedure discussed in Section 3.6. The radiation temperature measured in an ECRH modulation experiment with 85 kW of launched power, using the absorption calculated from Thomson scattering measurements of the electron temperature and density,

is shown in Figure 3.15. There is no electron temperature shortfall in the core, and the radiation temperature is approximately equal to the electron temperature measured by Thomson scattering, implying an effective wall reflectivity of 1 across the minor radius of HSX.

3.6 The Electron Temperature from ECE

An iterative procedure is used to determine the electron temperature from the radiation temperature on HSX, independent to the Thomson scattering diagnostic. The multi-pass emission model, discussed in Section 2.6, is implemented by iterating upon the absorption calculation until the the electron temperature is self-consistent with the measured radiation temperature. The procedure is diagrammed in Figure 3.16.

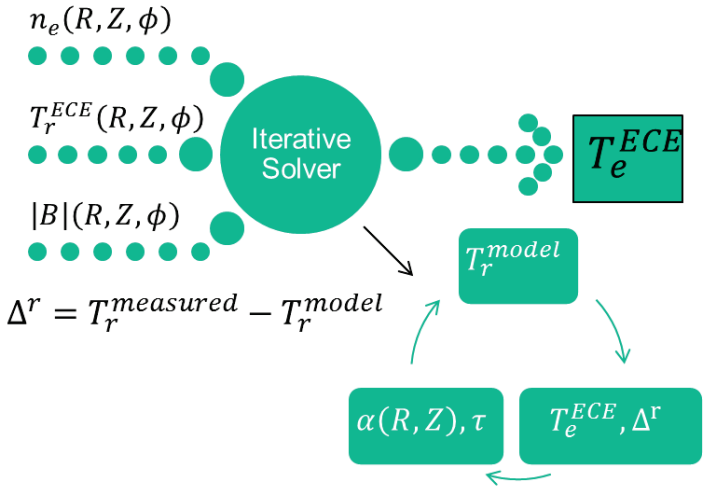

Figure 3.16: Flow diagram of the iterative procedure used to calculate the electron temperature from the ECE radiation temperature. In addition to the ECE radiation temperature, the solver requires $|B|$, and a plasma density profile.

The iterative solver is initialized by the ECE radiation temperature from the HFS channels and the density profile from the Abel inverted interferometer density profile, which are used to calculate a preliminary optical depth. Then Equation 2.10 is used to calculate a trial

electron temperature from,

$$\begin{aligned}
&\alpha(R,Z) = f(n_e, T_e, |B|) \rightarrow \tau, \\
&\frac{I_r^{model}}{I_{bb}} = \frac{1-e^{-\tau}}{1-\rho e^{-\tau}}, \\
&T_e = T_r \frac{I_{bb}}{I_r^{model}} \rightarrow \Delta T_e = |T_e - T_e^{model}|.
\end{aligned} \tag{3.7}$$

This procedure is iterated until the calculated electron temperature profile and the absorption calculation are self-consistent with the measured radiation temperature. The electron temperature is considered self-consistent when the difference between electron temperature iterations, ΔT_e, is less than 5 eV. The HFS radiation temperature is used to minimize the effect of suprathermal populations and down-shifted emission in the calculation. The iterative procedure of Equation 3.7 is extended to include the change in effective antenna aperture with absorption by adding the change in radiation temperature intermediate to calculating the electron temperature.

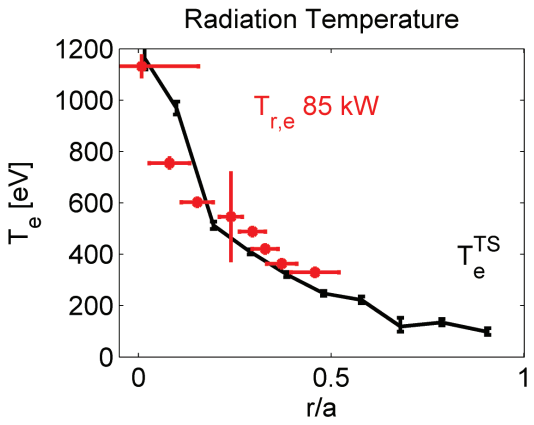

Figure 3.17: ECE radiation temperature, with the effective aperture correction from the iterative procedure, versus effective radius in an ECRH modulation experiments with 85 kW of total launched power.

In the limit of unity wall reflectivity, $\rho = 1$ in Equation 3.7, the radiation temperature is equal to the blackbody electron temperature, and the iterative procedure is used to calculate

the absorption across the ECE beam width in the 2D helical cut of the boxport of HSX. The resulting ECE radiation temperature is compared to the electron temperature measured by Thomson scattering in Figure 3.17. The radiation temperature is equivalent to the blackbody electron temperature in HSX, and the effective reflectivity is approximately unity.

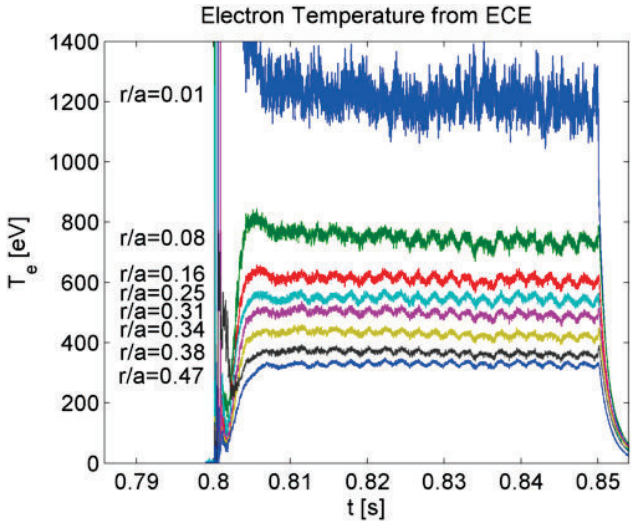

Figure 3.18: Temporal evolution of the ECE radiation temperature, with the effective aperture correction from the iterative procedure, in an ECRH modulation experiments with 85 kW of total launched power.

Although the temporal evolution of the absorption may also be included in the calculation, the optical depth is taken constant for the heat transport analysis in this work to avoid altering the phase between electron temperature perturbations. The temporal evolution of the electron temperature measured during an ECRH modulation experiment with 85 kW of total launched power is shown in Figure 3.18.

The radiation temperature measured by the ECE diagnostic, with the effective aperture correction from the iterative procedure, is shown for three launched powers in Figure 3.19. The iterative procedure is necessary to use the ECE as an independent electron temperature diagnostic.

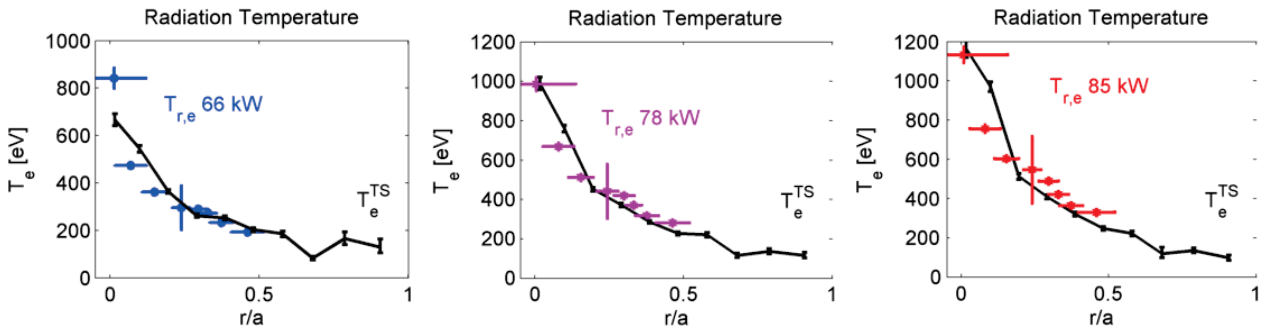

(a) $P_0 = 66$ kW (b) $P_0 = 78$ kW (c) $P_0 = 85$ kW

Figure 3.19: The radiation temperature using the effective aperture correction from the iterative procedure is compared to Thomson scattering at three launched powers: 66 kW (a), 78 kW (b), and 85 kW (c).

3.7 Conclusions from ECE Measurement and Modeling on HSX

The emission of the extraordinary wave at the 2nd harmonic of the electron cyclotron frequency is used as an electron temperature diagnostic on HSX. The antenna pattern of the ECE diagnostic has a significant impact on the antenna temperature measured by the absolutely calibrated 16 channel radiometer, and modeling of the emission sampled by the diagnostic is necessary to determine the radiation temperature. An iterative procedure is used to self-consistently determine the electron temperature from the measured radiation spectrum, and the electron temperature is in good agreement with the electron temperature measured through Thomson scattering. Relativistically down-shifted emission causes asymmetry in the ECE radiation temperature across the magnetic-axis at high ECRH power density in HSX; however, the channels on the high field side of the magnetic axis remain thermal. The spatial and temporal resolution of the ECE radiometer have been increased for use in heat pulse propagation experiments, and the ECE channels on the high-field side of the magnetic-axis are used in the analysis of heat pulse propagation experiments on HSX.

Bibliography

72. Hartfuss, H. J. & Geist, T. (*Fusion Plasma Diagnostics with mm-Waves*, John Wiley & Sons, 2013).

74. Bornatici, M., Cano, R., De Barbieri, O., *et al. Nucl. Fusion* **23,** 1153–1257 (1983).

79. Hartfuss, H. J., Geist, T. & Hirsch, M. *Plasma Phys. Control. Fusion* **39,** 1693–1769 (1997).

80. Watts, C., Hartfuss, H. J. & Hase, M. *Rev. Sci. Instrum.* **75,** 3177–3184 (2004).

83. Goldsmith, P. F., Theory, I. M. & Society, T. (*Quasioptical systems*, Piscataway, NJ : IEEE Press, 1998).

84. Goldsmith, P. F. *Proceedings of the IEEE.* **80,** 1729–1747 (1992).

85. Hartfuss, H. J. *Plasma Phys. Control. Fusion* **40,** A231 (1998).

86. Orfanidis, S. J. (*Electromagnetic Waves and Antennas*, www.ece.rutgers.edu/ orfanidi/ewa, New York, 2014).

87. Bornatici, M. *Plasma Phys.* **24,** 629–638 (1982).

88. Alikaev, V. V., Litvak, A. G., Suvorov, E. V., *et al.* in, 1–62 (*High-Frequency Plasma Heating*, AIP, 1992).

Chapter 4

ECRH Measurement and Modeling

To increase flexibility in experiments on HSX, a second gyrotron and transmission line have been installed. The second antenna includes a steerable mirror for off-axis heating, and the launched power may be modulated for use in heat pulse propagation experiments. The extraordinary wave at the second harmonic of the electron gyrofrequency or the ordinary wave at the fundamental resonance are used for plasma start-up and heating on HSX. The TRAcing VISualized ray tracing code [89] is used to estimate single-pass absorption and to model multi-pass wave damping in the 3D HSX geometry. These results are compared to the RAYS code that was used in the design of both antennas. The single-pass absorption of the ordinary wave at the fundamental resonance is calculated to be as high as 30%, while measurements of the total absorption indicate that 45% of the launched power is absorbed. A multi-pass ray tracing model correctly predicts the experimental absorption and indicates that the launched power is absorbed within the plasma core ($r/a \leq 0.2$).

4.1 ECRH on HSX

Electron cyclotron resonance heating (ECRH) has become a fundamental component of heating schemes in fusion experiments [90] [91], and modeling is necessary in the design of new systems, as well as in the characterization of implemented systems, in experiments with 3D magnetic fields.

For this work, the propagation and absorption of electron cyclotron waves is modeled using the TRAcing VISualized (TRAVIS) ray tracing code [89] [92]. At low plasma density, $n_e \leq 10^{19}\text{m}^{-3}$, the absorption of electron cyclotron waves is less than 50% for the electron temperatures achieved in HSX, $T_e \leq 2.5$ keV. The TRAVIS code calculates the absorption of electron cyclotron waves in plasma, and the code is capable of modeling multiple passes through the plasma upon reflection from the stainless steel vessel wall of HSX.

A second 200 kW, 28 GHz gyrotron and hybrid transmission line have been installed and tested on the HSX stellarator. According to the factory specifications, the dominant gyrotron mode is $\text{TE}_{0,2}$, while other modes account for less than 10% of the power in the output spectrum. To maximize the microwave power launched into the HSX vacuum vessel and to avoid arcing during transmission, two hybrid beam lines are used to deliver microwave power from the gyrotrons to the plasma. Both lines include a mode converter, mirrors and oversize waveguides. Additionally, the second launcher includes a steerable mirror inside the vacuum vessel.

The new transmission line on HSX is described in Section 4.2. Single-pass ray tracing calculations using the TRAVIS code are presented and compared to those from the RAYS code [93] [94] in Section 4.2.1, and multi-pass absorption calculations are compared to experimental measurements in Section 4.2.2.

4.2 A Second Transmission Line for ECRH on HSX

Two ECRH antennas are used for plasma start-up and heating in HSX. Each hybrid transmission line is connected to a 28 GHz Varian Gyrotron (VGA-8050M). The gyrotron has been rated for 200 kW of output power for a 75 ms pulse length. The hybrid beam line was designed to avoid internal arcing and to increase its transmission efficiency [95]. A Vlasov mode converter is used to convert the $\text{TE}_{0,2}$ mode output from the gyrotron into a

$TEM_{0,0}$ wave [96]. The Vlasov mode converter converts 83% of the power in the $TE_{0,2}$ mode into an elliptic Gaussian beam. The Vlasov mode converter is followed by an ellipsoidal and a cylindrical focusing mirror that transform the beam shape from elliptical to circular. A mirror that controls the polarization of the wave also redirects the beam into a 5 m long, 100 mm diameter copper waveguide in which the $TE_{1,1}$ and $TM_{1,1}$ modes are excited.

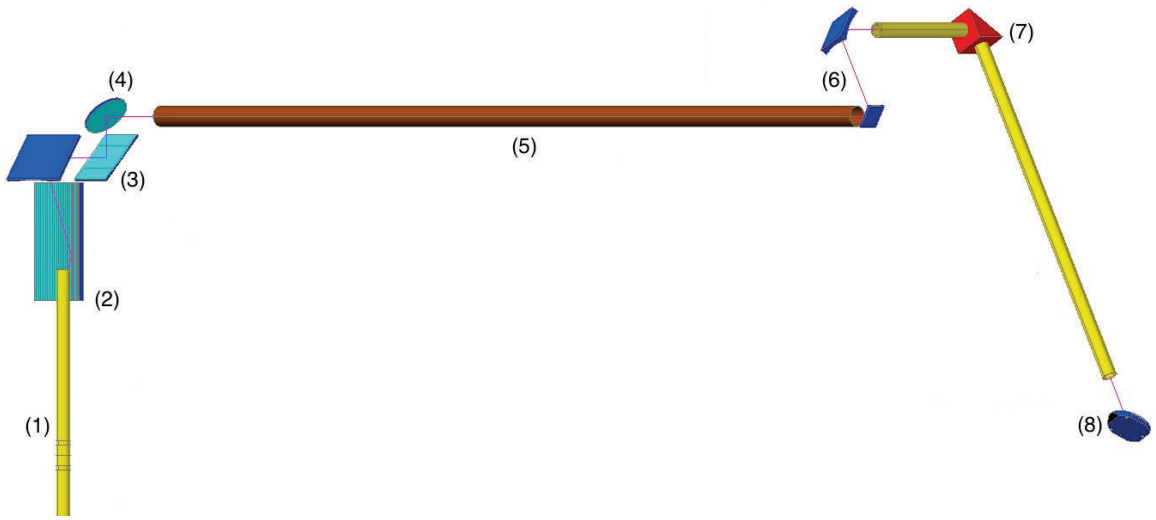

Figure 4.1: The optical path and the main components of the second transmission line on HSX. (1) Gyrotron output (2) Vlasov mode converter (3) Focusing mirrors (4) Polarizer (5) Copper waveguide (6) Beam optics matching mirrors (7) Miter bend (8) Steerable launching mirror.

Two ellipsoidal mirrors match the output from the 100 mm diameter copper waveguide to the input of the 63 mm diameter oversize aluminum waveguide with two dominant modes on the HSX side of the transmission line. A miter bend directs the beam into the vacuum vessel through a quartz window. The internal ECRH antenna includes a steerable ellipsoidal mirror that focuses the beam to a 4.2 cm diameter spot (e^{-2} power level) at a distance 30 cm from the launch mirror. The full divergence of the vacuum beam is 18.6°. For 1T experiments, the wave launched into the plasma is in the ordinary mode; however, for 0.5T experiments,

the polarization of the wave launched into HSX is rotated 90° into the extraordinary mode by replacing the smooth planar mirror used for the ordinary wave with a grooved mirror [97].

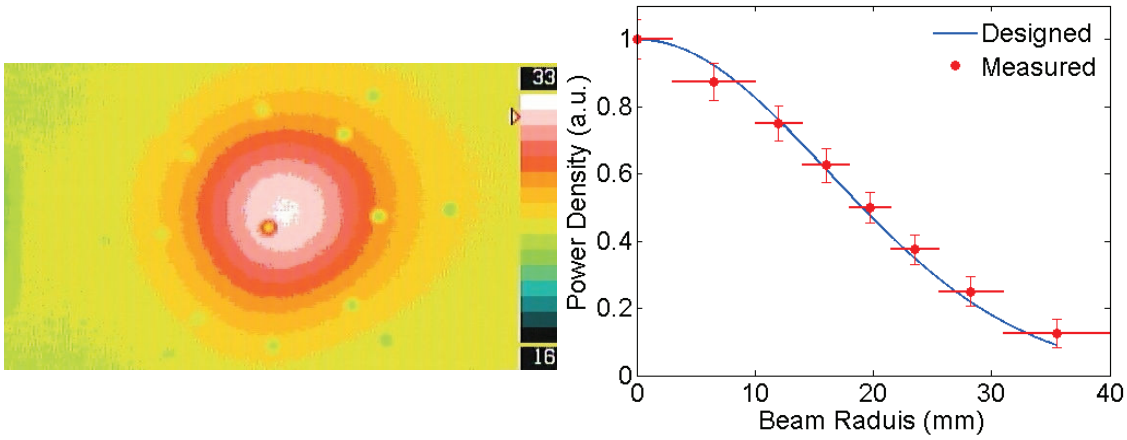

Figure 4.2: As-designed versus as-measured beam power density (right) inverted from thermal imaging of a ceramic target at the aperture of the copper waveguide during an ECRH pulse (left, Courtesy of Konstantin Likin).

The final alignment of the transmission line was achieved using an infrared camera to measure the thermal imprint of the beam on ceramic and LCD targets at different locations along the transmission line. The thermal images were also used to optimize the operational regime of the gyrotron by reducing the content of spurious modes (non-$TE_{0,2}$). The power in the side-lobes at the aperture of the copper waveguide was measured to be less than 20 dB. A thermal image of the circular beam at the aperture of the copper waveguide and its inversion into beam power density are shown in Figure 4.2. The beam diameter at the e^{-2} power level is measured to be 65 mm, which is close to the optimal value for efficient coupling (99%) of the beam into a superposition of the $TE_{1,1}$ and $TM_{1,1}$ modes.

The total RF power output from the gyrotron was measured at the input (gyrotron side) and at the output (HSX side) of the ECRH beam line using a quasi-optical calorimeter

[95]. The results are shown in Figure 4.3. The transmission efficiency of the beam line was measured to be 70%, and most of these losses are due to mode conversion and filtering of gyrotron spurious modes. The gyrotron output power was also optimized versus the main gyrotron magnet currents.

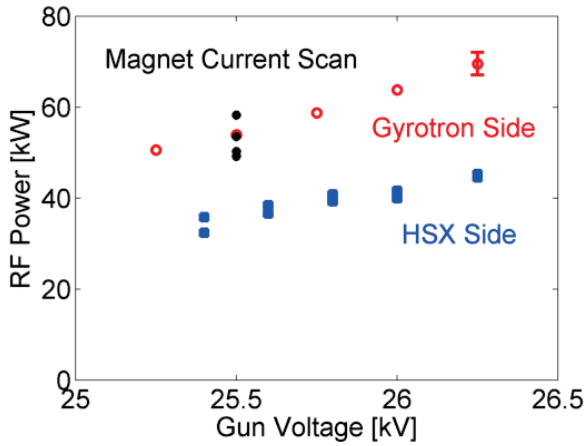

Figure 4.3: The power measured on the gyrotron side (red open circles) and HSX side (blue filled squares) of the transmission line. The power was also measured at several gyrotron magnet currents (black asterisks).

In experiments at fixed launched power the second gyrotron is tuned to the maximum output power, while in experiments with modulated heating the power is modulated within the calibrated range of Figure 4.3. For simplicity, this range of operating parameters is referred to as 50 kW of launched power for the remainder of this work; however, the as-measured launched power is used in the calculations.

4.2.1 Ray Tracing Calculations and First Results

The axis of the second beam can move from 10 cm above the helical magnetic axis to 18 cm below by tilting the internal mirror of the second antenna. The ray trajectories launched from the second antenna at an angle of $\theta = 10^\circ$ with respect to the major radial direction are shown in Figure 4.4. The absorption profiles calculated for three magnetic field strengths

at this launch angle are shown in Figure 4.5. Wave refraction is significant in the presence of a strong density gradient, and ray tracing calculations are necessary to determine the resonance location in the plasma.

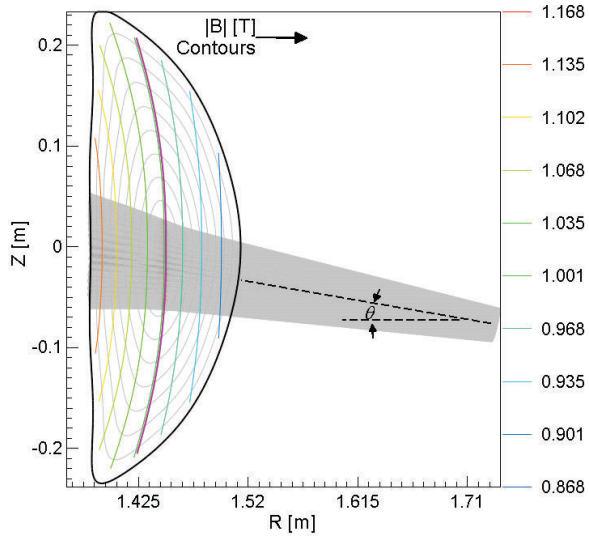

Figure 4.4: A projection of the rays launched from the second antenna into the vertical plane of the launcher.

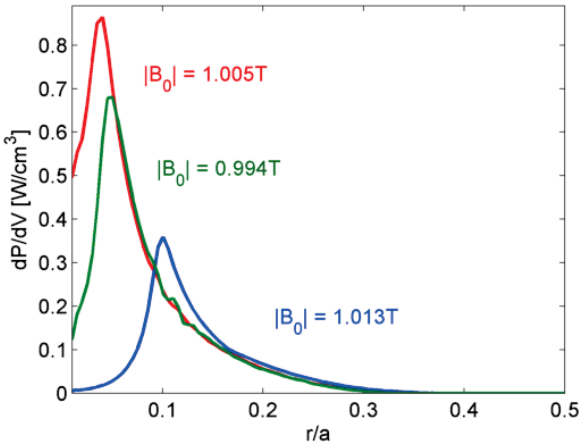

Figure 4.5: Absorption profiles and absorbed power for three magnetic field strengths at a $\theta = 10°$ launch angle, and a launched power of 50 kW.

The ray tracing codes RAYS and TRAVIS have been used to calculate the ray trajectories and absorption profiles in HSX. The RAYS code was used in the design of both ECRH

antennas; however, the TRAVIS package includes additional features that are used on HSX. TRAVIS is capable of modeling multiple passes through the plasma, the results of which are reported in this work, and the TRAVIS code also includes a module for Electron Cyclotron Emission (ECE) studies [92]. The ECE module can be used in the analysis of the ECE diagnostic on HSX, and this is suggested as future work in Chapter 7. The TRAVIS code produces almost identical results to the RAYS code when applied to either ECRH antenna on HSX. In this chapter, the predictions from the TRAVIS code are presented and compared to experimental measurements.

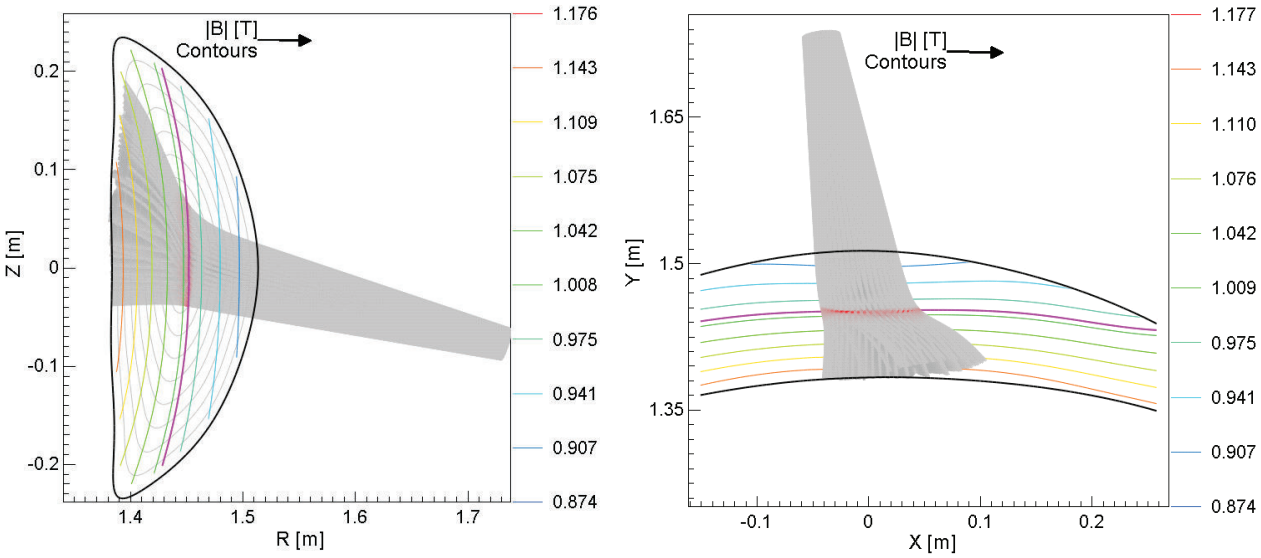

Figure 4.6: Two projections of rays launched from the second antenna into a high density plasma. A vertical plane (left) and a horizontal plane (right) are shown.

The first antenna launches the beam along the electron density gradient in the HSX symmetry plane, and while no deviation of the beam-axis occurs, the beam divergence is increased by refraction. The second beam is launched toward the plasma from below the symmetry plane to accommodate the viewing optics of the charge exchange recombination spectroscopy diagnostic. The asymmetrical density gradient sampled by the second beam causes the beam axis to deviate away from the plasma axis, especially at moderate to high

plasma densities. Figure 4.6 shows projections of the ray trajectories launched toward the magnetic axis from the second antenna at an angle of $\theta = 15°$ in a plasma with a central density of $8{\times}10^{18}$ m^{-3}.

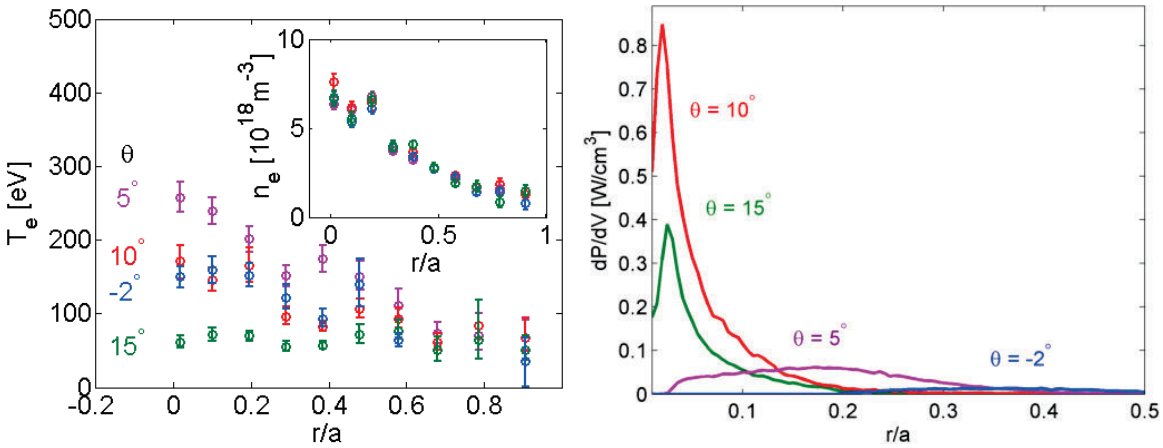

Figure 4.7: Electron temperature and density (left), and calculated power deposition profiles (right) at four launching angles for a plasma produced and maintained by 50 kW of ECRH power launched solely from the second antenna.

A launch angle scan with a 1.00T on-axis magnetic field was performed in plasma produced and maintained solely by 50 kW of ECRH power from the second antenna. Peaked stored energies were measured while aiming the beam slightly below the magnetic axis. Thomson scattering measurements of the plasma electron density and temperature are shown at left in Figure 4.7. The absorbed power profiles calculated from TRAVIS are shown at right in Figure 4.7. The axis of the beam launched from the second antenna is refracted away from the core of HSX in plasma with high densities such as those shown in Figure 4.7, resulting in reduced absorption. The absorbed power density drops quickly outside of the core due to the low electron temperatures and high electron density gradients produced solely by ECRH power launched from the second antenna.

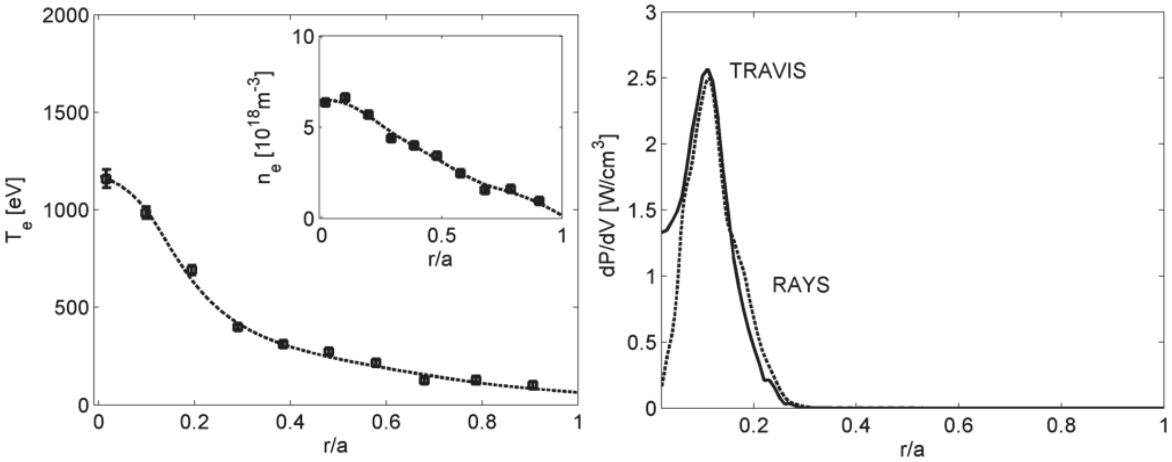

Figure 4.8: Electron temperature (left) and plasma density (inset, left) and calculated power deposition profile for on-axis heating (right) using both ECRH systems from TRAVIS (solid) and RAYS (dashed).

The electron temperature and plasma density profile for a plasma supported by both ECRH systems is shown in Figure 4.8. When 50 kW of microwave power is launched from the second antenna into a target plasma supported by 50 kW launched from the first antenna, the stored energy, electron temperature and plasma density profiles are comparable to those of a plasma supported by 100 kW solely from the first antenna. The calculated absorption is higher and the absorbed power profile is more peaked with a target plasma where higher stored energies and electron temperatures are observed. Figure 4.8 shows that RAYS and TRAVIS calculate the same resonance location and absorption efficiencies that differ by less than 1%.

The on-axis magnetic field strength, plasma density, and electron temperature were varied about the experimental parameters shown in Figure 4.8, and the calculated first-pass absorption and its profile are shown in Figure 4.9. To facilitate a comparison between the absorption shapes at different plasma parameters, the absorbed power profiles are normalized to launched power.

In the first row of Figure 4.9 the plasma density and temperature are held constant, and the on-axis magnetic field is varied from 0.96 T to 1.02 T. During the magnetic field scan, the first-pass absorption efficiency increases as the resonance moves from the high field side to the low field side of HSX until the resonant plasma volume becomes large, plasma density and electron temperature drop and the power density decreases above 1.01T. The absorbed power profile broadens and decreases in magnitude as the resonance moves away from the magnetic axis.

In the second row of Figure 4.9, the electron temperature and the magnetic field strength are held constant, and the plasma density is varied from 10^{18} m^{-3} to 10^{19} m^{-3}. Similarly, in the third row of Figure 4.9, the plasma density and magnetic field strength are held constant, and the electron temperature is varied from 100 eV to 2000 eV. The first-pass absorption efficiency increases with electron temperature and plasma density, as expected for 1^{st} harmonic ordinary mode [88], until the density approaches the cut-off value. In all three sets of calculations, the power launched from the first antenna (ECRH1) has slightly lower first-pass absorption than the power launched from the second antenna (ECRH2), because the second beam has a longer path through the resonance layer.

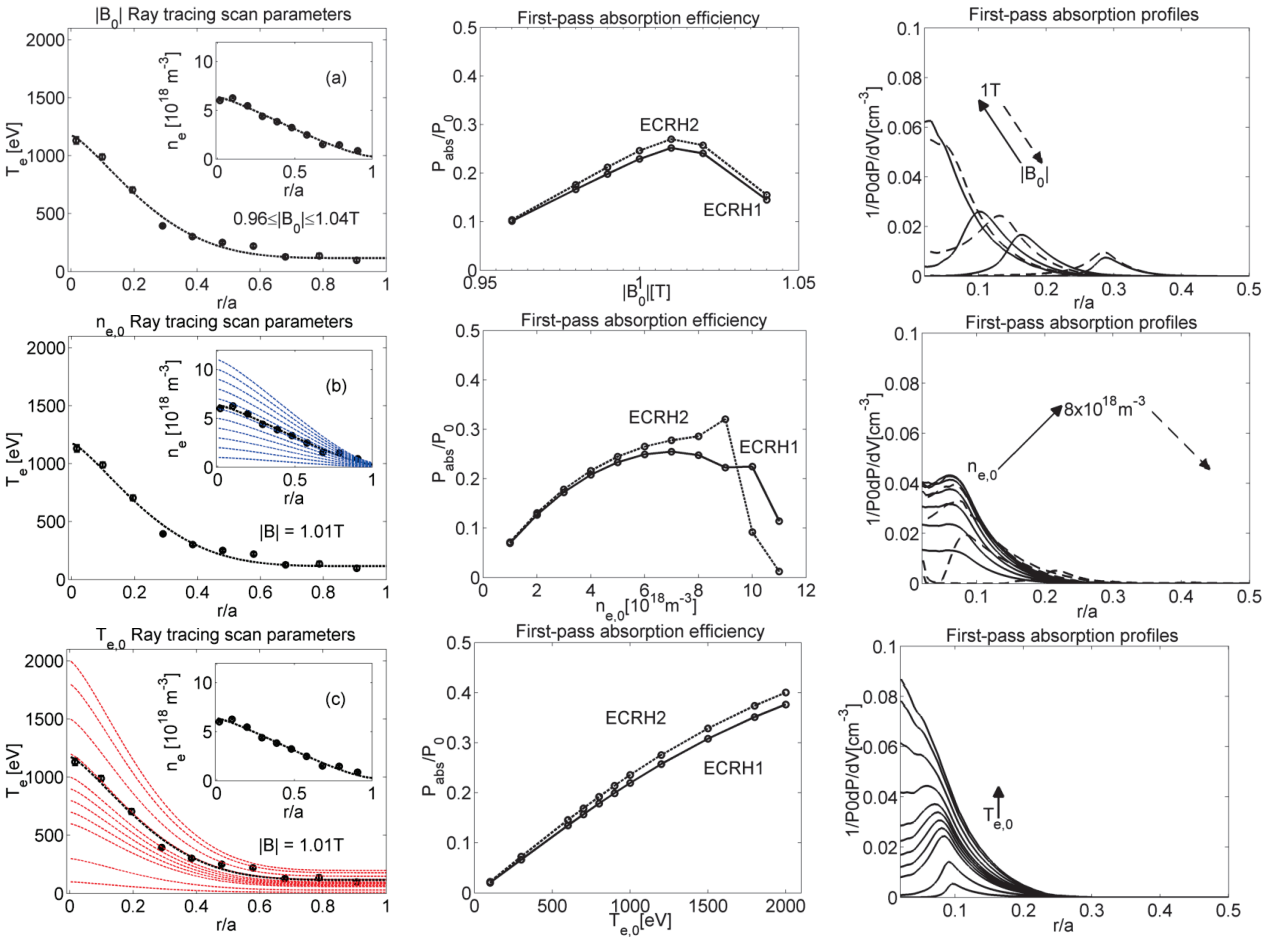

Figure 4.9: Predicted single-pass absorption and its profile as a function of main magnetic field (a), central plasma density (b) and central electron temperature (c).

4.2.2 Multipass Ray Tracing Calculations and Comparison to Measurements

The relatively low plasma density in HSX leads to reduced absorption of the launched power during the first-pass through the plasma. After its first pass through the plasma, the beam is reflected from the stainless steel vessel wall and undergoes multiple reflections before it is absorbed by the plasma. Electron cyclotron waves are strongly damped in the toroidal direction in HSX and an effective reflection coefficient of 0.9 has been previously been inferred from absorption measurements [98].

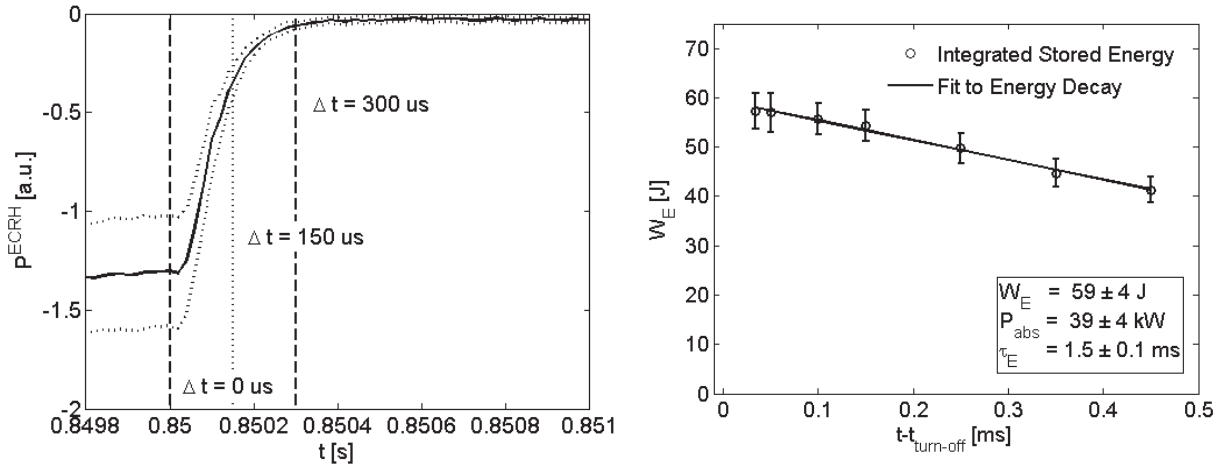

Figure 4.10: The ECRH power monitor signal during ECRH turn-off (left). The absorbed power, P_{abs}, is measured from the damping rate of the integrated plasma stored energy, W_E (circles), using Thomson scattering (black) measurements after ECRH turn-off (right).

The absorbed power is determined using the difference in energy balance before and after ECRH turn-off, $P_{abs} = \frac{dW_E}{dt}|_{t^+}^{t^-}$, by measuring the change in the plasma stored energy over a time-scale that is much shorter than the energy confinement time. The microwave power, shown at left in Figure 4.10, requires 300 μs to completely turn-off, and this is the time-scale used for total power absorption measurements on HSX. The change in plasma stored energy is determined by measuring the change in electron temperature and density

using a 10-channel Thomson scattering diagnostic and then integrating the profiles. The experimental absorption efficiency is measured to be 45%, which is higher than the 30% first-pass absorption calculated by the TRAVIS code. The decay of the energy in the integrated profiles is shown in Figure 4.10, along with the linear fits that is used to determine the temporal derivative of the stored energy.

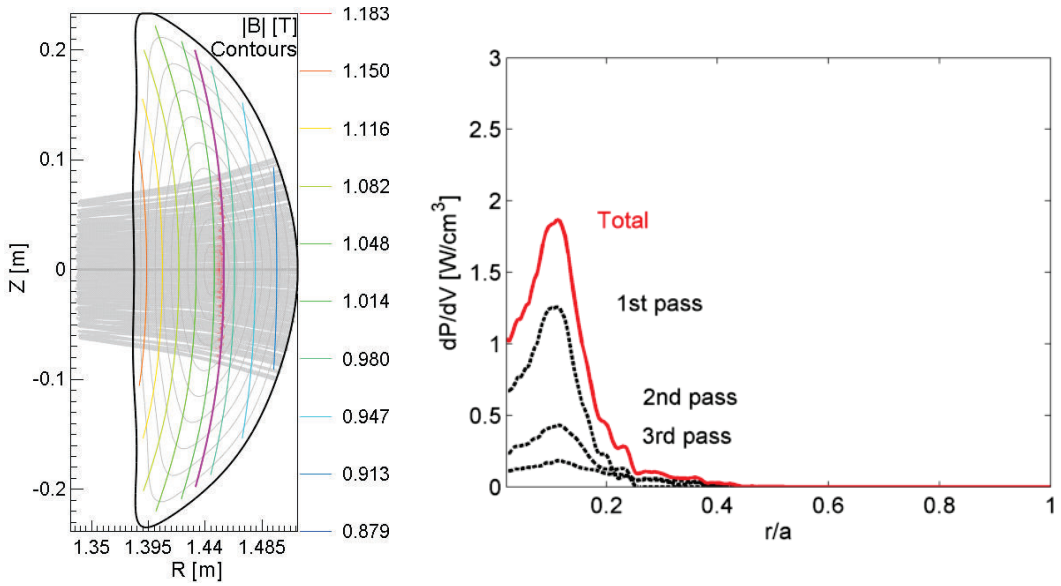

Figure 4.11: A projection of the rays launched from ECRH1 into the vertical plane during their second pass through the plasma (left) and the absorption profiles calculated for each pass (right).

The emission from the plasma at the second harmonic of the electron cyclotron frequency is measured by the 16-channel ECE radiometer on HSX, which is described in detail in Chapter 3. The energy decay rate of the plasma stored energy, determined by using the ECE temperature and constant plasma density, is the same as that measured through Thomson scattering. The total absorbed power is measured to be 39 ± 4 kW. The characteristic decay rate of the plasma stored energy is representative of the energy confinement time which is

inferred from energy balance to be $\tau_E = W_E/P_{abs} = 1.5 \pm 0.1$ ms in the QHS configuration of HSX.

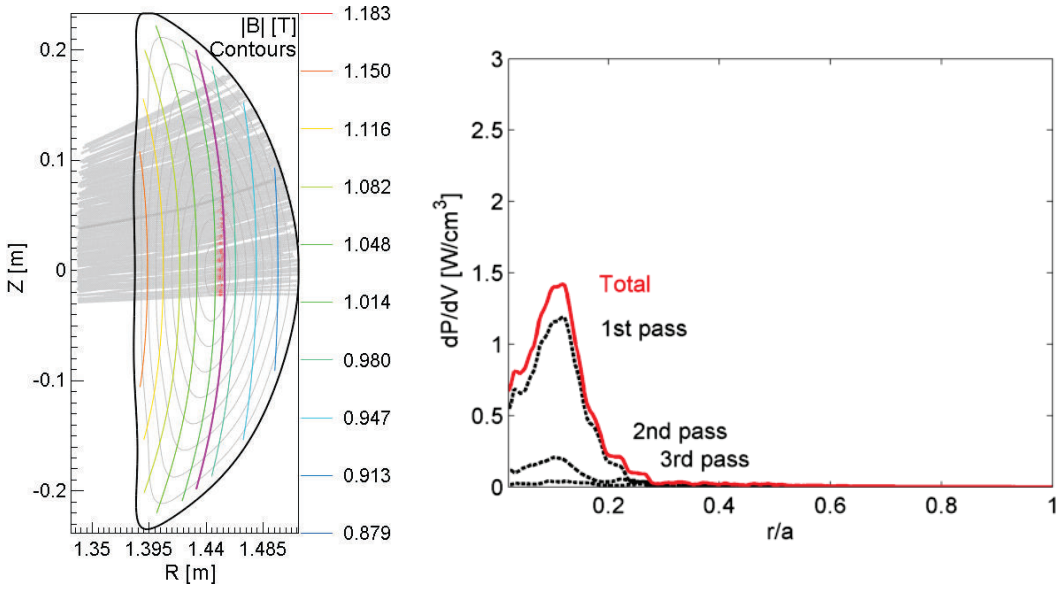

Figure 4.12: A projection of the rays launched from ECRH2 into the vertical plane during their second pass through the plasma (left) and the absorption profiles calculated for each pass (right).

Reflection from the HSX vacuum vessel is modeled using the TRAVIS code and higher multi-pass absorption is calculated for ECRH1 than for ECRH2. Figure 4.11 shows the projection of the ray trajectories into the vertical plane after their first reflection from the vacuum vessel wall for the beam launched from the first antenna. The central chord of the beam is reflected back through the plasma core. Although the beam divergence of the second pass through the plasma is larger than the beam divergence of the first pass, the majority of the absorption occurs in the hot, dense core of HSX resulting in high localization of the absorption. The beam divergence is large, and the absorbed power density is small after the first pass through the plasma leading to lower multi-pass absorption outside of the core of the plasma.

Table 4.1: Launched and absorbed power from multi-pass ray tracing calculations for ECRH1 and ECRH2 in the QHS configuration.

	$P_{launched}$	P_{abs} Total	1st Pass	2nd Pass	3rd Pass
ECRH1	44 kW	19.2 kW	10.9 kW	6.0 kW	2.2 kW
ECRH2	41 kW	15.2 kW	10.9 kW	3.2 kW	1.2 kW
Combined	85 kW	34.4 kW	21.8 kW	9.2 kW	3.4 kW

Figure 4.12 shows the projection of the ray trajectories from the second antenna into the vertical plane after their first reflection from the vacuum vessel wall. In addition to a large beam divergence and resulting low density of absorbed power, the central chord of the second beam travels away from the hot, dense plasma core. These effects result in the majority of the absorption coming from the first pass through the plasma. There is very little absorption outside of the plasma core and the absorbed power from the second antenna remains localized within $r/a \leq 0.2$. The multi-pass absorption calculations shown in Figures 4.11 and 4.12 are summarized in Table 4.1.

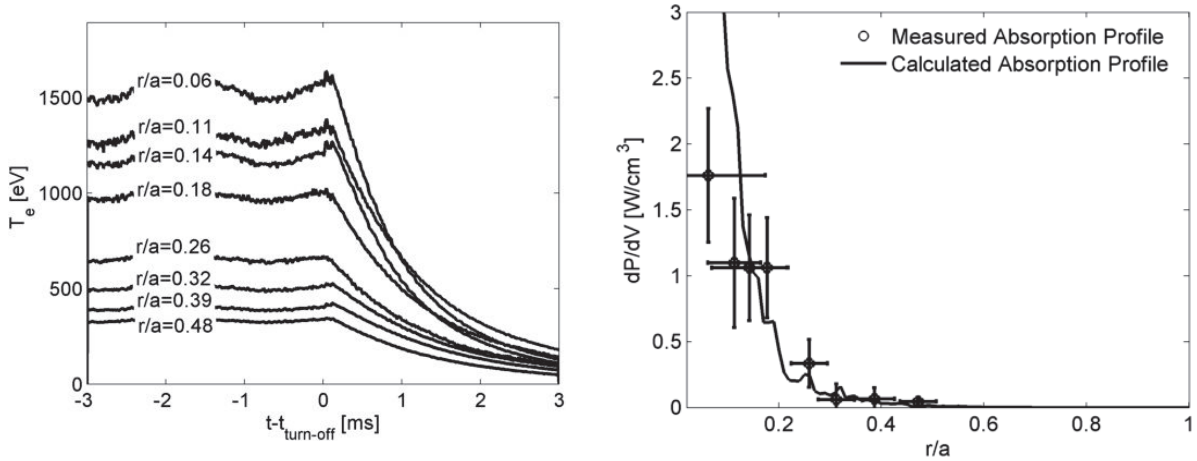

Figure 4.13: ECE traces (left) and power deposition profile measured using the change in ECE (right) after ECRH turn-off during an ECRH modulation experiment with 85 kW of launched power.

The time-traces of the ECE electron temperature during ECRH turn-off are shown at left in Figure 4.13 for an ECRH modulation experiment with 85 kW of launched power. During this experiment, a 1.00T on-axis magnetic field was used and a 10% modulation of the power launched from the second antenna was imposed by changing the gun voltage of the second gyrotron from 26.0 to 25.4 kV at 500 Hz. The electron temperature response is visible in the time-traces of the ECE in Figure 4.13. The power launched from both antennas is turned off simultaneously. The absorbed power profile determined from the change in electron temperature from ECE with a constant plasma density over a 50 μs window after ECRH turn-off is shown at right in Figure 4.13. The multi-pass ray tracing calculation that is also shown in Figure 4.13 indicates that the absorption is localized to the core, which is consistent with the absorption measurements shown in the same figure.

The single-pass ray tracing calculations of Figure 4.9 were repeated using the multi-pass ray tracing model in Figure 4.14. The peak in the absorption efficiency of both launchers does not change between the first-pass model and the multi-pass model. The absorption peaks at an on-axis magnetic field strength of 1.01 T. In multi-pass ray tracing calculations, the absorption efficiency of ECRH1 increases by more than 15% over the first-pass model, while that of ECRH2 increases by less than 10% as the on-axis magnetic field varies between $0.96 \leq |B_o| \leq 1.04$ T.

The absorption efficiency of ECRH1 peaks near the experimental core plasma density shown in Figure 4.8. Above this density, the beam divergence is large after the first-pass through the plasma, and the multi-pass component of the absorption decreases. This is also true for ECRH2; however, the absorption of ECRH2 is dominated by the first-pass through the plasma and the decrease in multi-pass absorption is not as significant as it is for ECRH1. The multi-pass absorption efficiency of ECRH1 and of ECRH2 increase with increasing temperature, as expected for the ordinary wave at the fundamental resonance,

and this is similar to the first-pass absorption of each system. Although the magnitude of the multi-pass absorption profile is larger than that of the first-pass profile, the calculated shape does not change significantly over either the density or the temperature scan presented in Figure 4.14.

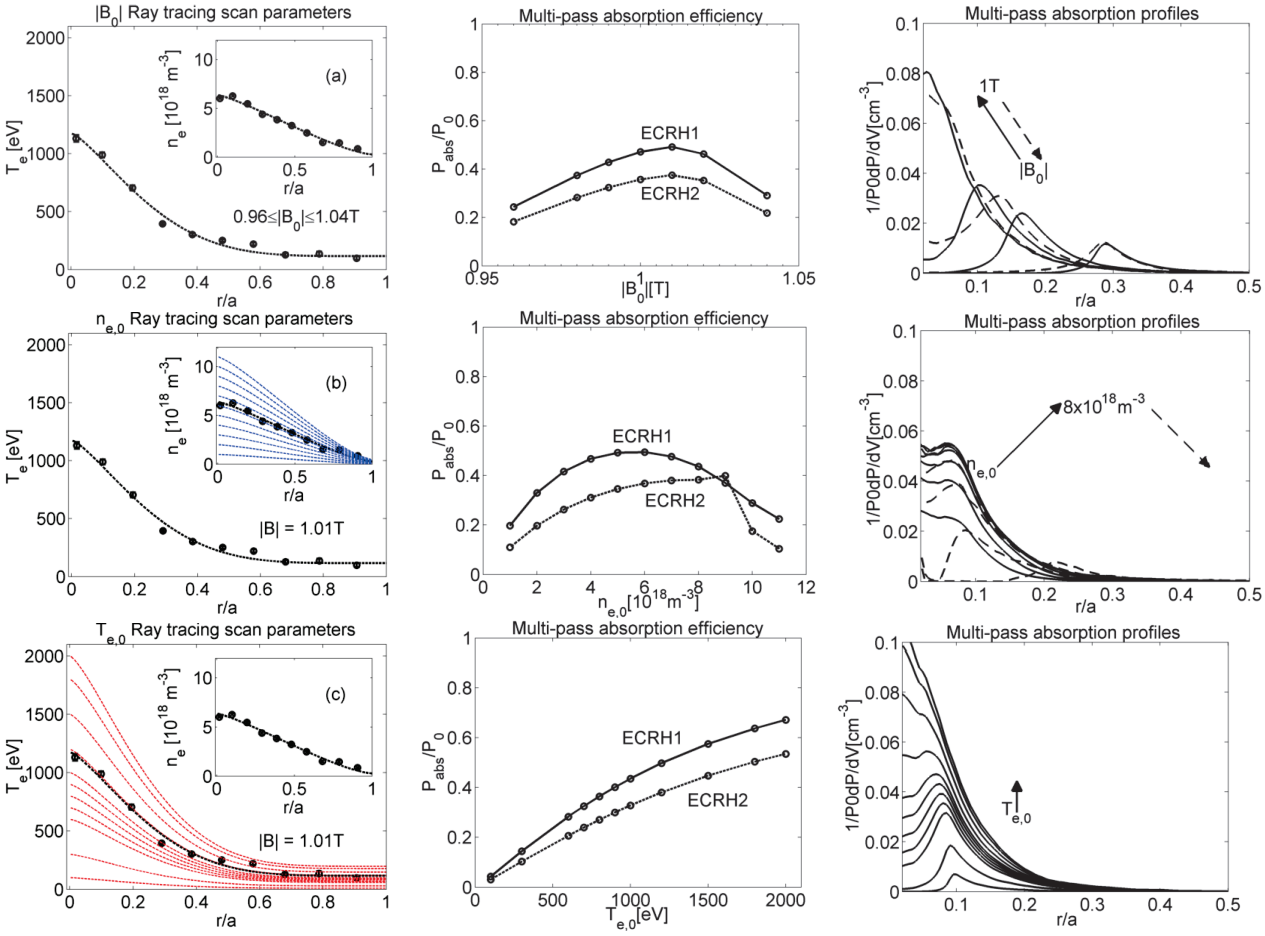

Figure 4.14: Predicted multi-pass absorption and its profile as a function of main magnetic field (a), central plasma density (b) and central electron temperature (c).

The present version of the TRAVIS code does not take into account wave polarization changes upon wall reflection or wave refraction by density gradients outside of the last closed magnetic surface, so that only a few passes through the plasma are accurately modeled. Additionally, the code is not capable of modeling ports in the vacuum vessel. These effects would result in lower absorbed power density and smaller multi-pass absorption [92]. Previous measurements have shown that the toroidal damping length is short [98] and these effects are expected to be negligible in HSX. The absorption profiles shown for ECRH1 in Figure 4.11, and for ECRH2 in Figure 4.12, should be interpreted as upper limits for the absorption after three passes through the plasma in HSX. The multi-pass ray tracing calculations show good agreement with the absorbed power and its profile that are inferred from the change in stored energy and electron temperature after ECRH turn-off.

4.3 Conclusions from ECRH Measurement and Modeling on HSX

A second gyrotron with a hybrid transmission line has been installed and tested on HSX. The second antenna includes a steerable mirror for off-axis heating, and the output power of the second gyrotron can be modulated to facilitate heat pulse propagation experiments. Ray refraction modifies the propagation and absorption of the beam launched from the second antenna with the beam-axis deviating strongly from straight propagation at high density. The TRAVIS code predicts 30% single-pass absorption efficiency of the ordinary wave at the fundamental resonance frequency in HSX, while the subsequent passes through the plasma increase the total efficiency up to the measured absorption efficiency of 45%. It has been shown that the heating from the first launcher is reinforced by multi-pass absorption, while the heating from the second antenna is less sensitive. Modeling shows that rays launched from the second antenna do not intersect the hot, dense core of HSX after the first reflection

from the wall, and the reflected beam also has large divergence and low power density. Multi-pass ray tracing calculations show good agreement with measurements of the absorbed power determined at ECRH turn-off, and the absorption is localized in the plasma core of HSX.

Bibliography

88. Alikaev, V. V., Litvak, A. G., Suvorov, E. V., *et al.* in, 1–62 (*High-Frequency Plasma Heating*, AIP, 1992).

89. Marushchenko, N. B., Erckmann, V., Hartfuss, H. J., *et al. J. Plasma Fus. Res.* **2,** S1129–S1129 (2007).

90. Editors, I. P. B. *Nucl. Fusion* **39,** 2495 (1999).

91. Lloyd, B. *Plasma Phys. Control. Fusion* **40,** A119–A138 (1998).

92. Marushchenko, N. B., Turkin, Y. & Maassberg, H. *Comput. Phys. Commun.* **185,** 165–176 (2014).

93. Goldfinger, R. C., Lee, D. K., Likin, K. M., *et al. Nucl. Fusion* **31,** 2305–2313 (1991).

94. Likin, K. M. & Ochirov, B. D. *Sov. J. of Plasma Phys.* **18,** 42–46 (1992).

95. Radder, J. W., Likin, K. M., Anderson, F. S. B., *et al. Int. J. Infrared Millimet. Waves* **29,** 360–372 (2008).

96. Vlasov, S. N. & Orlova, I. M. *Radiophys Quantum Electron* **17,** 115–119 (1974).

97. Hanfling, J., Jerinic, G. & Lewis, L. *IEEE T. Antenn. Propag.* **29,** 622–629 (1981).

98. Likin, K. M., Abdou, A., Almagri, A. F., *et al. Plasma Phys. Control. Fusion* **45,** A133–A142 (2003).

Chapter 5

Power Balance and Heat Pulse Propagation: Experimental and Analytic Techniques

The physics goal of this work is to measure the electron heat flux as a function of temperature gradient in the QHS configuration of HSX using steady state and perturbative techniques, and to compare these experimental results to gyrokinetic simulations of ETG and TEM turbulence. This chapter introduces the experimental methods used to determine the heat pulse and power balance electron thermal diffusivities, as well as the steady-state heat flux that is compared to gyrokinetic simulations in Chapter 6.

Measurements of the diffusivity are introduced in Section 5.1. The experimental method used to determine the steady-state heat flux is described in Section 5.1, and the standard analysis used to determine the power balance electron thermal diffusivity is described in Section 5.2. The power balance diffusivity depends on the sources and sinks of electron heating within the plasma, and the multi-pass absorption model used in Chapter 4 is compared to the power balance diffusivity from the first-pass model in Section 5.2.1. A Monte Carlo power balance analysis is discussed in Section 5.2.2, where it is used to check the results of the standard analysis.

The analysis of heat pulse propagation experiments to determine the incremental, or heat pulse, electron thermal diffusivity is introduced in Section 5.3. The model used to determine the diffusivity is introduced in Section 5.3.1, and a Green's function solution to the cylindrical

heat equation is used to verify that the amplitude and phase of the perturbation are self-consistent in Section 5.3.2. The sources of systematic error in the analysis are discussed in Section 5.3.3. Finally, measurements of the heat pulse diffusivity at multiple modulation frequencies are discussed in Section 5.3.4, and the results from a heat pulse propagation experiment in a methane plasma are discussed in Section 5.4.

5.1 Thermal Transport Analysis

Steady state analysis of the power balance thermal diffusivity requires knowledge of the zero-order sources and sinks, as well as any convective contributions. Commonly the particle flux, which contributes to convection is unknown, and the power balance thermal diffusivity is an effective thermal diffusivity that includes the particle flux and other off-diagonal contributions from the transport matrix [44].

The electron energy evolution equation is

$$\frac{3}{2}n_e\frac{\partial T_e}{\partial t} + \vec{\nabla}\cdot\vec{q_e} = P_{ECRH}(\rho,t) + \sum_{sinks} Q_e(\rho,t) = S_e(\rho,t), \tag{5.1}$$

where $S_e(\rho,t)$ includes all of the sources and sinks of electron heat. In the core of HSX, there are no significant electron energy sinks. Previous modeling using the DEGAS code [99] has shown that the ionization profile is peaked in the edge, and although the energy lost through neutralization can be significant in the edge, the electron energy lost to ionizing the neutral gas is not significant within $r/a < 0.6$ [100]. The radiated power is measured by two AXUV photodiodes that are used as bolometers [101]. One bolometer views the core of the plasma and has a narrow solid angle, while the other views the entire plasma cross-section. The radiated power measured during an ECRH modulation experiment with 85 kW of launched power is approximately 3 kW, shown in Figure 5.1a. The energy lost through electron-ion drag is calculated using the measured electron temperature and plasma density profiles, and

the ion temperature fit used in Section 2.4, from

$$P_{ei} = -P_{ie} = -\nu^{e/i} n_e \left(T_e - T_i\right), \tag{5.2}$$
$$\nu^{e/i} = \frac{4}{\sqrt{\pi}} \frac{4\pi n_e Z_i^2 e^4 \ln\lambda}{m_e m_i v_{Tei}^3},$$
$$v_{Tei}^2 = \frac{2T_e}{m_e} + \frac{2T_i}{m_i}.$$

Here $\ln\lambda$ is the Coulomb logarithm [102], and there are no other sources of ion heating on HSX. The power collisionally transferred from the electrons to the ions within $r/a < 0.6$ is 1.1 kW, while the total power transferred to the ions is 1.4 kW. These electron energy sinks are small in comparison to the 39 kW of absorbed power that was measured in Section 4.2.2. The source in Equation 5.1 is approximated by the ECRH absorption profile calculated by ray tracing.

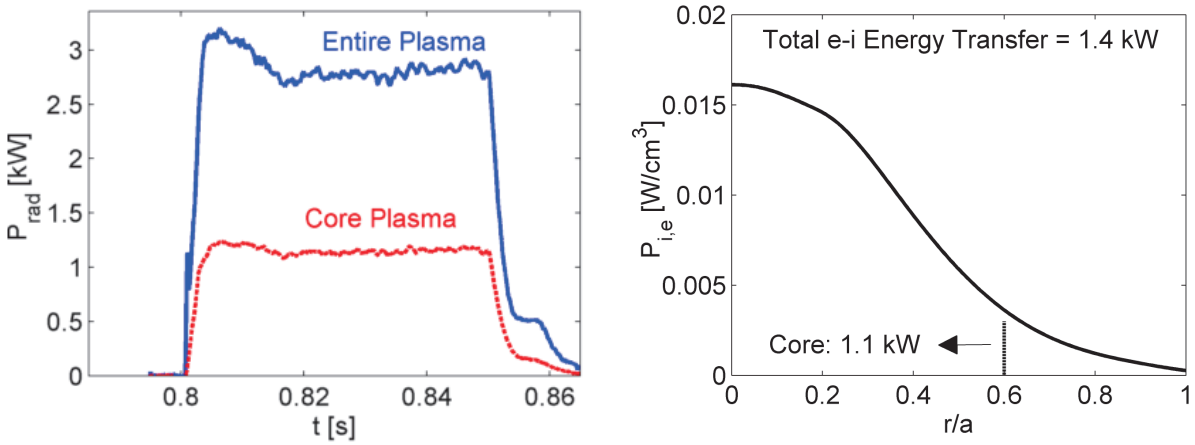

(a) Radiated power measured by two bolometers.

(b) Electron-ion energy exchange.

Figure 5.1: Radiated power (a) and electron-ion energy transfer rate (b) during an ECRH modulation experiment with 85 kW of launched power.

The power balance and heat pulse thermal diffusivities are determined from the linearized and flux-surface averaged energy equation (Equation 5.1). After integration, Fourier's law of conduction is used to yield both a power balance electron thermal diffusivity, χ_e^{PB}, at zero

order in the heating modulation depth, $\varepsilon = \frac{\delta P}{P}$, and a heat pulse thermal diffusivity, χ_e^{HP}, at first order (as is done in Appendix B),

$$\varepsilon^0: \quad \langle \vec{q}_e \cdot \nabla\rho \rangle = \frac{1}{V'} \int_0^\rho \langle S_e \rangle V' d\rho, \tag{5.3}$$

$$\varepsilon^1: \quad \langle \delta\vec{q}_e \cdot \nabla\rho \rangle = \frac{1}{V'} \int_0^\rho \left[\langle \delta S_e \rangle - \frac{3}{2} \langle n_e \rangle \frac{\partial \langle \delta T_e \rangle}{\partial t} \right] V' d\rho, \tag{5.4}$$

$$\chi_e^{PB} = -\frac{\langle \vec{q}_e \cdot \nabla\rho \rangle}{\langle |\nabla\rho|^2 \rangle \langle n_e \rangle \frac{\partial \langle T_e \rangle}{\partial \rho}} \quad \text{and} \quad \chi_e^{HP} = -\frac{\langle \delta\vec{q}_e \cdot \nabla\rho \rangle}{\langle |\nabla\rho|^2 \rangle \langle n_e \rangle \frac{\partial \langle \delta T_e \rangle}{\partial \rho}}.$$

Here $\langle ... \rangle$ is the flux-surface average operator, δS_e is the modulated part of the electron heating, V is the flux-surface volume and $'$ indicates a derivative with respect to the effective minor radius. The effective minor radius is defined as the square-root of the enclosed flux normalized to the total flux within the last closed flux surface, $\rho = \sqrt{\frac{\Psi}{\Psi_{lcfs}}}$.

The heat pulse diffusivity determined from the time-domain analysis in Equation 5.4 is prone to large systematic errors from the uncertainty in the spatial and the temporal derivative of the temperature perturbation. Consequently, a frequency domain analysis is introduced in Section 5.3 and used to determine the heat pulse diffusivity in Section 5.3.4.

5.2 Power Balance Analysis

The power balance thermal diffusivity is determined by rearranging Equation 5.3 into

$$\frac{\partial \langle T_e \rangle}{\partial \rho} = \frac{-1}{V' \langle |\nabla\rho|^2 \rangle \langle n_e \rangle \chi_e^{PB}} \int_0^{\rho'} \langle S_e \rangle V' d\rho', \tag{5.5}$$

numerically integrating, and solving the resulting least squares problem using Thomson scattering data with χ_e^{PB} as the variational parameter. The least squares problem is solved using the Matlab algorithm for least-squares minimization, "lsqnonlin," which also outputs the numerical Jacobian of the solution. The residual in the solution and the Jacobian are used to estimate the scaled covariance of the problem at each radial position. This procedure is advantageous because it yields a thermal diffusivity across the plasma minor radius, avoids

evaluating the temperature gradient, and allows rigorous error analysis by including the variance in the fitting parameters.

During standard power balance analysis on HSX, the diffusivity in Equation 5.5 is parametrized by a 4th order polynomial within an exponential function, $\chi_e(r) = \exp\left[\chi_0 + \chi_1 r + \chi_2 r^2 + ...\right]$; however, any analytic function that is not under-constrained may be used to parametrize the diffusivity. An example of this is provided in Appendix A. In Appendix A, a Heaviside function on a quadratic background is used to parametrize the diffusivity, and the power balance analysis is used to test whether the change in electron temperature with an electron internal transport barrier or a region of stochastic magnetic field lines is measurable in HSX.

The residuals in the least-squares analysis are the weighted difference between the Thomson scattering electron temperature measurement and the fit that results from integrating the electron temperature gradient given by Equation 5.5. Fits for $\langle|\nabla\rho|\rangle$ and $\langle|\nabla\rho|^2\rangle$ from Reference [13] were made using vacuum magnetic field line following, and these functions vary slowly across the plasma radius. $\langle|\nabla\rho|\rangle$ and $\langle|\nabla\rho|^2\rangle$ are approximately $1.2/a$ and $1.6/a^2$ respectively, where a is the plasma minor radius.

5.2.1 First-pass versus Multi-pass Absorption

The source used in Equation 5.3 to determine the steady-state electron heat flux, and in Equation 5.5 to determine the power balance electron thermal diffusivity, is modeled as the ECRH absorption profile. In Section 4.2.2, Thomson scattering measurements after ECRH turn-off were used to measure the total absorbed power, and this measurement was 15% higher than the first-pass ray tracing calculation. A multi-pass model accurately reproduced the total absorption after three passes through the plasma, and the spatial extent of the multi-pass absorption profile matched the shape of the profile measured by the ECE after

heating turn-off. The difference between the first-pass and multi-pass absorption is significant in the power balance analysis.

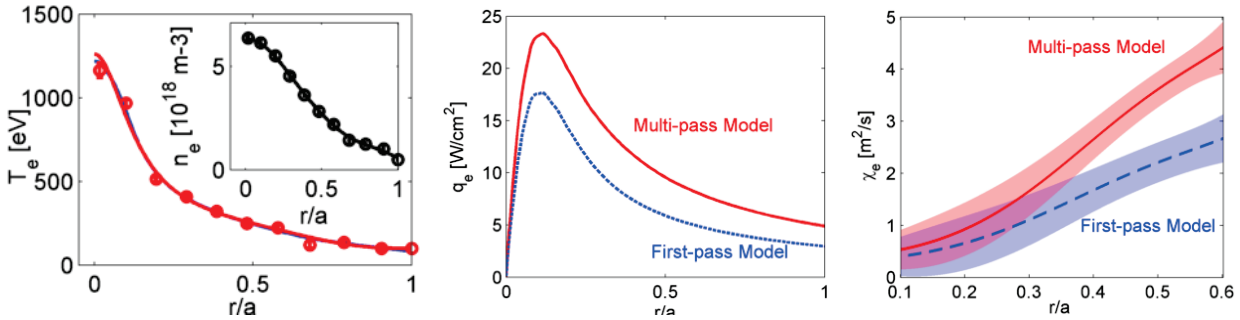

(a) Electron temperature and plasma density fits.

(b) Heat flux from first-pass and multi-pass ray tracing.

(c) χ_e^{PB} from a standard analysis.

Figure 5.2: Electron temperature and plasma density profiles measured during an ECRH modulation experiment with 85 kW of launched power from power balance analysis (a), the heat flux from the first-pass (blue dashed line) and multi-pass ray tracing model (red solid line)(b), and the power balance electron thermal diffusivity in each case (c).

The electron temperature and density profiles from Thomson scattering measured during an ECRH modulation experiment with 85 kW of launched power, and the fitted electron temperature and plasma density profiles from the least-squares analysis are shown in Figure 5.2a. The first-pass and multi-pass ray tracing model of the electron heat flux are shown in Figure 5.2b, and there is no significant change in electron temperature fit between the two cases, as can be seen in the nearly overlaid n_e and T_e profile fits in Figure 5.2a. The first-pass absorption is 15% lower than the multi-pass absorption, which leads to a smaller peak in the first-pass absorption case. Additionally, the first-pass absorption is more narrow than the multi-pass absorption, and the peak in the first-pass absorption occurs slightly closer to the magnetic-axis.

5.2.2 Monte Carlo Error Propagation

The standard analysis described in Section 5.2 includes the statistical uncertainty from plasma density and electron temperature measured by Thomson scattering and the covariance in the analytic fitting parameters. However, there is also systematic uncertainty from the form of the fitting function used in the analysis. This is tested by using polynomials of varying order, and the exponential of polynomials of varying order, to determine whether the standard analysis is sufficient to calculate the power balance electron thermal diffusivity. Additionally, a Monte Carlo analysis is used to test the sensitivity of the fitting function to the experimental uncertainties. In the Monte Carlo analysis, the plasma density and electron temperature are varied within their uncertainties, and the thermal diffusivity is calculated for each test profile. A test population of 30 densities and temperatures for each spatial channel are sufficient to reproduce the experimental mean and variance measured by the Thomson scattering diagnostic.

Figure 5.3 shows the electron temperature and thermal diffusivity profiles that result from using polynomials of order 2-7 and their exponentials in the power balance analysis. In the polynomial fitting case, shown in Figure 5.3a and Figure 5.3b respectively, the 2^{nd} and 3^{rd} order fits do not accurately reproduce the experimental electron temperature. Outside of $r/a > 0.2$, both fits are consistently higher than the electron temperature. Within $r/a < 0.2$, the 2^{nd} order polynomial under estimates the electron temperature, while the 3^{rd} order polynomial over estimates the electron temperature. The 7^{th} order polynomial fit to the thermal diffusivity has large variation, and this causes an innacurate electron temperature gradient calculation.

In the (radially) exponential fit case, the 7^{th} order fit under estimates the core electron temperature and does not accurately represent the temperature gradient for $r/a < 0.2$.

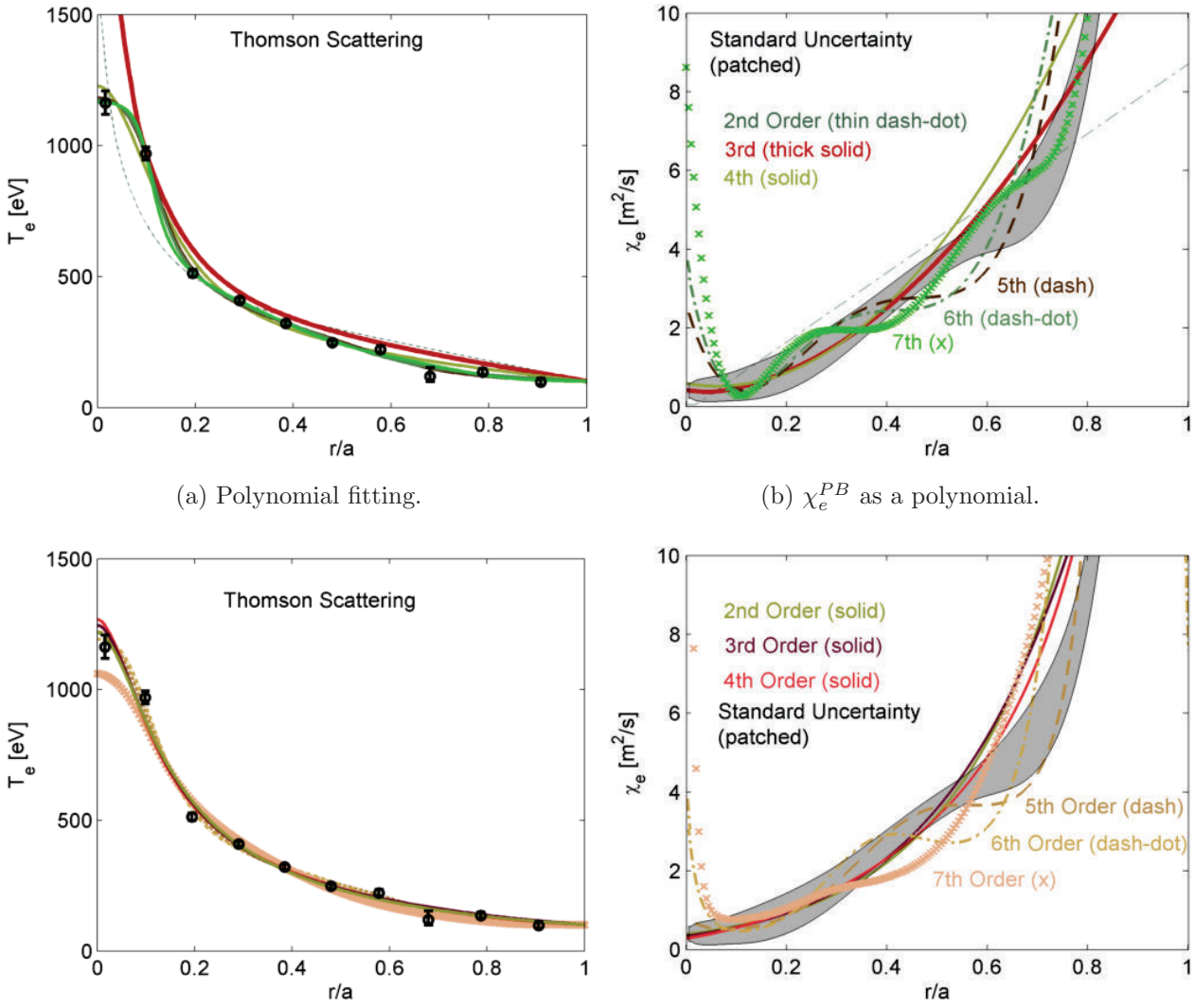

(a) Polynomial fitting.

(b) χ_e^{PB} as a polynomial.

(c) Exponential fitting.

(d) χ_e^{PB} as an exponential.

Figure 5.3: Power balance analysis sensitivity to fitting functions. The temperature fit (a,c) and diffusivity (b,d) from using polynomials of order 2-7 (first row), and the exponential of those polynomials (second row) in the power balance analysis.

Additionally, the 6^{th} and 7^{th} order fits have large variation that lead to innacurate electron temperature gradient calculations.

The six fitting functions that remain are polynomials of order 4-6, and exponential functions of order 3-5. In the region that heat pulse propagation data is available

$(0.2 \leq r/a \leq 0.4)$, the results of these six fitting functions are well-represented by the standard least-squares power balance analysis. The systematic uncertainty from the form of the fitting function becomes large for $r/a > 0.6$. This is because the electron temperature gradient becomes shallow, and the diffusivity becomes large in this region. The steady-state power balance analysis is limited to within $r/a < 0.6$ in this work due to uncertainty in the experimental heat flux outside of this region, and the standard analysis captures the statistical and systematic uncertainty in the analysis sufficiently well for $r/a < 0.6$. Consequently, the standard analysis is used for the power balance electron thermal diffusivity throughout this work.

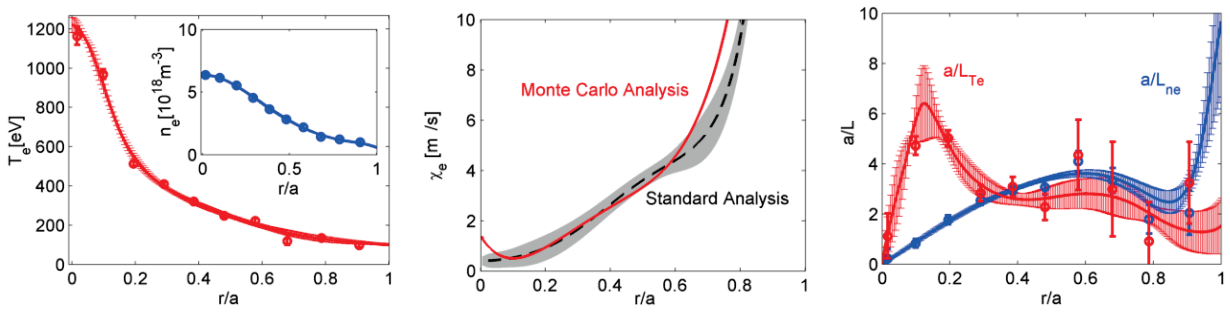

(a) Temperature, density and fits. (b) χ_e^{PB}. (c) Gradient scale lengths.

Figure 5.4: Electron temperature and plasma density from the Thomson scattering diagnostic and the Monte Carlo fits for each (a). The power balance diffusivity from a standard and a Monte Carlo analysis (b). The electron temperature and density gradient scale lengths from Monte Carlo analysis (red and blue lines respectively) and finite differences (circles) (c).

The electron temperature and plasma density gradients are calculated during the Monte Carlo analysis, which is advantageous for generating flux-gradient diagrams (used in Chapter 6) and for comparing power balance results to heat pulse propagation experiments. The final electron temperature and density profile scale lengths calculated from a Monte Carlo analysis are shown with the scale lengths calculated from finite-differences in Figure 5.4c. The

Monte Carlo calculation captures the uncertainty in the core electron temperature gradients, $r/a < 0.3$, better than the finite differences, and the scale lengths and gradients are calculated through Monte Carlo analysis throughout this work.

5.3 Heat Pulse Propagation Analysis

Measurements of the incremental thermal diffusivity require more extensive analysis than power balance measurements and yield additional information about the heat transport. A modulated heat source or sink causes the plasma temperature and other parameters to evolve. In the limit of negligible density perturbations, the incremental electron thermal diffusivity can be solved for from the propagation of heat pulses through the plasma.

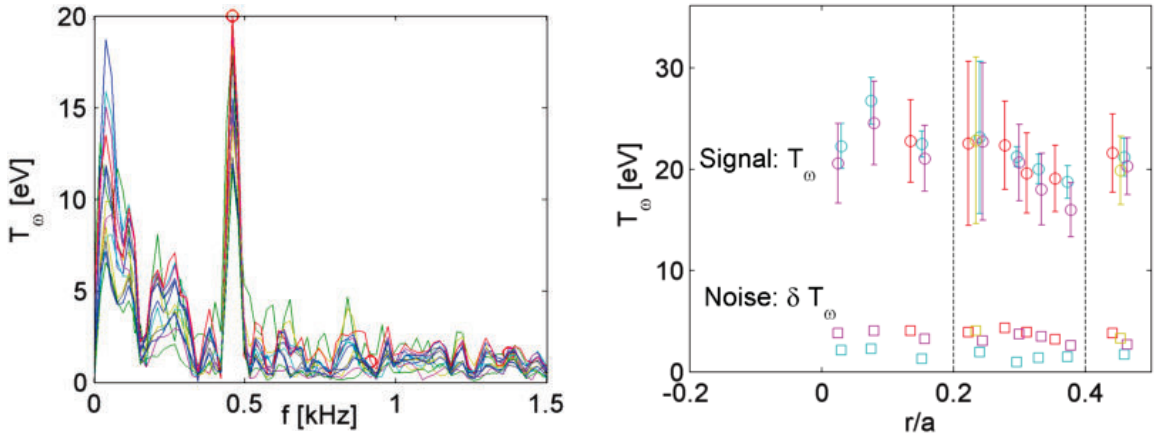

Figure 5.5: FFT spectrum of the ECE radiation temperature (left), and the radial amplitude of the electron temperature perturbation (right).

There is a strong response in the spectral amplitude of the electron temperature measured by the ECE to square wave ECRH modulation at 500 Hz. This is evident in the FFT spectrum of the ECE radiation temperature and is shown in Figure 5.5. Harmonics of the electron temperature perturbation are in the noise level in Figure 5.5 and are not used in this work. The amplitude of the perturbation is shown for 4 separate plasma discharges in Figure 5.5, and the signal-to-noise ratio is greater than 5 for the channels shown. The

amplitude decays outside of the power deposition region ($r/a < 0.2$), but there is a non-monotonic feature that appears above the noise level for $r/a > 0.4$. This non-monotonic feature is robust, and also appears in the phase of the perturbation. This behavior was also observed during heat pulse propagation experiments in the standard configuration of the ECE radiometer, and is discussed further in Section 5.3.3.

The coherence between the modulated ECRH source and each ECE channel at the ECRH modulation frequency represents the fraction of power output from each ECE channel that is driven by the ECRH source. The presence of noise or non-linearities in the response decreases the coherence between the ECE and the chosen reference. The ECE channels shown in Figure 5.5 and used in the heat pulse propagation analysis have high coherence and signal-to-noise ratio greater than 3.

Experimentally, the upper limit of the modulation frequency is the inverse energy confinement time, $f_{mod}\tau_E < 1$ [52]. In the QHS configuration, the energy confinement time was measured to be 1.5 ms during an ECRH modulation experiment with 85 kW of launched power described in Section 4.2.2. This corresponds to an upper modulation frequency limit of 650 Hz for perturbative heat transport experiments with 85 kW of launched power. Above this frequency, the analysis no longer yields information about thermal transport but provides information about the power deposition. In the limit of high frequency modulation, where transport occurs on a much longer time-scale than the time-scale of analysis, the power deposition profile can be determined from the amplitude of the harmonic temperature perturbation,

$$P_{abs}(r) = -\frac{3}{2} i\omega n_e(r) \delta T_{e,\omega}(r). \tag{5.6}$$

The amplitude of the temperature perturbations decreases with frequency, so that Equation 5.6 is frequency independent in the absence of heat transport.

Another way to express the upper limit of the modulation frequency is through the modulation damping length, $\lambda = (4\chi_e/3\omega)^{0.5}$. For the experiment shown in Figures 5.5, during which a 500 Hz ECRH modulation was used, the diffusivity near the core is of order 1 m^2/s and λ =2 cm, which is of the same order as the deposition profile width along the ECRH heating beam. For absorption measurements, the damping length must be much smaller than the deposition profile width, requiring high ECRH modulation frequencies. The equivalent bandwidth of the 50 μs window used for profile measurements in Section 4.2.2 is 20 kHz, corresponding to a damping length of 0.3 cm. This damping length is approximately 5% of the QHS minor radius along the ECE view and is sufficient for absorption profile measurements outside of the core, $r/a > 0.1$ in HSX.

5.3.1 The Heat Pulse Diffusivity Model

The Fourier transformed homogeneous cylindrical heat equation,

$$\left[r^2\frac{\partial^2}{\partial r^2} + \frac{1}{r}\frac{\partial}{\partial r} - \frac{3in\omega}{2\chi_e}r^2\right]\delta T_n(r) = 0, \tag{5.7}$$

is a zero-order Bessel equation for the temperature perturbation $\delta T(r,t) = \Sigma_n \delta T_n(r)\exp(in\omega t - i\varphi)$. The amplitude and the phase of the perturbation are each related to the thermal diffusivity in Equation 5.7, and the thermal diffusivity can be derived from either the amplitude decay of the perturbation, δT_e, or the phase-delay between the perturbation and the source, $\delta\varphi$ [29]. The amplitude-decay is calculated from the FFT spectrum of each ECE channel, and the phase-delay is the cross-phase between each ECE channel and a reference signal at the modulation frequency, ω_{mod}.

As is shown in Appendix B, ECRH modulation experiments are described by the large argument limit of Equation 5.7. In this limit, the lowest-order phase of the electron temperature perturbation increases linearly with radius and varies inversely with thermal diffusivity

[103], $\varphi_n \approx \left(\frac{3n\omega}{4\chi_e}\right)^{0.5} r$. Thus the incremental thermal diffusivity derived from the phase-delay of the perturbation is proportional to the inverse of the squared radial derivative of the phase,

$$\chi_e^{\varphi} = \frac{3n\omega}{4}\left(\frac{d\varphi_n}{dr}\right)^{-2}. \tag{5.8}$$

In the large argument limit, the lowest order contribution to the amplitude of the perturbation is asymptotic to a cylindrical wave, $\delta T_n \sim \frac{\exp x/\sqrt{2}}{\sqrt{2\pi x}}$, so that the incremental thermal diffusivity derived from the logarithmic derivative of the amplitude is

$$\chi_e^{A} = \frac{3n\omega}{4}\left(\frac{d\ln\delta T_n}{dr} + \frac{1}{2r}\right)^{-2}. \tag{5.9}$$

The heat transfer occurs between magnetic flux surfaces in the actual experiment, and (in flux co-ordinates) the surfaces may be represented as a cylinder. The flux-surface averaged form of Bessel's equation is solved in Appendix B not only to take into account the flux surface averaged geometry of the actual experiment, but also to facilitate comparisons with the power balance electron thermal diffusivity. The effect of the density profile may also be included to yield the electron thermal diffusivity from the phase and amplitude of the perturbation,

$$\chi_e^{\varphi} = \frac{3n\omega}{4\left\langle|\nabla\rho|^2\right\rangle}\left(\frac{d\varphi_n}{d\rho}\right)^{-2} \quad \text{and} \quad \chi_e^{A} = \frac{3n\omega}{4\left\langle|\nabla\rho|^2\right\rangle}\left(\frac{d\ln\delta T_n}{d\rho} + \frac{1}{2}\frac{d}{d\rho}\ln n_e V'\right)^{-2}.$$

Here $V' = \frac{dV}{d\rho}$ is the radial derivative of the flux surface volume, and in the cylindrical limit $\frac{d\ln V'}{d\rho}$ reduces to ρ^{-1},

$$\chi_e^{\varphi} = \frac{3n\omega}{4\left\langle|\nabla\rho|^2\right\rangle}\left(\frac{d\varphi_n}{d\rho}\right)^{-2} \quad \text{and} \quad \chi_e^{A} = \frac{3n\omega}{4\left\langle|\nabla\rho|^2\right\rangle}\left(\frac{d\ln\delta T_n}{d\rho} + \frac{1}{2\rho} + \frac{1}{2}\frac{d\ln n_e}{d\rho}\right)^{-2}. \tag{5.10}$$

The expressions for the electron thermal diffusivity from the amplitude decay, χ_e^A, and from the phase-delay, χ_e^{φ}, in Equation 5.10 are used in the analysis of heat pulse propagation experiments on HSX.

5.3.2 Self-Consistency in the Measurements: a Green's Function Solution

A Green's function solution to the inhomogeneous cylindrical heat equation is used to calculate the electron thermal diffusivity from the amplitude of the electron temperature perturbation, and the results are used to calculate a numerical phase that is compared to the experimental measurement. The numerical solution is also used to check the model used in Section 5.3.4 and Chapter 6 for self-consistency.

The Green's function solution for the cylindrical heat equation, Equation 5.7, is [104],

$$\frac{3}{2}i\omega G(r,r') - \frac{\chi_e}{r}\frac{\partial}{\partial r}\left(r\frac{\partial}{\partial r}G(r,r')\right) = \frac{\delta(r-r')}{2\pi r'},$$

where

$$G(r,r') = \begin{cases} \frac{1}{2\pi\chi_e}\left[K_0(zr) - \frac{K_0(za)}{I_0(za)}I_0(zr)\right]I_0(zr'), & r > r' \\ \frac{1}{2\pi\chi_e}\left[K_0(zr') - \frac{K_0(za)}{I_0(za)}I_0(zr')\right]I_0(zr), & 0 < r < r'. \end{cases} \tag{5.11}$$

In Equation 5.11 K_0 is the zero order McDonalds function, I_0 is the zero order modified Bessel function, $z^2 = \frac{3i\omega}{2\chi_e}$ is the complex wave-vector in this equation. The Green's function solution to the cylindrical heat equation assumes constant plasma density and electron thermal diffusivity profiles, an instantaneous source located at $r = r'$, with Neumann boundary condition on the axis $\frac{dT_\omega}{dr}(0) = 0$, and Dirichlet boundary condition at the minor radius $T_\omega(a) = 0$.

The superposition principal yields the solution to the inhomogeneous cylindrical heat equation in terms of the Green's function solution in Equation 5.11 [105] [64],

$$\begin{aligned} \frac{3}{2}i\omega T_\omega - \frac{\chi_e}{r}\frac{\partial}{\partial r}\left(r\frac{\partial T_\omega(r)}{\partial r}\right) &= \frac{P_\omega}{n_e}, \\ T_\omega(r)e^{i\varphi_\omega(r)} &= 2\pi\int_0^r G(r,r')\frac{P_\omega(r')}{n_e(r')}r'dr'. \end{aligned} \tag{5.12}$$

Here the modulated heating source, P_ω, is an absorbed power profile from the multi-pass ray tracing model. The perturbation amplitude and phase are both calculated from the Green's function solution, and this is used to check that the experimental phase is self-consistent with the measured amplitude.

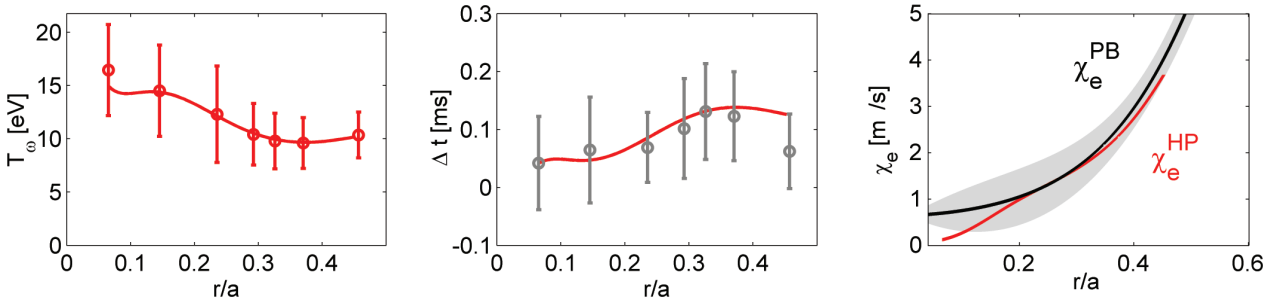

(a) Linear amplitude decay and fit. (b) Time delay and solution. (c) χ_e^{HP} and χ_e^{PB}

Figure 5.6: The electron temperature response to 500 Hz ECRH modulation and a least squares fit to the amplitude (a). The measured time delay and the calculated time delay (b). χ_e^{HP} that results from a least squares fit to the amplitude, from the Green's function solution to the cylindrical heat equation (c).

A least squares solution is used to fit the amplitude data while using χ_e^{HP} as the fitting parameter. The analysis is very similar to the power balance analysis discussed in Section 5.2. The amplitude from an ECRH modulation experiment with 66 kW of launched power, and the numerical fit resulting from Equation 5.12 are shown in Figure 5.6a.

The numerical solution is independent of the measured phase delay (which is cast as a time delay using $\Delta t = -\varphi_\omega/(2\pi\omega_{mod})$), and the experimental time-delay is shown with the numerical time-delay in Figure 5.6b. The numerical time delay is consistent with the measured time delay. Additionally, the resulting heat pulse electron thermal diffusivity, shown in Figure 5.6c, matches the power balance solution, indicating that the plasma is not stiff and there is no convective electron heat flux in this experiment within $r/a < 0.4$. The

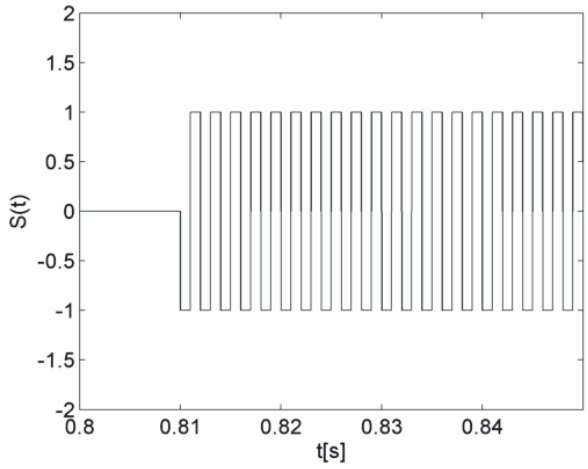

Figure 5.7: A pre-generated square-wave reference signal used in the cross-phase calculation.

measured time delay and amplitude decay are non-monotonic outside of $r/a > 0.4$, and the numerical time delays reflect this behavior.

5.3.3 Systematic Uncertainty and its Mitigation in the Analysis

There are two primary sources of error in the phase measurement. The first is aliasing in the phase from under sampling the ECE diagnostic. The measured time delays between channels are on the order of 30-40 μs, and heat pulse propagation measurements in the standard ECE configuration (discussed in Chapter 3) were under-sampled. The increased resolution configuration of the ECE radiometer is limited by the 300 kHz video bandwidth of the radiometer; however, the sampling time of the increased resolution configuration is sufficient to accurately measure the phase during heat pulse propagation experiments.

The second source of systematic uncertainty in the cross-phase is due to noise in the reference signal. The systematic uncertainty arising from the use of a noisy reference, such as an ECE channel near the core of the plasma, adds systematic covariance to all of the measurements that is highly correlated and cannot be removed during post-processing.

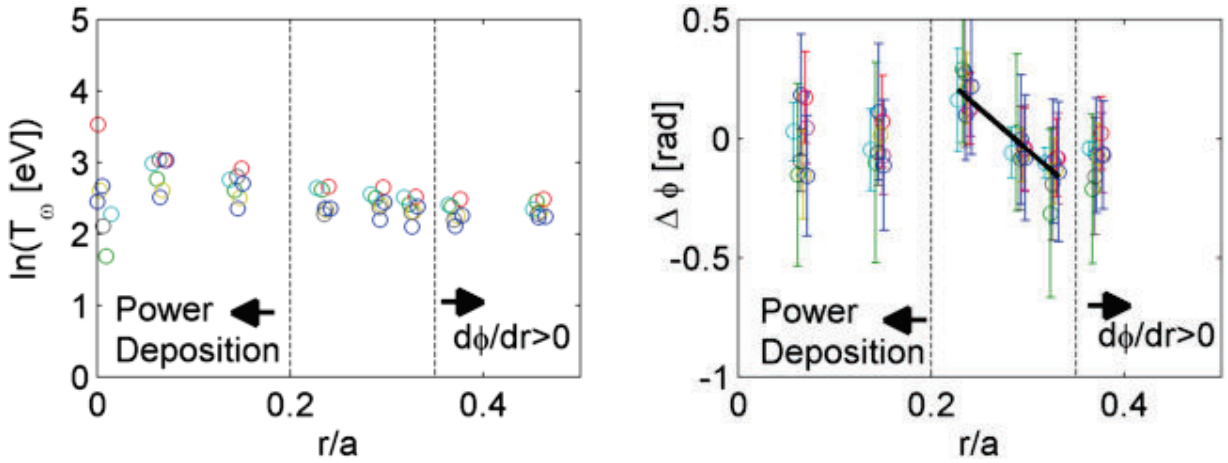

(a) Logarithmic Amplitude.

(b) Cross-phase (offset removed).

Figure 5.8: Logarithmic amplitude (a) and cross-phase (b) from an ECRH modulation experiment with 66 kW of launched power.

This covariance leads to higher variation in the phase data. If a pre-generated square-wave signal is used as a reference, then the phase has significantly less variation, because the offset is uncorrelated. The pre-generated square-wave signal used as a reference for the phase measurement is shown in Figure 5.7. The mean phase of the ECE channels used in the heat pulse analysis is subtracted from the cross-phase to remove the arbitrary offset, resulting in the reproducible cross-phase that is shown in Figure 5.8b.

The logarithmic amplitude for each plasma discharge in the 66 kW launched power ensemble is shown in Figure 5.8a. There is variation in the spectral amplitude that is measured between shots; however, the logarithmic gradient remains reproducible. The difference in amplitude is due to shot-shot variability in the launched ECRH power. The logarithmic gradient is unmodified by removing the average offset between shots resulting in a reproducible logarithmic gradient.

Due to the limited number of channels outside of the power deposition zone and inside the point at which the phase becomes non-monotonic, several identical shots are necessary

to robustly fit the amplitude and phase. The radial location of each channel changes slightly on each shot because the main current varies within a small margin between shots. Although ECE channel 15 has non-monotonic phase, its amplitude is consistent with the amplitude decay of the other channels, and has been included in the analysis below in Section 5.3.4.

The cross-phase of the ECE electron temperature with an artificial reference signal is reproducible at high sampling frequency, when a constant offset phase is removed. The offset has no effect on the derivative of the phase, and removing it does not affect the measured thermal diffusivity.

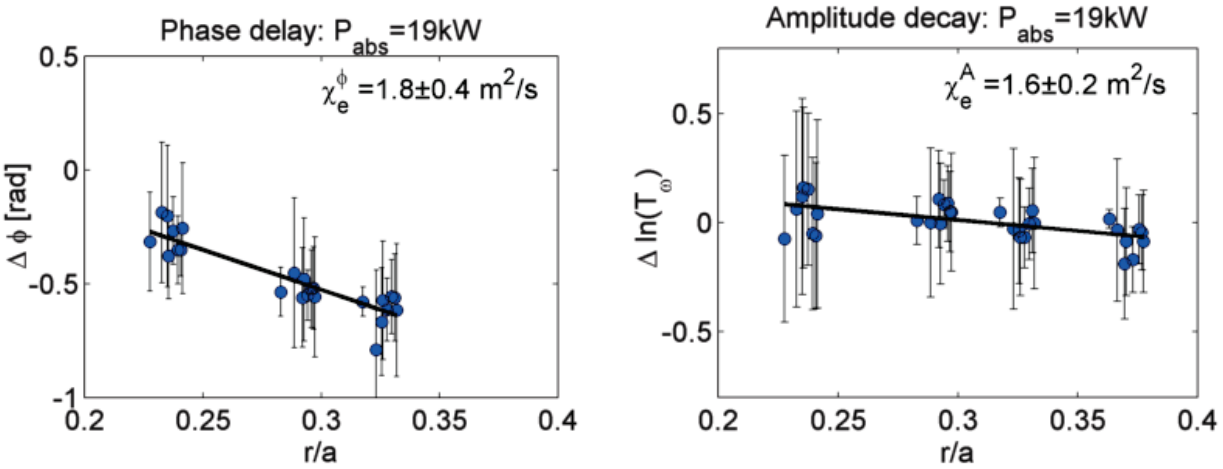

(a) Cross-phase.

(b) Logarithmic Amplitude.

Figure 5.9: Phase delay (a) and amplitude decay (b) of heat pulses during an ECRH modulation experiment with 66 kW of launched power (with offsets removed).

In Figure 5.9, linear fits are used to determine the derivative of the phase and the derivative of the logarithmic amplitude after offset removal. Between $0.20 < r/a < 0.35$, the thermal diffusivity from the phase is $\chi_e^{\varphi} = 1.8 \pm 0.4$ m^2/s, and the thermal diffusivity from the amplitude is $\chi_e^{A} = 1.6 \pm 0.2$ m^2/s. The diffusivity from the amplitude shows good agreement with the diffusivity from the phase, and this indicates that 500 Hz is high enough frequency to estimate the heat pulse diffusivity from either measurement with 66 kW of

launched power. The resulting heat pulse electron thermal diffusivity is $\chi_e^{HP} = 1.7 \pm 0.2$ m^2/s. These results are discussed further in Chapter 6.

5.3.3.1 Systematic Uncertainty due to Low Optical Depth

During modulation experiments in optically thin plasmas, the electron cyclotron emission diagnostic observes both temperature and density perturbations as a consequence of the finite optical depth. For modulation experiments neglecting density perturbations, the minimum optical depth for observation of temperature modulations accepting a 15% relative error in $\delta T_e/T_e$ is $\tau > 1.0$ for a vacuum vessel wall reflectivity of 0.8 and $\tau > 3.0$ for zero reflectivity [106].

The maximum allowable density perturbation to keep the systematic error in interpreting $\delta T_r/T_r$ as $\delta T_e/T_e$ below 15% is shown as a function of the optical depth and reflectivity in Figure 5.10. The requirement for interpreting absolute intensity perturbations as temperature perturbations is less stringent than the requirement for the relative temperature perturbation, which extends the applicability of heat pulse propagation experiments to lower optical depths. Density perturbations limit the applicability of the ECE as a diagnostic for electron temperature perturbations to regions where the density perturbation is approximately less than 5%. Local density measurements are unavailable on HSX, so the interferometer is used to estimate the level of density perturbations during modulation experiments. With 85 kW of launched power the observed density perturbation is 1.2% at the ECRH modulation frequency and 2.3% at the neutral gas puffer frequency.

The measurement of interest in heat pulse propagation experiments is the perturbed electron temperature, δT_e, and the requirement for interpreting the perturbed radiation temperature,δT_{re}, as the perturbed electron temperature is less stringent than that for interpreting the average radiation temperature as the electron temperature. This is also true

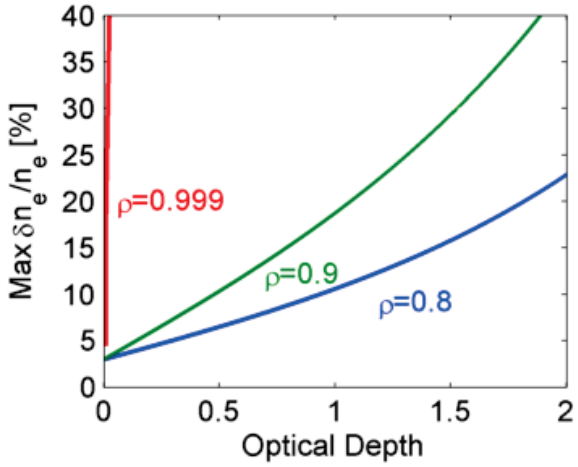

Figure 5.10: Maximum acceptable density perturbation to keep the systematic error less than 10% while interpreting $\delta T_{re}/T_{re}$ as $\delta T_e/T_e$ as a function of optical depth and reflectivity (assuming 15% $\delta T_e/T_e$).

for interpreting the relative perturbation in radiation temperature, $\delta T_{re}/T_{re}$ as a relative perturbation in electron temperature, $\delta T_e/T_e$. Reference [106] showed that the systematic error in interpreting $\delta T_{r,e}$ as δT_e was below 15% for an optical depth greater than 0.7 with a wall reflectivity of 0.8. Accepting a 10% systematic error, this limit drops to 0.3 with a wall reflectivity of 0.9, and the limit drops to very small optical depths for a wall reflectivity of $\rho = 0.999$. The disadvantage of high reflectivity walls is that without a viewing dump, multi-pass emission generally leads to spatial averaging.

Spatial averaging over the resonance would modify the ECRH absorption in a similar way that it modifies the ECE measurement, and would lead to a broad power deposition profile if it were significant. Additionally, a measurement of the absorption profile using the ECE diagnostic would also be modified by spatial averaging and appear broad. The absorption profile measured using the ECE during ECRH turn-off is presented in Section 4.2.2. The measured absorption is narrow and agrees with calculations of the multi-pass absorption, indicating that the spatial averaging effect is not significant in HSX at high

density. As is shown in Section 5.3.2, Section 5.3.4, and Chapter 6, measurable changes in the perturbation amplitude and phase between closely spaced ECE channels are observed in heat pulse propagation experiments on HSX.

For the data shown in this work, the optical depth is greater than 0.3, unless the signal-to-noise ratio and coherence in the data are high and the low-optical depth channels follow the same trend as the high-optical depth channels. The more significant limitation on the range of heat pulse propagation experiments in HSX is the non-monotonic phase feature that occurs for $r/a > 0.35$.

5.3.3.2 Non-Monotonic Features in the Amplitude and Phase Measurements

The amplitude-decay and time-delay (or equivalently the phase delay) in Figure 5.6 is non-monotonic. The non-monotonic phase feature has also been observed on TJ-II [64] and on W7-AS [51] during ECRH modulation experiments and has not been completely explained. An ECRH driven flux of fast trapped particles was invoked to explain the non-monotonic phase profile on TJ-II, and down-shifted emission from fast particles located in the ECRH resonance was used to explain the non-monotonic phase profile in W7-AS.

One possibility for the non-monotonic phase profile in HSX is out-gassing from the wall due to incomplete first-pass absorption of the launched ECRH, seeding cold pulses at the edge. Another source of cold pulses in HSX is from the neutral gas puffer. To decrease the possible impact of cold pulses generated by the neutral gas puffer, the frequency of the fueling puffer was increased from a value close to the ECRH modulation frequency, 650 Hz, up to 1111 Hz; however, no change in the non-monotonic phase feature was observed during heat pulse propagation experiments.

Finally, the non-monotonic phase profile may also be due to the presence of an internal transport barrier. Experiments on the JET tokamak [68] showed that the propagation of heat pulses was strongly affected by the presence of an Internal Transport Barrier (ITB). Heat pulses sourced from either side of the barrier in JET were strongly damped, and the electron thermal diffusivity was significantly reduced within the ITB layer. Experiments with two modulated electron heating sources (one inside and one outside of the ITB layer) showed that the amplitude of the heat wave was strongly damped within the ITB layer, and that the phase measured on either side of the ITB layer was discontinuous [68]. As discussed in Section 5.4, it is possible that an electron internal transport barrier exists in the region of heat pulse propagation experiments, and further studies are proposed in Section 7.2.4.

Simulations of the coupling between plasma density and temperature transport with ECRH modulation were performed at W7-AS with the coupling of temperature perturbations into the particle flux up to 20% of the thermal diffusivity, $D_{1,2} = 0.2\chi_e$. These simulations determine that the highest coupling coefficient yielded a maximum relative density perturbation of 1% for this experiment and generated a maximum error of 10% in the measurement of the thermal diffusivity. The measured perturbation to the line-integrated electron density from the interferometer measurement was 2% [51].

During heat pulse propagation experiments on HSX, the perturbation to the central chord of the interferometer at the ECRH modulation frequency was measured to be 1.2%. The measured perturbation to the central chord of the interferometer is smaller on HSX than that measured on W7-AS, and a systematic error of 10% in the measurement of the thermal diffusivity is acceptable for this work.

5.3.3.3 Damping Terms in the Heat Transport Equation

In the cylindrical heat equation, the terms that are proportional to the perturbed electron temperature are not accounted for in the analysis of heat pulse propagation experiments [105] (see Equation B.4 for a general heat equation in a plasma). Damping terms cause χ_e^A to under-predict and χ_e^φ to over-predict the thermal diffusivity [105]. This effect cancels in the geometric mean so that the incremental thermal diffusivity is more accurately determined by $\chi_e^{HP} = \sqrt{\chi_e^\varphi \chi_e^A}$. Some unavoidable terms that contribute to damping in magnetically confined plasma are inhomogeneities in the thermal diffusivity and density profiles [29], but other terms, such as electron-ion drag and neutral ionization, can also contribute.

As the modulation frequency increases and the separation in time-scales between damping and modulation increases, the effect of damping becomes less important and both χ_e^A and χ_e^φ approach χ_e^{HP}. In this limit, either may be used to estimate the electron thermal diffusivity. This was observed in Section 5.3.2 and Section 5.3.3, where the diffusivity from the amplitude and from the phase agreed in a plasma supported by 66 kW of launched ECRH power.

Table 5.1: The thermal difusivity from the amplitude, the phase, and the total heat pulse diffusivity for three launched powers.

P_0	χ_e^A m^2/s	χ_e^φ m^2/s	χ_e^{HP} m^2/s
66 kW	1.6 ± 0.2	1.8 ± 0.4	1.7 ± 0.2
78 kW	1.4 ± 0.2	2.5 ± 1.1	1.9 ± 0.4
85 kW	0.6 ± 0.1	6.8 ± 2.6	2.1 ± 0.4

The heat pulse diffusivity, as well as the diffusivity from the amplitude and phase, are shown in Table 5.1 for the launched power scan discussed in Chapter 6. The heat pulse diffusivity does not vary significantly, but the diffusivity from the amplitude and phase are different in the 78 kW and 85 kW cases. The effective damping time necessary to drive the

difference observed in the 78 kW case is on the order of 1 ms (using formulas in Reference [105]). In the 85 kW case, the effective damping time is on the order of 150 μs.

It is unclear what is driving the divergence between the amplitude and the phase measurement. The heat pulse diffusivity measured in both cases is very similar, and in agreement with the power balance analysis. Multiple frequency measurements are used to investigate the damping, and the effect of a convective heat flux on the analysis is also dicussed in Section 5.3.4.

5.3.4 Multi-Frequency Measurements

In general, the electron heat flux contains contributions from conduction and convection. Convection affects the amplitude decay of the perturbation, but to first order has no effect on the phase, leading to a decay length that is asymmetric. The decay length is longer in the direction of convection and shorter in the opposite direction. As the frequency of the perturbation increases the decay length of the perturbation decreases, so that the contributions from conduction and convection can be separated using multiple frequency measurements [105], if a difference is measured.

Table 5.2: The heat pulse diffusivity determined during a modulation frequency scan with 78 kW of launched power.

f_{mod}	χ_e^A m^2/s	χ_e^φ m^2/s	χ_e^{HP} m^2/s
200 Hz	0.4 ± 0.1	5.3 ± 2.8	1.5 ± 0.4
500 Hz	1.4 ± 0.2	2.5 ± 1.1	1.9 ± 0.4
1000 Hz	1.9 ± 0.7	1.1 ± 0.5	1.5 ± 0.4

A modulation frequency scan is summarized in Table 5.2. There is not a measurable difference in the heat pulse thermal diffusivity, and no convective heat transport is measured

in the range that heat pulse propagation data is available $0.2 \leq r/a \leq 0.4$ during this experiment. This is consistent with measurements presented in Section 5.3.2 in which the heat pulse electron thermal diffusivity agreed with the power balance electron thermal diffusivity.

5.4 Heat Pulse Propagation and Low Stiffness with Methane

Peaked electron temperature profiles with core temperatures of up to 2.5 KeV have been measured in with 100 kW of launched power in the QHS configuration when plasmas were formed with methane (CH4) fueling. An electron internal transport barrier (eITB) has been invoked to explain the strong increase in electron temperature in these profiles [13]. These profiles have a large temperature gradient between $0.10 < r/a < 0.30$, and neoclassical modeling indicates that there is strong shear in the ambipolar radial electric field in this region. The shear results from rapid transition from edge ion root confinement to core electron root confinement and is thought to drive strong flow shear, which has been observed to stabilize trapped electron mode turbulence, and lead to an eITB [4].

Thomson scattering measurements of the electron temperature and density during an ECRH modulation experiment in methane plasmas supported by 85 kW of launched power are shown in Figure 5.11a. The absorption profile calculated using the multi-pass ray tracing model and the power balance electron thermal diffusivity are shown in Figure 5.11b, and the heat pulse amplitude decay and phase delay are shown in Figure 5.11c and Figure 5.11d respectively.

The volume average power balance diffusivity in the region between $0.2 \leq r/a \leq 0.4$ is $\chi_e^{PB} = 1.7 \pm 0.2$ m^2/s, and the heat pulse diffusivity measured in this region is $\chi_e^{HP} = \sqrt{\chi_e^A \chi_e^\phi} = 0.7 \pm 0.2$ m^2/s. The resulting stiffness in the electron heat flux is $S = \chi_e^{HP}/\chi_e^{PB} = 0.4 \pm 0.1$, which is indicative of an eITB. These results are consistent with the neoclassical eITB predicted in [4], and they are also consistent with the ITB studies on JET [68] referenced

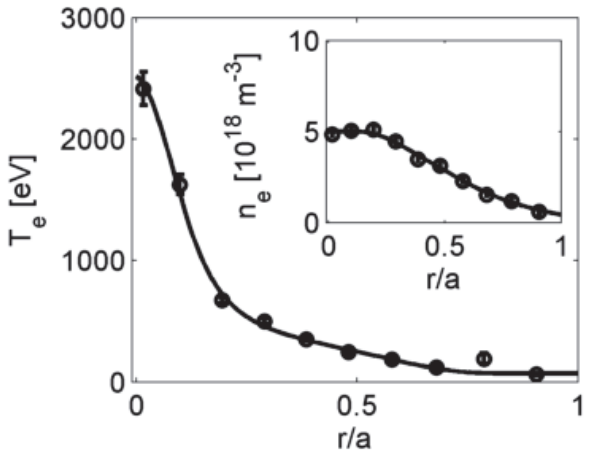

(a) Electron temperature and plasma density.

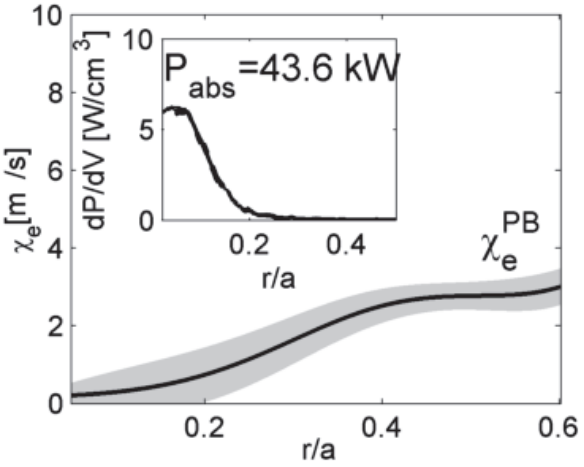

(b) Power balance analysis.

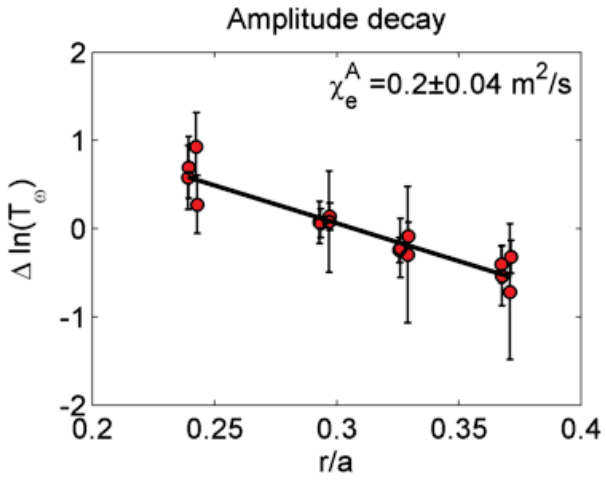

(c) Heat pulse amplitude decay.

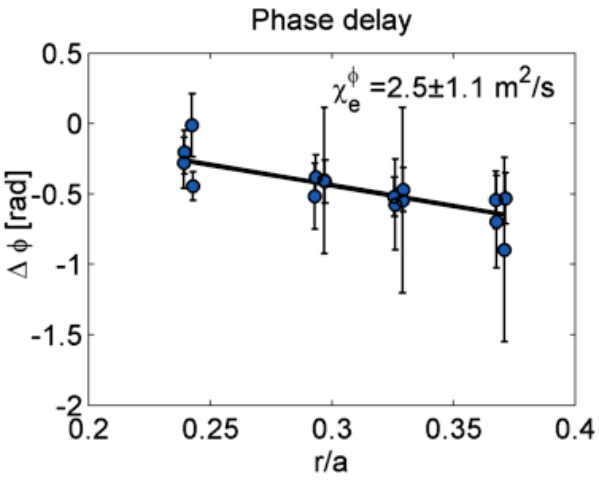

(d) Heat pulse phase delay.

Figure 5.11: Electron temperature and plasma density (a), the multi-pass power deposition profile and power balance electron thermal diffusivity (b), the heat pulse amplitude decay (c), and the heat pulse phase delay (d) from an ECRH modulation experiment in a methane plasma.

in Section 5.3.3.2. Core radial electric field measurements are necessary to confirm the existence of an eITB and additional measurements are proposed as future work in Section 7.2.4.

5.5 Summary

Power balance analysis is used to characterize the steady-state electron heat transport, and a least squares analysis is used to determine the effective thermal diffusivity of the electrons in HSX. This quantity is compared to the electron thermal diffusivity determined from heat pulse propagation experiments to yield the stiffness in the electron heat flux and the convective heat velocity. The heat pulse diffusivity is inferred using a frequency domain analysis based on measurements of the amplitude and phase of electron temperature perturbations from the ECE diagnostic. Low first-pass optical depth can lead to large systematic errors in heat pulse propagation experiments; however, with high wall reflectivities the systematic error is small. The effective wall reflectivity to the ECE diagnostic is between 0.9-1, and this sets a condition for the optical depth, $\tau > 0.3$, to keep the systematic error below 10%. The measured amplitude and phase are reproducible, and the results from several plasma discharges are combined to increase the spatial resolution of the diagnostic. There is a non-monotonic feature in the heat pulse propagation that limits the region of analysis; however, a numerical solution indicates that the amplitude and the phase of the heat pulses are self-consistent. This analysis also yields a heat pulse diffusivity that is consistent with the power balance value within $r/a \leq 0.4$. This indicates that the transport is diffusive in this region, it has little to no convective component, and that the stiffness in the core of the plasma is $\chi_e^{HP}/\chi_e^{PB} \approx 1$. Multi-frequency heat pulse measurements of the thermal diffusivity also indicate a lack of convective transport. Peaked electron temperatures of up to 2.5 keV have been measured in methane plasma, and heat pulse propagation experiments have measured low stiffness between $0.2 \leq r/a \leq 0.4$; $\chi_e^{HP}/\chi_e^{PB} = 0.4 \pm 0.1$, where the heat pulses are strongly damped. A neoclassical electron internal transport barrier has been

previously predicted to exist in the core of the plasma [5], and the measured stiffness and strong damping of heat pulses are consistent with a transport barrier [68].

Bibliography

4. Lore, J., Guttenfelder, W., Briesemeister, A., *et al. Phys. Plasmas* **17,** 056101 (2010).
5. Guttenfelder, W., Lore, J., Anderson, D. T., *et al. Phys. Rev. Lett.* **101,** 215002 (2008).
13. Lore, J. PhD thesis (The University of Wisconsin - Madison, United States, 2010).
29. Mantica, P. & Ryter, F. *Comptes Rendus Physique* **7,** 634–649.
44. Wagner, F. & Stroth, U. *Plasma Phys. Control. Fusion* **35,** 1321–1371 (1993).
51. Giannone, L., Erckmann, V., Gasparino, U., *et al. Nucl. Fusion* **32,** 1985–2000 (1992).
52. Cardozo, N. J. L. *Plasma Phys. Control. Fusion* **37,** 799–852 (1995).
64. Eguilior, S., Castejon, F., De la Luna, E., *et al. Plasma Phys. Control. Fusion* **45,** 105–120 (2003).
68. Mantica, P., Van Eester, D., Garbet, X., *et al. Phys. Rev. Lett.* **96,** 095002 (2006).
99. Heifetz, D., Post, D., Petravic, M., *et al. Journal of Computational Physics* **46,** 309–327 (1982).
100. Canik, J. PhD thesis (The University of Wisconsin - Madison, United States, 2007).
101. Boivin, R. L., Goetz, J. A., Marmar, E. S., *et al. Rev. Sci. Instrum.* **70,** 260–264 (1999).
102. Callen, J. D. (*NEEP/Physics/ECE 725 notes*, U of Wisconsin-Madison, 1989).
103. Fredrickson, E. D., Callen, J. D., McGuire, K., *et al. Nucl. Fusion* **26,** 849 (1986).
104. Carslaw, H. S. & Jager, J. C. (*Conduction of Heat in Solids*, Oxford: Oxford Science Publications, 1959).
105. Jacchia, A., Mantica, P., Luca, F. D., *et al. Phys. Fluids B* **3,** 3033–40 (1991).
106. Peters, M., Gorini, G. & Mantica, P. *Nucl. Fusion* **35,** 873–875 (1995).

Chapter 6

Stiffness Measurements and Comparisons to Gyrokinetic Simulations

It has been observed in tokamaks that temperature profiles are resilient to changes in the heating deposition profile, i.e. large changes in the electron heat flux lead to only small changes in the electron temperature gradient [48]. This effect has not been observed in conventional stellarators. In W7-AS, it has been shown that the electron temperature profile can vary over a broad range with different heating methods, deposition profiles and confinement regimes [107]. The ratio of the electron thermal diffusivity from transient heat transport experiments to the steady-state diffusivity from power balance is a measure of the stiffness in the electron heat flux. In tokamaks with profile resiliency, the thermal diffusivity obtained from heat pulse propagation is typically much larger than the thermal diffusivity from steady state power balance. In contrast, experiments in LHD [58], W7-AS [108] and TJ-II [64] have shown that heat pulse and power balance diffusivities are comparable.

Electron heat transport experiments in tokamaks have been compared to gyrokinetic calculations [47]. This chapter reports the first comparisons between non-linear gyrokinetic calculations and experimental measurements in a stellarator. The saturated electron heat flux driven by the Trapped Electron Mode (TEM) and the Electron Temperature Gradient (ETG) mode are compared to the experimental electron heat flux.

These experiments were performed in the Helically Symmetric eXperiment [30] (HSX), which has a direction of symmetry in the magnetic field strength along the helical direction. Previous experimental results have shown that the neoclassical transport is reduced so that the electron heat diffusivity is dominated by anomalous transport [3]. The low neoclassical transport in HSX allows for a study of profile resiliency and stiffness in the electron heat flux in an optimized stellarator.

Experimental measurements of the electron heat flux are introduced in Section 6.1, and linear and non-linear gyrokinetic calculations are compared to these measurements in Section 6.2.

6.1 Electron Heat Transport Measurements

The steady state thermal diffusivity is the ratio of the normalized heat flux with respect to temperature gradient, $\chi_e^{PB} = -q_e/(n_e \nabla T_e)$, while the transient diffusivity is a measure of the local gradient of the heat flux with respect to temperature gradient, $\chi_e^{HP} = -\partial q_e/(n_e \partial \nabla T_e)$ [109]. The stiffness in the electron heat flux is parametrized by the logarithmic gradient of the heat flux with respect to the temperature gradient. The stiffness is experimentally quantified by the ratio of thermal diffusivities measured using transient and steady-state techniques, $\partial(\ln q_e)/\partial(\ln \nabla T_e) = \chi_e^{HP}/\chi_e^{PB}$ [27]. Steady-state and transient transport analysis techniques are used concurrently to determine the experimental stiffness in the electron heat flux and to investigate anomalous heat transport in HSX.

To measure the stiffness, two sets of Electron Cyclotron Resonance Heating (ECRH) experiments have been conducted. In the first experiment, the ECRH resonance location was moved across the plasma minor radius to change the temperature gradient in the region between $0.2 \leq r/a \leq 0.4$. In the second experiment, the launched ECRH power was modulated

with on-axis heating to facilitate measurements of the transient electron thermal diffusivity in the same region. The plasma density profiles were matched between both experiments.

Figure 6.1 shows the electron temperature and plasma density measured by a 10 spatial channel Thomson scattering diagnostic during the ECRH resonance scan. The resonance location was moved from $r/a = 0.3$ on the inboard side of the plasma to $r/a = 0.2$ on the outboard side of the plasma by changing the on-axis magnetic field from $|B_o| = 0.96$T to $|B_o| = 1.02$T. The core electron temperature measured by Thomson scattering varied between 400 and 1200 eV. Three of the electron temperature profiles are shown in color for easy comparison with the absorbed power profiles shown in Figure 6.2.

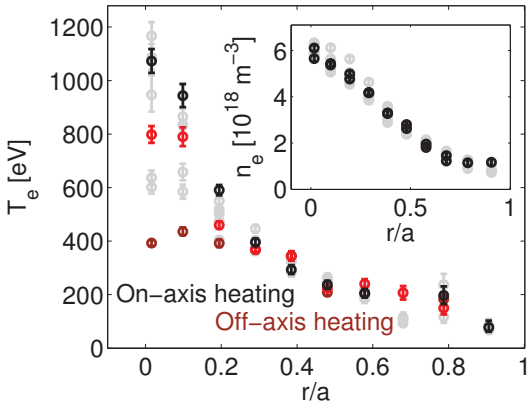

Figure 6.1: Eight Thomson scattering profiles of the electron temperature and plasma density measured during an ECRH resonance scan (gray). Heating on-axis ($r/a \approx 0$, Black), off-axis ($r/a \approx 0.3$, brown), and an intermediate point ($r/a \approx 0.1$, red).

Two ECRH antennas are used on HSX. Measurements with on-axis heating, discussed in Chapter 4, show that the absorption of the ordinary wave is localized within $r/a \leq 0.2$ for both ECRH antennas. The profile shape and total absorption are reproduced by a multi-pass ray tracing model using the TRAVIS code [89] in Section 4.2.2. The absorbed power profile for each of the cases in Figure 6.1 are shown in Figure 6.2. As the cyclotron

resonance is moved away from the magnetic axis, the electron temperature becomes less peaked and flattens inside the radius of the peak absorption. The temperature gradient within $0.2 \leq r/a \leq 0.4$ decreases with off-axis heating, while the volume average electron temperature across this region varies by less than 100 eV.

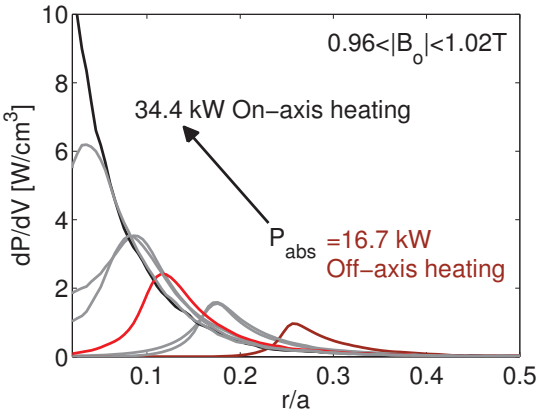

Figure 6.2: Multi-pass ray tracing calculations of the absorbed power profile from an ECRH resonance scan (gray) shown in Figure 6.1. Heating on-axis ($r/a \approx 0$, black), off-axis ($r/a \approx 0.3$, brown), and an intermediate point ($r/a \approx 0.1$, red).

There are no significant electron energy sinks in the region of the plasma considered during these experiments. The total radiated power is less than 5 kW and is localized to the outer half-radius, and the collisional coupling to ions is small, because the plasma density in HSX is limited by the cut-off density of the ordinary wave, $1 \times 10^{19}\text{m}^{-3}$. Consequently, the experimental heat flux is estimated by the integrated energy deposition during the ECRH.

During the ECRH modulation experiment, the power launched from the first antenna was scanned from 25 to 50 kW, while the power launched from the second antenna was held at 50 kW and modulated by 10%. This range of powers correspond to the power scan introduced in Section 3.5. The power deposition profile shape did not change during this second experiment, but the total absorbed power increased with the launched ECRH

power. The volume average heat flux over the region that heat pulse propagation data is available, $0.2 \leq r/a \leq 0.4$ (the foot of the steep electron temperature gradient region), is plotted as a function of electron temperature gradient scale length, $a/L_{Te} = -a\nabla T_e/T_e$, for both experiments in Figure 6.3. The heat flux scales linearly with temperature gradient between $1.8 \leq a/L_{Te} \leq 3$, and the average density gradient scale length was held constant at $a/L_{ne} = 2.5 \pm 0.1$ in both experiments.

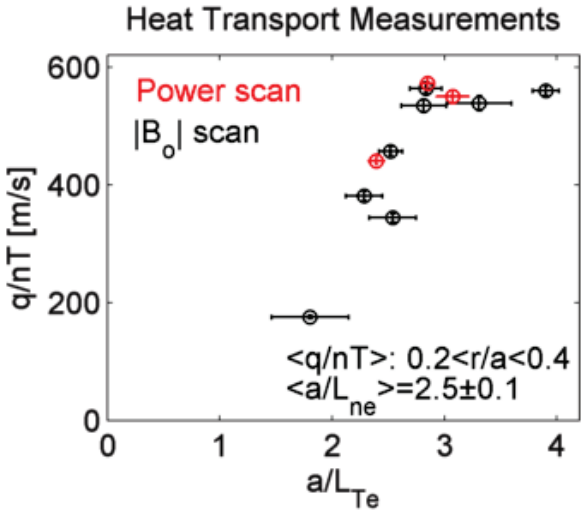

Figure 6.3: Volume average normalized heat flux versus temperature gradient scale length between $0.2 \leq r/a \leq 0.4$ in ECRH power and resonance location scans.

The power balance thermal diffusivity is determined through a non-linear least-squares fit to the electron temperature measured by Thomson scattering, by using χ_e^{PB} as the fitting parameter. The power balance analysis is described in Section 5.2. The electron temperature and density profiles measured by Thomson scattering for on-axis heating during the ECRH modulation experiment are shown in Figure 6.4, along with the fits that result from the power balance analysis. The core electron temperature increases from 600 eV to 1200 eV as the absorbed power is increased from 19 kW to 34 kW.

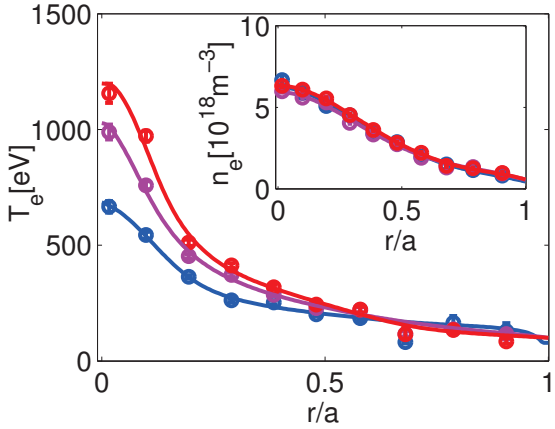

Figure 6.4: Electron temperature and density profiles measured by Thomson scattering for on-axis heating at three absorbed powers: 19 kW (blue), 29 kW (magenta), and 34 kW (red). The lines are the fits that result from power balance analysis.

The χ_e^{PB} profiles corresponding to the fits of Figure 6.4 are shown in Figure 6.5. The power balance thermal diffusivities between $0.2 \leq r/a \leq 0.4$ are similar and the volume average diffusivity across this region is tabulated versus absorbed power in Table 6.1. The uncertainty in the power balance diffusivity is determined through a Monte Carlo calculation by varying the plasma density and temperature within their experimental uncertainties, and varying the analytic form of the trial diffusivity. Within $r/a \leq 0.4$, the thermal diffusivity profile is almost the same, which indicates that of electron heat transport is not stiff.

Heat pulse propagation measurements of the transient electron thermal diffusivity require a high resolution electron temperature diagnostic. The temporal evolution of the electron temperature is measured using an absolutely calibrated Electron Cyclotron Emission (ECE) diagnostic that is described in Chapter 3. Although the Low Field Side (LFS) and the High Field Side (HFS) channels are symmetric across the plasma, and in good agreement with Thomson scattering measurements of the electron temperature at moderate heating powers, the LFS channels sample relativistically down-shifted emission from the core in the

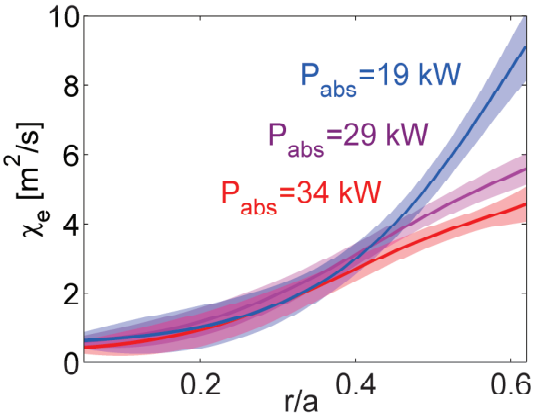

Figure 6.5: Electron thermal diffusivity from a power balance analysis for on-axis heating at three absorbed powers: 19 kW (blue), 29 kW (magenta), and 34 kW (red).

hot plasma analyzed in this work. Consequently, only the HFS channels are used in heat pulse propagation experiments.

The temporal response of the electron temperature to modulated heating carries heat transport information at the modulation frequency in the amplitude, T_ω, and phase, φ_ω, between radially separated channels of the ECE radiometer. The heat pulse thermal diffusivity is determined using methods that are described in detail in Section 5.3 from the logarithmic amplitude and the phase in cylindrical geometry through

$$\chi_e^{HP} = -\frac{3}{4}\frac{\omega_{mod}}{\langle|\nabla\rho|^2\rangle}\left[\frac{d\varphi_\omega}{d\rho}\left(\frac{d\ln T_\omega}{d\rho}+\frac{1}{2\rho}+\frac{1}{2}\frac{d\ln n_e}{d\rho}\right)\right]^{-1}. \tag{6.1}$$

Equation 6.1 is the cylindrical model from [105] with the radial coordinate replaced by the effective radius and the heat pulse diffusivity replaced by the effective heat pulse diffusivity, $\langle|\nabla\rho|^2\,\chi_e^{HP}\rangle \approx \chi_e^{HP}\langle|\nabla\rho|^2\rangle$. Equation 6.1 is derived in Appendix B, and is discussed in Section 5.3.1. The logarithmic amplitude and phase of the electron temperature perturbation are determined from Fourier analysis of the pulse propagation at the modulation frequency, ω_{mod}, and the background density gradient scale length from Thomson scattering measurements of the electron density profile.

The phase of the radially separated ECE channels is measured with respect to the ECRH modulation reference signal. The ECE channels used to determine the amplitude and phase of the heat wave have high coherence with the reference. The ECE data is shown in Figure 6.6. The inner limit for the analysis region is set by the radial extent of the modulated source calculated from ray tracing, $r/a \geq 0.2$ (Chapter 4), and a requirement on the systematic error from low optical depth, $\tau > 0.3$, and a non-monotonic feature in the phase, set the outer limit for the analysis region, $r/a \leq 0.4$ (Chapter 5).

Multiple shots with similar parameters are combined to increase the spatial resolution of heat pulse propagation experiments; however, the perturbation amplitude and phase are offset by a small amount between shots. The heat pulse diffusivity is dependent on the radial derivative of these quantities, which is independent of the offset. The amplitude and phase used in the analysis and shown in Figure 6.6 have the offset removed.

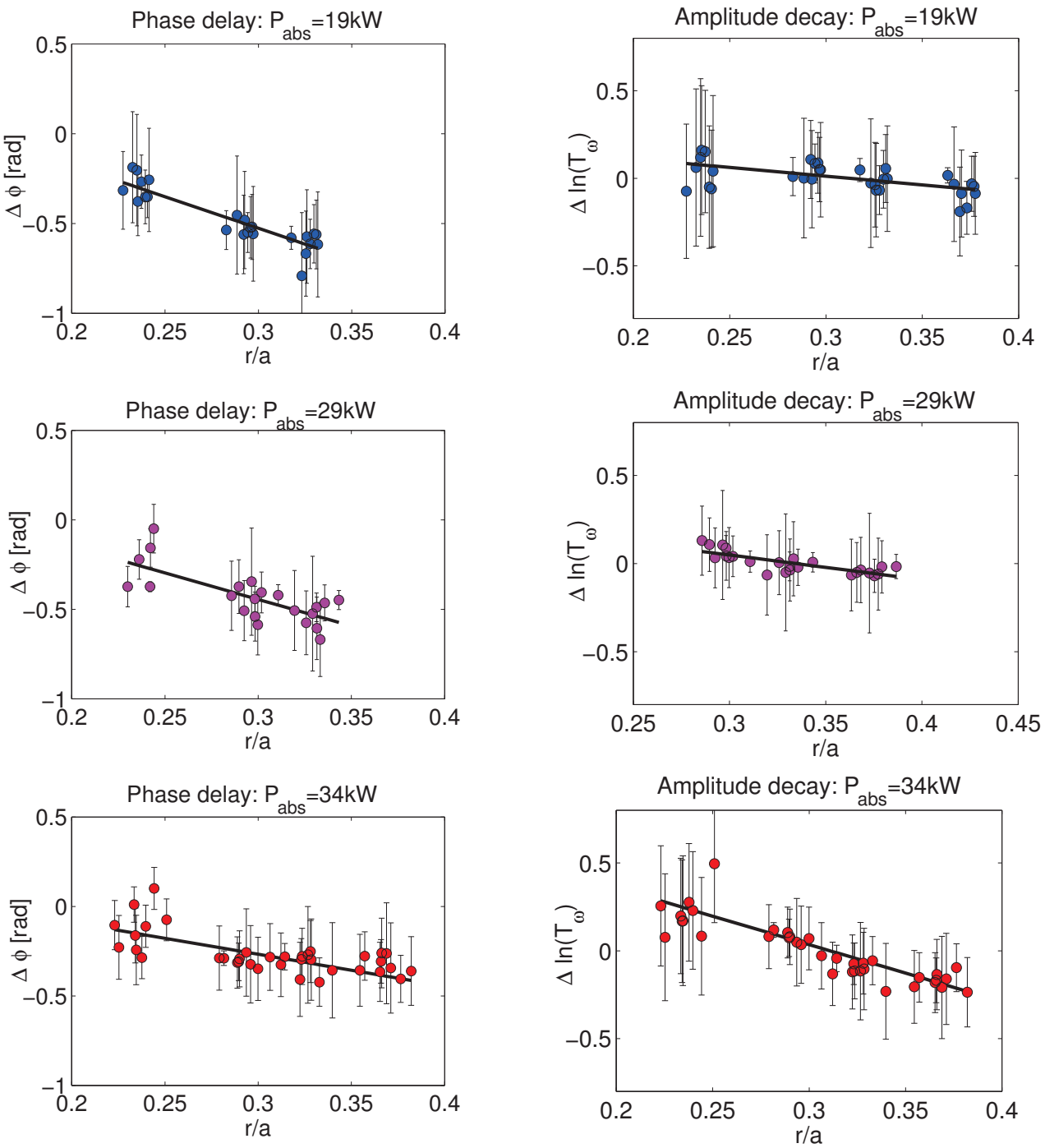

Figure 6.6: Phase delay (left column) and logarithmic amplitude (right column) at the ECRH modulation frequency for three heat pulse propagation experiments with different absorbed powers: 19 kW (1st row), 29 kW (2nd row), and 34 kW (3rd row).

The derivative of the fits in Figure 6.6 are used in Equation 6.1 to determine the heat pulse diffusivities shown in Table 6.1. The stiffness is approximately unity for all three powers.

Table 6.1: Power-balance and heat-pulse diffusivities, and the resulting stiffness, are tabulated versus absorbed power.

P_{abs}	χ_e^{PB}	χ_e^{HP}	χ_e^{HP}/χ_e^{PB}
19 kW	2.3 ± 0.1	1.7 ± 0.2	0.7 ± 0.1
29 kW	2.1 ± 0.1	1.9 ± 0.4	0.9 ± 0.2
34 kW	1.9 ± 0.1	2.1 ± 0.4	1.1 ± 0.2

6.2 Comparison to Gyrokinetic Calculations

HSX is optimized for neoclassical transport, but HSX is not optimized for anomalous transport driven by turbulent microinstabilities. The non-planar magnetic axis and high effective transform of HSX lead to large normal curvature and short connection lengths in comparison to other stellarators like LHD [110]. The regions of bad normal curvature and particle trapping are highly correlated, and previous linear gyrokinetic modeling has indicated that the Trapped Electron Mode (TEM) is highly localized in the bad curvature region of HSX [5]. Combined with temperature or density gradients, there is strong drive for curvature driven modes such as the TEM [8].

The gyrokinetic calculations presented in this section were performed by Benjamin Faber, for comparison with this experimental work. Figure 6.7 shows the normal curvature and magnetic field strength in normalized units as a function of helical angle for the most and least unstable flux tubes in HSX (each flux tube samples a full field period of the device). The most unstable flux tube samples the region of low magnetic field strength at the outboard

mid-plane of HSX. The least unstable flux tube samples the region of low magnetic field strength on the inboard side of the device. In both flux tubes, the regions of bad normal curvature and particle trapping overlap significantly.

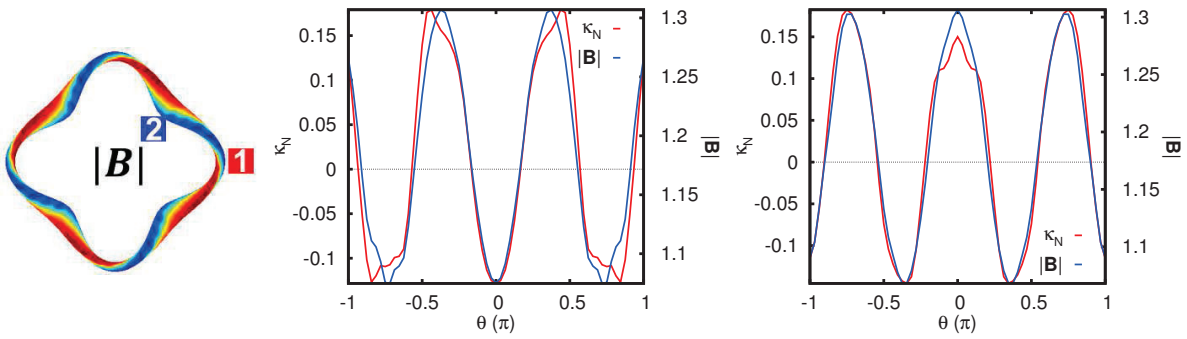

Figure 6.7: Normal curvature and magnetic field strength (normalized units) for the most (1, left) and least (2, right) unstable flux-tubes in HSX as a function of helical angle. A plan view of the magnetic field strength (high field in red, low field in blue) at the half-radius is also shown.

The Gyrokinetic Electromagnetic Numerical Experiment (GENE) [111] is used to model micro-instabilities in HSX. GENE solves the Vlasov-Maxwell system of equations for the change in the perturbed distribution function due to gyro-radius scale instabilities. Simulations of micro-instabilities on HSX are collisionless, electrostatic ($\beta \ll 1$) calculations in the three-dimensional flux-tube geometry calculated by the GIST code [112]. The TEM is simulated using kinetic electrons and ions, while the Electron Temperature Gradient (ETG) mode is simulated using kinetic electrons and adiabatic ions.

Linear gyrokinetic calculations at TEM and ETG scales indicate that the TEM is linearly unstable for all accessible parameters in HSX. For a density gradient scale length of $a/L_{ne} = 1.5$ and the experimental temperature gradients, the ETG mode is unstable. At the higher density gradient scale length, $a/L_{ne} = 2.5$, the TEM is only weakly dependent on the

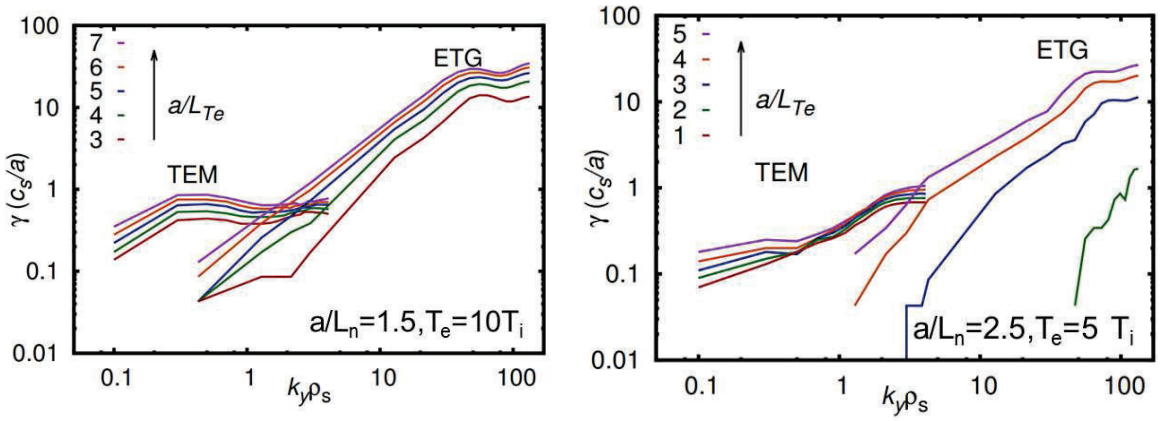

Figure 6.8: Linear growth rates of the TEM and the ETG mode versus normalized wave number in the most unstable flux tube at low (left) and high (right) density gradient scale length.

temperature gradient, and is primarily driven by the density gradient. In this case, the ETG mode is stabilized by the increased density gradient and a linear critical gradient exists between $0.4 \leq \eta_{e,c} \leq 0.8$, where $\eta_e = L_{ne}/L_{Te}$. HSX has very low magnetic shear, and this calculation is consistent with previous estimates of the critical gradient for ETG modes in a shearless slab, $\eta_{e,c} = 2/3$ [38].

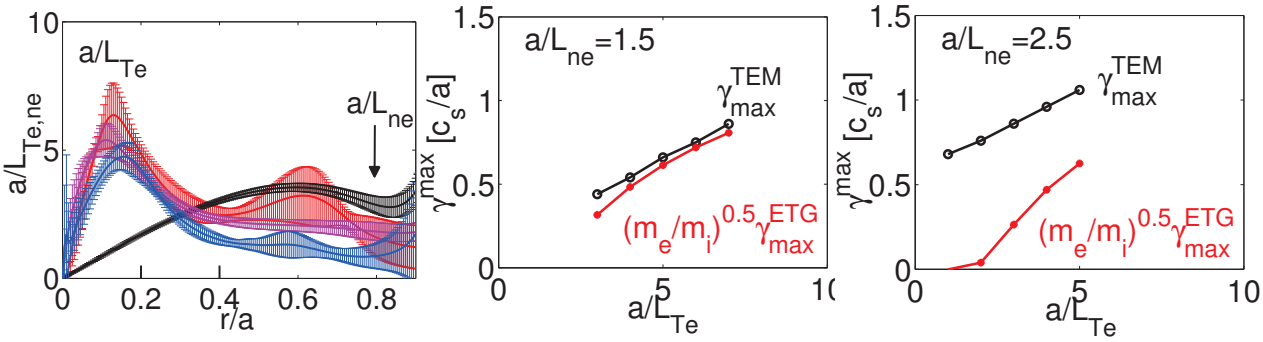

Figure 6.9: Experimental density (black) and temperature gradients at three launched powers: 19 kW (blue), 29 kW (purple), 34 kW (red). The growth rate of the TEM and ETG modes at the maximum quasi-linear heat flux for $a/L_{ne} = 1.5$ (middle), and $a/L_{ne} = 2.5$ (right).

At left in Figure 6.9 are the experimental temperature and density gradient scale lengths for the three heat pulse propagation experiments described in Section 6.1. The temperature is peaked in the core, and the temperature gradient scale length increases with heating power. From quasi-linear estimates, the ETG mode is expected to drive significant transport in nonlinear simulations when the ratio of the ETG to TEM growth rate in linear simulations is comparable to the separation in scales between the modes. This is true in the low-density gradient case ($a/L_{ne} = 1.5$), but this is not true in the high-density gradient case ($a/L_{ne} = 2.5$). The growth rates of the TEM and ETG modes at the maximum in the quasi-linear heat flux for the two density gradients are shown in Figure 6.9 versus normalized temperature gradient. In the low-density gradient case, the growth rate of the ETG mode is the square-root of the ion to electron mass ratio larger than the TEM growth rate. This case is representative of the inner 20% of the HSX minor radius, where the ETG mode may be important, and the simulated density gradient is comparable to experiment; however, this is not true at the foot of the steep electron temperature gradient region where the average density gradient scale length is $a/L_{ne} = 2.5$, and the TEM is the dominant microinstability. The high density gradient scale length case is representative of the experimental parameters in the region that heat pulse propagation data is available.

The saturated heat flux driven by the TEM is significantly higher than the saturated heat flux driven by the ETG mode in non-linear simulations of the most unstable flux tube of HSX. At left in Figure 6.10, the electron heat flux normalized by the gyro-Bohm heat flux in hybrid units, $Q_e^{GB} = n_e T_e c_s (\rho_s/a)^2$, is shown for the most and least unstable flux tubes in HSX. At right in Figure 6.10, the saturated electron heat flux driven by the ETG mode is shown in electron units, $Q_e^{GB} = n_e T_e c_e (\rho_e/a)^2$. To change the heat flux driven by the ETG mode into hybrid units, the ETG result should be divided by the square root of the mass

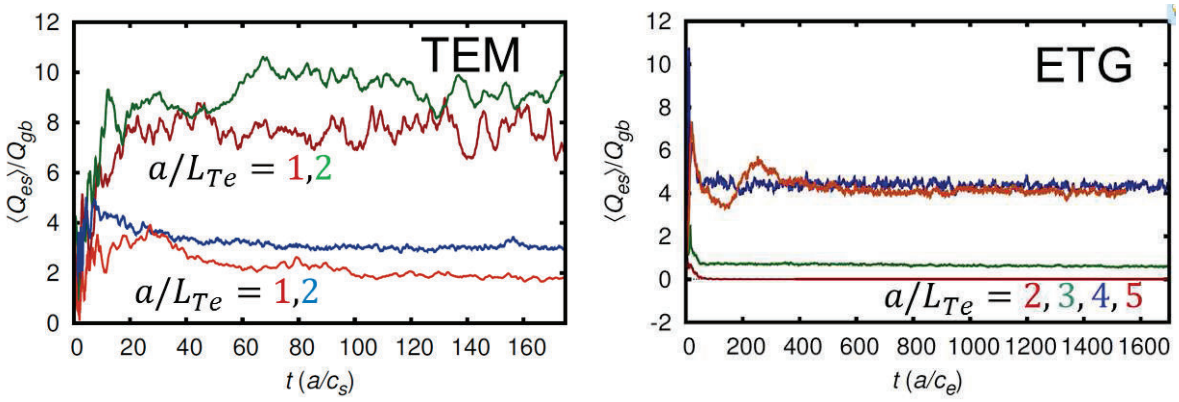

Figure 6.10: Non-linear simulations of the electron heat flux driven by the TEM in two flux tubes at two temperature gradients (left), and non-linear simulations of the electron heat flux driven by the ETG mode in the most unstable flux tube (right).

ratio. This results in significantly smaller heat flux from the ETG mode than is calculated for the TEM.

The saturated heat fluxes are compared to the experimental heat flux normalized by the gyro-Bohm heat flux (hybrid units) in Figure 6.11. In Figure 6.11, the experimental heat flux (from both the resonance and power scan) is shown in black. Although the volume average electron temperature changed by less than 100 eV in the region considered, the strong temperature scaling of the gyro-Bohm heat flux ($Q_e^{GB} \propto T_e^{5/2}$) alters the scaling of the experimental heat flux between Figure 6.3 and Figure 6.11. The non-linear ETG calculation drives a very small level of transport, but it does reproduce the critical gradient that was predicted by the linear model. The saturated heat flux driven by the TEM in both flux tubes is comparable to the experimental level.

6.3 Conclusions

The first comparisons of non-linear gyrokinetic calculations and experimental heat flux measurements are presented in the quasihelically symmetric experiment HSX. The amplitude

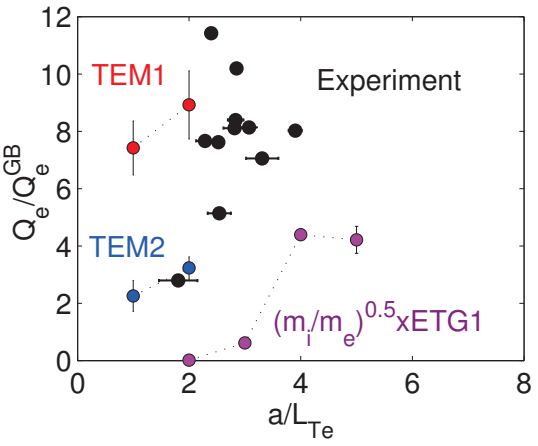

Figure 6.11: The heat flux driven by the ETG mode (scaled to hybrid units in purple) in the most unstable flux tube, and the heat flux driven by the TEM in the most (red) and least (blue) unstable flux tube are compared to the experimental heat flux in HSX (black).

and phase of the perturbation through the foot of these steep electron temperature gradient region of the plasma are used to determine a transient electron thermal diffusivity and it is equal to the steady-state diffusivity. The low stiffness between $0.2 \leq r/a \leq 0.4$ agrees with the linear scaling of the steady-state heat flux with temperature gradient in this region. These experimental results have been compared to gyrokinetic calculations (performed by Benjamin Faber for the plasma parameters from this work) using the GENE code with two kinetic species. Linear calculations demonstrate that the Trapped Electron Mode (TEM) is the dominant long-wavelength microturbulence instability across most of the HSX minor radius, and that the TEM is primarily driven by the density gradient. The saturated heat flux driven by the TEM is comparable to the experimental heat flux. Although linear simulations show that the Electron Temperature Gradient (ETG) mode may be experimentally relevant within $r/a \leq 0.2$, the saturated heat flux driven by the ETG mode in non-linear simulations is not experimentally relevant outside of this region.

Bibliography

3. Canik, J. M., Anderson, D. T., Anderson, F. S. B., *et al. Phys. Rev. Lett.* **98,** 085002 (2007).

5. Guttenfelder, W., Lore, J., Anderson, D. T., *et al. Phys. Rev. Lett.* **101,** 215002 (2008).

8. Kadomtsev, B. B. & Pogutse, O. P. *Nucl. Fusion* **11,** 67–92 (1971).

27. Stroth, U. *Plasma Phys. Control. Fusion* **40** (1998).

30. Anderson, F. S. B., Almagri, A. F., Anderson, D. T., *et al. Fusion Technol.* **27,** 273–277 (1995).

38. Horton, W., Hoang, G. T., Bourdelle, C., *et al. Phys. Plasmas* **11,** 2600–2606 (2004).

47. Ryter, F., Camenen, Y., DeBoo, J. C., *et al. Plasma Phys. Control. Fusion* **48,** B453–B463 (2006).

48. DeBoo, J. C., Petty, C. C., White, A. E., *et al. Phys. Plasmas* **19,** 082518–082518–8 (2012).

58. Inagaki, S., Takenaga, H., Ida, K., *et al. Nucl. Fusion* **46,** 133–141 (2006).

64. Eguilior, S., Castejon, F., De la Luna, E., *et al. Plasma Phys. Control. Fusion* **45,** 105–120 (2003).

89. Marushchenko, N. B., Erckmann, V., Hartfuss, H. J., *et al. J. Plasma Fus. Res.* **2,** S1129–S1129 (2007).

105. Jacchia, A., Mantica, P., Luca, F. D., *et al. Phys. Fluids B* **3,** 3033–40 (1991).

107. Wagner, F., Hirsch, M., Hartfuss, H. J., *et al. Plasma Phys. Control. Fusion* **48,** A217 (2006).

108. Hirsch, M., Baldzuhn, J., Beidler, C., *et al. Plasma Phys. Control. Fusion* **50,** 053001 (2008).

109. Ryter, F., Angioni, C., Beurskens, M., *et al. Plasma Phys. Control. Fusion* **43,** A323 (2001).

110. Rewoldt, G., Ku, L. P. & Tang, W. M. *Phys. Plasmas* **12,** 102512–102512–10 (2005).

111. F., J., Dorland, W., Kotschenreuther, M., *et al. Phys. Plasmas* **7,** 1904 (2000).

112. Xanthopoulos, P., Cooper, W. A., F., J., *et al. Phys. Plasmas (1994-present)* **16,** 082303 (2009).

Chapter 7

Summary and Suggestions for Future Work

7.1 Summary

It has been observed in tokamaks that temperature profiles are resilient to changes in heating, and that this effect has not been observed in conventional stellarators. Electron temperature profile resiliency in tokamaks is attributed to anomalous transport driven by turbulent micro-instabilities, and the resulting stiffness in the electron heat flux is measured using a combination of steady-state and perturbative heat transport experiments. The measured stiffness has been compared to gyrokinetic calculations in tokamaks, but not in stellarators. In this dissertation, stiffness measurements have been presented in the quasihelically symmetric configuration of the Helically Symmetric eXperiment (HSX), in which the neoclassical transport is comparable to that in a tokamak and turbulent transport dominates throughout the plasma.

To facilitate heat pulse propagation experiments, a second gyrotron with a hybrid transmission line has been installed and tested on HSX. The second antenna includes a steerable mirror for off-axis heating, and the output power of the second gyrotron can be modulated. The ray tracing code TRAVIS is used to model the single- and multi-pass absorption of microwave power in the real three-dimensional geometry of the device. Ray refraction modifies the propagation and absorption of the beam launched from the second antenna with the beam-axis deviating strongly from straight propagation at high density. The TRAVIS

code predicts 30% single-pass absorption efficiency of the ordinary wave at the fundamental resonance frequency in HSX, while the subsequent passes through the plasma (up to 3) increase the total efficiency up to the measured absorption efficiency of 45%. Multi-pass ray tracing calculations show good agreement with experimental measurements of the absorbed power determined by ECRH turn-off, and the absorption is localized in the plasma core of HSX. It has been shown that the heating from the first launcher is reinforced by multi-pass absorption, while the heating from the second antenna is less sensitive. Modeling shows that rays launched from the second antenna intersect the hot, dense core of HSX during their first pass through the plasma; however, on subsequent passes through the plasma, after their first reflection from the vessel wall, the rays do not intersect the plasma core. Additionally, after the first reflection from the wall the reflected beam has large divergence and low power density.

An absolutely calibrated 16 channel ECE radiometer is used to measure the electron temperature and its response to modulated heating in HSX plasmas. The radiation temperature is in good agreement with the blackbody electron temperature measured through Thomson scattering, and it is significantly larger than the first pass radiation temperature calculated using an analytic model, implying an effective wall reflectivity close to 1. The antenna pattern of the ECE diagnostic has a significant impact on the measured radiation temperature, and modeling of the emission sampled by the diagnostic is necessary to determine the radiation temperature. An iterative procedure is used to self-consistently determine the electron temperature from the measured radiation spectrum. Relativistically down shifted emission causes asymmetry in the ECE radiation temperature across the magnetic-axis at high ECRH power density in HSX; however, the channels on the high field side of the magnetic axis remain thermal. The spatial and temporal resolution of the ECE radiometer have been increased for use in heat pulse propagation experiments, and the ECE channels that are

on the high field side of the magnetic-axis are used in the analysis of heat pulse propagation experiments on HSX.

The electron temperature perturbation from modulated ECRH propagates through the foot of the steep electron temperature gradient region of the plasma, $0.2 \leq r/a \leq 0.4$, and measurements of the amplitude and phase of the perturbation are used to determine a transient electron thermal diffusivity that it is equal to the steady-state diffusivity. The low stiffness between $0.2 \leq r/a \leq 0.4$ agrees with the linear scaling of the steady-state heat flux with temperature gradient in this region. These experimental results have been compared to gyrokinetic calculations using the GENE code with two kinetic species. Linear calculations demonstrate that the Trapped Electron Mode (TEM) is the dominant long-wavelength microturbulence instability across most of the HSX minor radius, and the TEM is primarily driven by the density gradient. Although linear simulations show that the Electron Temperature Gradient (ETG) mode may be experimentally relevant within $r/a \leq 0.2$, the saturated heat flux driven by the ETG mode in non-linear simulations is not experimentally relevant outside of this region. The measured heat flux is comparable to the saturated heat flux driven by TEM in non-linear calculations.

7.2 Suggestions for Future Work

Over the course of this research, several interesting phenomena have been observed that were not directly related to this dissertation. Additionally, there are several avenues for continuing and expanding upon this research. Turbulence optimization studies in multiple magnetic configurations are proposed, and three diagnostics are suggested for use in this project in Section 7.2.1. Kinetic modeling of the ECRH power deposition and the neoclassical transport of high energy trapped electrons is proposed in Section 7.2.2. This modeling can be compared to absorbed power profile measurements from ECRH experiments with

high frequency power modulation. Measuring the change in distribution function due to ECRH at low plasma density through an integrated data analysis is separately proposed in Section 7.2.3. Finally, heat pulse propagation measurements in methane plasma indicate very low stiffness, and core radial electric field measurements are necessary to investigate the existence of a neoclassical electron Internal Transport Barrier (eITB). An eITB has been predicted to form in HSX through core electron root confinement [13]. Further heat pulse propagation measurements and stiffness studies in methane plasma, and comparisons to core radial electric field measurements are proposed in Section 7.2.4.

All of the work proposed in this section incorporates the ECE diagnostic, and to maintain flexibility for future experiments a diagnostic upgrade is suggested. The increased resolution configuration of the ECE radiometer, discussed in Section 3.4, and the standard configuration of the ECE radiometer, discussed in Section 3.1, can be combined to form a 24-channel radiometer. The 24 channel diagnostic can be used for core heat pulse propagation and correlated ECE studies, as well as edge distribution function modeling. One channel with a tunable IF filter can be used as a correlation ECE diagnostic by varying the overlap between the other 23 channels. This configuration also allows 23 channels to operate as a time-resolved and electron temperature diagnostic with high spatial resolution.

7.2.1 Turbulence Measurements and Stellarator Optimization

There is strong interest in understanding turbulence in stellarators [110] [113] and turbulence optimization in neoclassically optimized stellarators [114] [115] [116]. There is a lack of turbulence diagnostics on the HSX stellarator, and a turbulence diagnostic is necessary to participate in turbulence optimization studies. The viability of three core turbulence diagnostics should be investigated on HSX: a radial correlation reflectometer [117] to measure the radial correlation length and density fluctuation level driven by turbulence [118]

(and possibly the wave number spectrum of the turbulence [119]), a Doppler reflectometer to measure the wave number spectrum of the turbulence [120], and a correlation electron cyclotron emission radiometer to measure the radial correlation length and temperature fluctuation level of the turbulence [121]. One or more of these diagnostics should be implemented to measure turbulent quantities that can be directly compared to the result of non-linear gyrokinetic calculations. These comparisons are necessary to develop proxy functions for stellarator optimization [114].

7.2.2 Modeling the Kinetic Relaxation of the Distribution Function at High ECRH Power Density

Bursty behavior is observed in the electron cyclotron emission at high ECRH power density in the core, and this phenomenon is also measured at the half-radius. This meaurement was introduced in Section 2.4 and presented in Figure 2.5 (reproduced in Figure 7.1).

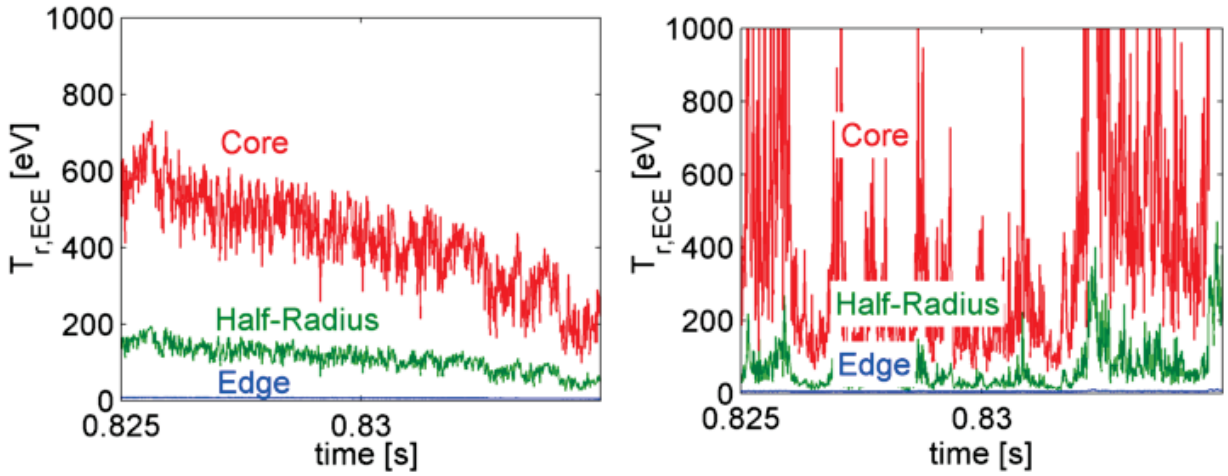

(a) Low P/n: 44 kW, 4.3×10^{12}cm^{-3}

(b) High P/n: 96 kW, 2×10^{12}cm^{-3}

Figure 7.1: Edge (blue), half-radius (green), and core (red) ECE radiation temperature for two ECRH power densities.

This bursty behavior was also observed on the W7-AS stellarator in plasma with high ECRH power density. In the W7-AS experiment, the measurement was attributed to local degradation of the ECRH power absorption due to flattening of the distribution function, which was followed by increased absorption by collisionless ripple trapped electrons that were resonant at high energies. The bursty behavior changed as the ECRH heating location was moved from magnetic field ripple bottom to the magnetic field ripple top [76], and HSX can produce similar magnetic configurations.

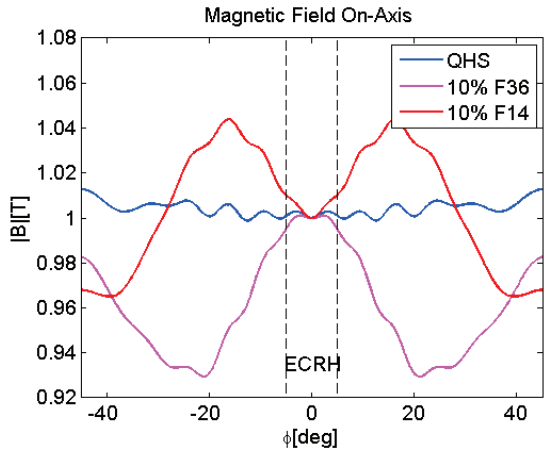

Figure 7.2: Magnetic field strength along the magnetic axis in three realizable magnetic configurations on HSX: the QHS, 10% Flip-14 Mirror, and 10% Flip-36 Mirror configurations.

The QHS, 10% Flip-14 Mirror, and 10% Flip-36 Mirror configurations are similar to the magnetic configurations tested on W7-AS, and the magnetic field strength along the magnetic axis is shown versus helical angle in each configuration in Figure 7.2. The measurement on HSX may be investigated by determining the threshold at which the bursty behavior begins, and by measuring the rate of trapped particle losses in each of these configurations. The absorption may be determined from the toroidal array of absolutely calibrated microwave diodes. The fast radial drift of trapped particles leads to broadening of the ECRH absorption profile, which may be modeled using a 5-dimensional Fokker-Planck code as in reference [76].

High frequency ECRH modulation experiments can be used to measure the broadening of the absorption, and this effect can be used as another test of the quality of neoclassical optimization in the quasi-helically symmetric configuration of HSX.

7.2.3 Modeling the Change in Distribution Function

A measurable fraction of the total plasma stored energy is carried by nonthermal particles in HSX at low plasma density. The energy carried by fast particles is inferred from the difference between the kinetic stored energy and the diamagnetic stored energy measurements, which were introduced in Section 2.4 and presented in Figure 2.10 (reproduced in Figure 7.3).

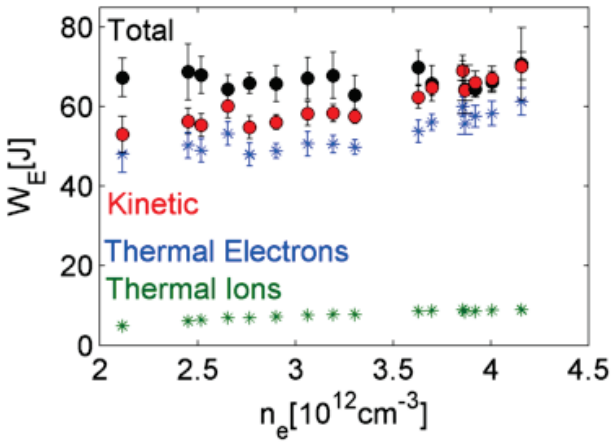

Figure 7.3: Total stored energy measurement (W_E^{diam}, black circles), electron stored energy measurement ($W_{E,e}$, blue asterisks), an estimate of the energy carried by the ions ($W_{E,i}$, green asterisks), and the kinetic stored energy ($W_E^{kin} = W_{E,e} + W_{E,i}$, red circles).

An Integrated Data Analysis (IDA) including multiple diagnostics is proposed to model the experimental distribution function on HSX. The plasma density and electron temperature from the thermal part of the distribution function are measured by Thomson scattering, and the non-thermal electron temperature can be measured using a combination of soft and hard

X-ray diagnostics. The non-thermal electron density is then constrained by the difference in kinetic and diamagnetic stored energy.

The TRAVIS ray tracing code includes a module for modeling the ECE from a 3D plasma and is capable of modeling single- and multi-pass electron cyclotron emission by including a vacuum vessel of finite reflectivity in the ray tracing calculation [92]. Numerical modeling of the ECE radiation spectra in a nonthermal plasma can be calculated using TRAVIS, and this result can be compared to the measured ECE spectra at high ECRH power density to test the result of the integrated data analysis.

The change in the distribution function due to ECRH can also be modeled using a code such as the relativistic Collisional/QuasiLinear 3D (CQL3D) code, which solves the bounce averaged Fokker-Planck equation in a toroidal geometry, or by using the GNET code [16], which solves the 5D drift kinetic equation in a general stellarator geometry. The ECE spectra can then be calculated from the modeled distribution function using a code such as the GENral RAY tracing code (GENRAY) [122] or TRAVIS.

7.2.4 Stiffness and Core Radial Electric Field Measurements in Methane Plasma

Low stiffness is measured in plasma with a significant fraction of methane, and this is consistent with previous predictions of a neoclassical electron Internal Transport Barrier (eITB) in HSX [4]. This measurement was introduced in Section 5.4 and presented in Figure 5.11 (reproduced in Figure 7.4).

Peaked electron temperatures of up to 2.5 KeV have been measured during ECRH modulation experiments, and Thomson scattering measurements of the electron temperature and density are shown in Figure 7.4a. In this experiment, 85 kW of power was launched into the plasma, and 10% of the power launched from the second antenna was modulated. The

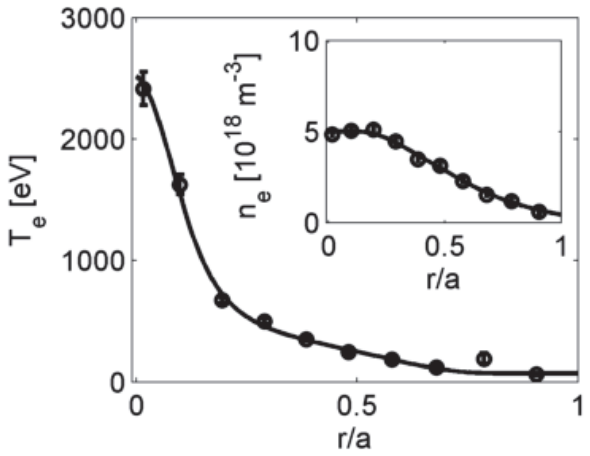

(a) Electron temperature and plasma density.

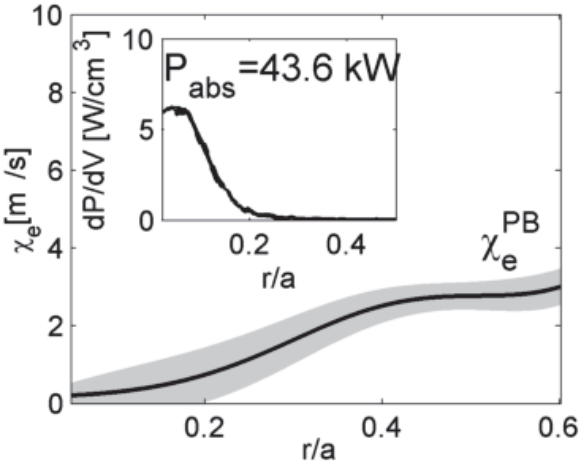

(b) Power balance analysis.

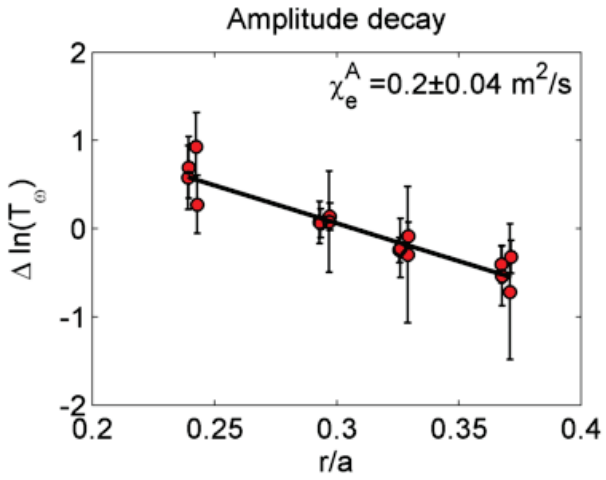

(c) Heat pulse amplitude decay.

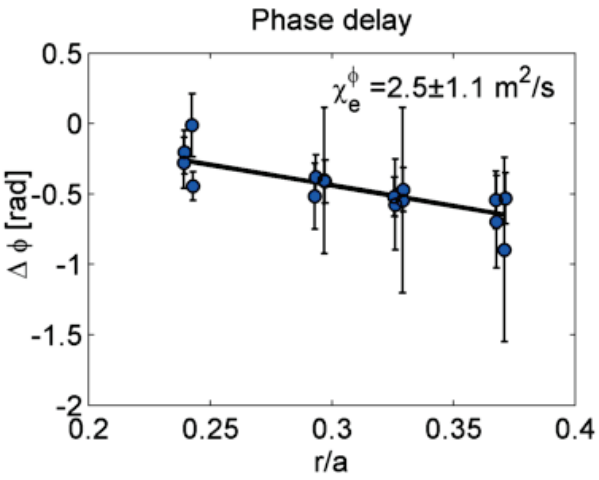

(d) Heat pulse phase delay.

Figure 7.4: Electron temperature and plasma density (a), the multi-pass power deposition profile and power balance electron thermal diffusivity (b), the heat pulse amplitude decay (c), and the heat pulse phase delay (d) from an ECRH modulation experiment in a methane plasma.

absorption profile calculated using the multi-pass ray tracing model and the power balance electron thermal diffusivity are shown in Figure 7.4b, and the heat pulse amplitude decay

and phase delay are shown in Figure 7.4c and Figure 7.4d respectively. The volume average power balance diffusivity in the region between $0.2 \leq r/a \leq 0.4$ is $\chi_e^{PB} = 1.7 \pm 0.2$ m^2/s. The heat pulse diffusivity measured in this region is $\chi_e^{HP} = \sqrt{\chi_e^A \chi_e^\phi} = 0.7 \pm 0.2$ m^2/s. The resulting stiffness in the methane plasma is $S = \chi_e^{HP}/\chi_e^{PB} = 0.4 \pm 0.1$, which can be interpreted as evidence for an eITB.

The radial electric fields measured through CHarge Exchange Recombination Spectroscopy (CHERS) on HSX are much smaller than the neoclassically predicted radial electric field in the core of the plasma, but they are consistent with the radial electric field predicted across most of the plasma effective radius. The CHERS diagnostic on HSX cannot currently resolve the core of the plasma [31], and measurements of the core radial electric field are necessary to confirm the existence of an eITB.

If the eITB exists, further measurements are necessary to determine the neoclassical transition to core electron root confinement. In this case, high frequency ECRH modulation can be used to change the time-average launched power by varying the duty cycle and depth of the modulation. This technique can be used to produce a fine scale heat flux scan and determine the power threshold for transition into core electron root confinement. The heat pulses are strongly damped in Figure 7.4c, leading to low χ_e^A, which is indicative of an eITB when accompanied by a thermal diffusivity with a negative temperature scaling.

Experiments on the LHD stellarator showed that the thermal diffusivity required a negative scaling with electron temperature for the eITB to form, and that there was a strong positive scaling with the electron temperature when no ITB was present (also outside of the ITB layer) [65]. Experiments also showed that the heat flux undergoes hysteresis during the transition to an eITB [17] [123]. Hysteresis in the electron heat flux is indicative of a transition into and out of an eITB and should be observable during heat flux scans in concurrent

heat pulse propagation experiments if an eITB is present. Heat pulse propagation experiments are proposed with on-axis and off-axis ECRH modulation to investigate the existence of an eITB in plasma with strongly peaked electron temperature profiles. Additionally, the scaling of the electron thermal diffusivity with electron temperature should be investigated during heat flux scans in methane plasma for comparison with the LHD result.

Bibliography

4. Lore, J., Guttenfelder, W., Briesemeister, A., *et al. Phys. Plasmas* **17,** 056101 (2010).

13. Lore, J. PhD thesis (The University of Wisconsin - Madison, United States, 2010).

16. Murakami, S., Gasparino, U., Idei, H., *et al. Nucl. Fusion* **40,** 693–700 (2000).

17. Shimozuma, T., Kubo, S., Idei, H., *et al. Plasma Phys. Control. Fusion* **45,** 1183–1192 (2003).

31. Briesemeister, A., Zhai, K., Anderson, D. T., *et al. Contrib. Plasm. Phys.* **50,** 741–744 (2010).

65. Ida, K., Inagaki, S., Shimozuma, T., *et al. Phys. Plasmas* **11,** 2551 (2004).

76. Rome, M. *Plasma Phys. Control. Fusion* **39,** 117–158 (1997).

92. Marushchenko, N. B., Turkin, Y. & Maassberg, H. *Comput. Phys. Commun.* **185,** 165–176 (2014).

110. Rewoldt, G., Ku, L. P. & Tang, W. M. *Phys. Plasmas* **12,** 102512–102512–10 (2005).

113. Helander, P., Beidler, C. D., Bird, T. M., *et al. Plasma Phys. Control. Fusion* **54,** 124009 (2012).

114. Mynick, H. E., Pomphrey, N. & Xanthopoulos, P. *Phys. Rev. Lett.* **105,** 095004 (2010).

115. Xanthopoulos, P., Mynick, H., Helander, P., *et al. Phys. Rev. Lett.* **113,** 155001 (2014).

116. Proll, J. H. E., Xanthopoulos, P. & Helander, P. *arXiv:1311.3127 [physics]* (2013).

117. Meneses, L., Cupido, L. & Manso, M. E. *Fusion Eng. and Des.* **86,** 552–555 (2011).

118. Kramer, G. J., Nazikian, R. & Valeo, E. *Rev. Sci. Instrum.* **74,** 1421–1425 (2003).

119. Gusakov, E. Z. & Kosolapova, N. V. *Plasma Phys. Control. Fusion* **53,** 045012 (2011).

120. Blanco, E. & Estrada, T. *Plasma Phys. Control. Fusion* **50,** 095011 (2008).

121. White, A. E., Schmitz, L., Peebles, W. A., *et al. Rev. Sci. Instrum.* **79,** 103505 (2008).

122. Harvey, R. W., Brien, M. R. O., Rozhdestvensky, V. V., *et al. Phys. Fuids B.* **5,** 446 (1993).

123. Shimozuma, T., Kubo, S., Idei, H., *et al. Nucl. Fusion* **45,** 1396–1403 (2005).

Appendix A: Power Balance Analysis with a Transport Barrier or a Magnetic Island

A neoclassical eITB has been predicted to exist in the QHS configuration due to the transition between electron-root and ion-root radial electric fields using the PENTA code [4]. For the plasma density and electron temperature profiles shown in Figure A.1a, the transition region is between $0.16 \leq r/a \leq 0.27$. Separately, magnetic field errors can result in the break-up of magnetic flux surfaces and regions of stochastic magnetic field lines. The parallel heat transport along the magnetic field line is very fast, and the effective perpendicular thermal diffusivity in a region of stochastic magnetic field lines is large.

These two effects are practical and interesting examples in which the sensitivity of power balance analysis to the fitting function can be demonstrated. Power balance analysis alone is insufficient for determining whether an eITB or a region of stochastic magnetic field lines exist in HSX or not. The thermal diffusivity in this section is parameterized by a Heaviside function on a quadratic polynomial to estimate the effect that these two phenomena have on the electron temperature profile.

In the eITB case, the Heaviside function is initialized near the predicted eITB region, and the least square algorithm used in the standard power balance analysis, discussed in Chapter 5, adjusts its spatial extent and magnitude(including the sign) until the fitted electron temperature profile is consistent with that measured by Thomson scattering. The final fit has a region of suppressed transport between $0.15 \leq r/a \leq 0.31$, which matches the predicted region of decreased transport. For comparison, the power balance diffusivity calculated using the Monte Carlo analysis is also shown in Figure A.1b. The change in the electron temperature due to a small region of suppressed electron thermal transport, shown in Figure A.1a, is not experimentally measureable on HSX. Additionally, the calculated

electron thermal diffusivity lies within the uncertainty of the Monte Carlo analysis across most of the plasma, which is shown in Figure A.1b.

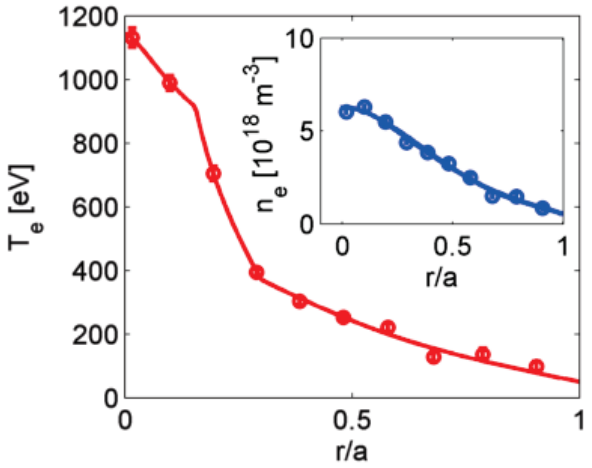

(a) Electron temperature and plasma density fits.

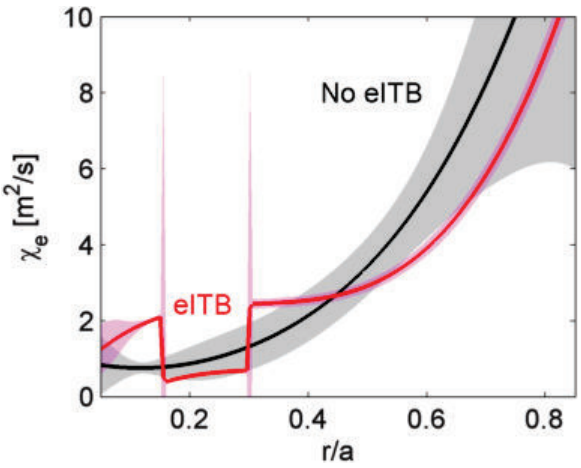

(b) Power balance analysis.

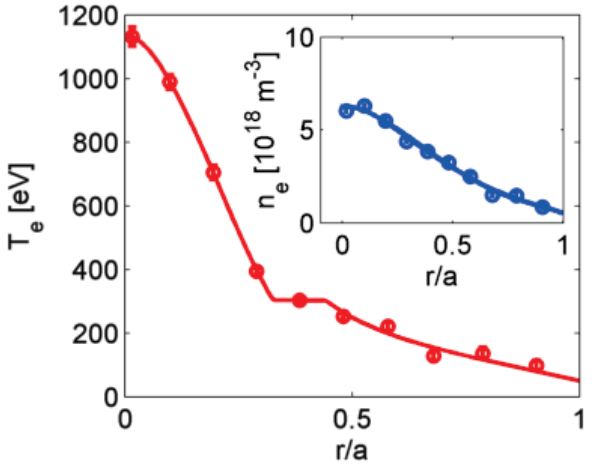

(c) Electron temperature and plasma density fits.

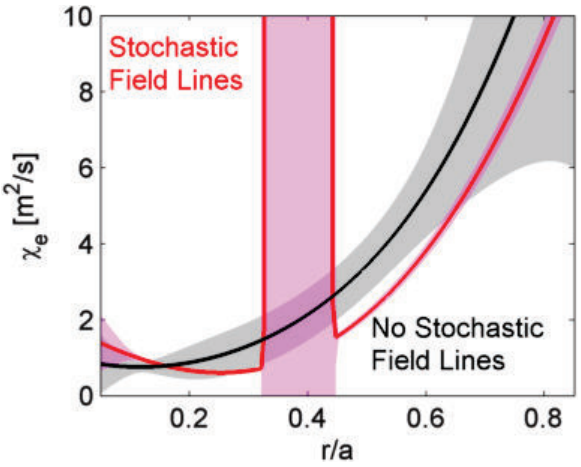

(d) Power balance analysis.

Figure A.1: Electron temperature and plasma density measured through Thomson scattering, and fits from power balance analysis allowing for an eITB (a) and a region of stochastic magnetic field lines (c). The diffusivity resulting from a Monte Carlo analysis (black), and an analysis allowing for an eITB (red) (b) and a stochastic field (d).

Similarly, a region of stochastic magnetic field lines is not detectable on HSX using the Thomson Scattering diagnostic. In this example, the Heaviside function is initialized between $0.30 \leq r/a \leq 0.35$, and the algorithm adjusts its spatial extent and magnitude (including its sign). The resulting electron temperature fit has a flat gradient region between $0.33 \leq r/a \leq 0.44$ in Figure A.1c. The corresponding power balance diffusivity is shown in Figure A.1d.

Appendix A: Bibliography

4. Lore, J., Guttenfelder, W., Briesemeister, A., *et al. Phys. Plasmas* **17,** 056101 (2010).

Appendix B: Power Balance Analysis and the Heat Pulse Thermal Diffusivity

B.1 The Heat Transport Equation

The electron heat transport equation is derived by including known sources and sinks in Equation 1.2, and splitting the divergence of the pressure tensor into convective flows, $\vec{u}_s \cdot \vec{\nabla} p_s$, compressible flows, $\vec{\nabla} \cdot \vec{u}_s$, and a term due to the non-diagonal pressure components, $\overline{\pi} : \nabla \vec{u}_s$. Including electron-ion drag, $Q_{e,i}$, and heating power, Q_e, yields an equation for the pressure evolution, Equation B.1. Defining the scalar electron pressure, $p_e = n_e T_e$, and the convective flow, $\vec{u}_e = \frac{\vec{\Gamma}_e}{n_e}$, allows Equation B.1 to be put in terms of electron temperature, plasma density, and electron heat flux, $\vec{q}_e$, and particle flux, $\vec{\Gamma}_e$,

$$\frac{3}{2}\frac{\partial p_e}{\partial t} + \frac{3}{2}\vec{u}_e \cdot \vec{\nabla} p_e + \frac{5}{2} p_e \vec{\nabla} \cdot \vec{u}_e = -\vec{\nabla} \cdot \vec{q}_e + \overline{\pi} : \nabla \vec{u}_e - Q_{e,i} + Q_e - \sum_{sinks} Q, \tag{B.1}$$

$$\frac{3}{2}\vec{u}_e \cdot \vec{\nabla} p_e + \frac{5}{2} p_e \vec{\nabla} \cdot \vec{u}_e = -\vec{\Gamma}_e \cdot \frac{\nabla p_e}{n_e} + \vec{\nabla} \cdot \frac{5}{2} T_e \vec{\Gamma}_e,$$

$$\frac{3}{2}\frac{\partial}{\partial t}(n_e T_e) + \vec{\nabla} \cdot [\vec{q}_e + \frac{5}{2} T_e \vec{\Gamma}_e] = P_{ECRH}(r,t) + \vec{\Gamma}_e \cdot \frac{\nabla (n_e T_e)}{n_e} + \sum Q. \tag{B.2}$$

Here $\sum Q$ represents all other energy sources and sinks, and P_{ECRH} represents the HSX specific contribution from Electron Cyclotron Resonance Heating (ECRH).

The plasma density evolution is included by using the continuity equation, Equation B.3, to determine $\frac{\partial n_e}{\partial t}$ in Equation B.2, to yield the temperature evolution equation for arbitrary sources, sinks, heat and particle flux B.4,

$$\frac{\partial n_e}{\partial t} = \sum_{part.} S_e - \vec{\nabla} \cdot \vec{\Gamma}_e, \tag{B.3}$$

$$\frac{3}{2} n_e \frac{\partial T_e}{\partial t} + \vec{\nabla} \cdot (\vec{q}_e + \vec{\Gamma}_e T_e) = \sum_{heat} Q_e - \frac{3}{2} T_e \sum_{part.} S_e + \vec{\Gamma}_e \cdot [\nabla (\frac{5}{2} T_e) + T_e \frac{\nabla n_e}{n_e}]. \tag{B.4}$$

Combining the terms on the right hand side of Equation B.4, into an effective source term, S_e, and using the total heat flux, $q_e = -n_e \chi_e \nabla T_e + q_{conv}$, makes the problem tractable.

In cylindrical geometry, the heat transport equation is expanded in the ECRH modulation depth, $\varepsilon = \delta S_e/S_e$, while assuming the source drives heat flux perturbations that are first order in ε, and density perturbations that are second order in ε, and solving for the effective thermal diffusivity within the ordered expansion,

$$\frac{3}{2}\frac{\partial}{\partial t}(n_e T_e) + \vec{\nabla}\cdot\vec{q}_e = S_e, \qquad S_e(r,t) = S_{e,o}(r) + \delta S_e e^{-i\omega t},$$

$$q_e = q_{e,o}(r) + \delta q_e(r,t), \qquad q_{e,o}(r) = n_{e,o}\chi_e \nabla T_{e,o}, \quad \delta q_e(r,t) = n_{e,o}\chi_e \nabla \delta T_e,$$

$$\varepsilon^0: \quad \vec{\nabla}\cdot\vec{q}_{e,o} = S_{e,o}, \qquad \chi_e^{pb} = -\frac{1}{r n_{e,o}\frac{\partial T_{e,o}}{\partial r}}\int_0^{r'} S_{e,o} r' dr',$$

$$\varepsilon^1: \quad \vec{\nabla}\cdot\delta q_e = \delta S_e - \frac{3}{2}n_{e,o}\frac{\partial \delta T_e}{\partial t} \qquad \chi_e^{inc} = \frac{1}{r n_{e,o}\frac{\partial \delta T_e}{\partial r}}\int_0^{r'} [\frac{3}{2}n_{e,o}\frac{\partial \delta T_e}{\partial t} - \hat{S}_e] r' dr'.$$

This calculation is reproduced in flux coordinates to yield the appropriate geometry factors, where ρ is the square root of normalized toroidal flux, V' is the derivative of the plasma volume with respect to ρ, and $\langle\rangle$ represents flux surface averaging [41],

$$\varepsilon^0: \quad \frac{1}{V'}\frac{\partial}{\partial \rho}\langle q_e\rangle = \langle S_e\rangle, \qquad \chi_e^{PB} = \frac{-1}{V'\langle|\nabla\rho|^2\rangle n_o \frac{\partial T_o}{\partial \rho}}\int_0^{\rho'} \langle \hat{S}_o(t)\rangle V' d\rho',$$

$$\varepsilon^1: \quad \frac{1}{V'}\frac{\partial}{\partial \rho}\delta q_e = \delta S_e - \frac{3}{2}n_o\frac{\partial \delta T_e}{\partial t}, \quad \chi_e^{INC} = \frac{-1}{V'\langle|\nabla\rho|^2\rangle n_o \frac{\partial \delta T_e}{\partial \rho}}\int_0^{\rho'} [\frac{3}{2}n_o\frac{\partial \delta T_e}{\partial t} - \hat{S}_e(t)] V' d\rho'.$$

B.2 Fourier Analysis of Heat Pulse Propagation

The incremental electron thermal diffusivity is determined from the temporal response of the electron temperature to changes in heating. The amplitude and phase of the perturbation with respect to the source are used to determine the diffusivity by applying models for the response from solutions to the heat equation. The following sections derive and describe the common models for the propagation of heat pulses in terms of the amplitude and phase of the perturbation.

B.2.1 Historical Solutions to the Cylindrical Heat Equation for Heat Pulse Propagation Experiments

The homogeneous cylindrical heat equation, using Fourier's law of conduction for the heat flux, is

$$\frac{\partial}{\partial t}\frac{3}{2}nT - \frac{1}{r}\frac{\partial}{\partial r}rn\chi\frac{\partial T}{\partial r} = 0. \tag{B.5}$$

For constant density and thermal diffusivity profiles, the homogeneous cylindrical heat equation for a time-harmonic temperature perturbation, δT_n, is

$$\left[\frac{3}{2}\frac{in\omega}{\chi} - \frac{1}{r}\frac{\partial}{\partial r}r\frac{\partial}{\partial r}\right]\delta T_n = 0. \tag{B.6}$$

Replacing the partial derivatives with total derivatives and expanding yields Bessel's equation,

$$\begin{gathered}\left[\frac{d^2}{dr^2} + \frac{1}{r}\frac{d}{dr} + \frac{3}{2}\frac{in\omega}{\chi}\right]\delta T_n = 0, \\ \left[r^2\frac{d^2}{dr^2} + r\frac{d}{dr} + \frac{3}{2}\frac{in\omega}{\chi_s}r^2\right]\delta T_n = 0.\end{gathered} \tag{B.7}$$

The solution to Bessel's equation for the nth Fourier harmonic are zero-order (Kelvin) Bessel functions of argument $x = \left(\frac{3}{2}\frac{n\omega}{\chi}r^2e^{\frac{i\pi}{2}}\right)^{\frac{1}{2}} = \left(\frac{3n\omega}{2\chi}\right)^{\frac{1}{2}}re^{\frac{i\pi}{4}}$. Note that the phase factor in the argument of the Bessel function turns them into Kelvin functions (real and imaginary parts of $J_\nu\left[xe^{\frac{3\pi i}{4}}\right] = Ber_\nu(x) + iBei_\nu(x)$). For real x,

$$\delta T_n(r) = CJ_0[x] = C\left(Ber_0[x] + iBei_0[x]\right).$$

The magnitude and the phase of the perturbation are then

$$\delta T_n(r) = M_0(x)\,e^{i\varphi_{\mathrm{n}}(\mathrm{x})}, \quad \text{where} \quad M_0(x) = |CJ_0| \quad \text{and} \quad \varphi_n(x) = \operatorname{atan}\left(\frac{Bei_0}{Ber_0}\right).$$

The small argument series expansions of $\mathrm{Ber}_0(\mathrm{x})$ and $\mathrm{Bei}_0(\mathrm{x})$ are

$$Ber_0[x] = 1 + \Sigma_{k\geq 1}\frac{(-1)^k\left(\frac{x}{2}\right)^{4k}}{[(2k)!]^2}, \quad Bei_0[x] = \Sigma_{k\geq 0}\frac{(-1)^k\left(\frac{x}{2}\right)^{4k+2}}{[(2k+1)!]^2}. \tag{B.8}$$

Applying these expansions to the phase of the perturbation, and taking the lowest order term in the expansion gives the phase in terms of the electron thermal diffusivity,

$$\tan\left[\varphi_n\left(x\right)\right] = \left(\frac{x}{2}\right)^2 \frac{\Sigma_{k\geq 0}\frac{(-1)^k}{[(2k+1)!]^2}\left(\frac{x}{2}\right)^{4k}}{1+\Sigma_{k\geq 1}\frac{(-1)^k}{[(2k)!]^2}\left(\frac{x}{2}\right)^{4k}} \approx \left(\frac{x}{2}\right)^2 = \left[\frac{1}{2}\left(\frac{3n\omega}{2\chi}\right)^{\frac{1}{2}} r\right]^2,$$

$$\tan\left[\varphi_n\left(x\right)\right] \approx \frac{3n\omega}{2\chi}\frac{1}{4}r^2 = \frac{3n\omega}{8\chi}r^2.$$

The phase of the perturbation is related to the thermal diffusivity and the squared distance from the axis. If the perturbation were generated off-axis this would result in a linear shift of the argument, and $r \rightarrow r - r_s = \Delta r$. Using the time-delay, $t_d = -\frac{\varphi_n}{n\omega}$, the incremental electron thermal diffusivity can be determined purely from the phase delay of a perturbation,

$$\chi_e^{inc} \approx \frac{3}{8}\frac{\Delta r^2}{t_d}. \tag{B.9}$$

This is the original model used to determine the thermal diffusivity from analysis of sawteeth perturbations on the Oak Ridge Tokamak (ORMAK). This model was determined by solving the cylindrical heat equation using Laplace transform techniques with an experimentally determined heat-pulse boundary condition [124]: $n_e\chi_e\frac{\partial \Delta T_e}{\partial r}|_{r=a_d} = -\Delta Q \Sigma_n \delta\left(t - nt_o\right)$. Here ΔQ is the electron energy density within a heat pulse generated by a sawtooth crash, t_o is the saw-tooth repetition time, and a_d is referenced as the "disruption radius" or saw-tooth inversion radius. This is effectively a delta-function initial condition to the cylindrical heat equation.

The result, $\chi_e \approx \frac{3}{8}\frac{\Delta r^2}{t_d}$, is contrary to the result found in Reference [125] on heat pulse propagation from saw-teeth on ORMAK, which used a dipole initial condition in a Green's function solution to the cylindrical heat equation to yield $\chi_e \approx \frac{1}{8}\frac{\Delta r^2}{t_d}$. This factor of 3 difference comes from the initial condition used in the solution. Both solutions were found using a small-parameter expansion of the Bessel function solution for the temperature perturbation.

This problem was revisited for application to TFTR data where a large argument expansion yielded $\chi_e \approx \frac{1}{9}\frac{\Delta r^2}{t_d}$. The magnitude of the argument is large at the time of the peak in the perturbation [103]. The difference between the 1/9 and 1/8 solution is only about 10% and so the authors chose to use the 1/8 solution for simplicity in comparing with other experiments.

The normalized scale length of the diffusivity is the expansion parameter of Section B.2, $x = 2\pi\frac{r}{\lambda} = kr$, where λ is the characteristic damping length of a heat pulse due to thermal diffusion at the modulation frequency, and $k = \left(\frac{3n\omega}{2\chi}\right)^{0.5}$. This parameter isn't small compared to unity across most of the minor radius of HSX, and it cannot be used to make a small argument expansion of the solution to the heat equation for HSX parameters.

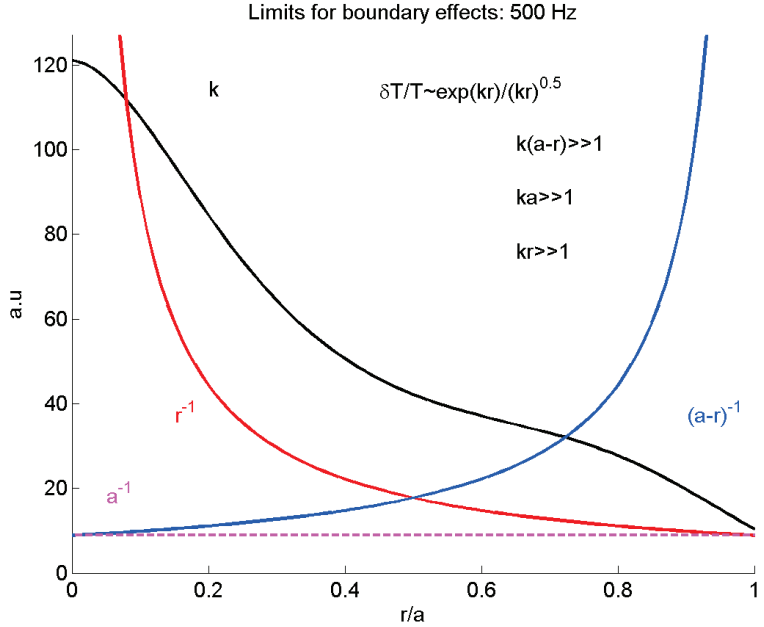

Figure B.1: Scale length of the diffusivity, k, versus effective radius. Boundary effects in the solution to Bessel's equation may be neglected when $kr \gg 1$, $ka \gg 1$, and $k(a-r) \gg 1$.

A representative value for the scale length at a modulation frequency of 500 Hz is 70 m^{-1}. The scale length, k, is plotted for 500 Hz modulation in Figure B.1 versus plasma effective radius. Boundary conditions in the solution to Bessel's equation (zero flux through the axis,

$\delta T'(0) = 0$, and zero perturbation at the minor radius, $\delta T(a) = 0$) may be neglected and the asymptotic form of the solution may be used when $ka \gg 1$, $k(a-r) \gg 1$, and $kr \gg 1$.

The Bessel function argument is not small, $x \ll 1$ in HSX. For a large argument expansion of the zero-order Bessel equation, $x \gg 1$, the zero-order Kelvin-Bessel functions are asymptotic to

$$Ber_0[x] \sim \frac{\exp\left(\frac{x}{\sqrt{2}}\right)}{\sqrt{2\pi x}}\cos\left(\frac{x}{\sqrt{2}} - \frac{\pi}{8}\right), \tag{B.10}$$
$$Bei_0[x] \sim \frac{\exp\left(\frac{x}{\sqrt{2}}\right)}{\sqrt{2\pi x}}\sin\left(\frac{x}{\sqrt{2}} - \frac{\pi}{8}\right).$$

The magnitude of each term in the large argument expansion are identical, but each term has a different phase. The phase difference between the source and the perturbation is asymptotic to the argument of the trigonometric functions. The phase of the temperature perturbation relative to the source is

$$\varphi_n(x) \sim \operatorname{atan}\left(\frac{\frac{\exp\left(\frac{x}{\sqrt{2}}\right)}{\sqrt{2\pi x}}\sin\left(\frac{x}{\sqrt{2}} - \frac{\pi}{8}\right)}{\frac{\exp\left(\frac{x}{\sqrt{2}}\right)}{\sqrt{2\pi x}}\cos\left(\frac{x}{\sqrt{2}} - \frac{\pi}{8}\right)}\right) = \frac{x}{\sqrt{2}} - \frac{\pi}{8} = \frac{1}{\sqrt{2}}\left(\frac{3n\omega}{2\chi}\right)^{\frac{1}{2}} r - \frac{\pi}{8}. \tag{B.11}$$

Similarly, the amplitude of the temperature perturbation is

$$\delta T_n(r) \sim C\frac{\exp\left(\frac{x}{\sqrt{2}}\right)}{\sqrt{2\pi x}} = C\exp\left(\left(\frac{3n\omega}{4\chi}\right)^{\frac{1}{2}} r\right)\left(6\pi^2\frac{n\omega}{\chi}r^2\right)^{-\frac{1}{4}}.$$

In the large argument limit, the incremental thermal diffusivity can be determined purely from the amplitude of the temperature perturbation, or purely from the phase between the temperature perturbation and the source. The logarithmic derivative of the perturbation amplitude reduces the problem, and removes the constant, so that the incremental thermal

diffusivity determined from the perturbation amplitude is

$$\frac{d\delta T_n}{dr} \sim \left[\left(\frac{3n\omega}{4\chi}\right)^{\frac{1}{2}} - \pi^2 \frac{3n\omega}{\chi} r \left(6\pi^2 \frac{n\omega}{\chi} r^2\right)^{-1}\right] \delta T_n,$$
$$\frac{d\ln \delta T_n}{dr} \sim \left(\frac{3n\omega}{4\chi}\right)^{\frac{1}{2}} - \frac{1}{2r} \rightarrow \left(\frac{d\ln \delta T_n}{dr} + \frac{1}{2r}\right)^2 \sim \frac{3n\omega}{4\chi},$$
$$\chi_e^{inc} \sim \frac{3n\omega}{4}\left(\frac{d\ln \delta T_n}{dr} + \frac{1}{2r}\right)^{-2}.$$

Similarly, taking the derivative of the phase removes the dependence on the distance from the source, and solving for the diffusivity yields

$$\frac{d\varphi_n}{dr} \sim \frac{1}{\sqrt{2}}\left(\frac{3n\omega}{2\chi}\right)^{\frac{1}{2}} \rightarrow 2\left(\frac{d\varphi_n}{dr}\right)^2 \sim \frac{3n\omega}{2\chi} \rightarrow \chi \sim \frac{3n\omega}{4\left(\frac{\varphi_n}{dr}\right)^2}. \tag{B.12}$$

In the large argument limit, the incremental thermal diffusivity can be determined purely from the derivative of the phase of a time-harmonic temperature perturbation,

$$\chi_e^{inc} \sim \frac{3n\omega}{4}\left(\frac{d\varphi_n}{dr}\right)^{-2}. \tag{B.13}$$

This is the model used for analysis of TFTR data [103]. There are several advantages to this analysis technique. One advantage is that the analysis is independent of the origin of the heat pulse; the analysis does not depend on the spatial variable, r, or the distance between a diagnostic channel and the source position, Δr. Additionally, this technique is insensitive to the shape of the heat pulse, which is in contrast to the time-to-peak analysis that was originally derived from the magnitude of the heat pulse generated by a sawtooth crash.

B.2.2 Solutions to the Time-Harmonic Heat Equation

The flux-surface averaged time-harmonic energy equation is

$$\frac{3}{2} i\omega n_e T_\omega - \frac{1}{V'}\frac{d}{d\rho} V' n_e \left[\langle \chi_e |\nabla \rho|^2 \rangle \frac{dT_\omega}{d\rho}\right] = \sum \langle \delta P_\omega \rangle, \tag{B.14}$$

where $\langle P_\omega \rangle$ is the flux-surface averaged source of the time-harmonic perturbation, and T_ω is the electron temperature response at the perturbation frequency. The inhomogeneity in Equation B.14 is most easily dealt with by dividing through by the temperature perturbation, the density (n_e), and the thermal diffusivity ($\langle \chi_e |\nabla\rho|^2 \rangle$), so that the heat-flux term can be written as the sum of logarithmic gradients,

$$\frac{3}{2} i\omega n_e T_\omega - \frac{1}{V'} \frac{d}{d\rho} V' n_e T_\omega \left[\langle \chi_e |\nabla\rho|^2 \rangle \frac{d \ln T_\omega}{d\rho} \right] = \sum \langle\ P_\omega \rangle,$$

$$-\frac{3}{2} \frac{i\omega}{\langle \chi_e |\nabla\rho|^2 \rangle} - \frac{1}{V' n_e T_\omega \langle \chi_e |\nabla\rho|^2 \rangle} \frac{d}{d\rho} n_e T_\omega V' \langle \chi_e |\nabla\rho|^2 \rangle \frac{d \ln T_\omega}{d\rho} = \sum \frac{\langle\ P_\omega \rangle}{n_e T_\omega \langle \chi_e |\nabla\rho|^2 \rangle},$$

$$\frac{3}{2} \frac{i\omega}{\langle \chi_e |\nabla\rho|^2 \rangle} + \frac{d \ln T_\omega}{d\rho} \frac{d}{d\rho} \ln n_e T_\omega V' \langle \chi_e |\nabla\rho|^2 \rangle + \frac{d}{d\rho} \frac{d \ln T_\omega}{d\rho} = -\sum \frac{\langle P_\omega \rangle}{n_e T_\omega \langle \chi_e |\nabla\rho|^2 \rangle},$$

$$\frac{3}{2} \frac{i\omega}{\langle \chi_e |\nabla\rho|^2 \rangle} + \frac{d \ln T_\omega}{d\rho} \frac{d}{d\rho} \ln n_e V' \langle \chi_e |\nabla\rho|^2 \rangle + \left(\frac{d \ln T_\omega}{d\rho} \right)^2 + \frac{d}{d\rho} \frac{d \ln T_\omega}{d\rho} = -\sum \frac{\langle\ P_\omega \rangle}{n_e T_\omega \langle \chi_e |\nabla\rho|^2 \rangle}.$$

Following the solution for a cylindrical geometry and representing the logarithmic gradients by the scale length ρ_g,

$$\frac{1}{\rho_g} = \frac{1}{\rho_n} + \frac{1}{\rho_{V'}} + \frac{1}{\rho_{\langle \chi_e |\nabla\rho|^2 \rangle}} = -\frac{d}{d\rho} \ln \left(n_e V' \langle \chi_e |\nabla\rho|^2 \rangle \right), \tag{B.15}$$

the flux-surface averaged heat equation as

$$\frac{3}{2} \frac{i\omega}{\langle \chi_e |\nabla\rho|^2 \rangle} + \left[\frac{d}{d\rho} \frac{d \ln T_\omega}{d\rho} + \left(\frac{d \ln T_\omega}{d\rho} \right)^2 - \frac{1}{\rho_g} \frac{d \ln T_\omega}{d\rho} \right] = -\sum \frac{\langle\ P_\omega \rangle}{n_e T_\omega \langle \chi_e |\nabla\rho|^2 \rangle}.$$

To check this formulation, it can be converted into a cylindrical, zero-order Bessel equation, which is the well-known solution for the simplified situation, by using

$$\left[\frac{d}{d\rho} \frac{d \ln T_\omega}{d\rho} = \frac{1}{T_\omega} \frac{d^2 T_\omega}{d\rho^2} - \left(\frac{d \ln T_\omega}{d\rho} \right)^2 \right],$$

$$\left[\frac{d^2}{d\rho^2} - \frac{1}{\rho_g} \frac{d}{d\rho} + \frac{3}{2} \frac{i\omega}{\langle \chi_e |\nabla\rho|^2 \rangle} \right] T_\omega = -\sum \frac{\langle\ P_\omega \rangle}{n_e \langle \chi_e |\nabla\rho|^2 \rangle}.$$

Outside of the power deposition zone, $\sum \langle\ P_\omega\rangle = 0$, and for a flat thermal diffusivity and a flat density profile in cylindrical coordinates, $\langle\chi_e|\nabla\rho|^2\rangle = \chi_e$, $\frac{d\ln V'}{d\rho} = \frac{1}{\rho}$, $\rho \to \frac{r}{a}$, so that

$$\left[\frac{d^2}{d\rho^2} + \left(\frac{d\ln V'}{d\rho} + \frac{d\ln n_e}{d\rho} + \frac{d\ln\chi_e}{d\rho}\right)\frac{d}{d\rho} + \frac{3}{2}\frac{i\omega}{\chi_e}\right]T_\omega = 0 \to \left[\frac{d^2}{dr^2} + \frac{1}{r}\frac{d}{dr} + \frac{3}{2}\frac{i\omega}{\chi_e}\right]T_\omega = 0,$$

$$\left[r^2\frac{d^2}{dr^2} + r\frac{d}{dr} + \frac{3}{2}\frac{i\omega}{\chi_e}r^2\right]T_\omega = 0.$$

This is identical to the zero-order Bessel equation solved in Section B.2.1.

The flux-surface averaged heat equation used to determine the thermal diffusivity from the phase and amplitude of the temperature perturbation from

$$\frac{3}{2}\frac{i\omega}{\langle\chi_e|\nabla\rho|^2\rangle} + \left[\frac{d}{d\rho}\frac{d\ln T_\omega}{d\rho} + \left(\frac{d\ln T_\omega}{d\rho}\right)^2 - \frac{1}{\rho_g}\frac{d\ln T_\omega}{d\rho}\right] = -\sum\frac{\langle\ P_\omega\rangle}{n_e T_\omega\langle\chi_e|\nabla\rho|^2\rangle}.$$

For under-damped plane wave solutions in a slab-like geometry, $\langle\chi_e|\nabla\rho|^2\rangle \to \chi_e$,

$$T_\omega = Ae^{-\alpha x}e^{i(kx-\omega t)}, \qquad \frac{d\ln T_\omega}{dx} = -\left(\alpha - ik\right),$$

$$\frac{d}{dx}\frac{d\ln T_\omega}{dx} = \frac{1}{T_\omega}\frac{d}{dx}\left[-\left(\alpha-ik\right)Ae^{-\alpha x}e^{i(kx-\omega t)}\right] - \left(\alpha-ik\right)^2 = -\frac{d}{dx}\left(\alpha-ik\right),$$

$$\left[-\frac{d}{dx}\left(\alpha-ik\right) + \frac{1}{\rho_g}\left(\alpha-ik\right) + \left(\alpha-ik\right)^2 + \frac{3}{2}\frac{i\omega}{\chi_e}\right] = -\sum\frac{\langle P_\omega\rangle}{n_e T_\omega\chi_e}.$$

This equation can be expanded outside of the power deposition zone,

$$\left[-\frac{d}{dx}\left(\alpha-ik\right) + \alpha^2 + \frac{1}{\rho_g}\alpha - k^2 - (2\alpha + \frac{1}{\rho_g})ik + \frac{3}{2}\frac{i\omega}{\chi_e}\right] = 0,$$

then split into real and imaginary parts to yield a thermal diffusivity and a constraint on the damping

$$\text{Real Part:} \qquad \alpha^2 - \frac{d\alpha}{dx} + \frac{1}{\rho_g}\alpha - k^2 = 0,$$

$$\text{Imaginary Part:} \qquad \left(2\alpha + \frac{1}{\rho_g}\right)k - \frac{dk}{dx} - \frac{3}{2}\frac{\omega}{\chi_e} = 0.$$

The thermal diffusivity comes from the imaginary part

$$\chi_e = \frac{3}{2}\frac{\omega}{\left(2\alpha + \frac{1}{\rho_g}\right)k - \frac{dk}{dx}}.$$

The damping rate and wave-vector can be written in terms of experimentally observable quantities by taking the amplitude decay to be the real part of the Fourier transformed temperature perturbation, $\alpha = Re[-\frac{d\ln T_\omega}{dx}]$, and using the relationship between the wave-vector and the phase of the perturbation, $\varphi = \int k dx$, to write $k = \frac{d\varphi}{dx} = \varphi'$. The incremental thermal diffusivity in this slab-like geometry with profile variation contained in ρ_g is then

$$\chi_e^{inc} = \frac{3}{4}\frac{\omega}{-\varphi'\left(\frac{\delta T_e'}{T_\omega} - \frac{1}{2\rho_g}\right) - \frac{1}{2}\varphi''}. \tag{B.16}$$

This is the exact model from Reference [105] in the absence of a heat pinch. If the heat pinch were included, $\rho_g^{-1} = \rho_n^{-1} + \rho_\chi^{-1} - \frac{U}{\chi_e}$, the thermal diffusivity would be

$$\chi_e^{inc} = \frac{3}{4}\frac{\omega}{-\varphi'\left(\frac{\delta T_e'}{T_\omega} - \frac{1}{2\rho_n} + \frac{\chi_e'}{2\chi_e} + \frac{U}{2\chi_e}\right) - \frac{1}{2}\varphi''}. \tag{B.17}$$

The constraint for neglecting the $\frac{1}{2}\varphi''$ term in Equation B.17 is $\varphi'' \approx -(\frac{\chi_e'}{2\chi_e})\varphi'$. Finite φ'' appears whenever χ_e' is not negligible or damping is large. The reduced model of Reference [105] neglects the $\frac{1}{2}\varphi''$ using this balance to leave

$$\chi_e^{inc} = \frac{3}{4}\frac{\omega}{-\varphi'\left(\frac{\delta T_e'}{T_\omega} - \frac{1}{2\rho_n} + \frac{\chi_e'}{4\chi_e} + \frac{U}{2\chi_e}\right)}. \tag{B.18}$$

Neglecting φ'' and using the reduced model leads to a maximum relative error of 10% when $kr > 2$ and $k(a-r) > 2.5$ [105]. The reduced form of the thermal diffusivity is valid between 20% and 50% of the effective plasma radius in HSX for a 500 Hz modulation in the absence of damping. This region expands with increasing frequency, and is valid between 10% and 60% for a 1kHz modulation in the absence of damping. The effect of damping is to extend the minor radial range of applicability of the reduced model.

In the absence of a heat pinch, the thermal diffusivity can be determined by neglecting the $\frac{\chi_e'}{4\chi_e}$ term in Equation B.18 for simplicity, and applying the reduced model; however, the convective contribution to the heat flux measured by modulation experiments is frequency

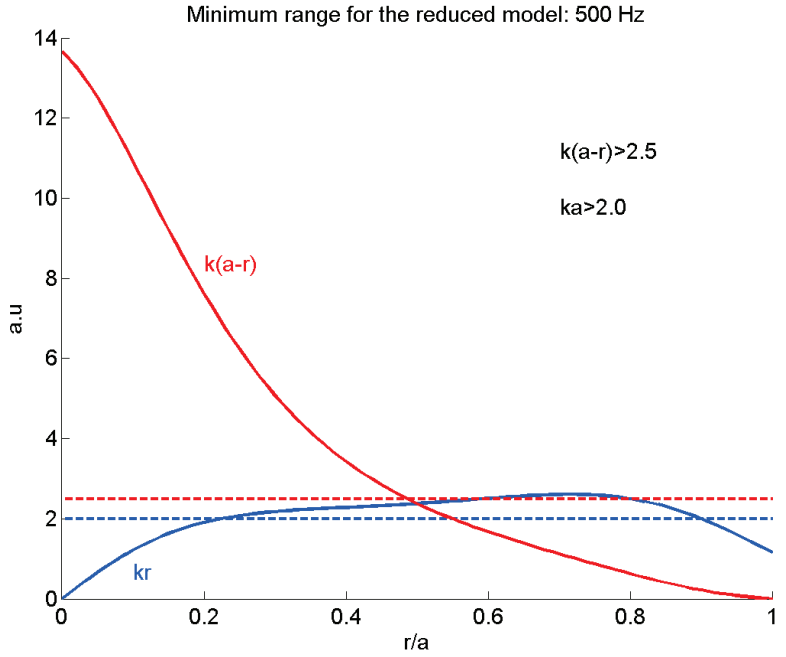

Figure B.2: Requirement on the damping rate of the scale length to neglect the effects of φ'' at 500 Hz modulation.

dependent, and multiple frequency measurements are necessary to reconstruct the diffusivity profile. This can be done by defining

$$\frac{1}{\chi_g} = \frac{1}{\chi_e}\left(1 + \frac{\beta}{v_\varphi}\right), \quad v_\varphi = -\frac{3\omega}{2\varphi'}, \quad \beta = U + \frac{\chi_e'}{2} \quad \text{and} \quad \chi_g = \frac{3}{4}\frac{\omega}{-\varphi'\left(\frac{\delta T_e'}{T_\omega} - \frac{1}{2\rho_n}\right)},$$

then fitting multiple frequency measurements of $\frac{1}{\chi_g}$ against $\frac{1}{v_\varphi}$. The intercept yields the electron thermal diffusivity, $\frac{1}{\chi_e}$, and the slope indicates the heat pinch velocity [105]. An example is shown in Figure B.3, where modulation data at various frequencies is simulated and the exact model Equation B.17, and the reduced model, Equation B.18, are used to interpret the results. Inward convective velocity corresponds to a positive slope, and outward convective velocity corresponds to a negative slope in Figure B.3.

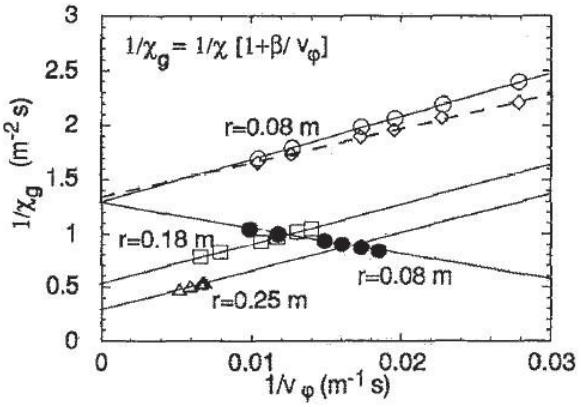

Figure B.3: Simulated modulation data at various frequencies, for different radial positions, and for inward (open symbols) and outward (full symbols) heat velocities U. Solid lines refer to the exact model while the dashed one refers to the reduced model. Reproduced from [105].

In the absence of multiple frequency measurements, neglecting the possibility of a heat pinch and taking $\frac{\chi_e'}{4\chi_e}$ small leaves the commonly used expression for the thermal diffusivity

$$\chi_e^{inc} = \frac{3}{4}\frac{\omega}{-\varphi'\left(\frac{d\ln T_\omega}{d\rho} - \frac{1}{2\rho_g}\right)}. \tag{B.19}$$

Equation B.19 can be written as the geometric mean of the contributions from the amplitude decay, and the phase delay as $\chi_e^{inc} = \sqrt{\chi_e^A \chi_e^\varphi}$. Here $\chi_e^A = \frac{3\omega}{4}\left(\frac{\delta T_e'}{T_\omega} - \frac{1}{2\rho_g}\right)^{-2}$, $\chi_e^\varphi = \frac{3\omega}{4}(\varphi')^{-2}$, and $\rho_g^{-1} = \rho_n^{-1} + \rho_{\chi_e}^{-1} \approx \rho_n^{-1}$. This is a general solution that includes the effects of damping, as the contribution to the phase and amplitude terms cancel [105].

To obtain the cylindrical geometry solution for the thermal diffusivity, the under-damped plane-wave solution must be replaced by an under-damped cylindrical wave solution, $T_\omega = \frac{1}{\sqrt{\rho}}Ae^{-\alpha\rho}e^{i(k\rho-\omega t)}$, so that

$$\frac{d\ln T_\omega}{d\rho} = \frac{1}{T_\omega}\frac{dT_\omega}{d\rho} = -\frac{1}{2\rho} - (\alpha - ik)\,, \qquad \frac{d}{d\rho}\frac{d\ln T_\omega}{d\rho} = \frac{1}{2\rho^2} - \frac{d}{d\rho}(\alpha - ik)\,,$$

$$\frac{1}{T_\omega}\frac{d^2T_\omega}{d\rho^2} = -\frac{1}{T_\omega}\frac{d}{d\rho}\left[\left(\frac{1}{2\rho} + (\alpha - ik)\right)\frac{1}{\sqrt{\rho}}Ae^{-\alpha\rho}e^{i(k\rho-\omega t)}\right],$$

$$\frac{1}{T_\omega}\frac{d^2T_\omega}{d\rho^2} = -\frac{d}{d\rho}\left[\left(\frac{1}{2\rho} + (\alpha - ik)\right)\right] + \left(\frac{1}{2\rho} + (\alpha - ik)\right)^2.$$

Now $\alpha = -Re\left[\frac{d\ln T_\omega}{d\rho} + \frac{1}{2\rho}\right]$, in place of $\alpha = -Re\left[\frac{d\ln T_\omega}{d\rho}\right]$, and the extra term can temporarily be folded into α, as $\alpha = \alpha + \frac{1}{2\rho}$,

$$\frac{d\ln T_\omega}{d\rho} = \frac{1}{T_\omega}\frac{dT_\omega}{d\rho} = -(\alpha - ik), \qquad \frac{d}{d\rho}\frac{d\ln T_\omega}{d\rho} = -\frac{d}{d\rho}(\alpha - ik),$$

and the equation has the same form as the slab case. There are no other cylindrical corrections to be made, except in the ρ_g^{-1} term. In the slab case $\rho_g^{-1} = \rho_n^{-1} + \rho_{\chi_e}^{-1}$, and in the cylindrical case $\rho_g^{-1} = \rho^{-1} + \rho_n^{-1} + \rho_{\chi_e}^{-1}$. In the cylindrical model,

$$\left[\frac{d}{d\rho}\frac{d\ln T_\omega}{d\rho} - \frac{1}{\rho_g}\frac{d\ln T_\omega}{d\rho} + \left(\frac{d\ln T_\omega}{d\rho}\right)^2 + \frac{3}{2}\frac{i\omega}{\chi_e}\right] = 0.$$

The incremental thermal diffusivity in the cylindrical model is obtained by replacing $\frac{\delta T_e'}{T_\omega} = \frac{\delta T_e'}{T_\omega} + \frac{1}{2\rho}$, and $\rho_g^{-1} = \rho_n^{-1} + \rho_\chi^{-1} = -\frac{d}{d\rho}\ln(n_e\chi)$,

$$\chi_e^{inc} = \frac{3}{4}\frac{\omega}{-\varphi'\left(\frac{d\ln T_\omega}{d\rho} + \frac{1}{2\rho} - \frac{1}{2\rho_n} - \frac{1}{2\rho_{\chi_e}}\right)}. \tag{B.20}$$

If the scale length of the diffusivity is neglected, Equation B.20 is the reduced model of Reference [105] in cylindrical geometry with no heat pinch. This is the model used in the analysis of ASDEX Upgrade measurements in Reference [54] .

The flux-surface averaged solution for the experimental geometry is approximated as a cylinder with flux-surface shaping. The flux-surface averaged incremental thermal diffusivity is an effective diffusivity $\chi_{e,eff}^{inc} = \frac{\langle\chi_e|\nabla\rho|^2\rangle}{\langle|\nabla\rho|^2\rangle}$, because of the flux surface average. The flux-surface shaping effect is retained by using $\rho_g^{-1} = \rho_n^{-1} + \rho_{V'}^{-1} + \rho_{\chi_e}^{-1} = -\frac{d}{d\rho}\ln(n_eV'\langle\chi_e|\nabla\rho|^2\rangle)$, so that in the cylindrical limit the $\rho_{V'}^{-1}$ term reduces to $-\rho^{-1}$, and in the slab limit the $\rho_{V'}^{-1}$ term reduces to 0. The full geometry including profile shapes and flux-surface shaping is

$$\frac{d}{d\rho}\frac{d\ln T_\omega}{d\rho} - \frac{1}{\rho_g}\frac{d\ln T_\omega}{d\rho} + \left(\frac{d\ln T_\omega}{d\rho}\right)^2 + \frac{3}{2}\frac{i\omega}{\langle\chi_e|\nabla\rho|^2\rangle} = 0,$$

and the resulting effective incremental thermal diffusivity is

$$\chi_{e,eff}^{inc} = \frac{\langle \chi_e |\nabla\rho|^2 \rangle}{\langle |\nabla\rho|^2 \rangle} = \frac{3}{4\langle |\nabla\rho|^2 \rangle} \frac{\omega}{-\varphi' \left(\frac{d \ln T_\omega}{d\rho} + \frac{1}{2}\frac{d}{d\rho} \ln \left[n_e V' \langle \chi_e |\nabla\rho|^2 \rangle \right] \right)},$$

$$\chi_{e,eff}^{inc} = \frac{3}{4\langle |\nabla\rho|^2 \rangle} \frac{\omega}{-\varphi' \left(\frac{d \ln T_\omega}{d\rho} - \frac{1}{2\rho_g} \right)}.$$

Additionally, if a heat pinch is allowed, it should be interpreted as a flux-surface averaged heat pinch $\langle U \left| \vec{\nabla}\rho \right| \rangle$, so that the effective heat pinch is $U_{eff} = \frac{\langle U \left| \vec{\nabla}\rho \right| \rangle}{\langle |\nabla\rho|^2 \rangle}$.

Appendix B: Bibliography

41. Kirov, K. K., Andreev, V. F., Leuterer, F., *et al. Plasma Phys. Control. Fusion* **48,** 245–262 (2006).

54. Ryter, F., Tardini, G., Luca, F. D., *et al. Nucl. Fusion* **43,** 1396–1404 (2003).

103. Fredrickson, E. D., Callen, J. D., McGuire, K., *et al. Nucl. Fusion* **26,** 849 (1986).

105. Jacchia, A., Mantica, P., Luca, F. D., *et al. Phys. Fluids B* **3,** 3033–40 (1991).

124. Jahns, G. L., Soler, M., Waddell, B. V., *et al. Nucl. Fusion* **18,** 609–628 (1978).

125. Soler, M. & Callen, J. D. *Nucl. Fusion* **19,** 703–714 (1979).

Appendix C: Quasi-optical Beams

Quasi-optical (QO) techniques were used in the design of the hybrid quasi-optical beam lines that transmit power from the gyrotrons to the plasma in HSX. Quasi-optical techniques are also used to model the antenna pattern of the ECE diagnostic on HSX. Quasi-optics makes use of the paraxial approximation to model the propagation of approximately Gaussian beams in the limit of finite wavelength [83].

C.1 The Gaussian Solution to the Paraxial Wave Equation

The paraxial wave equation describes the propagation of a wave with a well-defined direction of propagation, but slow (on the scale of the wavelength) transverse variation. The paraxial approximation is valid as long as the angular divergence of the beam is confined to 0.5 radians (30 degrees) [83],

$$\frac{\partial^2 u}{\partial r^2} + \frac{1}{r}\frac{\partial u}{\partial r} - 2jk\frac{\partial u}{\partial z} = 0, \tag{C.1}$$

$$u(r,z) = \frac{w_o}{w}\exp\left(\frac{-r^2}{w^2} - \frac{j\pi r^2}{\lambda R} + j\phi_o\right). \tag{C.2}$$

In cylindrical coordinates (r,φ,z), an axially symmetric wave of magnitude, $u(r,z)$, propagating along the z-direction is described by the paraxial wave equation, Equation C.1. Here $j = \sqrt{-1}$, and $k = \frac{2\pi}{\lambda}$ is the wave-number. The fundamental solution to Equation C.1 is a Gaussian beam mode, Equation C.2, in which $w(z)$ is the beam-waist, $w_o = w(0)$, $R(z)$ is the radius of curvature of the beam front and $\phi(r)$ is the phase along the direction of propagation. ϕ_o is initial phase, and q is the complex beam parameter. The beam waist is the radius at which the power in the beam has fallen to the e^{-2} power level.

The transverse wave-electric field of the fundamental Gaussian mode, along with other Gaussian beam parameters, are shown below. Higher-order solutions are also possible in

terms of Laguerre polynomials [83].

$$\text{Tansverse Field} \qquad E(r,z) = \left(\frac{2}{\pi w^2(z)}\right)^{0.5} \exp\left[\frac{-r^2}{w^2} - jkz - \frac{j\pi r^2}{\lambda R(z)} + j\phi_o\right]$$

$$\text{Beam Radius} \qquad w(z) = w_o\left[1 + \left(\frac{z}{z_R}\right)^2\right]^{0.5}, \text{where } z_R = \frac{\pi w_o^2}{\lambda}$$

$$\text{Curvature Radius of Phase Front} \qquad R(z) = z\left[1 + \left(\frac{z_R}{z}\right)^2\right],$$

$$\text{Beam Phase} \qquad \phi_o(z) = \tan^{-1}\left(\frac{z}{z_R}\right)$$

$$\text{Beam Parameter} \qquad q = z + jz_R$$

$$\text{Beam Power Distribution} \qquad \frac{P(r)}{P(0)} = \exp\left[-2(\frac{r}{w(z)})^2\right]$$

A graphical illustration of some of these parameters is provided in Figure C.1, where the Rayleigh range, $z_R = \frac{\pi w_o^2}{\lambda}$, occurs at $w(z_R) = \sqrt{2}w_o$. In the far-field, the angle of divergence of the beam is determined from the radius of curvature to be $\theta_0 = \frac{\lambda}{\pi w_o}$, and the angle of the full-width at half-max in the beam power is $\theta_{fwhm} = 1.18\theta_0$. A fixed frequency Gaussian beam is completely specified by its beam waist and radius of curvature.

C.2 Ray Transfer Matrices

In the paraxial approximation, the angle of propagation with respect to the beam axis is assumed to be small such that $\sin(\theta) \approx \theta$. Then the wave propagation can be described by a matrix equation for the ray position, and the ray slope. In Equation C.3, the 2x2 matrix is referred to as an ABCD matrix. A quasi-optical system can then be described as being composed of a set of elements that each possess their own ABCD matrix. Propagation through the system results in a single ABCD matrix that is the matrix product of the system

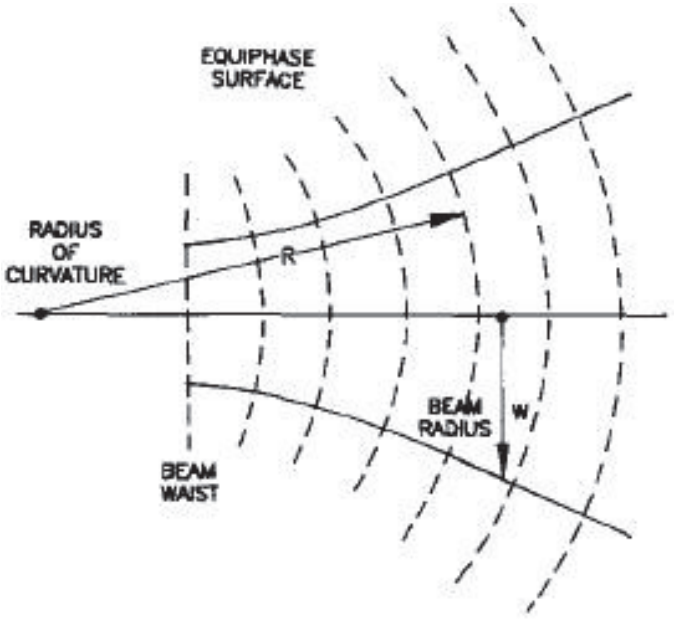

Figure C.1: Quasi-optical Gaussian beam waist, divergence, radius of curvature, and equiphase surfaces. Reproduced from [84]

elements ray transfer matrices,

$$\begin{pmatrix} r_{out} \\ r'_{out} \end{pmatrix} = \begin{pmatrix} A & B \\ C & D \end{pmatrix} \begin{pmatrix} r_{in} \\ r'_{in} \end{pmatrix}. \tag{C.3}$$

Since a Gaussian beam is completely specified by its beam waist and its radius of curvature, the propagation is completely described by the beam parameter. In terms of these two quantities, the beam parameter is $q^{-1} = R^{-1} - \frac{j\lambda}{\pi w^2}$. For quasi-optical transmission, the ray transfer matrices of a lumped element are the same as those from geometric optics, with the output beam parameter related to the input beam parameter through the ABCD law C.4 [84],

$$q_{out} = \frac{Aq_{in} + B}{Cq_{in} + D}. \tag{C.4}$$

A table of ray transformation matrices (RTMs) is available from many sources, including [84] and [83]. Some fundamental RTMs used in the analysis of the ECE and ECRH on HSX

are,

$$\begin{aligned}
&\text{Distance L in uniform media} && \begin{pmatrix} 1 & L \\ 0 & 1 \end{pmatrix}, \\
&\text{Thin lens of focal length } f && \begin{pmatrix} 1 & 0 \\ -\frac{1}{f} & 1 \end{pmatrix}, \\
&\text{Transformation by a thin lens} && \begin{pmatrix} 1-\frac{d_2}{f} & d_{in}+d_2(1-\frac{d_{in}}{f}) \\ \frac{-1}{f} & 1-\frac{d_{in}}{f} \end{pmatrix}.
\end{aligned} \tag{C.5}$$

Here d_2 represents the distance following the thin lens of focal length f, and d_{in} represents the distance to the next element. For a spherical mirror of radius of curvature R, the focal length is given by $f^{-1} = \frac{2}{R}$. For an ellipsoidal mirror, where d_1 and d_2 are the distances from the section center of the ellipsoid to the respective foci, the focal length is given by $f^{-1} = d_1^{-1} + d_2^{-1}$.

C.3 The ECE antenna

In the analysis of the ECE antenna in Chapter 3, the antenna reciprocity theorem [126] is used to model the TEM wave sampled by the ECE antenna as a Gaussian beam launched from the ECE antenna into the plasma. The wave electric field within the aperture of the pyramidal horn of the ECE antenna is constrained to be perpendicular to its walls, because copper may be considered a perfect electrical conductor to microwaves, and the radius of curvature of the equiphase surfaces of the beam is constrained by the horn geometry.

The length of the horn is 10.16 cm, and the aperture dimensions are $A = 3.76$ cm and $B = 3.5$ cm respectively. The horn couples power into a WR-42 waveguide that has dimensions $a = 1.1$ cm and $b = 0.43$ cm at the feed-end of the horn. For completeness, the distance between the horn aperture and the center of the ellipsoidal mirror is 7.5 cm.

The Gaussian beam that couples to the horn has a radius of curvature of 12.5 cm. Optimum coupling to the horn occurs for a beam waist at the aperture of the horn of $w_h = 0.35\frac{A}{2}$ in the plane containing the wave magnetic field, and $w_e = 0.5\frac{B}{2}$ in the plane containing the wave electric field [83]. The beam waist occurs within the aperture of the antenna, and the equivalent Gaussian beam is determined by propagating the wave into its throat using [83],

$$\frac{w_h}{w_{o,h}} = \sqrt{1 + \left(\frac{\pi w_h^2}{\lambda L_a}\right)^2}, \qquad \frac{w_e}{w_{o,e}} = \sqrt{1 + \left(\frac{\pi w_e^2}{\lambda L_b}\right)^2}. \tag{C.6}$$

The ellipsoidal mirror used in the ECE antenna is set at an angle of 54.5 degrees with respect to the incident wave, and is cut from an ellipsoid with minor- and major- radii of $a_{min} = 13.7$ cm and $b_{maj} = 23.6$ cm respectively. For a Gaussian beam incident on an ellipsoidal mirror at an angle $\phi = 54.5°$, the focal length may be written in terms of the curvature of the mirror. The radius of curvature of the ellipsoidal mirror perpendicular and parallel to the plane of incidence of the wave are $R_\perp = a_{min}$ and $R_\parallel = \frac{b_{maj}^2}{R_\perp}$ respectively. The corresponding focal lengths of the thin lens are $f_\perp = 0.5R_\perp/\cos\phi$ in the direction perpendicular to the plane of incidence, and $f_\parallel = 0.5R_\parallel \cos\phi$ parallel to the plane of incidence [83]. The focal length of the ellipsoidal mirror is $f_\parallel = f_\perp = 11.8$ cm. Other dimensions of the ECE antenna can be determined from the block diagram provided in Figure C.2.

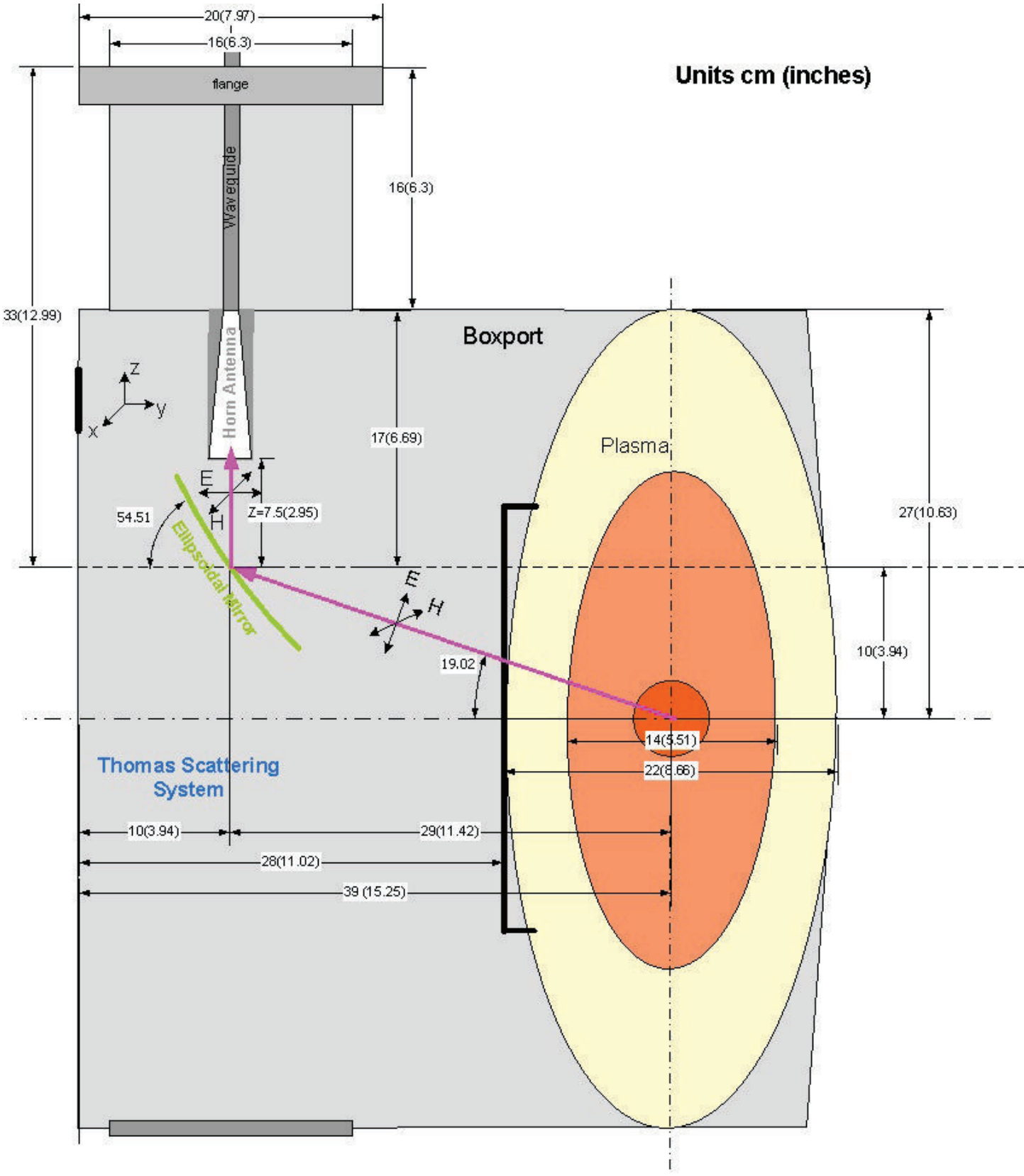

Figure C.2: The ECE antenna within boxport D of HSX. Dimensions are in cm (inches).

Appendix C: Bibliography

83. Goldsmith, P. F., Theory, I. M. & Society, T. (*Quasioptical systems*, Piscataway, NJ : IEEE Press, 1998).

84. Goldsmith, P. F. *Proceedings of the IEEE.* **80,** 1729–1747 (1992).

126. Balanis, C. A. *Advanced Engineering Electromagnetics*, 1st (John Wiley and Sons, New York, 1989).

Appendix D: Absolute Calibration of the Radiometer

This appendix is meant to provide the basic equations that relate the measured antenna temperature to the radiation temperature. The data sheet of the noise-source used during absolute calibration of the ECE radiometer is also included in Figure D.1. Additional documentation is available upon request, including the calibration procedure for the HSX ECE radiometer.

The radiometer gain in Section 3.2 relates the power through the waveguide to the voltage from the radiometer, but it does not include the gain of the ECE antenna. On HSX, modeling is necessary to determine the radiation temperature of the plasma from the antenna temperature measured by the radiometer, because the antenna is not fully illuminated by the core of the plasma (within $r/a < 0.2$). A thorough discussion of that modeling is included in Chapter 3. In this section, the antenna temperature will be related to the radiation temperature of the plasma assuming that the ECE antenna is fully illuminated by the plasma.

The power passing through the waveguide after the terminal of the ECE antenna is equivalent to the total power collected by the antenna, and that power is the product of the power flux through the aperture and the antenna efficiency, $P_A = \Phi A_e$. The power flux is related to the specific intensity of the electron cyclotron emission, which is discussed in detail in Chapter 2 and Chapter 3, and the antenna efficiency is determined by its radiation pattern, which is modeled in Chapter 3. The power flux is the product of the radiance of the source and the solid angle of the plasma subtended by the antenna, so that the total power collected by the antenna is $P_A = I_r \Omega A_e$. Finally, the radiance is related to the specific intensity of the source, $I_r = \int I_\omega d\omega = B I_\omega$, which is proportional to the radiation temperature.

The power at the terminals of the antenna in terms of the radiation temperature of the emission from the plasma, the wavelength of the radiation, the bandwidth of each channel, the effective aperture of the antenna, and the solid angle of the antenna is,

$$P_A \approx \Omega A_e B I_\omega = \Omega A_e \frac{\omega^2}{8\pi^3 c^2} k B T_{rad} = \frac{\Omega A_e}{2\pi\lambda^2} k B T_{rad}. \tag{D.1}$$

Then the signal measured by the radiometer is related to the radiation temperature through,

$$\begin{aligned} P_A = G V_{rad} + k B T_r &= \frac{\Omega A_e}{2\pi\lambda^2} k B T_{rad}, \\ k B T_{rad} &= \frac{2\pi\lambda^2}{\Omega A_e} \left(G V_{rad} + k B T_r \right). \end{aligned} \tag{D.2}$$

QUINSTAR TECHNOLOGY, INC.

NOISE SOURCE
DATA SHEET

CUSTOMER: University of Wisconsin-Madison PO# 414K304 114602

MODEL # QNS-FB15LV S/O# 015449-0001 S/N 15449001001

SPECIFICATIONS

FREQUENCY RANGE	50 to 75	GHz	
ENR VALUE	15	dB typ.	
FLATNESS VARIATION	+/- 2.0	dB typ.	
BIAS VOLTAGE	+28 (Pulsed)	VDC From HP8970A	
BIAS INPUT CONNECTOR	BNC (F)		
ENR OUTPUT WAVEGUIDE	WR-15	FLANGE:	UG-385/U

PERFORMANCE DATA

FREQ (GHz)	ENR (dB)	FREQ (GHz)	ENR (dB)	FREQ (GHz)	ENR (dB)	FREQ (GHz)	ENR (dB)
50	18.3	65	16.9				
51	17.6	66	17.5				
52	17.4	67	16.5				
53	16.5	68	16.7				
54	17.5	69	16.2				
55	17.4	70	16.1				
56	17.2	71	15.8				
57	16.6	72	17.0				
58	17.7	73	16.3				
59	17.3	74	16.4				
60	18.1	75	15.0				
61	17.4						
62	17.8						
63	17.4						
64	17.5						

NOTE: A matched Isolator is included.

TEST TECH: B. Chen DATE: 11/01/12

QUALITY: DATE: 11/2/12

DS 051 rev. A 01.05.10

Figure D.1: QuinStar Noise-Source Data Sheet